A DETAILED STUDY OF THE FLOWFIELD OF A SUBMARINE PROPELLER DURING A CRASHBACK MANEUVER

FINAL REPORT

David H. Bridges
Mississippi State University
Department of Aerospace Engineering
Mississippi State, MS 39762

August 2004

20041014 017

MSSU-ASE-04-01

DEPARTMENT OF AEROSPACE ENGINEERING

ANTHONY J. VIZZINI, PH. D.
HEAD, DEPARTMENT OF AEROSPACE ENGINEERING

DAVID L. LAWRENCE, P. E.
DIRECTOR, RASPET FLIGHT RESEARCH LABORATORY

JAMES WORTH BAGLEY COLLEGE OF ENGINEERING

ROBERT P. TAYLOR, PH. D.
INTERIM DEAN

For additional copies or information, address correspondence to:

Department of Aerospace Engineering
Mississippi State University
P.O. Box A
Mississippi State, MS 39762

Telephone (662) 325-3623
Fax (662) 325-7730

A DETAILED STUDY OF THE FLOWFIELD OF A SUBMARINE PROPELLER DURING A CRASHBACK MANEUVER

FINAL REPORT

David H. Bridges
Mississippi State University
Department of Aerospace Engineering
Mississippi State, MS 39762

August 2004

MSSU-ASE-04-01

ii

Abstract

In order to decelerate a forward-moving submarine rapidly, often the propeller of the submarine is placed abruptly into reverse rotation, causing the propeller to generate a thrust force in the direction opposite to the submarine's motion. This maneuver is known as the "crashback" maneuver. During crashback, the relative flow velocities in the vicinity of the propeller lead to the creation of a ring vortex around the propeller. This vortex has an unsteady asymmetry which produces off-axis forces and moments on the propeller that are transmitted to the submarine. These forces and moments prevent the submarine from moving forward in a straight path. This is a critical issue in shallow water or littoral regions where precise control is required. Tests were conducted in the Large Cavitation Channel (LCC) using an existing submarine model and propeller. Forces and moments were measured on the body using a dynamometer mounted between the sting and the body. Forces and moments were also measured on the propeller itself, using a new dynamometer that was mounted between the propeller and the propeller shaft. Laser Doppler velocimeter (LDV) measurements were made and flow visualization studies were also conducted. A range of steady crashback conditions with fixed tunnel and propeller speeds were investigated. The dimensionless force and moment data were found to collapse well when plotted against the parameter η, which is defined as the ratio of the actual propeller speed to the propeller speed required for self-propulsion in forward motion (the point where thrust is equal to drag). The force and moment coefficients were found to have local maxima around $\eta \approx -0.8$. Unsteady crashback maneuvers were also investigated with two different types of simulations. In the first type, the tunnel speed was held steady and the propeller was allowed to "windmill" in forward rotation. A reverse rotation rate was then commanded, and measurements were made through the propeller's deceleration and acceleration in the reverse direction. In the second type of simulation, the same procedure as the first type was repeated, but when the propeller first engaged in reverse rotation, the tunnel set speed was set to zero and the tunnel was allowed to decelerate on its own. This deceleration mimicked the deceleration the submarine would see during a crashback maneuver. It was noted during these simulations that the peak off-axis force and moment coefficient magnitudes could exceed those observed during the steady crashback measurements. The magnitude of these force and moment coefficients tracked the tunnel deceleration closely, suggesting the weakening of the ring vortex as the relative shear between the free stream flow and the propeller-induced flow decreased. The LDV studies showed that the ring vortex structure varied from an elongated vortex structure centered downstream of the propeller to a more compact structure that was located nearer the propeller as η became more negative, up to $\eta \approx -0.8$. Past that value of η, the vortex core appeared to move out toward the propeller tip. These types of vortex core behavior were also noted in the flow visualization experiments. The flow visualization experiments also revealed large-scale disturbances to the ring vortex through either apparent vortex-shedding events or large-scale disruptions in which the vortex ring seemed to disappear altogether. These disturbances seemed to be most periodic around $\eta \approx -0.8$, thereby providing a possible explanation for the peaks in the coefficients near this value of η.

iv

Table of Contents

List of Symbols

C_F	Generic force coefficient
C_M	Generic moment coefficient
C_{Mz}	Yawing moment coefficient obtained from root mean square value of the yawing moment
C_{th}	Thrust loading coefficient
D	Propeller diameter; drag force
D_h	Model hull diameter
F	Generic force
F_x	Body force in x direction
f	Hydrodynamic frequency
f_H	Propeller force in horizontal direction (relative to tunnel test section)
f_V	Propeller force in vertical direction (relative to tunnel test section)
f_x	Propeller force in x direction
F_y	Body force in y direction
f_y	Propeller force in y direction (in reference frame fixed to rotating propeller)
F_z	Body force in z direction
f_z	Propeller force in z direction (in reference frame fixed to rotating propeller)
J	Advance ratio
K_Q	Propeller torque coefficient
K_T	Propeller thrust coefficient
L	Model hull length
M	Generic moment
M_x	Body moment about the x axis (rolling moment)
m_x	Propeller moment about the x axis
M_y	Body moment about the y axis (pitching moment)
m_y	Propeller moment about the y axis
M_z	Body moment about the z axis (yawing moment)
M_z'	Root mean square value of yawing moment
M_z''	Root mean square value of M_z'
$M_{z,m}''$	Standard deviation of the mean value of M_z'
m_z	Propeller moment about the z axis
n	Propeller rotational speed
n_{sp}	Propeller rotational speed for self-propulsion point (thrust equal to drag)
q_∞	Free steam dynamic pressure
r	Radial coordinate measured from model axis
R_{prop}	Propeller radius
t	Time

t'	Dimensionless time
t_0	Propeller reverse rotation engagement time
U_x, u	Streamwise velocity component measured by LDV in LDV grid coordinates, positive downstream
u'	Fluctuating component of streamwise velocity measured by LDV
U_z, v	Transverse/radial velocity component measured by LDV in LDV grid coordinates, positive up from tunnel floor
V, V_∞	Free stream velocity
$V_{venturi}$	Tunnel free stream velocity as determined by calibration of pressure drop across tunnel contraction
v'	Fluctuating component of radial velocity measured by LDV
x	Body-fixed coordinate, positive forward; LDV grid coordinate, positive downstream
x_{prop}	Streamwise location of propeller plane in LDV grid coordinates
y	Body-fixed coordinate, positive starboard
y_p	Propeller-fixed coordinate
z	Body-fixed coordinate, positive down
z_p	Propeller-fixed coordinate
η	Propulsion similarity parameter; ratio of propeller speed to propeller speed for self-propulsion
θ	Propeller rotational position coordinate
ρ_∞	Free stream density
ω	Reduced hydrodynamic frequency

This page intentionally left blank.

1. INTRODUCTION

1.1   Statement of the problem

When a submarine is traveling in the forward direction and a rapid deceleration is required, the propeller of the submarine is put into reverse rotation. For some time the submarine continues to move forward while the propeller, operating in the reverse direction, is acting to decelerate the submarine. This condition of forward body velocity and reverse propeller rotation is referred to as *crashback*, and the maneuver is referred to as a *crashback maneuver*. All that is desired during the maneuver is a decrease in the submarine's forward velocity. No trajectory changes are commanded. However, because of the relative flow velocities in the vicinity of the propeller, a ring vortex develops around the propeller. This condition is illustrated schematically in Figure 1.1 (figures may be found at the end of the report). The velocities shown in this figure are relative to an observer fixed to the submarine. Because of the forward motion of the submarine, the flow velocities outside the propeller are directed rearward. However, because of the flow induced by the propeller operating in reverse, the velocities on the axis are directed upstream, toward the submarine. The shear between the velocities on the axis and the velocities outside the propeller causes the ring vortex to form. The ring vortex is not axisymmetric, however, and the asymmetry moves around the vortex. This asymmetry in the location and strength of the vortex results in force and moment components on the propeller about axes perpendicular to the propeller and submarine axis. These off-axis forces and moments are then transmitted to the submarine itself. The asymmetric forces and moments lead to uncommanded trajectory changes, so that in addition to continued forward motion, the submarine may pitch or yaw in an uncommanded fashion. In the shallow waters of littoral regions, where submarines have begun to operate, pinpoint control is a much larger issue than it was when most submarine actions took place in deep water (see Gruner and Payne (1992) and Wright (1995) for discussions of shallow-water submarine operations).

1.2   Previous work on crashback

The existence of a ring vortex around a propeller operating in a direction counter to forward motion has been known for some time, and according to Jiang *et al.* (1997) was first reported by Lock (1928), based upon observations of the flow past a propeller in a wind tunnel. Glauert (1934) presented an estimate of propeller performance in the vortex ring state using a blade element analysis. Glauert pointed out that the standard momentum analysis for propeller performance could not be performed, because a true slipstream did not form.

The vortex ring state is of some importance in helicopter aerodynamics, also. In a vertical descent, a ring vortex can form around the helicopter blade in such a fashion that in a time-averaged sense the stream surface around the blade is closed. Since no flow enters or leaves, there is no momentum change possible and the helicopter rotor can no longer generate lift. This phenomenon is discussed in some detail in the helicopter aerodynamics textbook by Prouty (1990).

One of the primary characteristics attributed to the vortex ring state by Prouty is the large unsteadiness in the flow. Flow visualization photographs of smoke flowing past a model helicopter shows a repeated pattern of ring vortex formation and ring vortex "bursting." If the helicopter has the capability of generating forward airspeed, that is usually sufficient to allow the helicopter to escape the vortex ring state.

The determination of propeller performance in crashback is a standard component of so-called "four-quadrant" propeller performance tests. The term "four-quadrant" is a reference to the fact that propeller performance in all four quadrants of the velocity-rotational speed (V-n) plane is measured: forward motion ($V > 0$, $n > 0$), backing motion ($V < 0$, $n < 0$), crashback ($V > 0$, $n < 0$) and crashahead ($V < 0$, $n > 0$). The reports by Hecker and Remmers (1971) and Boswell (1971) contain examples of such performance measures. In terms of actual flow physics, however, the work of Jiang et $al.$ (1997) appears to be one of the first studies of the fluid dynamic phenomena associated with the crashback maneuver on a submerged marine propeller. Jiang et $al.$ studied the flow past David Taylor Model Basin (DTMB) Propeller 4381 (more on this propeller in the next chapter) through the use of flow visualization and force measurements. These were propeller-only or open-water studies conducted with the propeller mounted on a drive shaft in the DTMB 24-inch water tunnel. Jiang et $al.$ noted the unsteadiness of the ring vortex and also its frequent "bursting" and re-formation. The force measurements indicated strong off-axis forces and moments generated on the propeller by the unsteady asymmetry of the ring vortex. The results of this study will be discussed in more detail later, in the context of the results to be presented in this report.

Propeller 4381 has been the subject of a number of experimental and numerical studies. Chen and Stern (1998) performed a four-quadrant computational study of P4381. This study used the unsteady, three-dimensional incompressible Reynolds-averaged Navier-Stokes equations in generalized coordinates and the Baldwin-Lomax turbulence model. Their computed results for thrust and torque were in generally good agreement with measured open-water values for P4381 as reported by Hecker and Remmers (1971) and cited by Chen and Stern. The results of Chen and Stern related to the crashback maneuver were confined to a comparison of their computed streamline patterns with the flow visualization photographs of Jiang et $al.$ (1997) and a comment that both the experiments and the computations indicate that the ring vortex grows in size and moves outboard as the advance ratio J increases, where J is defined as $J = V/nD$, with V equal to the velocity of flow, n equal to the rotational velocity of the propeller, and D equal to the propeller diameter.

The results of a considerably more in-depth computational study of the crashback maneuver are included in the report edited by Zierke (1997). These results are part of a larger study involving various aspects of submarine maneuvering problems. In these studies, the propellers were modeled as being mounted on the SUBOFF submarine body (see Groves et $al.$ (1989) for details of the SUBOFF geometry). The crashback studies in Zierke made use of P4381. The unsteady Reynolds-averaged Navier-Stokes equations for incompressible flow were used, along with an algebraic turbulence model. These studies examined not only the fluid mechanics of the ring vortex around the propeller but also the trajectory of the submarine during the crashback maneuver. The studies showed the existence of a ring vortex around the propeller with an unsteady asymmetry that essentially rotated around the submarine axis. The frequency of this rotation was matched to the frequencies of off-axis forces and moments obtained from the computations. The studies also demonstrated some of the behavior of the ring vortex relative to the propeller, such as instances where the ring

vortex "touched" a propeller blade and the corresponding pressure signatures on the blade. The submarine trajectories predicted by the computations demonstrated the "wandering" motion caused by the out-of-place forces and moments generated by the asymmetry of the ring vortex. It is precisely these "wanderings" that are the major concern for shallow-water maneuvers. The results of the computational studies did not demonstrate vortex bursting or re-formation, however, and the behavior of the ring vortex was generally much more benign than that usually observed in experiments.

1.3   Overview of report

An extensive study of crashback was performed in the U. S. Navy's William B. Morgan Large Cavitation Channel (LCC), located in Memphis, Tennessee. Propeller 4381 was attached to a standard axisymmetric submarine hull model (DTMB Model 5495-3) which was then suspended in the LCC. Forces and moments were measured on both the body and the propeller for steady and unsteady crashback conditions. The unsteady conditions were simulated by allowing the propeller to "windmill" in the forward direction and then engaging the propeller in the reverse direction, with the tunnel velocity held constant. Forces and moments were measured during the change in propeller speed. A further simulation was undertaken whereby the tunnel motor was shut off once the windmilling propeller engaged in reverse rotation, and the tunnel speed was allowed to coast down to zero. Forces and moments were measured during this simulation also. In addition to the force and moment measurements, laser Doppler velocimeter (LDV) measurements of the flow field around the propeller during steady crashback were obtained, in addition to extensive flow visualization measurements. The experimental apparatus and procedures used in this study are discussed in chapter 2. The results of the force and moment measurements for the steady and unsteady crashback studies are discussed in chapter 3, and the velocity field and flow visualization studies are discussed in chapter 4. Conclusions and recommendations for future work are contained in chapter 5.

2. EXPERIMENTAL APPARATUS AND PROCEDURE

2.1   Facility

The experiments to be described in this report were all conducted in the William B. Morgan Large Cavitation Channel (LCC), located in Memphis, Tennessee. This facility is part of the Carderock Division of the Naval Surface Warfare Center (NSWCCD) and was first made operational in 1991. The LCC has a test section that is 3.05 m (10 ft) high, 3.05 m (10 ft) wide, and 12.2 m (40 ft) long. The maximum test section speed is approximately 18 m/s (35 kts), and the pressurization range for the test section extends from 3.5 kPa (0.05 psia) to 415 kPa (60 psia). The freestream turbulence level is less than 0.5%. Details of the design, construction, and operation of this facility may be found in Etter and Wilson (1992; 1993). More recently Park, Cutbirth and Brewer (2002) have done an extensive study of the performance characteristics of the LCC and have documented in detail the flow temporal and spatial uniformity and the turbulence levels in the facility, as well as the data acquisition equipment and procedures for velocity measurements in the LCC test section. According to Park *et al.* (2002), the temporal stability of the LCC test section flow speed is ±0.15% for test section velocities between 0.5 and 18 m/s. The test section velocity is spatially uniform to within ±0.60% for velocities between 3 and 16 m/s. The turbulence level in the facility is between 0.2% and 0.5% for test section velocities from 0.5 to 15 m/s, with no harmonics appearing in the power spectra of the velocity signals. For all of the tests conducted during this study, the tunnel pressure was set at 50 psig at the test section top.

2.2   Model

The model used in these experiments was a standard axisymmetric hull with a sail and four standard cruciform stern appendages (DTMB Model 5495-3). The hull length L was 6.92 m (272.36 in) and the diameter D_h was 0.623 m (24.54 in). The hull outline is shown in Figure 2.1. The model was suspended using the standard LCC strut. The pivot point for the strut was located at $x/L = 0.22$. This was the reference point for the moment measurements. A fairing that essentially duplicated the sail was initially wrapped around the strut, but during preliminary tests it was decided that the fairing was not necessary and so it was removed before the actual testing began. A figure illustrating the placement of the stern appendages is shown in Figure 2.2. The fin cross-sections were NACA 0012 airfoil sections.

Past experience by LCC and NSWCCD staff had showed that the forces and moments and also the motions of the submarine model itself could be rather violent during crashback tests. Therefore, for the first phase of testing, tunnel and propeller conditions were limited and forces and moments were measured with both a body force and moment dynamometer, mounted between the strut and model, and a new propeller force and moment dynamometer (these two dynamometers will be discussed in detail below). When it was determined that the propeller dynamometer results were

consistent with the body dynamometer results, a stabilization strut was added to the rear of the model, connecting one of the stern fins to the LCC test section wall. This strut was available from a previous test (see Bridges, 2001) and is visible in Figure 2.2. This support strut was welded to the wall and extended out to the vertical rudder on the side of the model. The strut had a biconvex airfoil section for three-quarters of its length. This terminated in a axisymmetric body whose axis was aligned with the freestream flow direction. A threaded shaft extended from this body and spanned the remainder of the distance to the rudder. The threaded shaft was used to adjust the length of the support strut. The strut was added as a precaution, in order to prevent damage to either the model or the tunnel. With the strut attached, however, only propeller dynamometer results could be obtained.

2.3   Propeller

The propeller used in this test was DTMB Propeller no. 4381 (hereinafter referred to as P4381). This propeller was originally designed and built as part of a study of the effects of skew on marine propellers (Boswell 1971). P4381 was the unskewed propeller in this series. Interestingly, this study was funded by several commercial shipping companies, and so the propeller design itself and the results of the study were unclassified. The fact that P4381 has an unclassified geometry and that the actual model propeller still exists has resulted in a number of both experimental and computational studies being performed on it, including the current study.

P4381 is shown in Figure 2.3, in both a photograph (from Hecker and Remmers 1971) and an Autocad IGS file (courtesy Martin Donnelly, NSWCCD). A plan drawing of one of the blades (from Boswell 1971) is also included in the figure. P4381 is a five-bladed propeller with a diameter of 1 ft, an expanded area ratio of 0.725, an NACA $a = 0.8$ section meanline, and an NACA 66 section thickness distribution with NSRDC modifications to the nose and tail thicknesses. The design advance coefficient J was 0.889, and the design thrust loading coefficient C_{Th} was 0.534 (Boswell 1971). Open-water data for the thrust coefficient K_T and ten times the torque coefficient $10K_Q$ are shown in Figure 2.4 (data from Hecker and Remmers 1971).

P4381 was chosen for this test for both its existence, which saved the cost of manufacturing a new propeller, and for its status as an unclassified geometry. The drawback of using this propeller, however, was that it was not designed to be used on the hull model that was used. The overall propeller diameter D was smaller than that of propellers normally attached to the model hull used in the experiments, and the propeller hub was not tapered. The hub diameter was smaller than that of propellers normally attached to the model hull. This obstacle was overcome by attaching a tapered hull extension to the shaft of the motor in the model, and then attaching the propeller to this hull extension. The hull extension and dummy hub are shown in the drawing in Figure 2.5 (the shaded portion of the figure is the hull extension and dummy hub), and the hull extension and P4381 are shown mounted on the model hull in the photograph in Figure 2.5. The hull extension was designed such that it rotated with the propeller. The hull extension continued the hull slope down to the diameter of the hub on P4381. The "dummy hub," shown in the drawing in Figure 2.5, was used for calibration purposes. The effect of the spinning hub extension would be to increase measured forward thrust due to the larger area over which suction in the gap would act, and increase measured torque. These effects were not quantified, as the overall objective of the test was to quantify side forces experienced during crashback conditions. Bare-hub measurements would have been necessary to quantify and remove these effects from measured thrust and torque data.

An elliptic tip was attached behind the propeller, as shown in Figure 2.5. The model was located in the LCC test section such that the propeller would be centered in one of the test section windows, allowing ample room for LDV measurements and flow visualization photographs.

2.4   Instrumentation

2.4.1   Body force measurements

The forces on the model were measured using a AMTI 6-component dynamometer. This device is an internal force balance that was attached between the strut and the model. It was set up to measure forces in all three directions and moments about all three axes. The dynamometer was calibrated by a member of the NSWCCD staff who oversaw the setup and the initial use of the balance in the model at the LCC. The dynamometer voltages were converted to forces and moments using supplied calibration data. The systematic errors for this dynamometer are shown in Table 2.1 (the notation "2σ" indicates the value of twice the standard deviation).

Table 2.1 Estimates of systematic error for AMTI dynamometer

	F_x	F_y	F_z	M_x	M_y	M_z
% of full scale, max	0.18	0.17	0.6	0.59	0.19	0.65
% of full scale, min	-0.11	-0.28	-0.75	-0.49	-0.21	-0.67
2σ (% of full scale)	0.08	0.12	0.33	0.34	0.12	0.43
full scale, eng. units	5000 lbs	5000 lbs	5000 lbs	2500 ft-lbs	25000 ft-lbs	5000 ft-lbs
2σ, eng. units	4 lbs	6 lbs	16.5 lbs	8.5 ft-lbs	30 ft-lbs	21.5 ft-lbs

2.4.2   Propeller force and position measurements

The MicroCraft 6-component propeller dynamometer was a multi-component cylindrical assembly that attached to the propeller on its upstream face. The dynamometer is shown in Figure 2.5, just ahead of the hub extension. Strain gauges were glued to 12 flexures in order to measure three orthogonal forces and three moments. The gauges were arranged in Wheatstone bridge circuits with two to four arm circuits connected in parallel for each channel. The placement of multiple bridges was intended to cancel interactions from other forces and moments. This particular design had small interactions (<2%) except for bending moment interactions on the orthogonal side forces of about 41%. Care had to be taken to properly zero the balance so as to not artificially remove possible interactions.

A 6 x12 calibration matrix was used to calculate the forces and moments from the six input voltages. This matrix provided first and second order interactions of the various forces and moments and yielded a dynamometer error of less than 1% of each channel's full scale value. The multi-component construction of this dynamometer caused hysteresis effects that were the chief source of error. The estimates of the systematic error for this dynamometer are shown in Table 2.2.

Table 2.2 Estimates of systematic error for MicroCraft propeller dynamometer

Component	Load limit	Error as % of full scale (2σ)
f_x (thrust)	2000 lbs	0.40
f_y (side force)	500 lbs	0.55
f_z (normal force)	500 lbs	0.68
m_x (torque)	500 ft-lbs	0.17
m_y (pitch)	500 ft-lbs	0.17
m_z (yaw)	500 ft-lbs	0.02

The strain gage signals passed through slip rings to Vishay Model 2310 Instrumentation Amplifiers outside the tunnel. These amplifiers provided excitation voltage, bridge zeroing, gain, and filtering of the signals. For these tests, all filters were turned off, implying a wideband setting during the tests. The conditioned signals were then passed to the computer A/D inputs. Due to a limited number of slip ring connections it was necessary to group some of the bridge excitation lines to the dynamometer. Due to multiple bridges connected in parallel the current draw along these excitation lines could result in a voltage drop. As the dynamometer was calibrated with individual static excitation for each force or moment channel, additional calibration checks were conducted to adjust individually the gain of each channel to account for the lower excitation voltage. The details of these corrections are not discussed here except to state that the corrections adequately reduced any error introduced to levels quoted from calibration data.

An absolute position digital encoder, Model 25HN from Sequential Information Systems Inc., was used to monitor the angular location of the propeller and dynamometer. The encoder had a resolution of 2^{11} resulting in an angular position accuracy of 0.18°. This position information was used in the propeller weight subtraction procedure discussed below (Section 2.5.1). A separate optical pickup with a resolution of 60 pulses/rev was used to obtain propeller speed information. The output of this pickup was passed through a frequency-to-voltage converter so that the speed of the propeller could be recorded along with the force and moment and other data acquired by the computer. The resulting uncertainty in the propeller speed was approximately 1 rpm.

2.4.3 Velocity measurements

Measurements of the velocity field were obtained using the LCC's Dantec laser Doppler velocimeter (LDV) system. This system is described in great detail in the report by Park, Cutbirth and Brewer (2002). The system consists of 4 Dantec BSA 57N11 signal processors, 3 fiber optic probes, two Spectra Physics 6 W argon-ion lasers, a Dantec 3-D traverse, and Dantec Flow software. The LDV system was calibrated using a rotating disc. The resulting uncertainty in the calibration is reported by Park *et al.* (2002) to be less than 0.018 m/s at a disc speed corresponding to a tunnel speed of 15 m/s.

2.4.4 Data acquisition equipment

The data acquisition system was based on a Pentium III, 500 MHz computer running LabVIEW v5.1.1 and National Instruments data acquisition hardware. Analog signals were acquired with a 16-bit resolution multiple input output card with a maximum sampling rate of 125 kHz (National Instruments part # PCI-6031E). Digital signals, in particular the signal from the propeller position encoder, were acquired with a high-speed (13 Mbyte/s) digital interface card (National Instruments part # PCI-DIO32HS). These two cards were connected over the Real Time System Integration (RTSI) bus to enable signals from both cards to be acquired simultaneously. Near-simultaneous acquisition, limited by the rate at which the analog channels could be swept by the hardware, was essential so that propeller force data could be taken at known angular positions.

2.4.5 Flow visualization equipment

Laser sheet flow visualization was recorded for as many test conditions at which force data was acquired, as time permitted. The laser sheet delivery system included a fiber-optic connection to a 5W Coherent Argon-Ion laser and a set of sheet generating optics which could be mounted above the diagonal window and deliver a laser sheet to illuminate the propeller. The laser sheet was positioned such that it intersected the flow on the submarine axis. Both fluorescent dye and air bubbles emitted upstream from the submarine hull were used as flow trackers. A Betamax digital video camera and still 35mm camera provided and manned by the NSWC Carderock Media Lab was used to record all flow visualization. These were positioned to view the flow through the diagonal windows at the bottom of the LCC test section, so that the viewing direction was perpendicular to the laser sheet. A photograph of the laser sheet delivery system mounted to the LCC test section is shown in Figure 2.6. Due to the expansion angle of the laser sheet forming lens it was necessary to move the sheet upstream and downstream of the propeller in order to fully illuminate the areas of interest.

A review of the flow visualization videos after the tests were concluded revealed that a better understanding of the flow features could have been reached if an upstream release of flow tracers had been combined with a downstream release to seed vortex ring structures developed during crashback. The downstream particles would have been entrained into the flow moving upstream.

2.5 Data reduction procedures and types of measurements

2.5.1 Data reduction procedures

Data were collected from 16 channels: 3 propeller force components, 3 propeller moment components, 3 body force components, 3 body moment components, the tunnel pressure, the venturi velocity, the propeller speed, and the tunnel temperature. These were usually sampled at a rate of 200 Hz and the number of samples taken per channel was usually 48,000, yielding a total of 768,000 measurements for each test. The force and moment voltage data were passed through the calibration matrices for the body and propeller dynamometers and converted to values in engineering units. The coordinate system used was the standard body-fixed coordinate system. Positive x was taken to be forward, in the direction of forward motion. The coordinate y was taken to be positive to starboard, and z was positive down through

the keel, completing the right-handed coordinate system. Body forces in the x, y, and z directions are denoted as F_x, F_y, and F_z forces, respectively, and body moments about the x, y, and z axes are denoted as M_x, M_y, and M_z. Propeller forces in the x, y, and z directions are denoted as f_x, f_y, and f_z, respectively, and propeller moments about the x, y, and z axes are denoted as m_x, m_y, and m_z. Note that an upper case "F" or "M" is used to indicate a body force or moment, and a lower case "f" or "m" is used to indicate a propeller force or moment.

Figure 2.7 shows the coordinate systems of interest in the propeller dynamometer results. The coordinates y_p and z_p are fixed to the propeller dynamometer and rotate with the propeller. The corresponding forces measured by the dynamometer are denoted by f_y and f_z, as shown in the figure. The y and z coordinates shown in the figure are the same as the body-fixed coordinate system described above. When the off-axis propeller forces are resolved into body-fixed (inertial) components, the resulting components are f_H and f_V, as shown in the figure. The propeller-fixed coordinates are significant because the propeller dynamometer is attached to the propeller and rotates with the propeller, so that it measures forces on the propeller in its own, non-inertial reference frame. This means in particular that the propeller and dynamometer weight shows up as a rotating force vector in the output of the dynamometer. In order to obtain proper readings from the dynamometer, this weight force must be subtracted out of the signal. This was done in the following manner. As described above, an 11-bit encoder was attached to the propeller, yielding a resolution of 0.18 deg in propeller position (360 deg divided by 2048). The signal from the encoder was sampled with a high-speed digital interface so that all 11 bits could be sampled between transitions, yielding a noise-free signal and thus an unambiguous reading of propeller position (within ± 0.18 deg) at each instant.

The propeller dynamometer with propeller installed was rotated to a fixed angle and a 5-second average was taken of each channel. To account for non-linear interactions between the channels, the average voltage for each channel was multiplied by the calibration matrix, which converted these measurements into engineering units. The model motor was then jogged, or rotated slowly, to a new location and data were acquired. The jogging procedure was required since the model motor could not be rotated to a fixed location and stopped. This process was repeated sufficient times until data were collected at enough angular positions to determine the weight force as a function of angular position for one rotation of the propeller. The above procedure was also conducted with a dry test section in which the propeller could be rotated by hand a fixed amount. These data were only useful to determine encoder reference locations, as they did not include buoyancy effects in the weighting functions.

At this time polynomial curve fits to each component of the force balance were calculated for a normalized encoder position. The step of normalizing the encoder value was taken to avoid round-off errors in polynomial coefficients. It was determined that using polynomial curve fits to the average data resulted in errors at the bounds of the function, 0 and 1. This problem was corrected by using the fact that these functions are periodic and repeating data above and below the extremes, yet only evaluating the function between 0 and 1 during testing. This repetition of data improved the polynomial curve fit at the encoder extremes. Even though the propeller weight is well known and could be represented by a shifted sinusoidal function, it was decided to determine these functions experimentally. The experimental polynomial curve fitting procedure took into account all additional pieces hanging on the dynamometer (propeller, spacers, fairwater), the weight of the dynamometer itself, and accounted for buoyancy effects when conducted with the propeller submerged.

To determine the encoder references positions the f_y and f_z polynomial functions of θ were examined to determine their maximum and minimum encoder locations. The encoder position where f_y had its minimum (*i.e.*, largest negative) value corresponded to $\theta = 0$ deg. This encoder location was then subtracted from each encoder measurement so that the data were referenced to 0 deg at top dead center (TDC). The encoder position where f_y had its maximum (largest positive) value corresponded to $\theta = 180$ deg. These could be checked by noting the encoder positions where f_z had its minimum and maximum values and ensuring that they were 90 deg away from the corresponding positions for maximum and minimum values of f_y. Repetition of this procedure both dry and wet and on subsequent days of testing showed at most a $\pm$ 1.0 deg error in calculated reference positions. The error can be largely attributed to the number of data points taken around each maximum and minimum encoder location.

To set electrical zeroes the dynamometer was rotated by hand in a dry test section to the calculated encoder position at 0 deg. At this position f_z and m_y should have been equal to zero. These channels were then electrically zeroed at this location. The dynamometer was then rotated 90 deg based on encoder output to a position where f_y and m_z should have been zero. These channels were then electrically zeroed. For the reminder of the test day these channel offsets were not touched. At any point during the test in which there was a dry test section and the propeller could be rotated by hand the electrical zeroes were checked. If there was sufficient drift to require adjustment all channels were re-zeroed and a new set of rotating data was acquired. In hindsight it would be more appropriate to not only rotate to 0° but also 180° and take the average of these two measurements as a zero offset on these channels. By following these procedures carefully it was possible to obtain good propeller dynamometer data at precisely-known propeller locations, remove the effect of the rotating weight force, and then convert these data to inertial force components as needed.

2.5.2   The self-propulsion point and the similarity parameter η

Traditionally the dimensionless parameter associated with propeller performance data has been the advance ratio J, defined by

$$J = \frac{V}{nD}$$

where V is the forward velocity of the vehicle, n is the propeller rotational speed (usually in revolutions per second), and D is the diameter of the propeller. However, recent studies have shown that the data may also be collapsed well by using the similarity parameter η, defined as

$$\eta = \frac{n}{n_{sp}}$$

where n is the actual propeller speed and n_{sp} is the propeller speed required for self-propulsion; that is, the propeller speed at a given forward velocity V at which the thrust produced by the propeller is equal to the drag of the vehicle (*i.e.* the propeller speed such that $T - D = 0$). As will be seen later in this report, the data do collapse well when plotted versus η. However, the use of η requires the determination of n_{sp}, which must be determined experimentally and usually during

the test itself, since the thrust of the propeller and the drag of the vehicle will depend on such things as the propeller mount, the interaction between the propeller and the vehicle body, the manner in which the vehicle is mounted in the water tunnel, and so forth.

The values of n_{sp} were determined in the following manner. The propeller motor in the model was set for forward rotation. The tunnel speed V was set at a particular speed. Then the propeller speed was varied until the net thrust force as measured by the body force balance was nominally zero. Since it was usually not possible to get a reading of exactly zero, points were obtained on either side of zero and then a linear interpolation was performed to obtain the actual value of n_{sp}. These points were obtained at tunnel set speeds of 2.5 kts, 5 kts, 7.5 kts, and 10 kts (1.29 m/s, 2.57 m/s, 3.86 m/s, and 5.14 m/s, respectively). The variation of n_{sp} with tunnel speed V turned out to be very close to a straight line, and so a linear regression was performed to obtain a relation between n_{sp} and V. The resulting regression was

$$\frac{n_{sp}}{rpm} = 102.04 \frac{V_{venturi}}{kts} + 19.831$$

The results of these measurements are shown in Figure 2.8 (the uncertainty in these measurements will be discussed below). Ideally the intercept would be zero, since the propeller speed required for self-propulsion at zero forward velocity is zero. However, adding the intercept increased the accuracy of the linear regression so that the standard R^2 value for the regression was greater than 0.99995. The speed $V_{venturi}$ was the test section speed obtained by a calibration of the pressure drop across the tunnel contraction. A more accurate result might have been obtained using the tunnel speed obtained from the LDV system (as described by Park *et al.* 2002). However, the venturi velocity values were recorded and available in the same data files as the force and moment data, which meant that instantaneous values of $V_{venturi}$ were available for each force measurement and thus a value of n_{sp} and hence η could be calculated for each force measurement. Since these values were available for the self-propulsion points as well, it was decided to use the venturi velocity as the independent variable for the calculation of n_{sp} and thus η. The negative values of η to be found in the results simply indicate the reverse rotation of the propeller.

2.5.3   Forward rotation and zero-thrust studies

At various times during the tests the propeller was set to operate in forward rotation. These runs were conducted primarily to obtain the data necessary to determine the self-propulsion propeller speeds as described in the previous section. Additional forward rotation runs were conducted with the propeller speed adjusted so that the net thrust output of the propeller dynamometer was zero; in other words, the propeller was operating in a "zero-thrust" condition, rotating in the forward direction but producing no thrust or drag. These runs were made so that dynamic "signatures" of the body and propeller dynamometers could be obtained and checked for occurrences of rotating imbalance or any other phenomena that might affect the measurements made during crashback runs. The results of these runs will be discussed in the next chapter.

2.5.4   Steady crashback studies

The first set of tests conducted studied cases of steady crashback, which means that both propeller speed and tunnel speed were held constant and data were collected over a period of time. Data were collected from the body and propeller force balances for a set of crashback conditions and when it was ascertained that the propeller force balance was producing results in line with the body force balance, the restraint strut was added and further measurements were made.

Since the primary quantities of interest in these studies were the fluctuating components of the forces and moments, it was decided to examine the root-mean-square (RMS) value of each force or moment at a given test condition. Initially it had been decided to perform a spectral analysis and use the peak values as the measure of the unsteady component. However, despite the pristine fluctuating force and moment traces obtained in the computations discussed in Zierke *et al.* (1997), the experimental signals turned out to be quite a bit noisier, with a much less easily determined peak amplitude or corresponding frequency. These results and behaviors will be discussed in more detail in the next chapter. As will be seen there, the choice of the RMS value as the parameter for examination turned out to be a reasonable choice. In order to obtain the RMS values of forces and moments at a particular steady crashback condition, the entire record (48,000 readings) was averaged.

The possibility of using different dimensionless representations of the propeller speed, either advance ratio or the parameter η, was discussed earlier. It is also possible to nondimensionalize the resulting force and moment data in two different ways, depending on the quantities of interest. One is to use the dynamic pressure and model length scale as the normalizing values, so force and moment coefficients are calculated as follows:

$$C_F = \frac{F}{q_\infty L^2} , \quad C_M = \frac{M}{q_\infty L^2} , \quad q_\infty = \frac{1}{2}\rho_\infty V_\infty^2$$

In these formulae F and M are arbitrary forces and moments, C_F and C_M are the corresponding force and moment coefficients, q_∞ is the freestream dynamic pressure based on the freestream density and velocity, and L is a body length scale. The other way in which the forces and moments may be normalized is through the use of propulsive quantities, as follows:

$$C_F = \frac{F}{\rho_\infty n^2 D^4} , \quad C_M = \frac{M}{\rho_\infty n^2 D^5}$$

Here, n is the propeller speed in revolutions per second and D is the propeller diameter. Both of these definitions were used in reducing the data as necessary, and in particular they were used to normalize the RMS values of the forces and moments. Both definitions were found to collapse the data well. Generally coefficients based on dynamic pressure and model length scale were plotted against values of the advance ratio, and coefficients based on propulsive parameters were plotted against η.

2.5.5   Unsteady crashback studies

Two different types of unsteady crashback studies were conducted. Because of the way the power was connected to the propeller motor, the motor was "hard-wired" for either forward or reverse rotation in a given test. The only way to reverse propeller direction was to manually reverse the motor leads. This meant that the propeller could not be started in the forward direction, stopped, and then placed in reverse rotation. However, it was noted that with the propeller motor off and the tunnel speed set at some value, the propeller would "windmill" in forward rotation at some speed. The propeller motor could then be engaged in reverse rotation. Once engaged, it would slow its forward rotation to zero and then begin rotating in reverse, reaching its commanded reverse speed in a fairly short time. This behavior was used to simulate the initiation of the crashback maneuver. The change in direction of rotation caused encoder synchronization problems that led to errors in the weight-subtraction calculations. The installation of an external trigger for the data acquisition system solved this problem.   During these tests all channels were sampled at a rate of 1000 samples per second for 50,000 samples. The results indicated that these times were sufficient for the establishment of the asymmetric ring vortex and the corresponding off-axis forces and moments. These tests were all conducted at a tunnel set speed of 7.5 kts (3.86 m/s). Four different runs were made. The fact that the fluctuating force and moment component amplitudes were now functions of time required a modification to the data reduction procedure. RMS values of the forces and moments were obtained for 200-sample subsets of the complete record. The time associated with each RMS value thus obtained was taken as the time mid-point of the 200-sample subset. The variations of these RMS values with time were then studied. The value of 200 was chosen as a compromise between having a large enough subset to obtain a reasonable RMS value and a small enough subset so that significant time fluctuations would not be missed. Different numbers were used and the results compared before the value of 200 was chosen. The sample number trade-off studies will be discussed in more detail in the next chapter. These results were also examined as functions of dimensionless time $t' = Vt/L$, which essentially corresponded to the number of hull lengths traveled in a given period. The results were also examined as functions of instantaneous values of η, determined by using the instantaneous values of the venturi velocity measured during the ramp in propeller speed.

The second unsteady crashback study simulated the actual deceleration of the submarine. It had been noted previously that the tunnel deceleration time scale was generally of the same order as the submarine deceleration time scale. In the second set of unsteady crashback studies, the tunnel speed was set at a particular value (usually 7.5 kts) and the propeller was allowed to windmill in forward rotation. The propeller motor was then engaged. As soon as the personnel observing the test noted the propeller speed beginning to change, the tunnel operator set the tunnel speed to zero. This would cause the tunnel speed to gradually coast down to zero. All channels were sampled at either 1000 or 250 samples per second for 50000 samples. The initial tunnel speed was set at 7.5 kts, and the propeller speed varied from approximately 330 rpm in forward rotation (windmilling) to -500 rpm in powered reverse rotation. The same procedure for using 200-sample subsets to compute RMS values was implemented. The results were examined as functions of time, dimensionless time, and instantaneous η.

2.5.6   LDV and flow visualization studies

When the force and moment measurements were completed for the steady crashback studies, detailed LDV

surveys of the propeller flowfield were conducted at flow conditions of interested noted in the steady crashback results. Flow visualization studies using a laser sheet, fluorescent dye, and bubbles were also conducted at these flow conditions of interest. The results of the these studies will be discussed in detail in Chapter 4.

2.6   Uncertainty analysis

As discussed above, the majority of the tests conducted consisted of setting the tunnel and propeller speeds, measuring forces and moments, and then computing force and moment coefficients and examining how they varied with the similarity parameter η. Additional LDV surveys of the flow field were conducted. This section will concern itself with the uncertainties in the self-propulsion propeller speed n_{sp}, the parameter η, the measured velocities, and the force and moment coefficients. The uncertainty analyses will follow the procedures described in Coleman and Steele (1999).

The values of n_{sp} were obtained by varying the propeller speed in forward rotation until the body dynamometer output in the axial direction was essentially zero. Since it was not possible to obtain a reading of exactly zero, data points were obtained on either side of zero, and a linear interpolation was performed between the smallest negative and the smallest positive thrust values to obtain the propeller speed corresponding to zero thrust. The resulting data reduction equation (DRE) was of the form

$$n_{sp} = n_1 - \left(\frac{T_1}{T_2 - T_1} \right) (n_2 - n_1)$$

In this equation, T_1 and T_2 are the negative and positive thrust values, respectively, from the body dynamometer, and n_1 and n_2 are the corresponding values of the propeller speed. The thrust force produced by the propeller always increased with propeller speed over the range of propeller and tunnel speeds studied, so the relations between the values used in this equation were always $n_2 > n_1$ and $T_2 > 0 > T_1$. The value of the systematic uncertainty in F_x shown in Table 2.1 was used as the systematic uncertainty in T_1 and T_2, and twice the root-mean-square (RMS) value from the actual measurements was used as the random uncertainty in T_1 and T_2. According to the LCC staff, the systematic uncertainty in the propeller speed measurement had been estimated in previous tests to be approximately 1 rpm. Twice the standard deviation in propeller speed from the actual measurements was used as the random uncertainty in n_1 and n_2. The results of these calculations are shown as the uncertainty bars in Figure 2.8. The uncertainties in n_{sp} ranged from 17.8% of the mean value at the lowest speed V to 2.4% of the mean value at the highest value of V. At the lowest propeller speed studied, 200 rpm, the combination of systematic and random uncertainties yields a total uncertainty in n of only 0.6%, and this percentage goes down to 0.1% as n increases to 1000 rpm, near the maximum propeller speed studied. Since η is defined as the ratio of n to n_{sp} at any given condition, and since the uncertainty in n is much less than the uncertainty in n_{sp}, the uncertainty in η is essentially the same as the uncertainty in n_{sp}, on a percentage basis. It is believed that these values represent an overestimate in the uncertainty in η, since as will be seen the data were very repeatable, even at the large values of η corresponding to small values of n_{sp}. The reason for this overestimate is unclear.

Estimating the uncertainties in the force and moment coefficients presents something of a challenge, because twice the standard deviation (2σ) is usually used as the measure of the random uncertainty of the measurement, for a

sufficiently large number of samples. However, in these tests, the quantities of interest *are* the standard deviations or RMS values of the forces and moments, represented as dimensionless coefficients. It is the variations of these quantities, used as a measurement of the unsteadiness of the flow, that are being tracked as a function of the parameter η. Because of this, what follows will be an analysis of the uncertainty of a *single measurement* of the RMS body yawing moment. The uncertainty in this value should be representative of the uncertainties in the other force and moment coefficients. To avoid confusion, the following convention will be adopted. M_z' will be used to denote the RMS value of the yawing coefficient, computed from the entire data record of 48,000 samples in each run. This is the quantity of interest in the current study. The RMS value of M_z' will be denoted by M_z'', since it represents the RMS value of an RMS value.

In order to obtain an estimate of M_z'', a record of 40,000 samples obtained at a specific flow condition was broken down into subsets (the number 40,000 was arbitrarily chosen for ease in manipulating subsets). The flow condition used was a tunnel set speed of $V = 5$ kts and propeller speed $n = 400$ rpm. This condition corresponded to a value of η of approximately 0.76, which, as will be seen in the next chapter, was a condition of relatively large unsteadiness. The number of sets (N_{sets}) was varied, and the RMS of each set was computed from the number of points in each set. Thus, if the number of sets was 40, each set contained 1000 points, and the RMS value was obtained from each set, yielding 40 RMS values. Each set could be thought of as a sample of the data record. Then, the RMS value for all the sets was computed, and this was taken as a representation of M_z'', the standard deviation of M_z'. It was recognized that there would be problems at either extreme. If too few sets were chosen, the large number of points in each set would mean that the RMS value for each set were actually beginning to capture the flow physics which M_z', the RMS value of the entire data record, was intended to represent, and there would be an insufficient number of sets and corresponding RMS values to compute M_z''. If too many sets were chosen, there would not be enough points to get a good value of the RMS of each set. The results of this investigation are shown in Figures 2.9 and 2.10. Figure 2.9 shows M_z'' divided by the square root of the number of sets versus the number of sets. This number represents the standard deviation of the mean value of M_z', which is the value of interest (see Coleman and Steele 1999, p. 25) and will be referred to as $M_{z,m}''$. As can be seen in the figure, there is fluctuation in the value of $M_{z,m}''$ as the number of sets increases, as might be expected. Around $N_{sets} = 40$, the behavior of $M_{z,m}''$ settles down into the typical reduction with increase in number of samples (in this case N_{sets}) as is normally expected (it is this reduction in the standard deviation of the mean that is the reason one acquires as many samples as possible in a particular measurement). Obviously, it would be advantageous to be able to take a number of sets that would correspond to a location on the curve in Figure 2.9 as far to the right as possible. The larger the number of sets, however, the smaller the number of points in each set. Therefore we must examine Figure 2.10, which shows the variation in M_z'' with the number of points in each set. Increasing the number of sets implies decreasing the number of points and therefore moving from right to left on this figure. There is a peak in the value of M_z'' at $N_{pts} = 125$, corresponding to $N_{sets} = 320$. This peak would suggest that the "noise" in M_z' was being adequately captured by this combination of sets and points. Based on this figures, it seemed reasonable to take $N_{sets} = 320$, with 125 samples in each set, to compute $M_{z,m}''$. This procedure was followed for the range of propeller speeds at $V = 5$ kts, for both the body and propeller yawing moment measurements. The results are shown in Figure 2.11. In this figure, the standard deviation of the RMS value, divided by the RMS value for the entire sample, is shown as a function of η for both body and propeller yawing moments. These curves indicate a peak value

of $M_{z,m}''$ / M_z' of approximately 0.028 for the body yawing moment measurements over the range of η at this speed. Taking twice this value as the random uncertainty in M_z' results in a value of approximately 5.6% of the "mean" value. Since the RMS is computed by subtracting the mean value from each individual value, the systematic uncertainty can be taken to be zero.

As discussed in Section 2.5.4 above, the body yawing moment coefficient is represented as follows:

$$C_{M_z} = \frac{M'_z}{\rho n^2 D^5} \quad or \quad C_{M_z} = \frac{M'_z}{\frac{1}{2}\rho V^2 L^3}$$

In these defintions, M_z' is the RMS value of the yawing moment. The first definition represents propulsive scaling, and the second represents dynamic pressure scaling, as discussed above. Typical values for the systematic and random uncertainty in the propeller speed n were 1 rpm and 0.5 rpm, respectively. The systematic uncertainty in the tunnel velocity V was 0.018 m/s (Park, 2002) and a typical value of the random uncertainty in V was 0.04 m/s. The uncertainty in both the propeller diameter D and the body length L was estimated as 0.0032 m. The total uncertainty in the density was estimated as 0.0011 gm/cm^3 (see Blanton, 1995; Bridges, 2001). Using these values in a standard uncertainty computation results in an uncertainty in C_{M_z} of approximately 7.7% for propulsive scaling and 6.6% for dynamic pressure scaling.

Because of the somewhat *ad hoc* nature of this analysis, as well as the computational effort involved, the uncertainties were not computed for all measurements. It was hoped that with the particular choice of the body yawing moment as the most sensitive of the variables and the flow condition as one demonstrating the most significant variations (as will be seen in the next chapter), this analysis would give a reasonable estimate of the uncertainty of one value of the RMS yawing moment coefficient that would be representative of the uncertainties in the other measurements.

2.7   Test grid

Steady crashback tests were run with the unrestrained model at tunnel set speeds of 2.5 kts, 5 kts, 6.25 kts, 7.5 kts, and 10 kts. At each tunnel speed, the initial propeller speed began low, typically -200 rpm, and was then gradually increased in magnitude. Measurements were made at different values of propeller speed. The dynamometer readouts were monitored to make sure that the forces and moments did not exceed the maximum allowable values for the dynamometers, and the model itself was observed to make sure that vibrations did not become excessive. When the force and moment values began to approach their limits, or the model motion became excessive, the propeller speed was increased no further at that tunnel speed. Generally the larger the tunnel speed, the lower the propeller speed at which the forces and moments reached their limit. The maximum propeller speed reached at a tunnel speed of 2.5 kts was 1100 rpm, whereas a maximum propeller speed of only 700 rpm was obtained at a tunnel speed of 10 kts. In addition to the systematic variation of tunnel speed and propeller speed done to cover as large a range of advance ratio and η as possible, a set of runs were conducted at a fixed propeller speed of -281 rpm and a range of tunnel set speeds. These were chosen in an attempt to match some of the conditions presented in computations contained in the report edited by Zierke (1997). In subsequent tables and figures these conditions are referred to as "Zierke conditions."

When it was determined from these tests that the propeller and body dynamometer data were tracking each other very well, and thus confidence in the newly-acquired propeller dynamometer was acquired, the restraint strut was added to the model and further steady crashback runs were conducted. A relatively large number of steady crashback conditions were examined with the restraint on, and the parameter space was mapped thoroughly. The LDV surveys were also conducted with the model restraint on.

The initial ramped propeller speed tests did not work because of the triggering problem. Some ramped tunnel speed tests were conducted with fixed propeller speed, but the results of these were not as illuminating as the ramped propeller speed tests and the ramped propeller speed / tunnel speed tests, so they are not included here. Once the external trigger was installed, the ramped propeller speed tests were conducted. In each case the tunnel speed was set at 7.5 kts and the propeller speed was ramped from a forward (windmilling) speed of 330 rpm to a reverse rotation rate of -500 rpm. There was no way to actually control the rate at which the propeller speed changed. The tunnel operator commanded a final propeller speed, and the propeller motor's response dictated the rate at which the speed changed. After running 6 of these tests, three tests were run in which the tunnel speed was set to zero and the tunnel was allowed to coast down in speed after the propeller motor engaged. These tests all began at a tunnel speed of 7.5 kts and a propeller speed that started from a forward speed of 330 rpm to a reverse speed of -500 rpm. The number of such tests was limited due to the time required for the tunnel to reach steady flow conditions after being restarted.

3. FORCE AND MOMENT RESULTS

3.1 Steady crashback measurements

3.1.1 Dimensional data

Results for the forces and moments on the submarine body as measured by the body dynamometer (hereinafter referred to as "body" forces and moments, to distinguish from those measured by the propeller dynamometer, to be referred to as "propeller" forces and moments) are shown in dimensional form in Figures 3.1 through 3.12. Figures 3.1 through 3.6 show the mean body forces and moments as functions of propeller speed, and Figures 3.7 through 3.12 show the RMS values of the body forces and moments, also as functions of propeller speed. It is recognized that this is a nonstandard representation of the forces and moments, and the traditional dimensionless force and moment coefficient definitions will be used in subsequent analyses. However, it was thought that it would be of interest to be able to see the actual magnitudes of the forces and moments measured by the body dynamometer. In particular, as can be seen for example in Figs. 3.11 and 3.12, the off-axis RMS moments could get quite large, with maxima in excess of over 1000 ft-lb.

3.1.2 Body force and moment coefficients

The results of the steady crashback measurements are presented in the more traditional forms beginning with Figure 3.13. The coefficients for the root-mean-square (RMS) values of the body forces and moments are presented in Figures 3.13 through 3.24. The coefficients obtained using propulsive scaling,

$$C_F = \frac{F'}{\rho n^2 D^4}, \quad C_M = \frac{M'}{\rho n^2 D^5}$$

where F' and M' are the RMS values of the forces and moments, respectively, are presented first for each component as a function of the parameter η. Then, the coefficients obtained using the dynamic pressure scaling,

$$C_F = \frac{F'}{\frac{1}{2}\rho V^2 L^2}, \quad C_M = \frac{M'}{\frac{1}{2}\rho V^2 L^3}$$

are presented as a function of the advance ratio J for the same component (the coefficient definitions are discussed in

detail in Section 2.5.4 above). The force coefficients are shown in Figures 3.13-3.18 and the moment coefficients in Figures 3.19-3.24. In each figure the results are presented first for the entire range of η and J and then the results for small values of η or J are shown. The coefficients for the mean or time-averaged body forces and moments are shown in Figures 3.25 through 3.30.

All of the forces and moments measured in these experiments demonstrated a repeatable, characteristic behavior. As the magnitude of η or J increased, the coefficients tended to decrease first, increase to a relative maximum in the vicinity of $\eta = -0.8$ or $J = -1$, and then decrease asymptotically to some small value. The specific physical mechanisms behind these behaviors will be discussed in a later section of this report. The data for the body forces and moments tended to be a little more scattered than the propeller forces and moments (to be discussed in the next section), but nonetheless maintained a very repeatable behavior. It should be noted that with the variations of propeller speed n and tunnel speed V, the same value of η or J could be obtained with multiple combinations of n and V. The ability of the parameters η and J to collapse the data is demonstrated well by the coefficient plots.

As was noted in an earlier section, the data for $V = 6.25$ kts tended to be somewhat noisier than the data for other tunnel speeds. This led to higher values of the RMS forces and moments, as can be seen in Figures 3.13 through 3.24, most notably in the off-axis y-force (e.g. Fig. 3.15) and z-moment (e.g. Fig. 3.23). One other fact to note from these figures is that the body forces and moments seem to be collapsed slightly better when normalized with the dynamic pressure scaling and plotted against the advance ratio.

The coefficients for mean body forces and moments are presented in Figures 3.25 through 3.30. These are all presented in terms of dynamic pressure scaling and advance ratio. The body axial (x) force and moment (Figures 3.25 and 3.28, respectively) demonstrate a very repeatable variation with advance ratio. The off-axis mean forces and moments were expected to be zero, since the time-averaged flow was expected to be nominally axisymmetric and therefore create no mean off-axis forces and moments. The coefficients shown in the figures are generally small, but they do show some systematic variation. The coefficient of body side force shown in Figure 3.26 shows a fairly strong variation with advance ratio for the smallest tunnel velocity ($V = 2.5$ kts). At higher tunnel speeds, the side force coefficient is essentially independent of advance ratio. If the model were misaligned slightly with the flow, creating a small sideslip or drift angle, one might expect a small side force that would result in a side force coefficient that would be independent of tunnel speed, as long as the sideslip angle remained constant. This is what is observed at the higher tunnel speeds. For a fixed tunnel speed, the advance ratio magnitude decreases as the propeller speed increases ($J = V/nD$). At larger propeller speeds, the upstream influence of the backflow caused by the propeller operating in reverse is more pronounced. The effects of the propeller backflow on the flow over the body, and in particular on the sideslip angle, would be most pronounced at the lowest tunnel speed. Therefore, the largest variations in side force might be expected to occur at a combination of low tunnel speed and small magnitudes of the advance ratio, which is what is seen in Figure 3.26. Similar variations in body yawing moment can be seen in Figure 3.30. The variations in magnitudes of body side force coefficient and body yawing moment coefficient track each other very closely, which makes sense, since the yawing moment is effectively an integration of the side force along the body, and the flow characteristics that affect one would contribute to the other. Similar arguments may be made for the variations in body down force and body pitching moment shown in Figures 3.27 and 3.29, with the backflow from the propeller changing a small angle of attack

perhaps caused by a slight model misalignment. The one feature that is most different between the side force/yawing moment and down force/pitching moment variations is how the coefficients vary for the Zierke conditions. It should be noted that for most tests, the tunnel speed was fixed and different values of J were obtained by varying the propeller speed. However, the Zierke conditions were obtained by fixing the propeller speed and varying the tunnel speed. It would appear from the figures that over the range of J values examined in the Zierke conditions, the interaction between propeller backflow and tunnel speed had more effect on the effective angle of attack than on the effective sideslip angle. In Figures 3.26 and 3.30, the side force and yawing moment coefficients hardly vary with advance ratio over the range of J covered by the Zierke conditions. However, in Figures 3.27 and 3.29, there are large variations in down force and pitching moment coefficients with J over the range of J covered by the Zierke conditions.

3.1.3   Propeller force and moment coefficients

The results obtained from the propeller dynamometer are shown in Figures 3.31 through 3.50. The coefficients of the RMS values of the forces and moments are presented first, and then the coefficients of mean forces and moments are presented. Recall that the force and moment coefficients are defined in the same manner as in the previous section, except that now it is the forces and moments acting directly on the propeller only that are being considered. No body force data were collected with the restraint strut on, other than an occasional "spot check" to ensure that dynamometer limits were not being exceeded.

Figures 3.31 through 3.35 show the variations of the off-axis y and z RMS force coefficients with the parameters η and J. Recall that these forces are measured in the reference frame attached to the propeller. These forces demonstrate the very systematic variation of the RMS coefficient values with both η and J shown by the body forces and moments, with a distinct peak in the vicinity of $\eta = -0.8$ and $J = -1$. These figures include data acquired with the body restraint strut off (the unrestrained condition) and on (the restrained condition). The propeller forces in both cases track each other very well. In Figure 3.31, the values of C_y, for $V = 2.5$ kts and the Zierke conditions seem to fall slightly below the other values for $-1.5 < \eta < -1.0$ in a systematic fashion, but otherwise the data are very repeatable. The RMS force coefficients in Figure 3.35 were obtained by computing the resultant of the x and y RMS force coefficients. These coefficients also demonstrate the regular variation with η.

Figures 3.36 and 3.37 show the variations of the coefficients of the off-axis y and z RMS moments. They again show the regular variation with η. Figure 3.36 shows that the RMS y moment coefficients demonstrate a slightly different variation for $V = 2.5$ kts and for the Zierke conditions, as did the RMS y force coefficients. These coefficients also show very little difference between the restrained and unrestrained conditions.

As described in Section 2.5.1 above, the propeller position obtained by the encoder was used to resolve the x and y forces into horizontal (h) and vertical (v) forces in a reference frame attached to the tunnel test section (*i.e.* a non-rotating reference frame). The coefficients of the RMS horizontal and vertical forces are shown in Figures 3.38 through 3.41. Again the regular variation with η is demonstrated. Figures 3.40 and 3.41 highlight the similarities in the restrained and unrestrained data at $V = 5$ kts, indicating the validity of acquiring propeller force and moment data from a restrained model.

Selected mean propeller force and moment measurements are shown in Figures 3.42 through 3.50. The mean

thrust coefficient variation with η is shown in Figure 3.42 for the restrained condition. These data demonstrate an almost incredible repeatability, with essentially every point falling on a very distinct curve with a variation in behavior around $\eta = -0.8$, where the off-axis RMS coefficients had their local maxima. The thrust is not steady, however, as is demonstrated by Figure 3.43, which shows the RMS value of the thrust as a fraction of the mean thrust. It can be seen in this figure that the RMS values grow to around 25% of the mean thrust values as η approaches -1, then begin to decrease slightly. It should be noted here that the peak in the RMS values does not occur around $\eta = -0.8$, although the curves do show some peculiarities in behavior around $\eta = -0.8$. The mean torque coefficient shown in Figure 3.44 also demonstrates the very repeatable variation with η.

The mean values of the off-axis propeller forces and moments are shown in Figures 3.45 through 3.50. Nominally these would be expected to be zero. Where they are not zero indicates a possible model misalignment or offset associated with the propeller or propeller dynamometer. In Figures 3.45 and 3.46, the mean propeller y and z force coefficients have large magnitudes at small values of η which decrease as the magnitude of η increases. The fact that these variations tend to follow a "$1/n$"-like behavior would indicate a possible constant offset in the forces. The propeller mean y moment coefficient shown in Figure 3.47 shows a somewhat different variation, with a peak in the vicinity of $\eta = -0.5$. The reason for this behavior is unknown. The mean z moment coefficient shown in Figure 3.48 shows the "$1/n$"-like behavior, also suggesting a constant offset. The mean horizontal and vertical force coefficients shown in Figures 3.49 and 3.50 demonstrate the peak in the vicinity of $\eta = -0.5$, reflecting the behavior in the y moment coefficient. It should be noted that while these off-axis mean force and moment coefficients are not zero, they are considerably smaller in magnitude than the coefficients of the corresponding RMS values, as much as an order of magnitude in most cases. Because of the repeatability of the coefficients of the RMS forces and moments, and the relative sizes of the RMS and mean force and moment coefficients, it is not believed that any misalignments or offsets suggested by the non-zero mean values were significant enough to call into question the variations of the RMS values.

3.2   Frequency response

When the planning was being done for these tests, it was thought that it would be possible (and fairly easy) to determine at each operating condition the frequency at which a particular force or moment component would have its peak value, and the corresponding peak value. This frequency and peak value would then be plotted against the parameters η and J. As it turned out, these frequencies and peak values were not easily obtained, which is why the RMS values were used instead as the representative values of the unsteady component of the forces and moments.

As discussed in Section 2.5.3 above, measurements were made with the propeller in forward rotation and in a zero-thrust condition. These measurements were made to determine if there were any rotating imbalance effects or any other non-steady effects induced by the propeller rotation itself, independent of the unsteadiness expected in the ring vortex structure during crashback conditions. The results of these measurements for the body yawing moment and body side force are shown in Figures 3.51 and 3.52, respectively. These figures show the Fourier transform of the body yawing moment and side force at the three different zero-thrust conditions studied. Each of these conditions was at a different freestream speed V and thus a different propeller speed n that yielded zero thrust at the given flow condition.

The tunnel and propeller speeds were 5 kts and 275 RPM, 7.5 kts and 418 RPM, and 10 kts and 560 RPM, yielding values of η of approximately 0.523, 0.539, and 0.546, respectively. The yawing moment and body force response curves show peaks in the response at frequencies of approximately 95 RPM and 290 RPM, independent of the "forcing frequency" of the propeller rotation. These data indicate that the body dynamometer had a distinctive frequency response that would tend to drown out any frequencies generated by the flow itself. This was confirmed by later tests which showed that these peaks were larger than the peaks created by hydrodynamic phenomena. This type of behavior was demonstrated on all of the force and moment channels of the body dynamometer. Therefore, no frequency analysis was attempted for any of the body force and moment data. However, as has already been seen, the overall RMS values of the body forces and moments tended to demonstrate regular and consistent variations with η and J and thus the RMS data were retained and presented in Section 3.1.2.

The propeller data provided a different difficulty with regards to frequency analysis. The zero-thrust measurements indicated no distinctive frequency response from the propeller dynamometer. Figure 3.53 shows the development of the frequency response of the propeller y force with increasing reverse propeller speed. This figure shows the Fourier transform amplitudes as functions of frequency in RPM. For smaller magnitudes of n and in the vicinity of $\eta = -0.8$, the overall peak amplitude is distinct and is clearly separated from the peak associated with the propeller speed n. It is clear from the frequency response that this overall peak is associated with the unsteadiness in the flow itself, presumably with the unsteadiness of the vortex ring asymmetry. Because of this presumed relation between the asymmetry unsteadiness and the peak amplitude, the frequency at which the peak occurs will be referred to as the "hydrodynamic" frequency f, to distinguish it from the frequency of propeller rotation n. As the magnitude of n increases, and η moves away from the value of -0.8, the overall peak amplitude tends to decrease and the hydrodynamic frequency f tends to move toward the propeller frequency n, until the peaks merge. In this region it becomes difficult to isolate the peak associated with the vortex ring unsteadiness and its corresponding frequency f. Also, as can be seen from these figures, at lower values of η away from the conditions associated with the peaks in the RMS force and moment coefficients in the vicinity of $\eta = -0.8$, it is somewhat problematic to isolate a frequency that can clearly be identified with the vortex ring unsteadiness. Because of these difficulties the decision was made to concentrate on the RMS values of the forces and moments as indicators of the overall flow unsteadiness.

Some information can be gained, however, from the frequency response curves. The curves shown in Figure 3.53 were analyzed to determine the peak amplitude of the frequency response, and the frequency f at which the peak occurred, for the propeller y force. Since the Fourier transform amplitude does represent a force, a dimensionless force coefficient was computed using the peak amplitude and propulsive scaling. The variation with η of this coefficient of peak y force amplitude is shown in Figure 3.54, and once again the local maximum in the vicinity of $\eta = -0.8$ can be observed. It should be noted that these data are somewhat noisier than the RMS data presented earlier, for the reasons outlined in the previous paragraph. The frequency f corresponding to each peak amplitude represented in Figure 3.54 was determined and the propeller speed frequency n was subtracted. This frequency difference was converted to radians per second and made dimensionless by multiplying by the propeller diameter D and dividing by the tunnel speed V, to create a standard reduced frequency $\omega = 2\pi(f - n)D/V$. Figure 3.55 shows the variation of ω with η. There is significant scatter in the vicinity of $\eta = -1.5$ because this is the region where the presumed vortex ring frequency and the propeller

frequency tended to merge. These variations reveal something about the vortex ring behavior. When a submarine propeller is operating in forward rotation, it rotates clockwise when viewed from the stern looking forward. Thus in crashback the propeller is rotating counterclockwise. If the value of ω in Figure 3.55 is positive, it means that the frequency at which the vortex ring unsteadiness is interacting with the rotating propeller is higher than the propeller rotational speed. This would suggest that the side force associated with the vortex ring unsteadiness is rotating in the direction *opposite* to the propeller rotation. If the vortex ring asymmetry is rotating in the direction opposite to the propeller rotation, the propeller can be thought of as "cutting" the asymmetry at a higher frequency because of the opposite rotation directions, and thus the value of ω is positive. If the value of ω is negative, it would suggest that the vortex ring asymmetry is rotating in the same direction as the propeller, since the frequency at which the propeller "cuts" the vortex ring asymmetry is now less than the propeller rotational speed. What is shown in Figure 3.55 is that for low magnitudes of η, the vortex ring asymmetry is rotating in the same direction as the propeller. As the magnitude of η is increased (as η becomes more negative), the vortex ring asymmetry begins to rotate in the opposite direction to the propeller rotation. The positive peak in ω occurs around $\eta = -0.5$, and then there is a reduction in ω as the vortex ring and propeller frequencies approach each other. For large magnitudes of η, ω again become negative, indicating another reversal in the rotation of the vortex ring asymmetry relative to the propeller direction.

As discussed above, the propeller x and y forces were resolved into horizontal and vertical forces (measured relative to the tunnel test section) using the propeller position. This of course is an inertial reference frame. The horizontal force frequency response was analyzed for peak amplitudes and frequencies at peak amplitudes, and the results are shown in Figures 3.56 and 3.57. Coefficients formed from the peak amplitudes are shown in Figure 3.56, and these again demonstrate the relative maximum in the vicinity of $\eta = -0.8$, along with the relatively large amount of scatter. The frequencies are shown in Figure 3.57, defined as in Figure 3.55 except that now the propeller frequency is not subtracted out so that ω is based only on the flow frequency f. The horizontal force is referred to an inertial reference frame and so in a sense the propeller rotation has already been subtracted out. The frequencies shown in Figure 3.57 correspond now to forces that might be measured on the submarine itself. The fluctuations in forces on the submarine itself would correspond to only positive real frequencies, and this is reflected in the results shown in the figure.

Jiang *et al.* (1996) report a reduced frequency equivalent to the current ω of approximately 0.5 over a range of advance ratios $-1 < J < -0.5$. This would correspond roughly to a range $-1 > \eta > -2$ in the current experiments. Of course, in the experiments of Jiang *et al.*, there was only a propeller and no body. Without a hull, the concept of the self-propulsion propeller speed and hence the parameter η are irrelevant for those experiments. The current experiments show that ω varies continuously over the range of η just quoted, as demonstrated in Figures 3.55 and 3.57. The value of $\omega = 0.5$ from Jiang *et al.* is in reasonable agreement with the current measurements in the vicinity of $\eta = -1.2$.

3.3   Unsteady crashback measurements

3.3.1   Ramped propeller speed results

The crashback maneuver is intrinsically an unsteady maneuver. The submarine is traveling forward, the propeller rotation is reversed, and the submarine begins to decelerate immediately until it reaches the desired speed or

comes to rest (or even begins backing). During this time the vortex ring state develops around the propeller and then disappears when the shear that drives the formation of the ring disappears because of the cessation of forward motion of the submarine. The steady crashback results considered up to this point have simulated conditions at particular instances that might be imagined during a crashback maneuver, although only in a quasi-steady fashion. The limitations of such results were recognized, and attempts were made to simulate fully unsteady crashback maneuvers.

The first such attempt was a partial simulation in which the tunnel speed was held steady and the propeller speed was ramped into a crashback condition. As noted in an earlier section, there was no way to drive the propeller in forward rotation and then reverse rotation during a run. The propeller rotation direction was determined by cable connections which had to be rearranged manually (with the power off) in order to change the propeller direction. However, it was noted at the propeller would "windmill" in forward rotation with the propeller motor off and the tunnel speed at some value. At a tunnel set speed of 7.5 kts, the propeller would "windmill" at about 330 RPM. Thus for the first set of unsteady crashback simulations, the tunnel speed was set at 7.5 kts, the propeller was allowed to windmill in forward rotation, and then the propeller motor was engaged and the propeller stopped its forward rotation and began spinning in reverse. The commanded final reverse speed was -500 RPM. There was no way to control the rate at which the propeller speed changed; the particular propeller speed variation caused by the dynamics of the propeller, motor, and flow combination had to be accepted. These tests will be referred to as "ramped propeller speed" tests.

Similar to the difficulties presented by the uncertainty analysis discussed in Section 2.6, the problems presented by these tests were related to the determination of variations in RMS values of forces and moments where the mean values were also functions of time. In particular, these measurements required determining a sample size for the computation of RMS values large enough to obtain "good" RMS values without masking the unsteady features of the flow which the measurements were attempting to track. Figure 3.58 shows the results of one such study comparing the results obtained with 200 and 400 points per RMS "sample." This plot shows the variation of the RMS propeller y force with time. The RMS values were computed using 200 and 400 points per average. The time associated with each RMS value corresponded to the center time of each set of sample points. It can be seen from this figure that a sample size of 200 points was sufficient to obtain a "local" value of the RMS without obliterating flow fluctuations of interest.

Figure 3.59 shows the development of the RMS propeller y force with time for each of the four ramped propeller speed tests conducted. Since the data were obtained using a manual trigger, each set had a slightly different starting time. By examining the propeller speed output data as a function of time, it was possible to determine when the propeller motor engaged and the positive propeller speed began to reduce. This time was taken as the t_0 value shown in the figure. It can be seen from this figure that the propeller side force develops very rapidly. This is further emphasized in Figure 3.60, in which the tunnel speed and model length L have been used to convert time into a dimensionless distance x/L that essentially represents the number of "boat lengths" traveled. It can be seen from this figure that the RMS propeller side force develops to its maximum amplitude within one boat length. The details of the different runs are different, but it can be seen in this figure that the maximum amplitudes for the different runs are all approximately the same.

Figures 3.61 through 3.64 show the development of various quantities with dimensionless length traveled x/L. The figures show variations in propeller speed, η, RMS propeller y force, and RMS body y and z moments (the off-axis body moments). In order to fit all of these on a single graph, the propeller speed and the force and moments are scaled

by their maximum magnitudes. The actual values of η are shown. These figures show the reduction in positive propeller speed followed by the increase in negative propeller speed. The origin is set at the point where the propeller speed begins to reduce. Since the propeller reaches a maximum negative speed and since the tunnel speed is fixed, η approaches a constant value in these measurements. These figures show that the RMS propeller y force generally tends to reach a maximum amplitude quickly and stay there, for the most part, whereas the body moments tend to lag the propeller force somewhat and exhibit some lower frequency fluctuations. These can probably be tied to the low-frequency fluctuations associated with the force balance and observed during the zero-thrust measurements, although no specific effort was made to do so. Figures 3.65 through 3.69 show the corresponding variations in RMS propeller and body x (axial) forces and the propeller axial torque, again scaled by maximum magnitude. The negatives of the propeller and body axial forces are plotted for ease of comparison. It can be seen from these figures that these forces and moments track each other very well, as might have been expected.

Figures 3.69 and 3.70 collect the off-axis forces and moments for the propeller and body together for one of the ramped propeller speed runs. Figure 3.69 shows that all of the off-axis RMS propeller forces and moments track each other very well, whereas Figure 3.70 shows there is less correlation among the body off-axis RMS forces and moments, although these are not completely uncorrelated. This again is probably a reflection of the characteristic behaviors of the propeller and body dynamometers, although it could also reflect an interaction between the flow and the model as mounted in the tunnel.

3.3.2   Ramped propeller and tunnel speed results

The second set of unsteady crashback simulations involved changes in both propeller and tunnel speeds. The tunnel speed was set at 7.5 kts and the propeller was allowed to windmill at approximately +330 RPM in forward rotation. The propeller motor was engaged with a commanded reverse speed of -500 RPM and the propeller was observed through the test section windows. When the propeller visibly began to slow, the tunnel motor was shut down and the tunnel speed was allowed to coast down to zero. The combination of ramped propeller and tunnel speeds therefore mimicked a complete unsteady crashback maneuver. As in the case of the ramped propeller speeds, there was no way to control the rate at which the propeller or tunnel speeds changed; the particular propeller and tunnel speed variations caused by the dynamics of the propeller, propeller motor, tunnel motor and flow combination had to be accepted. These tests will be referred to as "ramped propeller and tunnel speed" tests, or sometimes simply as "unsteady" simulations, "unsteady" in this case denoting changes in *both* propeller and tunnel speeds. Because of the length of time involved in bringing the tunnel to the initial condition and then allowing the tunnel to coast down to zero velocity, the ramped propeller and tunnel speed simulations were only run three times.

Figure 3.71 shows the development of the RMS propeller y force with time for the three different runs. The RMS values were computed from 200-sample sets, as discussed in the previous section. Note the rapid development in the RMS propeller y force followed by the gradual decrease. Recall that the presumed mechanism for the off-axis forces and moments is an unsteady asymmetry in the vortex ring which forms around the propeller during crashback. As discussed in Section 1.1 and illustrated in Figure 1.1, it is the shear between the forward flow induced by the propeller in reverse rotation and the freestream flow outside the propeller created by the submarine's forward motion that drives

the creation and sustenance of the vortex ring around the propeller. As the submarine slows, the freestream velocity outside the propeller decreases, with a corresponding decrease in the shear. The vortex ring weakens and eventually disappears when there is no longer any shear to drive it. When the vortex ring weakens, any forces associated with an asymmetry of the vortex ring decrease. This is shown in the reduction of RMS propeller y forces in Figure 3.71. The details of the three different runs are different, but in each case the RMS propeller y force reaches approximately the same maximum magnitude.

Figure 3.72 shows the variation of the coefficient of RMS propeller y force with dimensionless distance. In this figure the coefficient is defined using propulsive scaling and therefore goes to infinity at the point where the propeller speed goes through zero. Figure 3.73 shows the same coefficient plotted against the instantaneous values of η computed from the instantaneous propeller and tunnel speeds. In these two figures the positive values of η correspond to the forward rotation of the propeller. Figure 3.74 compares the RMS propeller y force coefficients for the unsteady and the steady crashback tests as functions of η. In this figure the coefficients from the three different unsteady test runs have been averaged at the same values of η. Figure 3.75 shows a similar comparison. This time, however, the maximum and minimum coefficient values at each value of η have been plotted as functions of η, along with the steady crashback results. Figures 3.74 and 3.75 both demonstrate that the values of the RMS propeller y force coefficients for the unsteady runs can exceed the values obtained in the steady crashback tests. This result would suggest, in particular, the value of further unsteady crashback simulations.

Figures 3.76 through 3.80 repeat the sequence of plots just described for the RMS body yawing moment development. Figure 3.76 shows the growth and decay of actual RMS body yawing moment with time for the three different runs, and Figure 3.77 shows the variation of the coefficient of RMS body yawing moment (computed using propulsive scaling) with dimensionless distance traveled. Figure 3.78 shows the variation of the coefficient of RMS body yawing moment with the instantaneous value of η. Figures 3.79 and 3.80 compare the results for the steady and unsteady crashback maneuver tests. Despite the possible frequency response issues with the body dynamometer, all of these results tend to track the propeller force results relatively well. Figures 3.79 and 3.80 again demonstrate that the coefficient values for the unsteady crashback tests often exceed the steady crashback values. These two figures include the case of $V = 6.25$ kts for the steady crashback tests. As discussed previously, these data seemed to be somewhat noisier than those for the other tunnel speeds studied and tended to produce the highest peak coefficient values. These two figures show that the unsteady crashback values exceed significantly the steady crashback values for $V = 5$ kts, which are typical of most of the steady crashback results, but that the unsteady crashback values just barely exceed the maximum values for the steady crashback results at $V = 6.25$ kts, again illustrating the somewhat unique nature of the results at 6.25 kts.

The development of various forces and moments will now be examined in some detail. Figure 3.81 shows the variation of tunnel speed, propeller speed, η, RMS propeller axial force, and RMS propeller torque with dimensionless distance covered for each of the three unsteady crashback tests. The velocity, propeller speed, propeller force and torque have all been normalized by their maximum magnitudes (as was done for the ramped propeller speed studies). The negative of the RMS propeller axial force is plotted. Figure 3.81(a) shows the entire data record for each of the three tests and Figure 3.81 (b) expands the scale for each test to show the initial development. Since η is defined as the ratio

of the propeller speed n to the self-propulsion propeller speed n_{sp}, and since n_{sp} goes to zero as V goes to zero, η would tend to negative infinity as the tunnel speed approached zero. In Figure 3.81(a), a scaled value of η is shown. In Figure 3.81(b), which cuts off the record before the values get too large, the actual value of η is shown. This convention is repeated in subsequent figure pairs. Figure 3.81 shows the development of the RMS values of the propeller axial force and torque as the propeller enters reverse rotation and then the decline as the tunnel speed approaches zero. Since the propeller generates axial force and torque even at zero submarine speed, it is not expected that the RMS values would tend to zero as the tunnel speeds goes to zero. They do not and in fact level off at a non-zero value. In Figure 3.82, the RMS propeller and body axial forces are paired for comparison. They tend to track each other well, as might be expected.

Figure 3.83 shows the development of the off-axis RMS propeller moments. These do track the tunnel velocity almost all the way to the end, demonstrating the reduction in vortex ring strength as the tunnel velocity and hence the shear decreases. Figure 3.84 groups the RMS propeller y force and the body RMS y and z moments for comparison. It can be seen from this figure that the body off-axis moments lag the propeller off-axis force briefly and also seem to be damped out more quickly than the propeller off-axis force. Figure 3.85 groups the RMS horizontal and vertical propeller forces and the magnitude of the forces. These can be seen to track the tunnel speed closely. In Figure 3.86, the RMS horizontal propeller force and the RMS body yawing moment are paired for comparison. A horizontal force acting on the propeller would provide the largest contribution by the propeller to a submarine yawing moment. Again the lag in the body moment behind the propeller force can be seen, as well as the quicker damping of the body moment. Finally, in Figure 3.87 the RMS vertical propeller force and the RMS body pitching moment are paired for comparison. A vertical force acting on the propeller would provide the largest contribution by the propeller to a submarine pitching moment. There is an interesting difference in the behavior of this pair. The body moment lag behind the propeller force is less than in previous comparisons, and the pitching moment does not approach zero as the propeller vertical force approaches zero but actually increases and fluctuates about a significant non-zero value. This could represent a body-strut interaction. The model as mounted in the tunnel was stiffer in the vertical (pitching) plane than in the horizontal (yawing) plane and therefore would have a higher natural frequency. It is possible that the frequencies associated with the propeller thrust in reverse rotation and zero tunnel speed were exciting the natural frequencies of the model/strut combination. It was not possible with the tunnel filled to determine the natural frequencies of oscillation of the model/strut combination, and so this will have to remain a matter of speculation for now.

4. LDV AND FLOW VISUALIZATION RESULTS

4.1   Laser Doppler velocimeter (LDV) results

The grid for the LDV velocity field surveys is shown in Figure 4.1. The grid points were located in a vertical plane perpendicular to the floor of the LCC test section. The plane contained the model centerline. In Figure 4.1, the upper drawing shows the locations of the grid points in dimensional quantities. The coordinate x is in the streamwise direction and z is the vertical direction perpendicular to the LCC test section floor. The origin for z was set at the model centerline, which is shown in the figure. In these coordinates the centerplane of propeller disc, shown in Figure 4.1 as a bold line, was located at $x = x_{prop} = 790.37$ mm. The lower drawing in Figure 4.1 shows the same grid re-cast in terms of $(x - x_{prop})/R_{prop}$ and r/R_{prop}, where R_{prop} is the propeller radius of 6 inches = 152.4 mm. Note that both streamwise and transverse coordinates have been normalized by the propeller radius.

The results of the LDV surveys are shown as contour plots in Figures 4.2 through 4.26. Figures 4.2 through 4.21 show the results for a tunnel set speed of 5 kts and propeller speeds of -200, -300, -426, and -600 RPM, yielding values of η of -0.382, -0.565, -0.801, and -1.15, respectively. Figures 4.22 through 4.26 show the results for a tunnel set speed of 7.5 kts and a propeller speed of -680 RPM, yielding a value of η of -0.877. For each value of η there is a set of 5 figures. The first figure in each set is an overview of the results for that η and contains contour plots of mean and RMS streamwise (U_x) and transverse (U_z) velocity components, with mean velocity vectors overlaid on each plot. The following four figures of each set are larger views of the mean and fluctuating streamwise and transverse velocity components with the mean velocity vectors overlaid on each*.

The LDV measurements suffered from the standard limitation of such measurements, in that the LDV system acquired a given number of samples rather than sampling over a given amount of time. The sample sizes were taken as large as possible so that a reasonable average of the velocity at a point could be obtained. However, if the samples were acquired quickly, as was the case when the data rates were high, then low-frequency oscillations of the flow could be missed. Since the ring vortex generated by the propeller in crashback was expected to contain relatively low-frequency asymmetric oscillations, it was recognized that the vortex might not be in the same position (in a time-averaged sense) at every measurement. This effect tended to smear the vortex structure, as well as showing up in other measurements which will be discussed later. However, the LDV surveys give an indication of the extent and structure of the vortex structure and are therefore useful in that regard. It should also be noted that the velocity component perpendicular to the x-z plane, which in the figures to follow would essentially be the swirl velocity component, was not measured. All

---

*In preparing the contour plots in Figures 4.2 through 4.26, the abscissa of some of the plots was labeled as "y" instead of "x." The abscissa in all of the plots should be the coordinate "x." The plots are captioned consistent with the abscissa label.

discussions then are subject to this limitation.

Figures 4.2 through 4.6 show the contours for $\eta = -0.382$. As can be seen in these figures, the vortex structure appears somewhat elongated, with only the forward portion of the vortex appearing in the measurement region. The velocity vectors in the vicinity of $x = 820$ mm, $z = -60$ mm do show a somewhat unexpected component in the direction of the freestream. This component will be discussed in more detail below. The fluctuating u and v components shown in Figure 4.4 and 4.6 are good indicators of the extent of the vortical flow, serving essentially as tags of the regions of high shear.

Figures 4.7 through 4.11 show the contours for $\eta = -0.565$. At this higher reverse propeller speed, the vortex structure begins to assume a more readily-identifiable form, and the majority of the vortex appears in the measurement region. This indicates that the increase in magnitude of η has caused the vortex structure to "tighten" and lose some of the elongation demonstrated at $\eta = -0.382$. It is particularly interesting to note in Figure 4.9 how the velocity vectors are essentially tangent to the contours of the fluctuations in the streamwise velocity.

Figures 4.12 through 4.16 show the contours for $\eta = -0.801$. Recall that this is the value of η where the local maxima in the force and moment coefficients occurred. These figures show a definite vortical structure. The upstream velocity magnitudes at the top of Figure 4.13 are not much smaller than the downstream velocity magntiudes at the bottom of the figure, presumably near the edge or outside the vortex.

Figures 4.17 through 4.21 show the contours for $\eta = -1.15$. These also demonstrate a tight vortex structure, and one that is somewhat "noisier" than the others, in terms of the mean velocity contours and the levels of the fluctuating components. The mean streamwise and transverse velocity contours shown in Figures 4.18 and 4.20 are much less smooth than those in previous figures and demonstrate embedded peaks and valleys.

The detailed velocity field surveys shown in the figures just discussed were all conducted at a tunnel set speed of 5 kts. A survey was also conducted at a set speed of 7.5 kts and a propeller speed of -680 RPM as a check to make sure the fields were in fact dependent only upon η, which for this test case was -0.877. The check survey was conducted on a coarser survey grid than the previous measurements. The contours for this survey are shown in Figures 4.22 through 4.26. The contour plots and velocity vector fields demonstrate approximately the same behavior as shown in Figures 4.12 through 4.16 for $\eta = -0.801$, indicating that the flow field features discussed above were primarily dependent upon η. No further study or analysis of this particular case was conducted.

As noted in the previous discussion, the vortex structure became more well-defined as the magnitude of η increased. The apparent "core" position moved as η varied. To quantify this motion, the velocity field surveys were examined to determine the survey position where the minimum velocity magnitude was measured. This point was identified as an apparent vortex core position, and its movement with η is shown in Figure 4.27. This figure indicates an upstream and outward vortex core migration as η becomes more negative. Since the swirl velocity component was not known, and since the core position as defined was limited by the survey grid resolution (10 mm or $\Delta/R_{prop} = 0.066$) and by the low-frequency unsteadiness in the flow, these positions are only approximate positions, with no attempt at uncertainty analysis undertaken. The apparent vortex core positions measured by Jiang *et al.* (1996) demonstrate the same trend of upstream and outward motion with decreasing magnitudes of J (and hence increasing magnitudes of η).

In Figure 4.27, the vortex core positions corresponding to $\eta = -0.801$ and $\eta = -1.15$ are the two closest to the

propeller. Since it was known that there was a local maximum in the force and moment coefficients in the vicinity of η = -0.8, it was thought that perhaps this peak was related to the "closest approach" of the vortex core to the propeller. The distances from the apparent core positions shown in Figure 4.27 to the propeller tip and the propeller center were computed and the results are shown in Figure 4.28. This figure shows that the vortex core position corresponding to η = -0.801 is in fact the closest position to the propeller center, although by not very much over the core position at η = -1.15. The apparent core position is in fact closest to the propeller tip at η = -1.15.

In order to examine the vortex structure further, the velocity profiles in the radial direction at the vortex core positions were extracted from the velocity surveys for each value of η. These are shown in Figures 4.29 through 4.32. Each profile consists of the velocity data acquired during the survey in the z direction (corresponding to the radial direction r) corresponding to the x location identified as the vortex core position. The $(x - x_{prop})/R_{prop}$ locations of each survey are included in the caption for each profile. Since the LDV survey grids were located on the center plane of the LCC test section and since the origin for the transverse direction was located on the model centerline, the radial velocity component could be obtained from the transverse component simply by changing the sign of the velocity (up is the positive direction for z in the test-section-fixed coordinate system). This transformation was done for the data shown in Figures 4.29 through 4.32, as well as the data in Figures 4.33 through 4.36. In all of these figures, v indicates the radial velocity component.

Figure 4.29 contains the data for η = -0.382. The essentially zero value of the transverse (y) mean velocity indicate that the core position is fairly accurate in this case. A vertical slice through the core should show zero transverse velocities. The figure also shows the peak in streamwise velocity fluctuations at the location of maximum shear. The other figures show similar variations. In Figure 4.30, the slightly positive values of radial velocity v on either side of the radial position where the streamwise velocity u goes through zero indicate that this x position was somewhat upstream of the actual mean vortex core position. Similar slight discrepancies may be observed in Figures 4.31 and 4.32. The jagged nature of the u velocity profile in Figure 4.32 for η = -1.15 is in all likelihood due to the low-frequency oscillations of the vortex position that were not captured by the LDV system during its sampling of the flow field, as discussed previously.

One further velocity profile study was conducted. Since it was recognized that the primary mechanism by which fluctuations in the vortex structure would be communicated to the submarine propeller was through modifications to the inflow velocities into the propeller, the inflow velocities were examined by extracting velocity profiles from the overall surveys at the downstream position closest to the propeller plane for which a full traverse was conducted. In Figure 4.1, this corresponds to the row of grid points at x = 828.9 mm or $(x - x_{prop})/R_{prop}$ = 0.253; *i.e.*, the most upstream row of grid points which extends the full direction in z or r. These profiles are shown in Figures 4.33 through 4.36, each figure corresponding to one of the values of η.

Figure 4.33 shows the inflow profiles for η = -0.382. These profiles illustrate more clearly the phenomenon mentioned earlier, the downstream or positive u velocity at the radial positions closest to the centerline. This figure also shows that the largest velocity fluctuations occur for r/R_{prop} < 1, *i.e.* inboard of the propeller tip. Similar variations are shown in Figure 4.34 for η = -0.565. There is still a small region near the centerline where u > 0, but it is smaller than the region at η = -0.382. The behavior begins to change as η becomes more negative. In Figure 4.35, at η = -0.801,

the region of postive u has disappeared, and the regions of large fluctuations in velocity have begun to move out from the centerline to larger values of r. In this figure a local peak in u' occurs at $r/R_{prop} \approx 1.25$. In Figure 4.36, at $\eta = -1.15$, the overall peak in u' occurs at $r/R_{prop} \approx 1.25$ and the distribution of v' seems to be centered around $r/R_{prop} \approx 1.0$. When the peak fluctuations occur at greater values of r, the corresponding fluctuations in forces and moments on the propeller blades as a result of the fluctuating velocities (and hence fluctuating blade section angles of attack) act through a greater moment arm and thus transmit larger forces and moments to the submarine itself. It is possible that this change in the vortex structure as η changes is the reason for the relative maximum in the force and moment coefficient curves in the vicinity of $\eta = -0.8$.

4.2   Flow visualization results

The experimental apparatus for the flow visualization studies was described in Section 2.4.5. Some results of these studies are shown in Figures 4.37 through 4.46. The flow conditions were adjusted so that approximately equal values of η were obtained at different tunnel set speeds and propeller speeds. These flows were visualized using dye and bubble injection, and the flows were recorded on videotape. Still images were acquired from these videotape segments. These images were then grouped by values of η. The images for values of η of approximately -0.4, -0.6, -0.7, -0.8, -1.1, and -1.5 are shown in Figures 4.37 through 4.42. Each figure contains images obtained at different tunnel set speeds and propeller speeds. These flow conditions are noted on each image. In each figure, the free stream flow is from right to left.

A few general comments are in order before the figures are discussed in detail. Based on the computational results presented in Zierke et al. (1997), one might have expected to see in these experiments an asymmetric ring vortex "attached" to the propeller. The asymmetry in the vortex ring would cycle around the propeller, leading to the off-axis forces and moments. As the current experiments showed, however, this type of flow only occurred at small values of $|\eta|$. For larger values of $|\eta|$, two different types of large disturbances were observed. One was a frequent but not quite periodic vortex "shedding" event.* The apparent vortex on one side of the propeller would "detach" from the propeller and move downstream. A vortex would then reform to take the place of the one that was "shed." The other type of disturbance was a large-scale disruption of the flow. This is similar to the phenomenon noted by Jiang et al. (1996), who observed that "the ring vortex would sometimes suddenly disperse into a mayhem of random cloudy air bubbles only to reform later into a moving ring vortex again" (p. 86; Jiang et al. were using a laser sheet to illuminate bubbles in their flow, similar to the technique that was used here). The vortex shedding events and the large-scale disruptions of the flow did not appear to be quite periodic but did occur on a fairly frequent basis for the appropriate values of η. The "frequency" of these events seemed to be dictated more by the free stream flow speed than by the propeller speed. The sheddings and disruptions occurred more frequently at higher tunnel set speeds. Generally speaking, the large-scale disturbances were separated by intervals during which the formed vortex structure was present. These intervals tended to decrease as the magnitude of η increased.

---

*The discussion here will be influenced by the fact that a two-dimensional slice of the flow was obtained using the laser sheet, and so in most cases the fully three-dimensional aspects of the flow were not observed. For this reason terminology appropriate to the two-dimensional image will be used, keeping in mind the caveat just discussed.

32

There was a bit of subjectivity injected into the image selection process as a result of these low-frequency, large-scale disturbances. A vortex structure would form, hold for some period of time, and then be disturbed, either by a vortex-shedding event or a large-scale disruption. The vortex structure would then reform, and so on. Generally images were selected to demonstrate the more or less steady formed vortex structure. Additional images were then selected to demonstrate the large-scale disturbances to the flow.

Representative results for $\eta \approx -0.4$ are shown in Figure 4.37. At these values of η, the ring vortex structure was visibly present. The vortex ring seemed to be elongated in the streamwise direction, in agreement with the LDV measurements discussed earlier. The visible "edge" of the vortex ring exhibited behavior that resembled traditional shear layer behavior, including vortex rollup, although it was usually difficult to distinguish apparent vortex rollup from the possible shedding of tip vortices by the propeller blades. Figure 4.37(d) in particular demonstrates the downstream entrainment of flow back into the vortex structure. The bubbles on the left of the laser sheet at the same level as the propeller hub are moving upstream toward the propeller. As noted earlier, both dye and bubbles were injected into the flow. It was discovered that a tunnel set speed of 7.5 kts was the best for bubble flow visualization. At tunnel speeds lower than 7.5 kts, the bubbles, which were injected from within the model upstream of the propeller, would rise and miss being entrained into the propeller and vortex ring flow. At 7.5 kts, the bubbles were captured by the propeller/vortex flow field because they had not had time to rise outside of its reach.

Similar results are shown in Figure 4.38 for $\eta \approx -0.6$. There were occasional large disturbances seen, as shown in Figure 4.38(b). For the most part, however, the elongated vortex structure was present with no large disturbances. The flow field is best illustrated in Figure 4.38(e). The bubbles clearly demonstrate the full recirculating motion inside the ring vortex.

The images for $\eta \approx -0.7$ are shown in Figure 4.39. The vortex ring appears to be tighter in structure and closer to the propeller. Large disturbances began to become more frequent. Figures 4.39(e) and 4.39(g) demonstrate examples of vortex shedding events, while Figure 4.39(f) shows an example of a vortex re-forming after a shedding event. Figure 4.39(h) is actually an example of a large-scale disruption of the flow.

Figure 4.40 contains the images for $\eta \approx -0.8$. Recall from the discussion in Chapter 3 that the peak values of the dimensionless off-axis force and moment coefficients occurred in the vicinity of $\eta \approx -0.8$. The flow visualization studies showed that the ring vortex seemed to have its most coherent structure at this value of η. There were some large disturbances. Figure 4.40(c) illustrates a vortex shedding event, while Figures 4.40(h) through 4.40(j) demonstrate a vortex shedding sequence. The formed vortex is shown in Figure 4.40(h), and this same vortex is shown almost out of the laser sheet to the left in Figure (i). The "replacement vortex" has formed in Figure 4.40(j). Figure 4.40(l) shows what amounts to a large-scale disruption of the flow, which was less frequent at these flow conditions. Figure 4.40(k) is of most interest in this set of images. At the flow conditions of Figure 4.40(k) there was some cavitation from the propeller. This produced some very small bubbles that helped visualize what was happening in the wake. Recall the earlier discussion about the frequency of large disturbances. Generally these were separated by some interval of time where the formed vortex would remain "attached" to the propeller. At $\eta \approx -0.8$, these large disturbances, mostly vortex shedding events, exhibited their most periodic behavior. The ring vortex would form and shed in almost equal intervals of time. The resulting wake behind the propeller appeared to swirl about the propeller and acquired a corkscrew-like

appearance downstream. The bubbles from the propeller cavitation were significant in visualizing this aspect of the flow field. A coalescence of these bubbles can be seen in the portion of the vortex below the propeller in Figure 4.40(k). In the two-dimensional view, the flow most closely resembled that of vortex shedding behind a circular cylinder. Recall the earlier discussion which said that the large disturbance aspect of the flow seemed to be influenced more by the free stream speed than the propeller speed. In the author's opinion, the best way to describe what is happening in the flow at $\eta \approx -0.8$, as illustrated by these flow visualization images, is that the apparently free-stream dominated phenomenon that is causing the large disturbances is coupling with the vortex ring flow, creating a periodic large disturbance that in turn is producing the peak in the dimensionless off-axis force and moment coefficients.

This description is reinforced by the flow visualization images shown in Figure 4.41 for $\eta \approx -1.1$. The formed vortex appears to be located farther upstream and also farther outward radially, as illustrated in particular by Figures 4.41(a) and 4.41(h). At these values of η, there were more large-scale disruptions of the flow than vortex shedding events. Figure 4.41(k) illustrates a large-scale disruption of the flow. It is conjectured that because the large-scale disruptions disrupt the ring vortex so thoroughly that it takes some interval of time to reform, the resulting force that is applied to the propeller because of the flow asymmetry is reduced, particularly in RMS magnitude, and so the dimensionless off-axis force and moment coefficients are reduced from their values at $\eta \approx -0.8$. At $\eta \approx -0.8$, the vortex shedding event which predominates appears to be less of a disruption to the flow, allowing for quicker re-forming of the vortex ring and hence a greater chance for periodic behavior to develop.

The flow visualization images for $\eta \approx -1.5$ are shown in Figure 4.42. In many of these images, the vortex appears to be either just off the propeller tip in the radial direction, as in Figure 4.42(h), or actually upstream of the propeller, as in Figure 4.42(d). Figure 4.42(j) illustrates a vortex shedding event, with the shed vortex moving off downstream in the upper left corner of the image and the new vortex forming at the propeller tip. Figure 4.42(k) illustrates a large-scale disruption of the flow. Recall that values of η of large magnitude are obtained with high propeller speeds and low tunnel set speeds.

As discussed in the section on the LDV measurements, there seemed to be something of a correlation between the peak at $\eta \approx -0.8$ in the dimensionless coefficients and the vortex core location. The formed vortex location is shown as a function of η in Figure 4.43. This figure shows the progression in formed vortex structures as η varies from -0.387 to -1.521. Note that the vortex appears to move upstream and become tighter as the magnitude of η increases, up to η = -0.825. Then the vortex appears to move radially outward as the magnitude of η is increased past 0.825. Figure 4.44 shows an extreme case where η = -2.17. This figure shows the large radial extent of the ring vortex flow field and the upstream position of the formed vortex at this relatively large value of propeller speed and this relatively small value of tunnel set speed. The large-scale disruptions were generally of low frequency but of durations similar to the formed vortex structure.

In Section 3.3, the results of the unsteady crashback simulations were discussed. Among these tests were simulations of unsteady crashback in which both the propeller speed and the tunnel speed were allowed to vary. The propeller was allowed to windmill in forward rotation at a particular tunnel set speed. The propeller motor was then engaged for reverse rotation. When it was visually observed that the propeller had begun reverse rotation, the tunnel set speed was set to zero and the tunnel was allowed to decelerate. Some examples of these simulations were recorded

on videotape, and Figures 4.45 and 4.46 contain representative images from these flows. Figure 4.45 is an example of the appearance of the flow during forward rotation of the propeller. The tunnel set speed was 7.5 kts. At this speed, the propeller "windmilled" in forward rotation at 330 RPM. Figure 4.45 shows the flow through the propeller at this forward rotation speed. The propeller speed was then set to -500 RPM, and when the propeller engaged in reverse rotation, the tunnel set speed was set to zero. The sequence of images in Figure 4.46 were obtained after the propeller began its reverse rotation. These images were obtained at roughly one second intervals, but the interval is only approximate, and the images were chosen primarily to show the development of the flow through the unsteady crashback simulation. The similarities between Figure 4.46 and Figure 4.43 are evident. As the tunnel speed drops, the self-propulsion propeller speed also decreases, so that for the given propeller speed (which is achieved very quickly), η begins with a relatively small magnitude which increases as the tunnel speed decreases (recall that η is the ratio of the actual propeller speed to the propeller speed required for self-propulsion at a given tunnel speed). Thus in the sequence of images in Figure 4.46, η is beginning with a relatively small magnitude that then increases through the sequence. As can be seen from the images, the vortex core begins downstream at a radial position inside the propeller tip. As η increases in magnitude, the core moves upstream and becomes tighter (image 3 in the sequence) and then moves outboard of the propeller tip, eventually reaching a location upstream of the propeller.

The motions observed in the current experiments seemed to display less regularity than those reported by Jiang *et al.* (1996). Jiang *et al.* report a fairly regular oscillation of the vortex core, with occasional large-scale disruptions and less frequent vortex shedding events. Their measurements were made for two values of the advance ratio which correspond to maximum values of the magnitude of η in the current experiments. The current experiments did tend to show more large-scale disruptions than vortex-shedding events at the largest magnitudes of η, but these seemed to occur more frequently than in the experiments by Jiang *et al.*, based on their comments. Since they were performing "open water" experiments on a propeller only, they did not have the hull wake or the wakes of the fins and the model support strut as potential complicating factors. It is possible that these wakes contributed to the apparently greater unsteadiness of the flow in the current experiments, particularly the wakes of the strut and the fins that would have the tendency to roll up and provide temporal as well as spatial disturbances to the ring vortex flow.

5. CONCLUSIONS AND FUTURE WORK

5.1 Conclusions

The off-axis force and moment coefficient values obtained from both the propeller and body dynamometers for the steady crashback simulations were correlated well by the propulsion parameter η, defined as the ratio of the propeller rotational speed to the propeller speed required for self-propulsion. The data were very repeatable when plotted against η, even for widely varying flow conditions and especially for the propeller force and moment data. The coefficients demonstrated a relative maximum for values of η near -0.8 for both the propeller and body data. Spectral analyses of the propeller data indicated a reversal in the direction of the ring vortex asymmetry rotation relative to the propeller as the magnitude of η was increased past its lowest value. The magnitude of this relative rotation frequency then decreased in magnitude as the magnitude of η was increased further (*i.e.* as η became more negative).

The unsteady crashback simulations revealed that the magnitudes of the off-axis force and moment coefficients could exceed those obtained during the steady crashback measurements. The data from the ramped propeller and tunnel speed tests also indicated that the magnitudes of the coefficients tracked the tunnel speed fairly closely, suggesting that the strength of the ring vortex decreased as the relative shear between the free stream flow and the propeller-induced flow decreased.

The laser Doppler velocimeter (LDV) measurements revealed a variation in the vortex structure and core location as η varied. At the smaller magnitudes of η, the vortex structure appeared to be elongated somewhat in the streamwise direction. As the magnitude of η increased, the vortex structure became tighter and the vortex core appeared to move upstream. For $\eta \approx -0.8$, the apparent vortex core position was closest to the propeller hub. As η became more negative, the core moved radially outward toward the propeller tip. Profiles of the fluctuating velocity components at the LDV streamwise measurement position closest to the propeller showed that the spatial peaks in the fluctuations moved radially outward as η became more negative.

The flow visualization results confirmed the movements of the vortex core indicated by the LDV measurements and also showed that at very large negative values of η, the ring vortex could actually be located upstream of the propeller. The flow visualization experiments also revealed that the ring vortex could experience large-scale disturbances, either through apparent "vortex-shedding" events or through large-scale disruptions where the ring vortex essentially disappeared for brief periods of time. These large-scale disturbances did not appear to be periodic, except in the vicinity of $\eta \approx -0.8$, where the large-scale disturbances and the inherent unsteadiness in the ring vortex appeared to couple and produce a very large periodic disturbance to the wake, resulting in large periodic forces on the propeller and the submarine.

5.2   Recommendations for future work

One limitation of this study was that the propeller used in the experiments was not an actual submarine propeller. The propeller was originally designed and built as part of a study commissioned by a cruise ship company. The propeller had no skew and it was not actually the appropriate diameter for the submarine with which it was used. The propeller was chosen because it was available, it had an unclassified geometry, and a number of studies of this propeller had already been conducted and were available in the open literature. It would be of some value to repeat the study with a propeller more similar in shape and size to an actual submarine model propeller, in particular to see the effect on the critical value of η where the force and moment coefficients might exhibit a local maximum.

It would seem that the most logical conclusion that could be drawn from the results of these experiments is to avoid the critical value of η if possible, thereby avoiding the peak in the off-axis force and moment coefficients that occur at that value of η. This would be especially critical in the actual unsteady crashback maneuver, since the unsteady crashback simulations in these studies indicated that the coefficient values could exceed those of the steady crashback conditions. The drawback to the current experiments was that the rate of change of propeller speed could not be controlled. The propeller control system was set up such that a reversal of propeller direction required the physical disconnection and re-connection of the main power lines to the propeller motors, so that a propeller reversal from a selected forward speed to a selected reverse speed was not possible. The propeller had to be allowed to "windmill" in forward rotation at whatever speed was dictated by the tunnel speed and the characteristics of the propeller. When the reverse rotation speed was commanded, there was no way to adjust the rate at which the propeller changed speed. The rate was dictated by the response of the motor to the control input. It would be quite valuable to be able to construct a propeller speed profile, starting with a selected forward speed (presumably the self-propulsion speed at the given tunnel speed) and then tailoring the rate of speed change to the selected reverse speed. It might be possible to match the dynamics of the propeller and tunnel such that the critical ranges of η are either passed through quickly or avoided altogether. If experiments do indicate that by a judicious choice of propeller speed change profiles significant off-axis forces and moments can be avoided, then it might merit consideration for implementation on an actual submarine.

References

Bridges, D. H. 2001 A detailed study of the flow field of a submarine at large angle of drift. *Office of Naval Research Grant No. N00014-96-1-0911 Final Report, Dept. of Aerospace Engineering, Mississippi State University, Report No. MSSU-ASE-01-1, May 2001.*

Blanton, J. 1995 Laser Doppler velocimetry techniques in the Large Cavitation Channel. *Presented at the 24th American Towing Tank Conference, Texas A&M University, College Station, Texas, November 1995.*

Boswell, R. J. 1971 Design, cavitation Performance, and open-water performance of a series of research skewed propellers. *Naval Ship Research and Development Center Report No. 3339, March 1971.*

Chen, B. and Stern, F. 1998 Computational fluid dynamics of four-quadrant marine-propulsor flow. *Proceedings of the 1998 ASME Fluids Engineering Division Summer Meeting, 21-25 June 1998, Washington, DC, paper no. FEDSM98-4872.*

Coleman, H. W. and Steele, W. G., Jr. 1999 Experimentation and uncertainty analysis for engineers, 2nd ed.. *New York: John Wiley & Sons, Inc..*

Etter, R. and Wilson, M. 1992 The large cavitation channel. *In Proceedings of the 23rd American Towing Tank Conference, Univ. of New Orleans, New Orleans, LA, 1992, pp. 243-252.*

Etter, R. and Wilson, M. 1993 Testing ship designs in a water tunnel. *Mechanical Engineering, vol. 13, no. 10 (October 1993), pp. 74-80.*

Glauert, H. 1934 Airplane propellers. *In Durand, W. F., ed., Aerodynamic Theory, vol. IV, pp. 348-351.*

Groves, N., Huang, T., and Chang, M. 1989 Geometric characteristics of DARPA SUBOFF models. *David Taylor Research Center, Rept. SHD-1298-01, Bethesda, MD, March 1989*

Gruner, W. P. and Payne, H. E., III 1992 Submarine maneuver control. *Proceedings of the United States Naval Institute, vol. 118, no. 7 (July 1992), pp. 56-60.*

Hecker, R. and Remmers, K. 1971 Four quadrant open-water performance of propellers 3710, 4024, 4086, 4381, 4382, 4383, 4384 and 4426. *Naval Ship Research and Development Center Report 417-H01.*

Jiang, C.-W., Dong, R., Liu, H.-L., and Chang, M.-S.. 1997 24-inch water tunnel flow field measurements during propeller crashback. *Proceedings of the 21st Symposium on Naval Hydrodynamics, 24-26 June 1996, Trondheim, Norway, National Academy Press, Washington, D.C., pp. 86-96.*

Lock, C. H. H. 1928 Photographs of streamers illustrating the flow around an airscrew in the 'vortex ring state.' *British ARC R&M 1167.*

Park, J. T., Cutbirth, J. M., and Brewer, W. H. 2002 Hydrodynamic performance of the Large Cavitation Channel. *Naval Surface Warfare Center Carderock Division Report no. NSWCCD-50-TR-2002/068, December 2002.*

Prouty, R. W. 1990 Helicopter performance, stability, and control. *Malabar, FL: Robert E. Kreiger Publishing Company, pp.*

Wright, J. E. 1995 Submarine design for the littorals. *Proceedings of the United States Naval Institute, vol. 121, no. 12 (Dec 1995), pp. 39-41.*

Zierke, W. C., ed. 1997 A physics-based means of computing the flow around a maneuvering underwater vehicle. *Applied Research Laboratory, Pennsylvania State University, Technical Report TR 97-002, January 1997.*

freestream velocity

ring vortex (section)

velocity induced
by propeller in
reverse rotation

freestream velocity
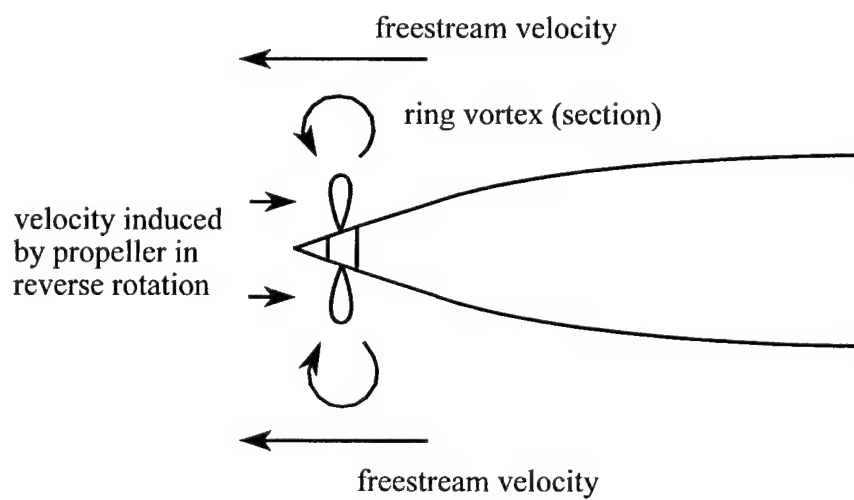
Figure 1.1 Schematic of flow (velocities in reference frame of submarine in forward motion)
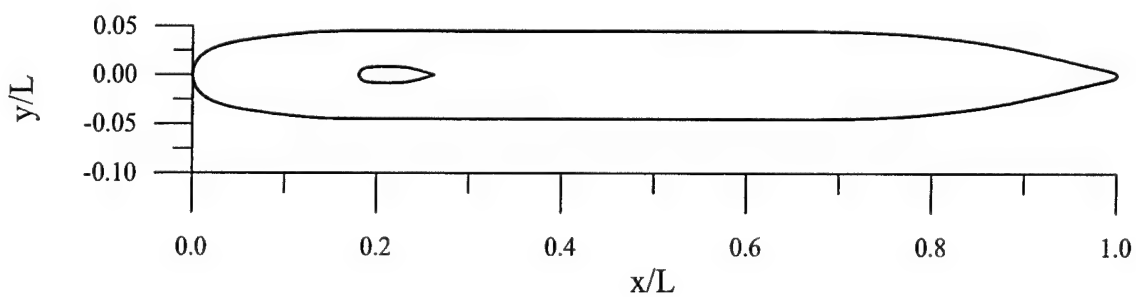
Figure 2.1 Submarine hull contour; sail not used in experiments but indicates location of strut
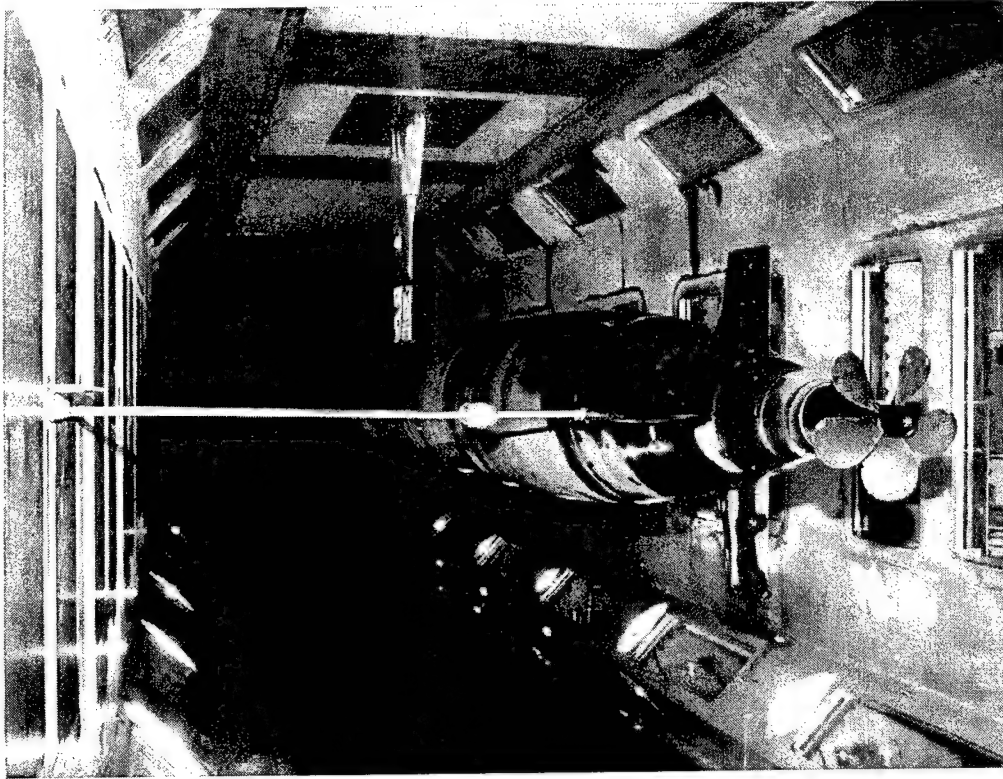
Figure 2.2 Illustration of propeller, stern appendage placement, and stabilization strut

PROPELLER 4381

EXPANDED
OUTLINE

r = 0.7 Section

PROJECTED
OUTLINE
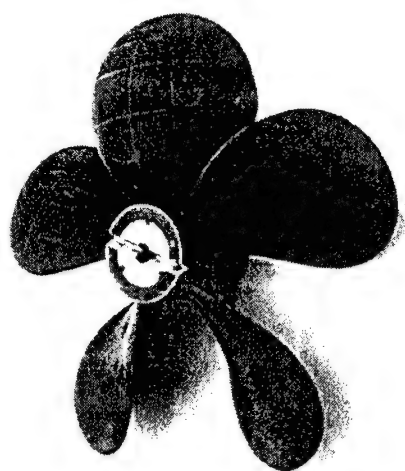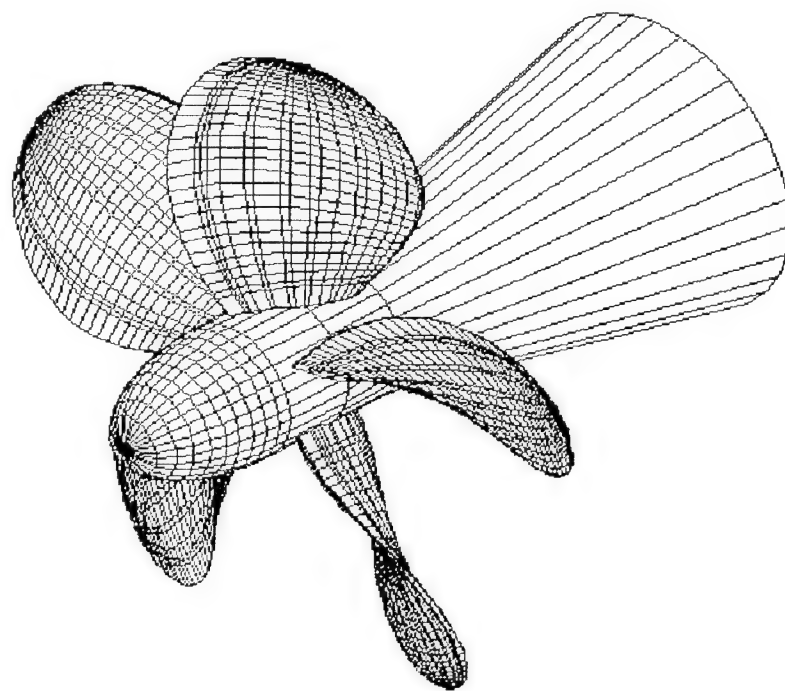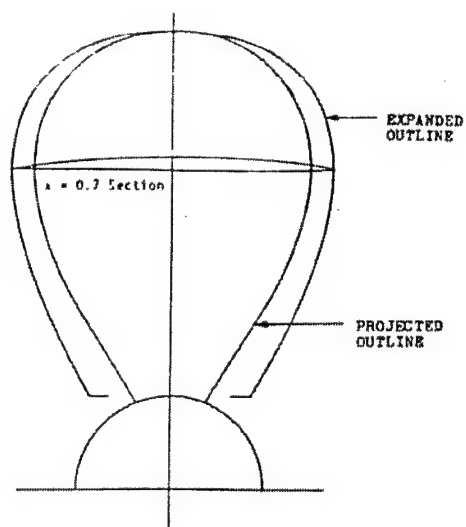
Figure 2.3 Propeller 4381 (photo from Hecker and Remmers 1971; blade diagram from Boswell 1971; IGS file courtesy Martin Donnelly, NSWCCD)
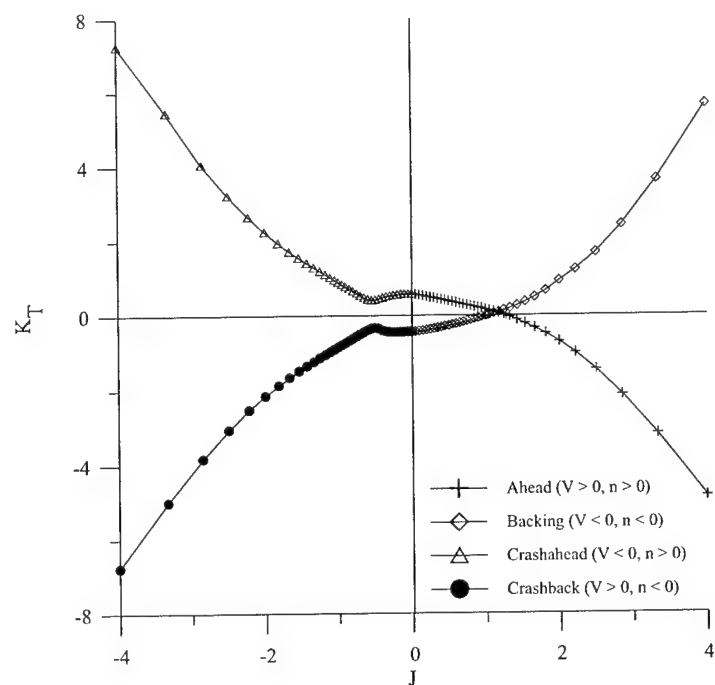
a. Thrust data
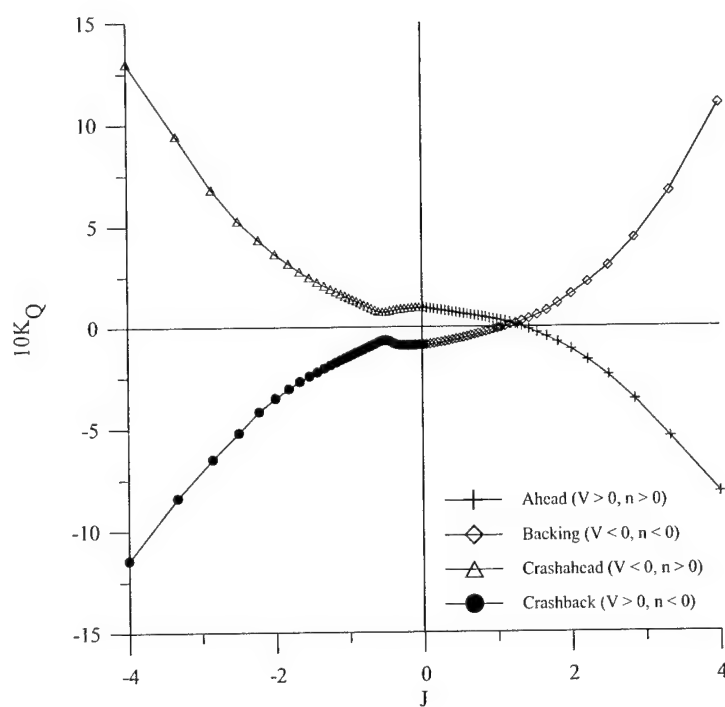
b. Torque data

Figure 2.4 Open-water data for Propeller 4381 (Hecker and Remmers 1971)
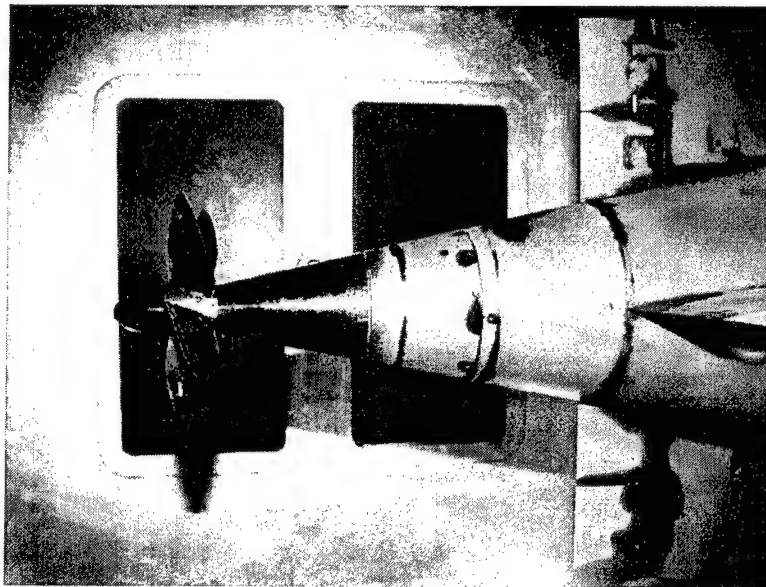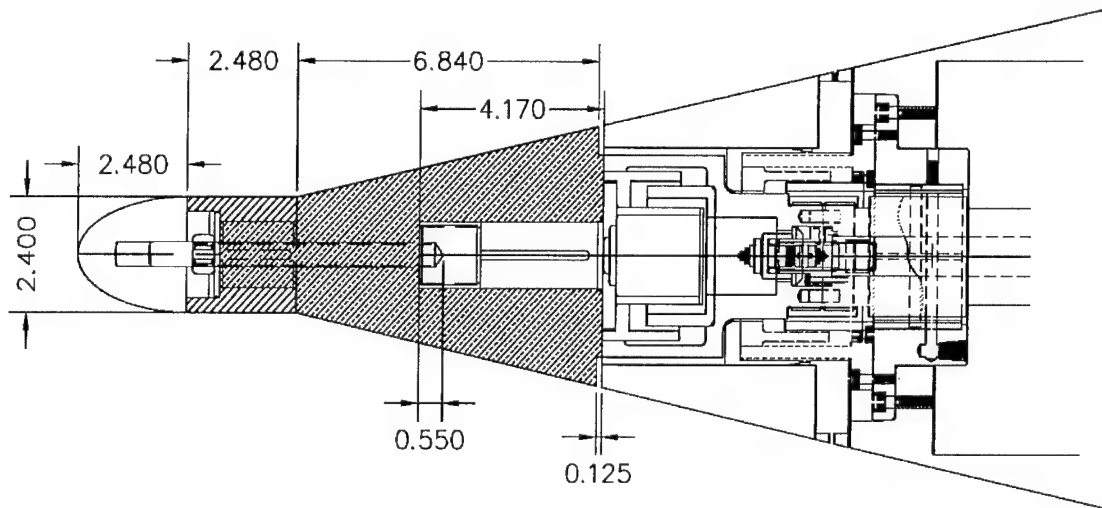
Figure 2.5 Hull extension and P4381 mounted on submarine hull (P4381 omitted from drawing)
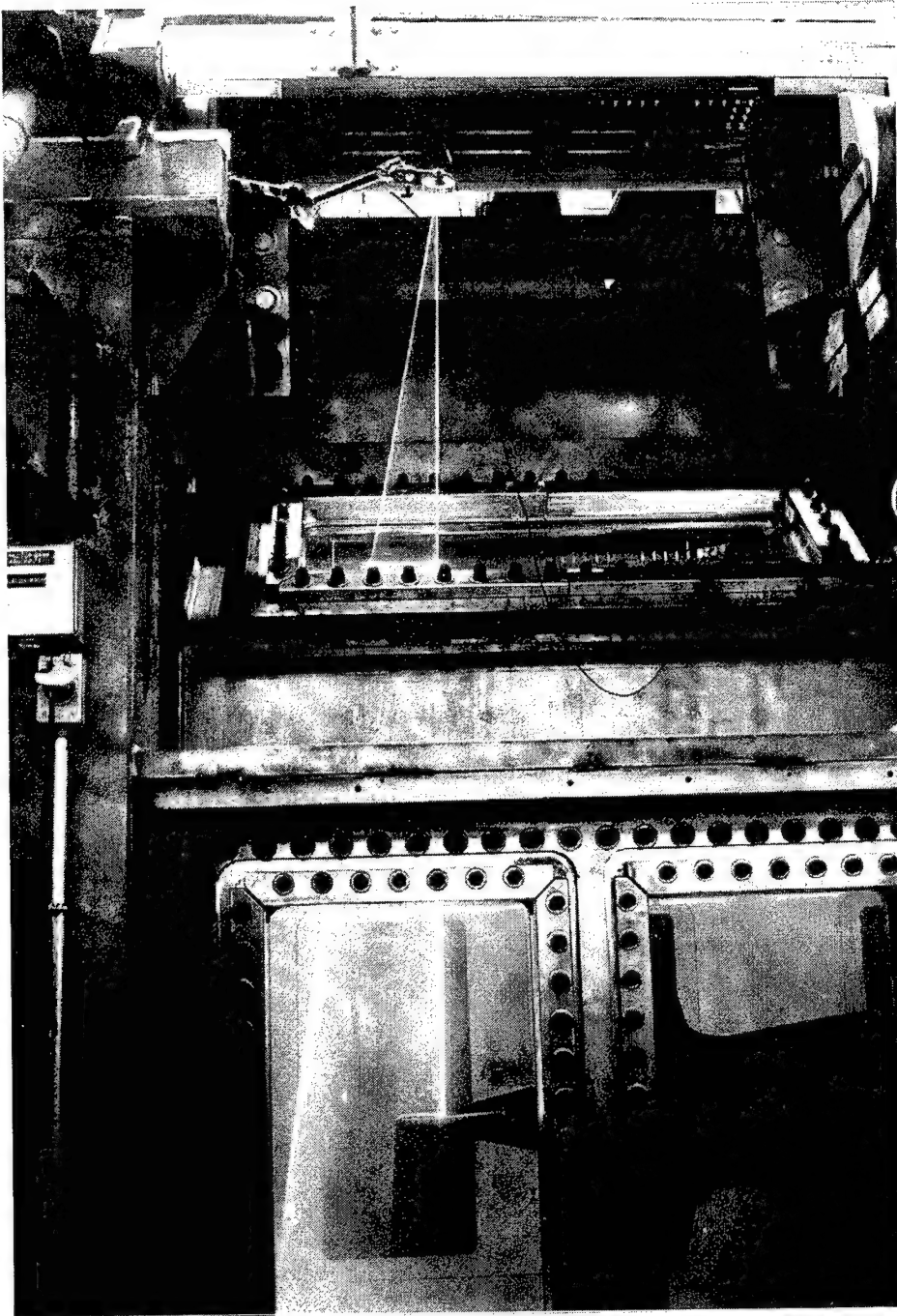
Figure 2.6 Laser sheet apparatus for flow visualization
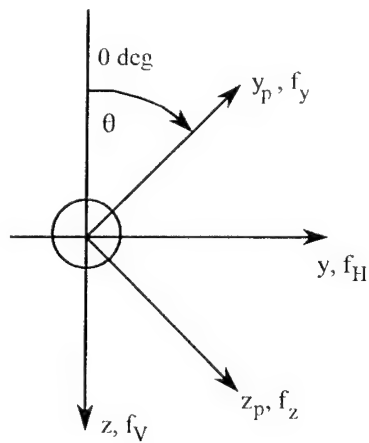
Figure 2.7 Propeller-fixed and body-fixed coordinate systems
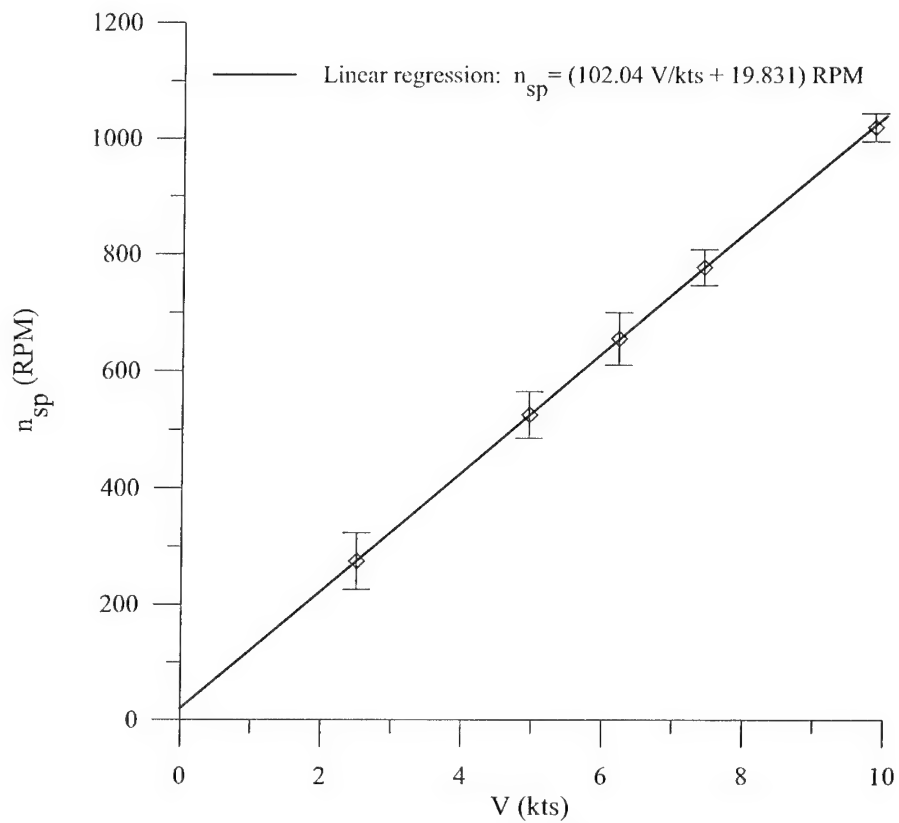
Figure 2.8 Results of self-propulsion propeller speed studies
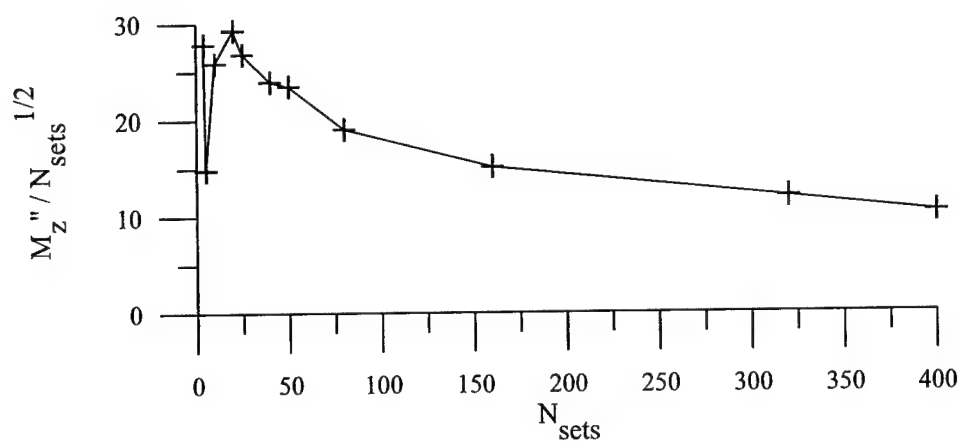
Figure 2.9 Standard deviation of RMS mean as a function of number of samples
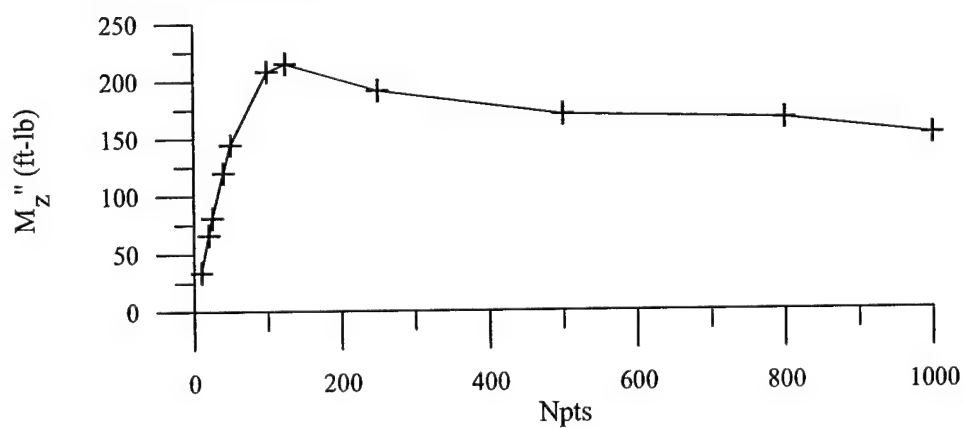
Figure 2.10 Standard deviation of RMS value as function of number of points per sample
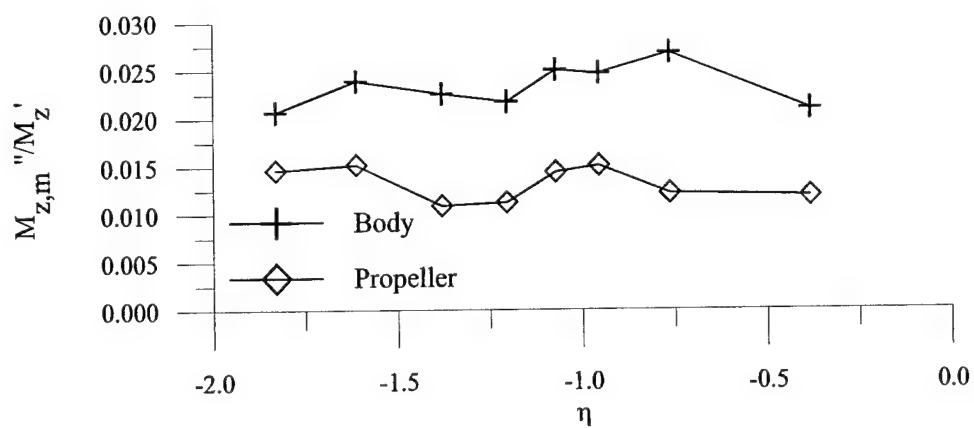
Figure 2.11 Standard deviation of mean M_z' as fraction of mean M_z'
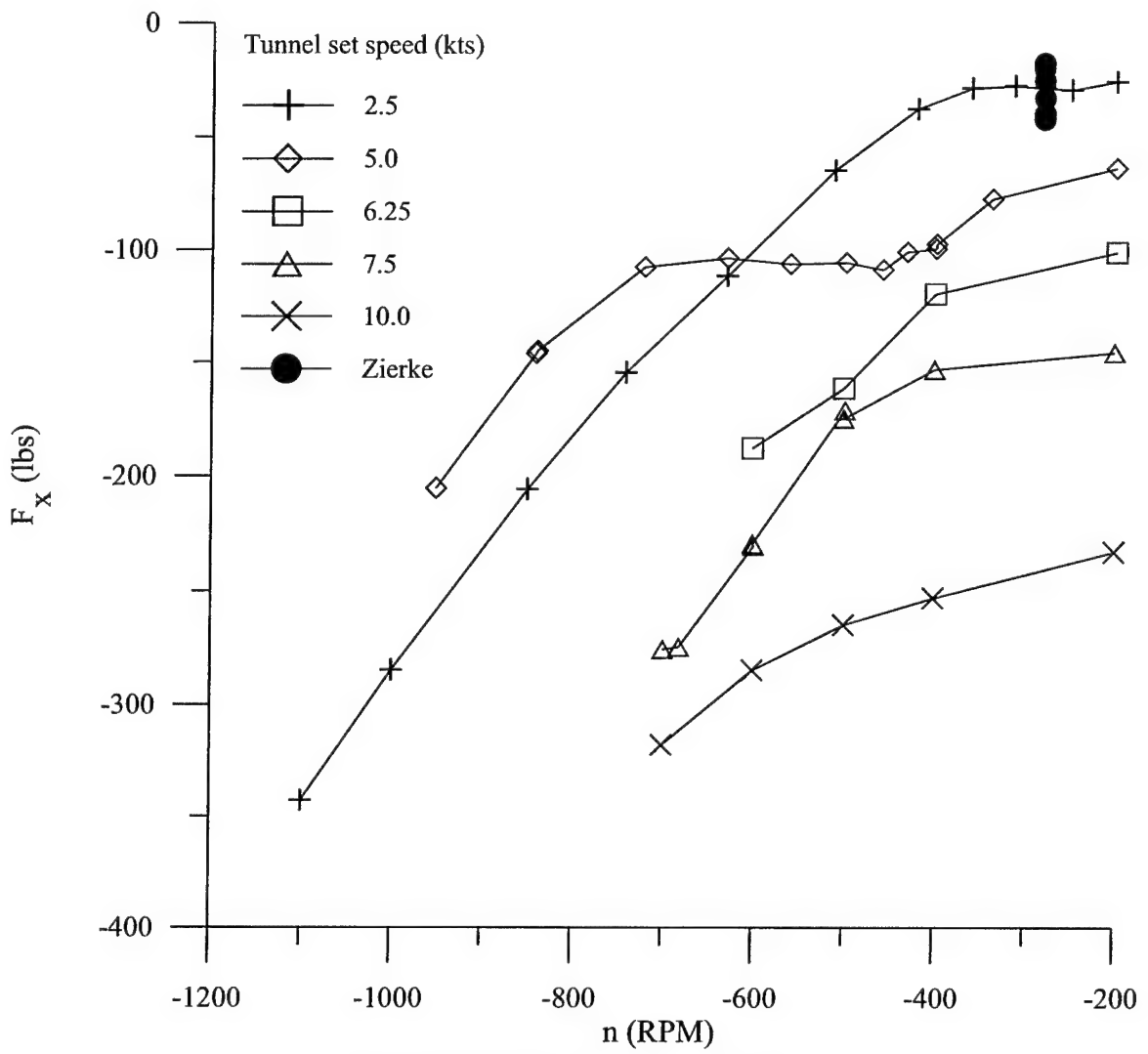
Figure 3.1 Dimensional mean body axial force
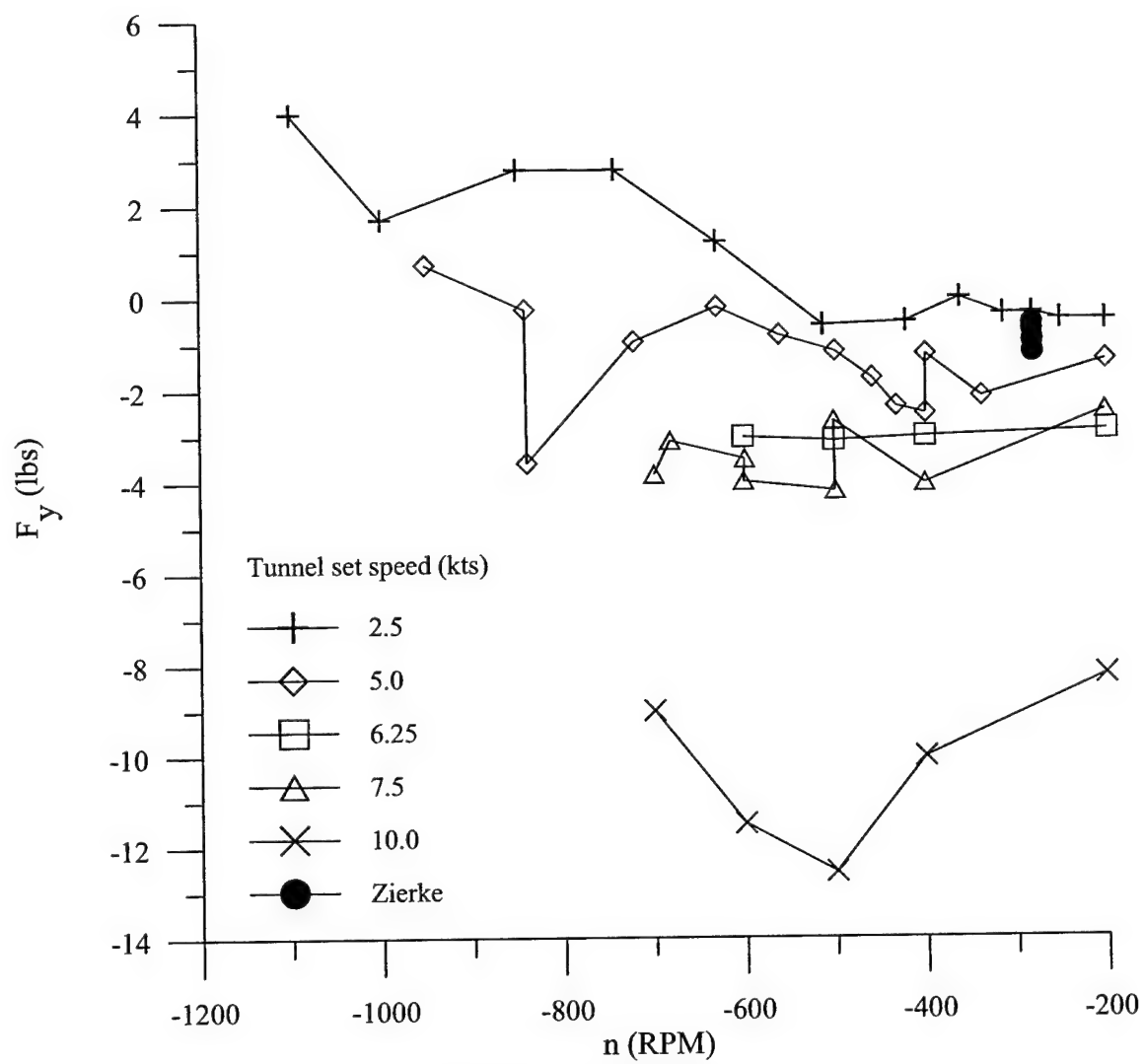
Figure 3.2 Dimensional mean body side force
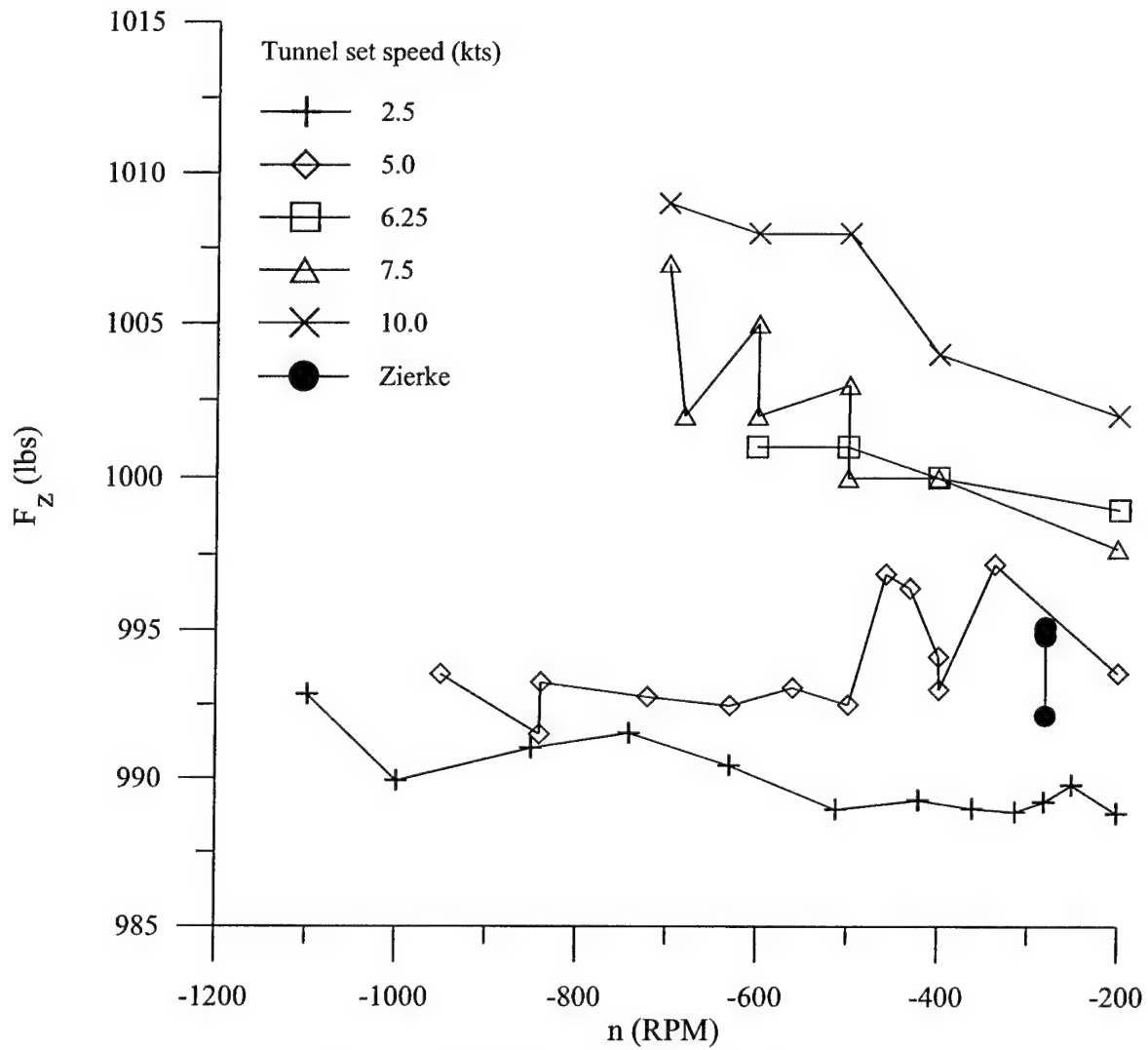
Figure 3.3 Dimensional mean body vertical force
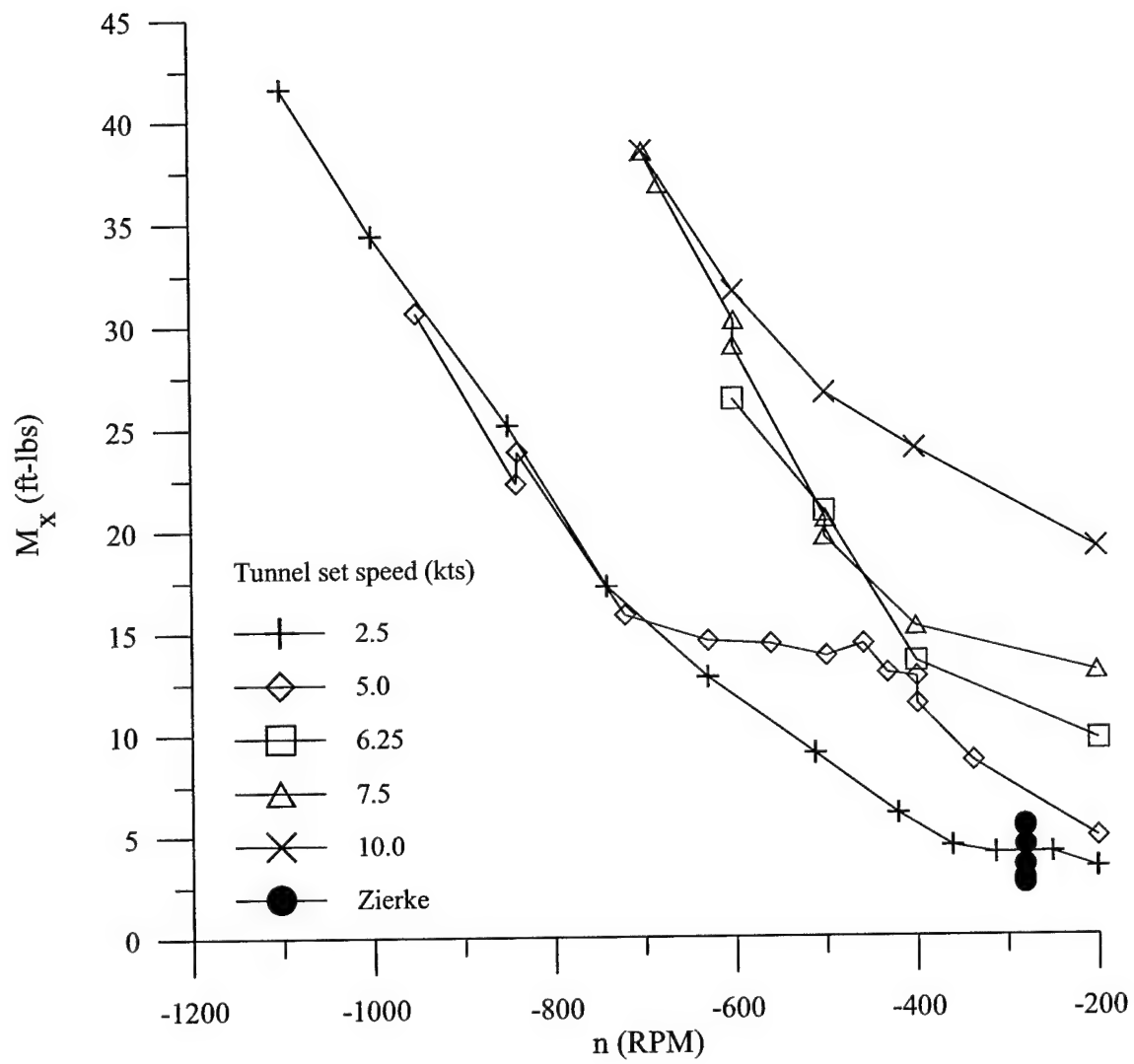
Figure 3.4 Dimensional mean body axial (rolling) moment
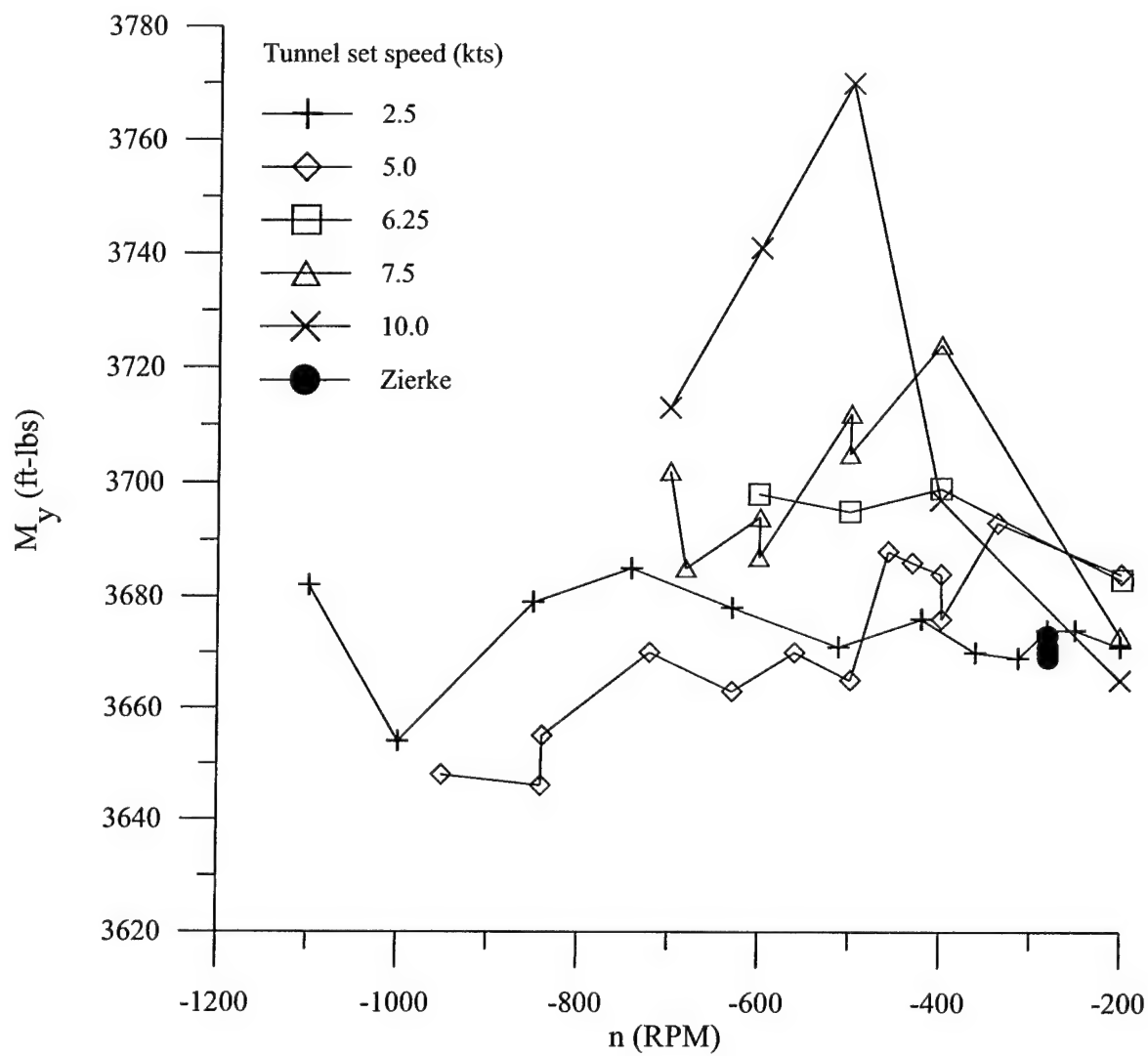
Figure 3.5 Dimensional mean body pitching moment
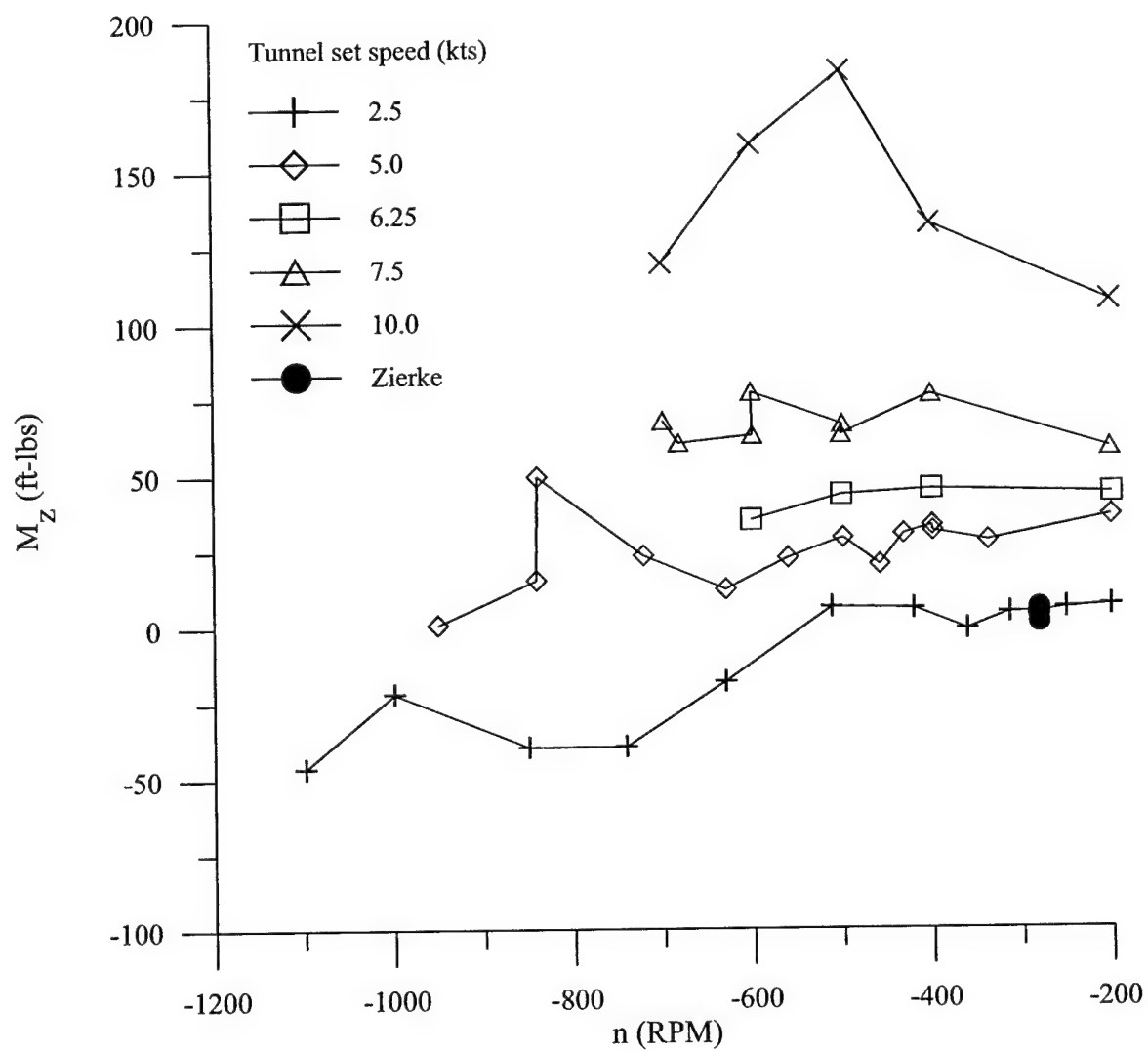
Figure 3.6 Dimensional mean body yawing moment
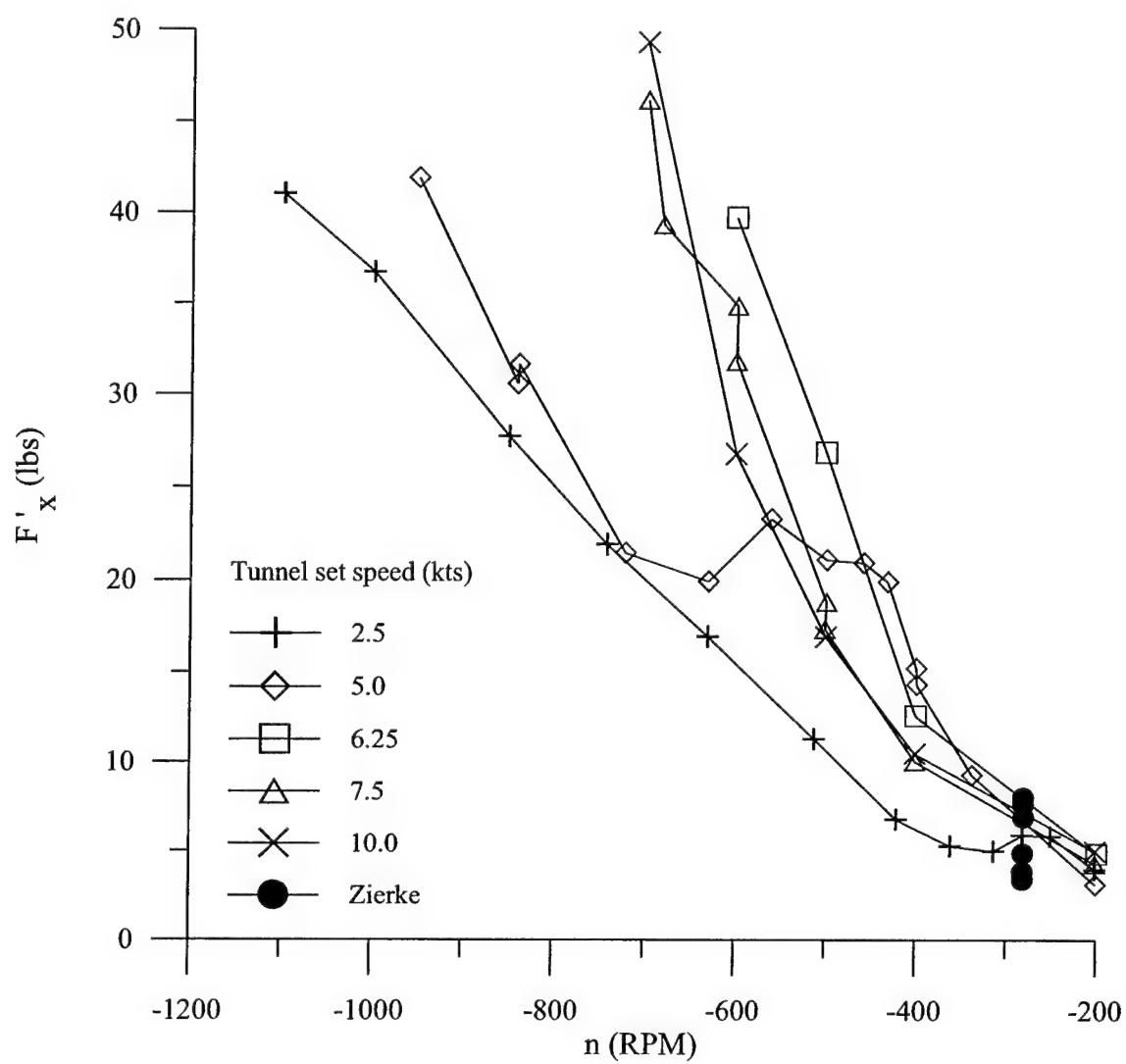
Figure 3.7 Dimensional RMS body axial force
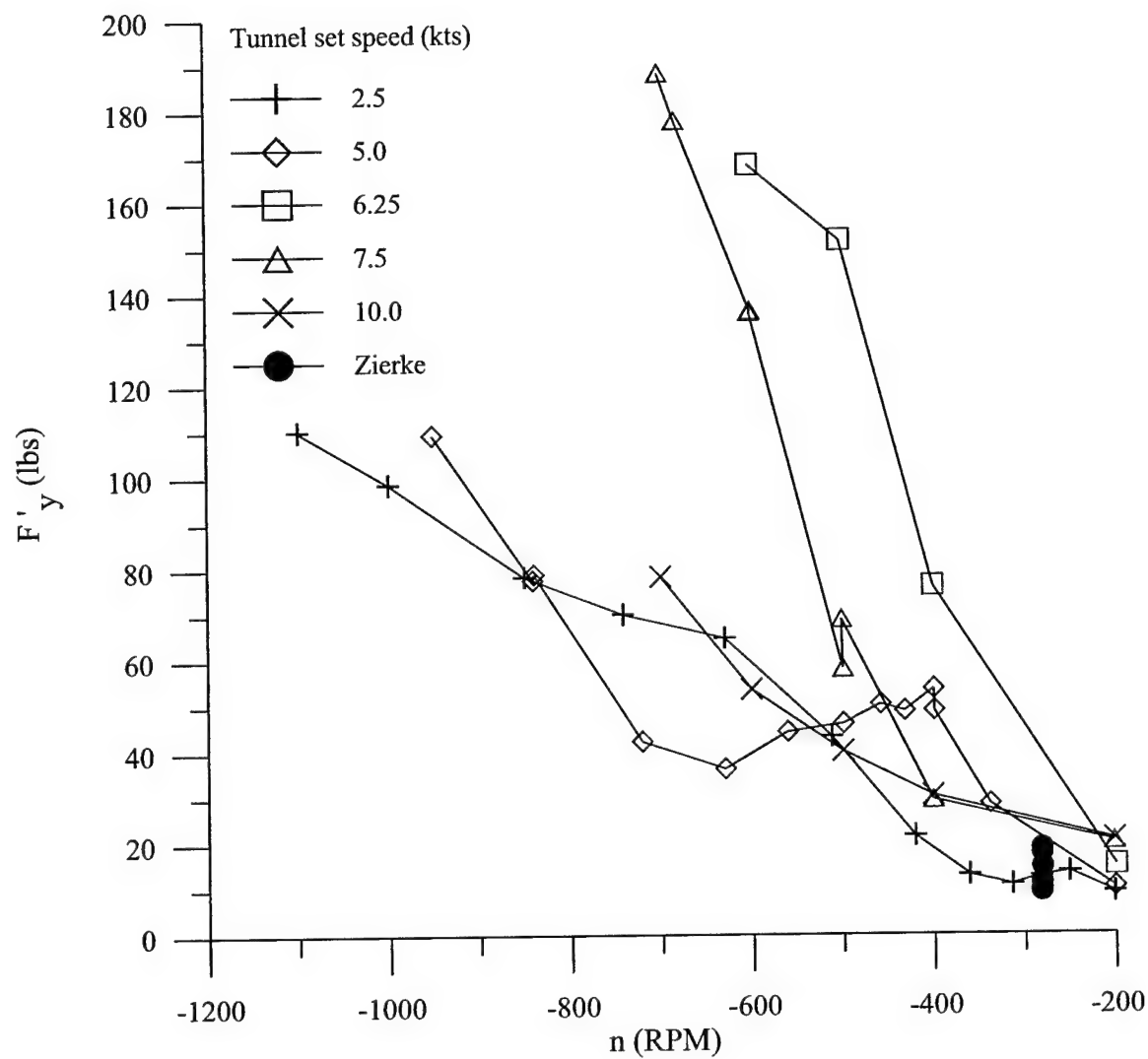
Figure 3.8 Dimensional RMS body side force
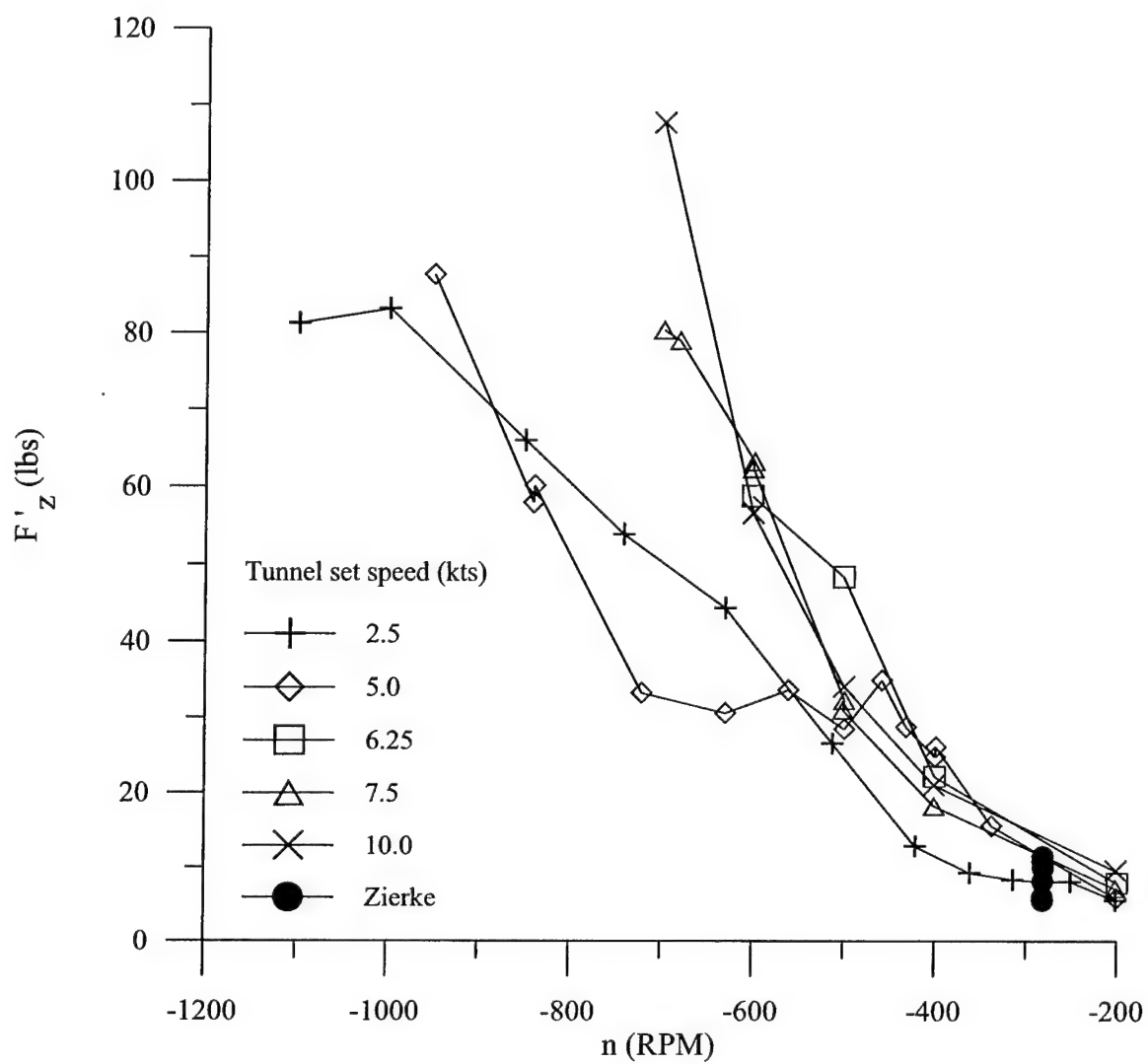
Figure 3.9 Dimensional RMS body vertical force
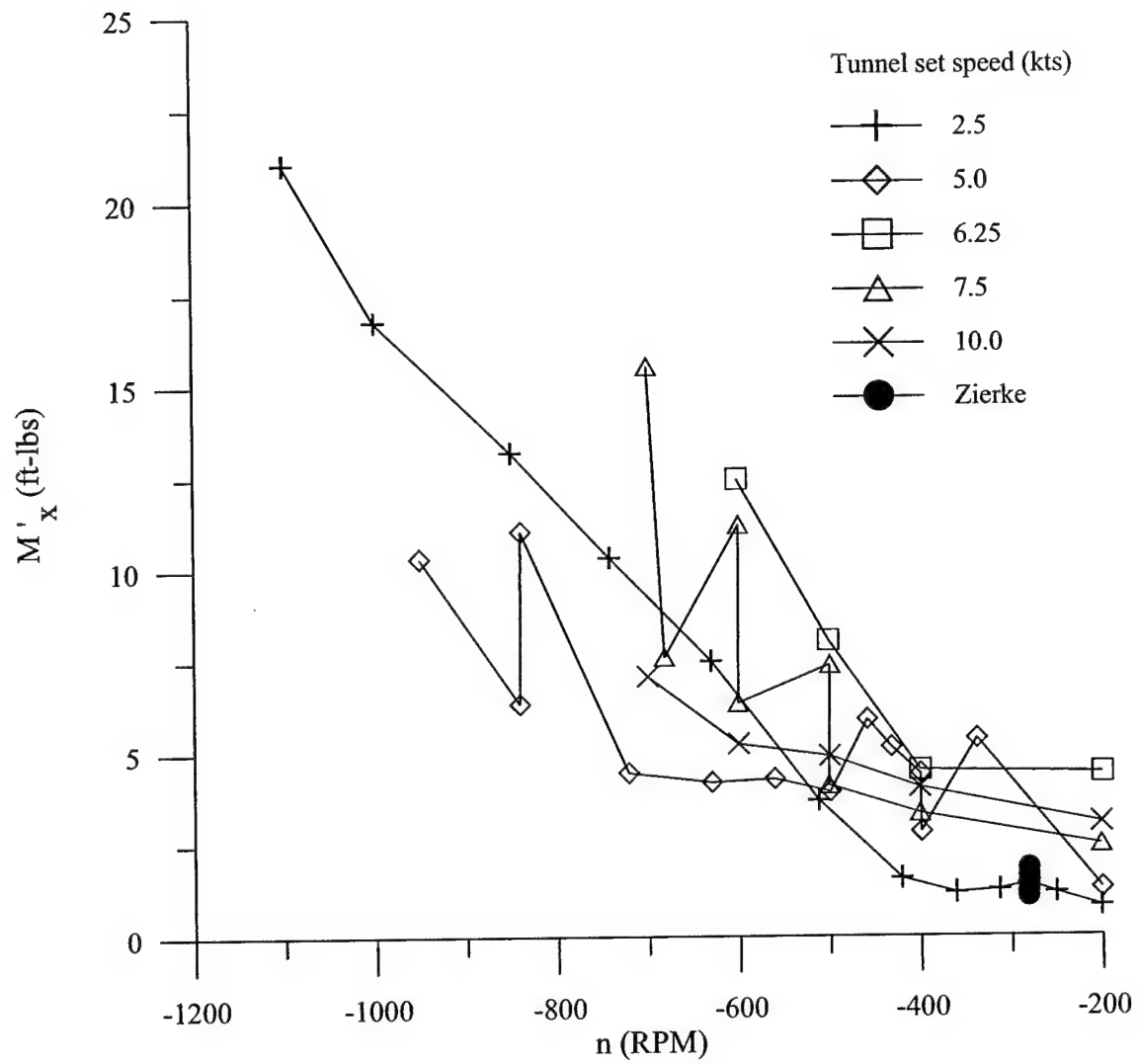
Figure 3.10 Dimensional RMS body axial (rolling) moment
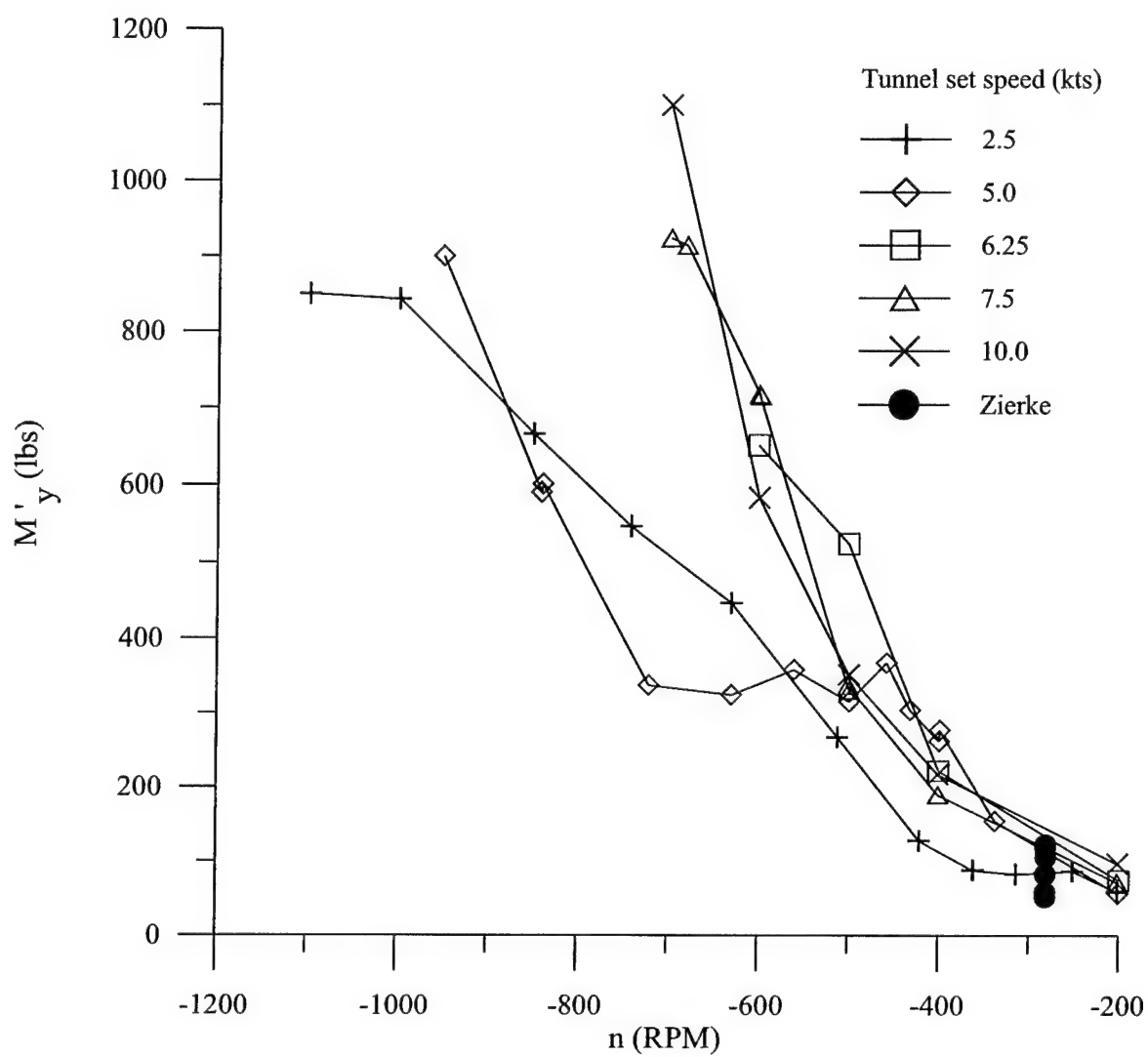
Figure 3.11 Dimensional RMS body pitching moment
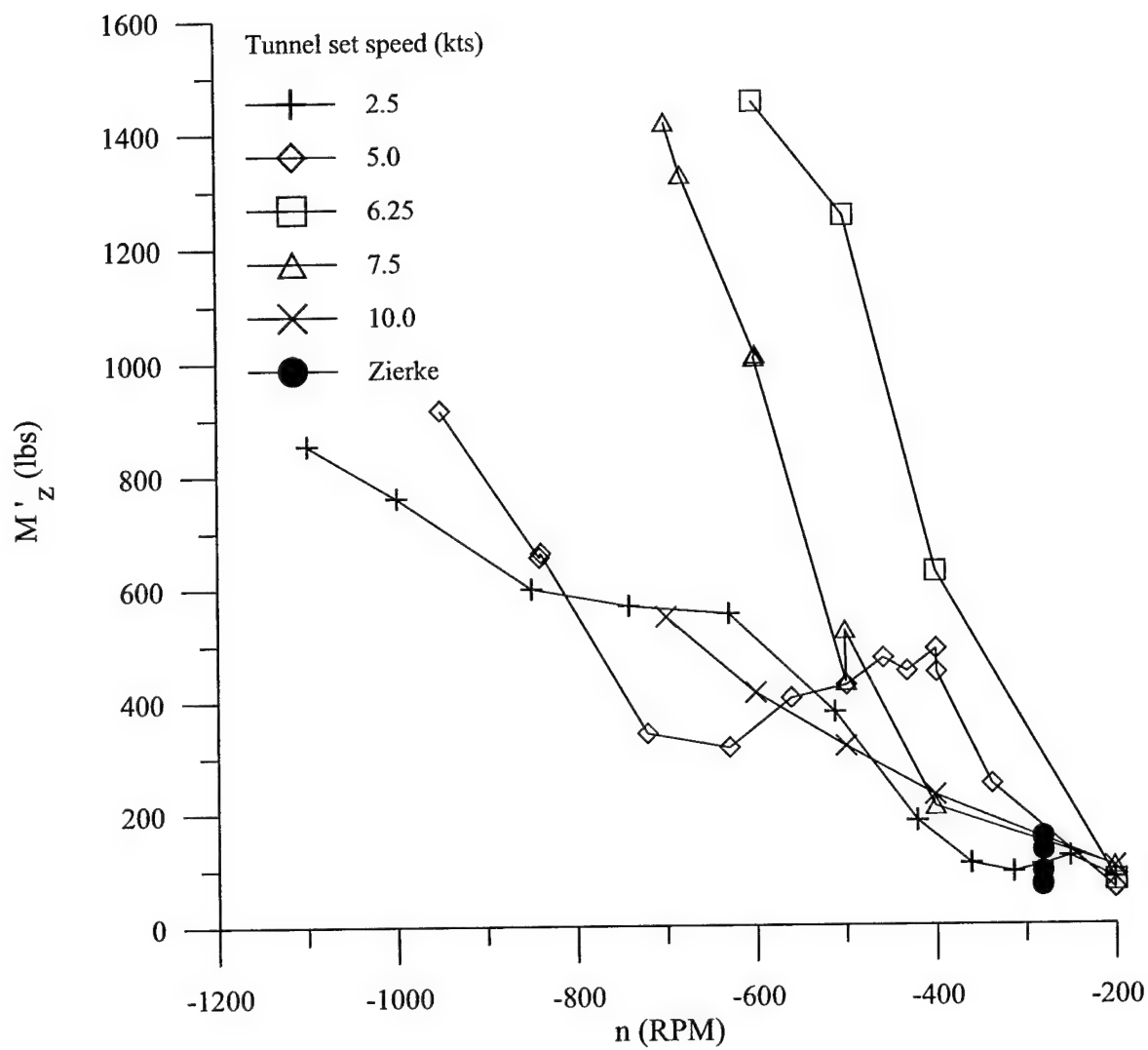
Figure 3.12 Dimensional RMS body yawing moment
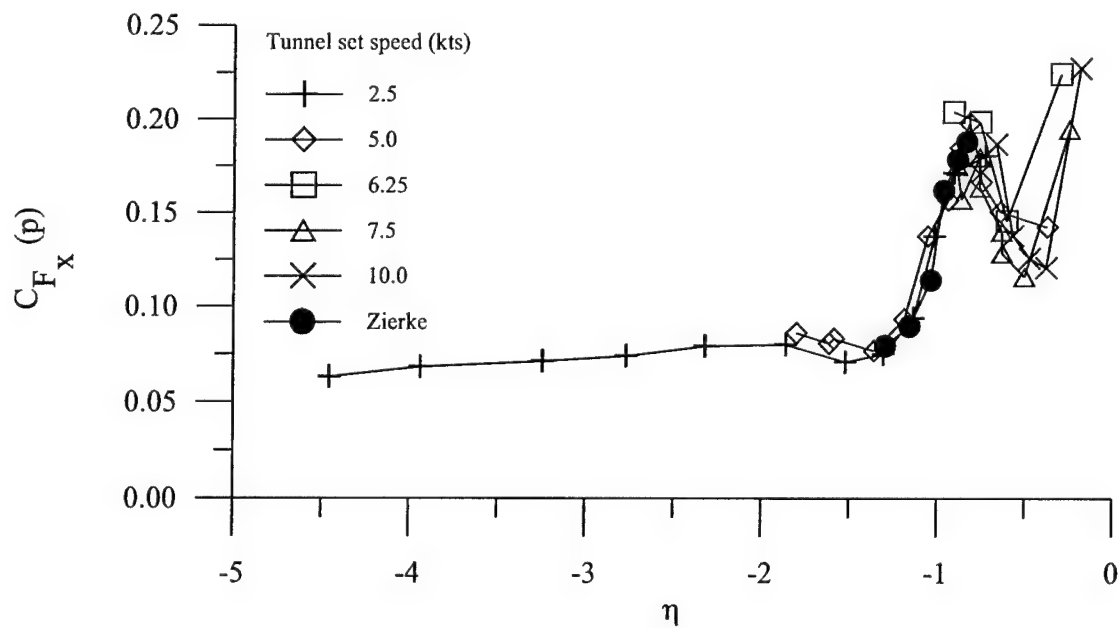
a. Complete data set
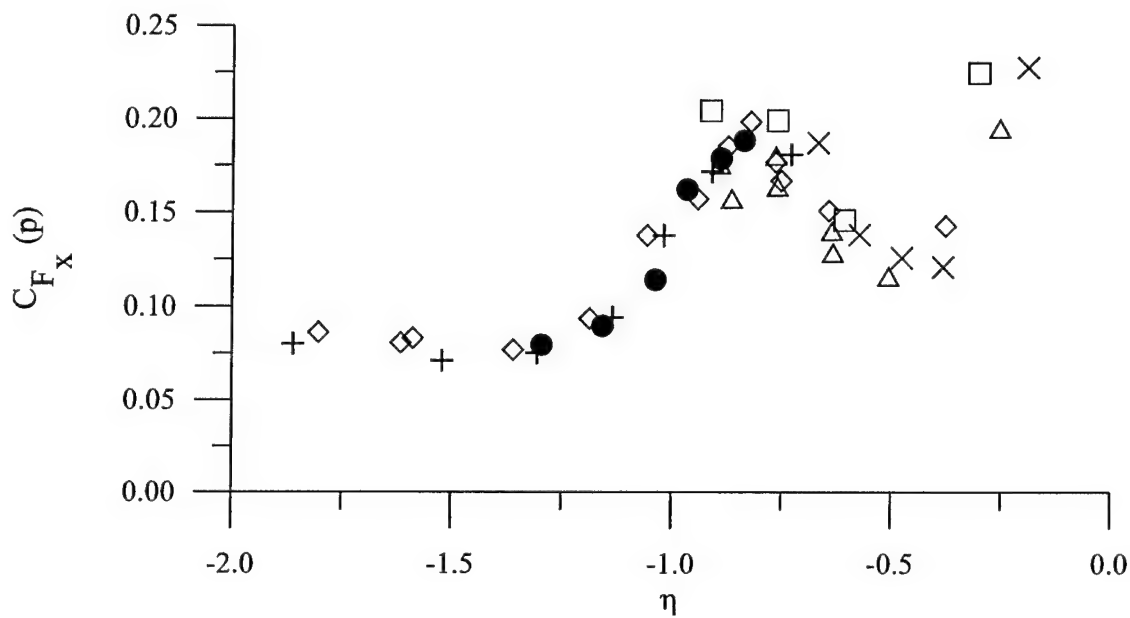
b. Expanded scale

Figure 3.13 Coefficient of RMS body axial force ("p" denotes propulsive scaling)
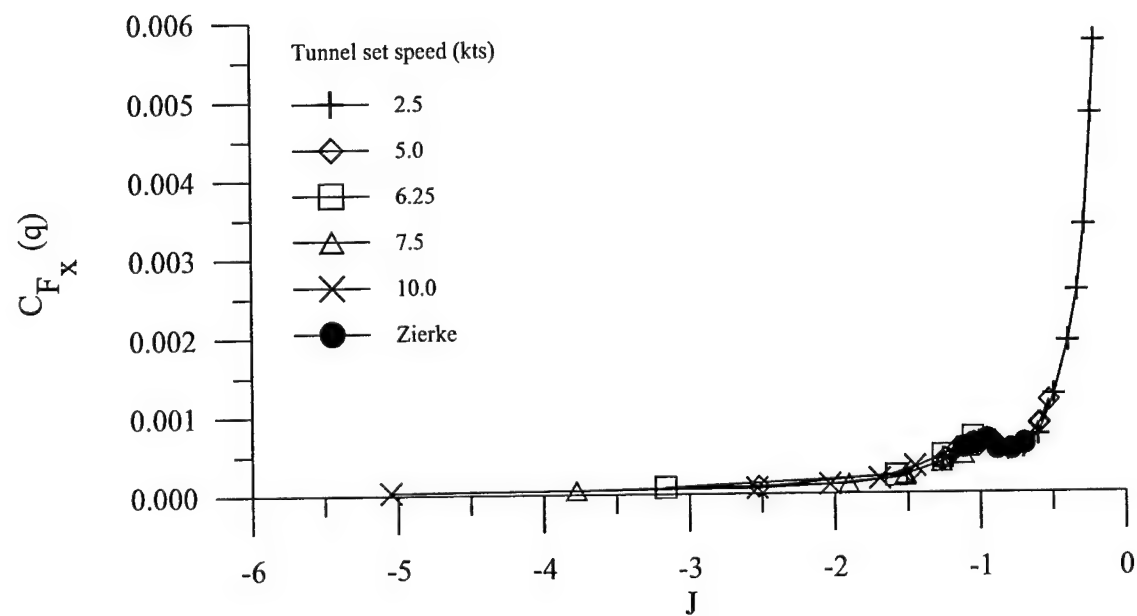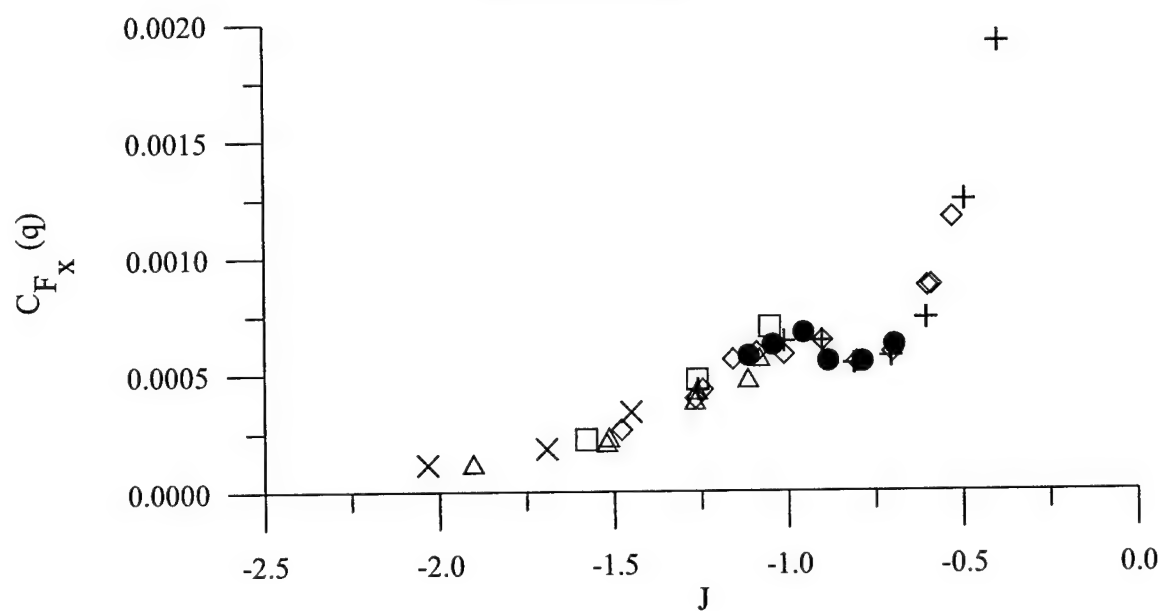
a. Complete data set

b. Expanded scale

Figure 3.14 Coefficient of RMS body axial force ("q" indicates dynamic pressure scaling)
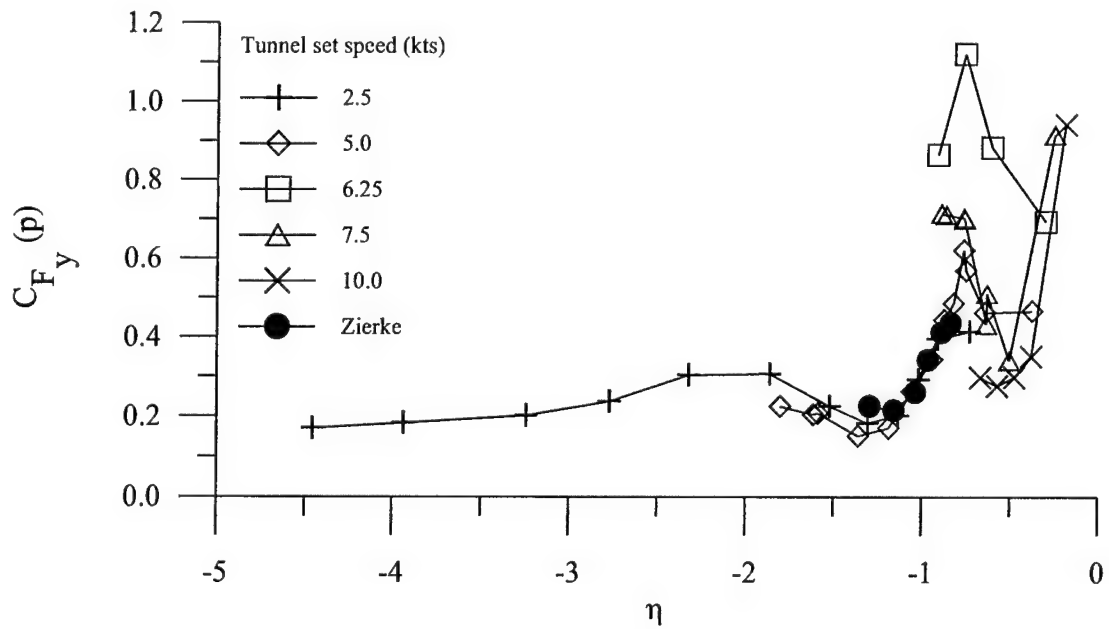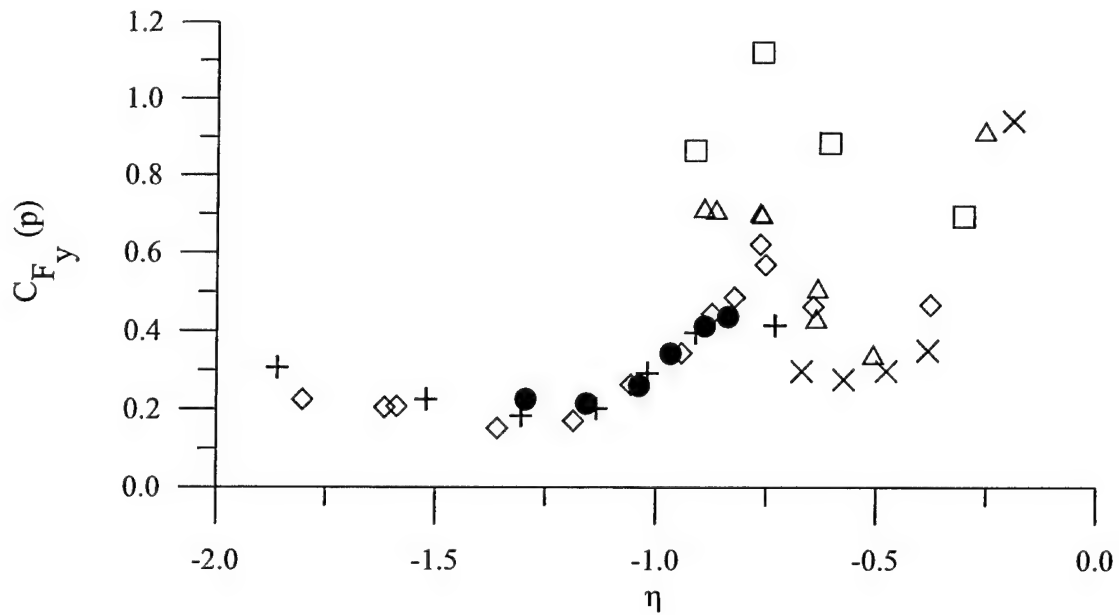
a. Complete data set

b. Expanded scale

Figure 3.15 Coefficient of RMS body side force ("p" indicates propulsive scaling)
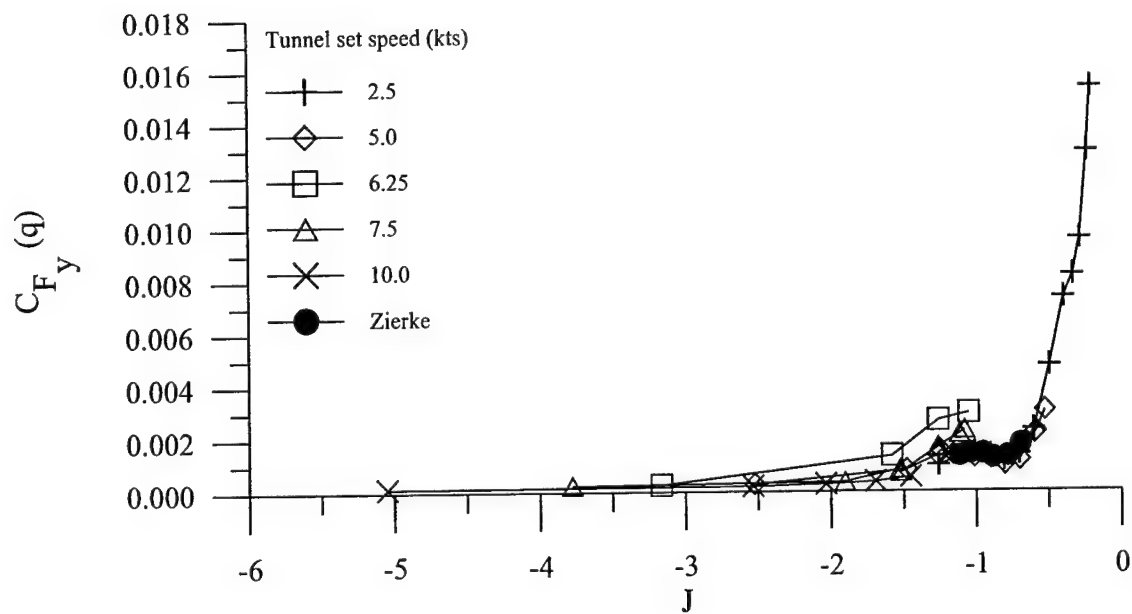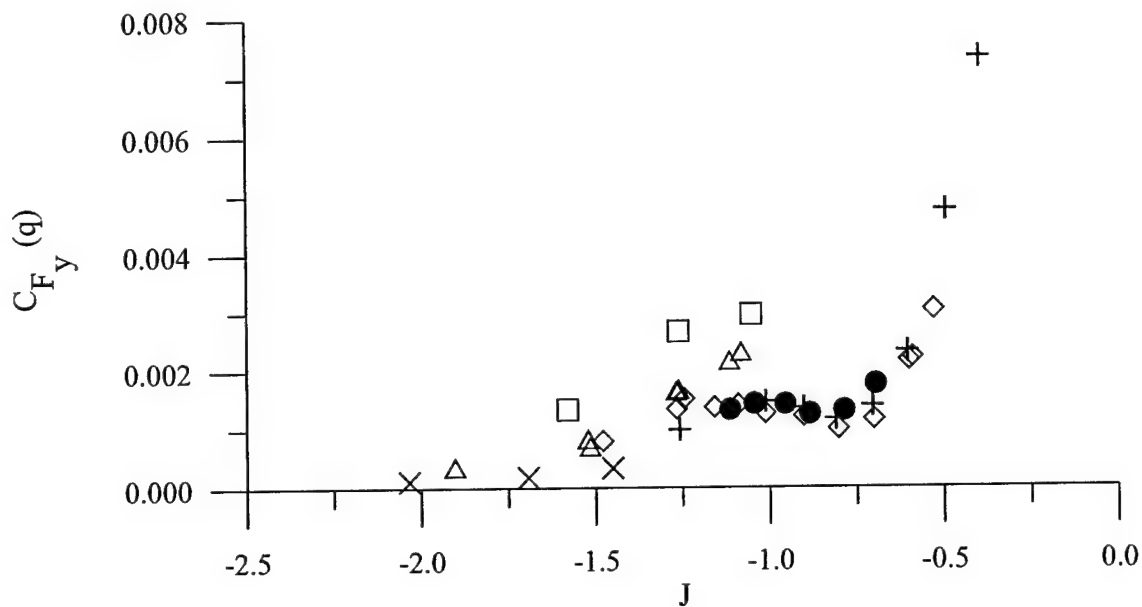
a. Complete data set

b. Expanded scale

Figure 3.16 Coefficient of RMS body side force ("q" indicates dynamic pressure scaling)
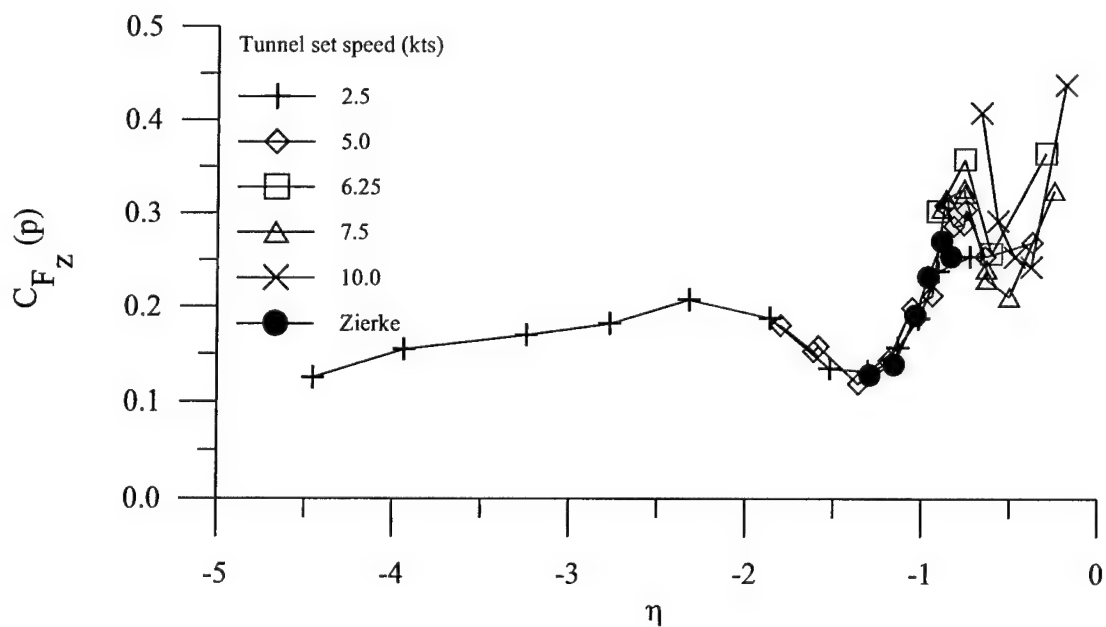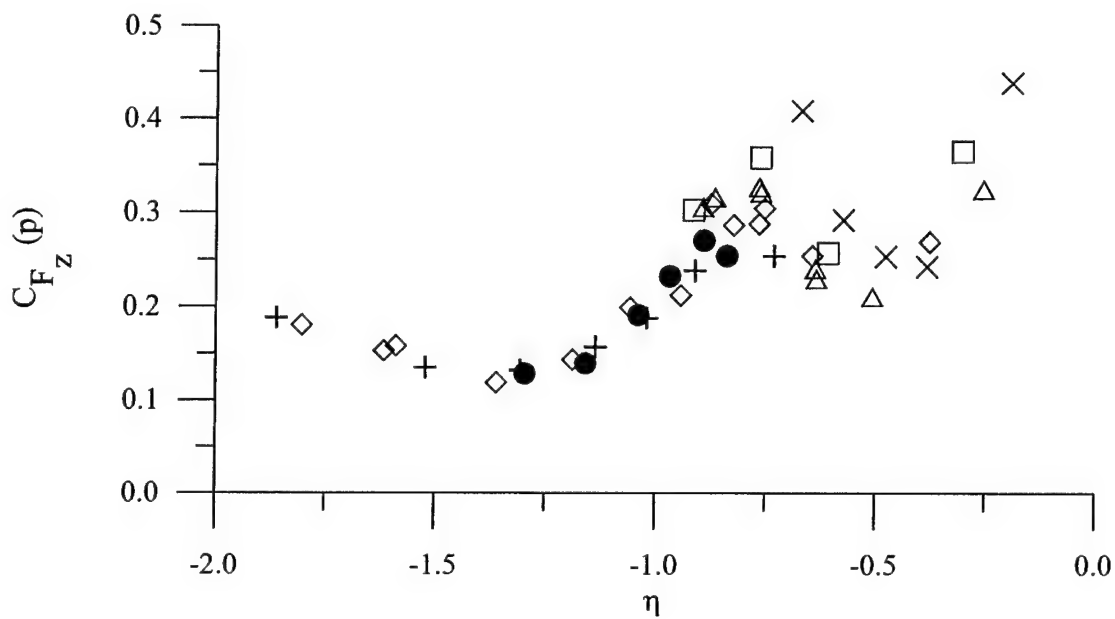
a. Complete data set

b. Expanded scale

Figure 3.17 Coefficient of RMS body vertical force ("p" indicates propulsive scaling)
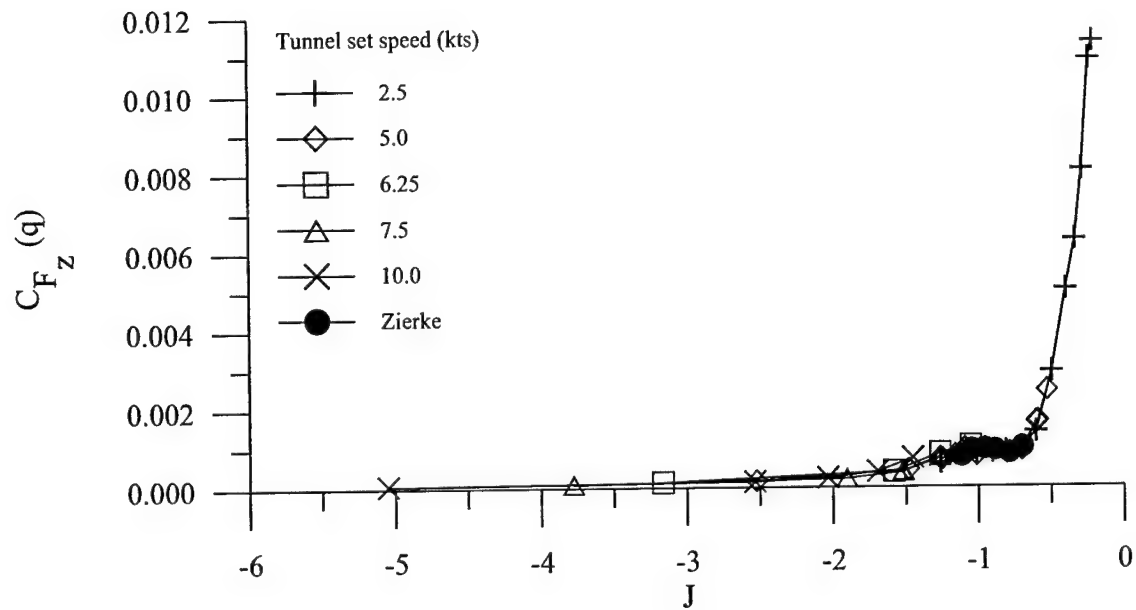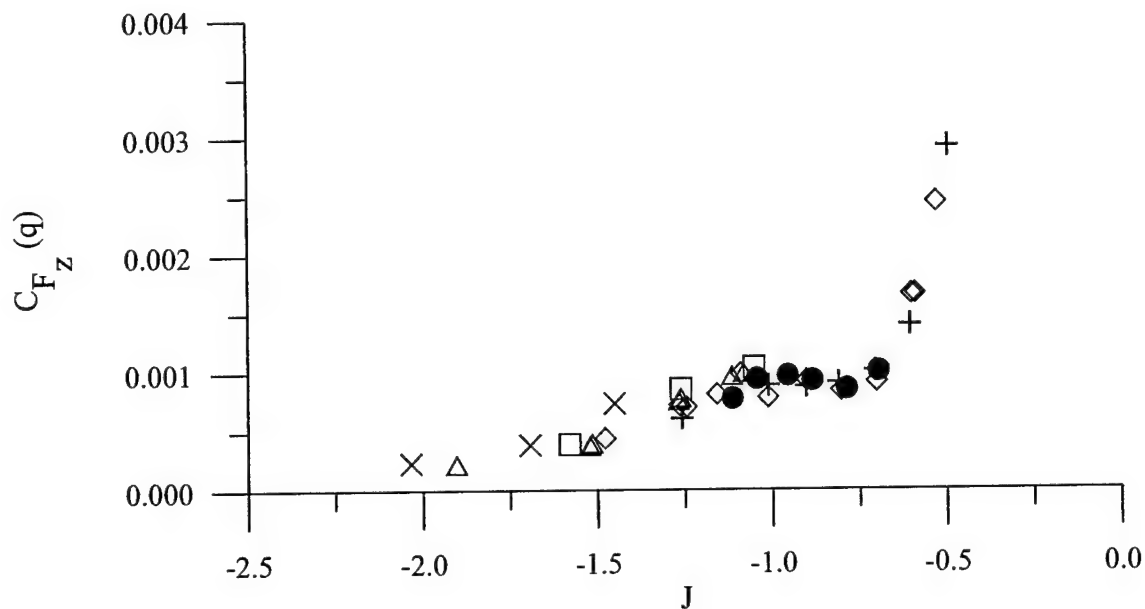
a. Complete data set

b. Expanded scale

Figure 3.18 Coefficient of RMS body vertical force ("q" indicates dynamic pressure scaling)
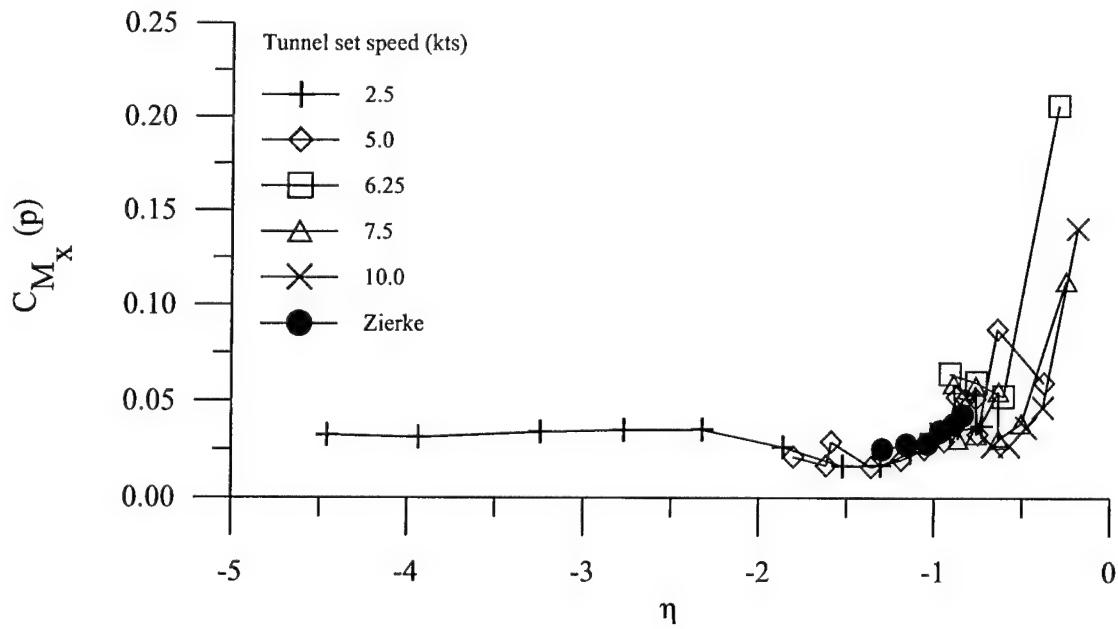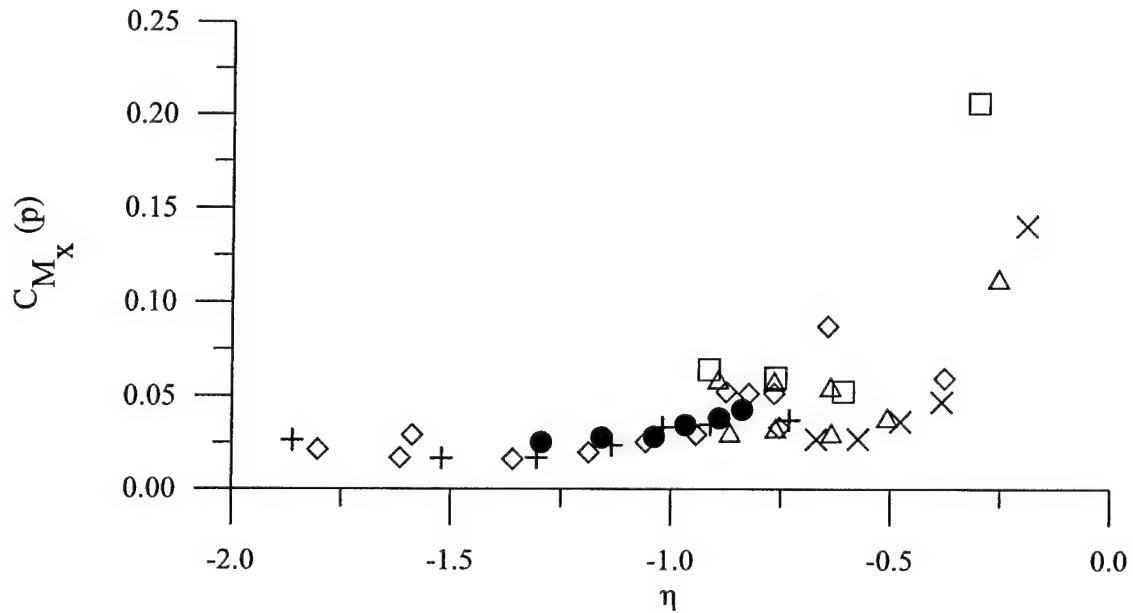
a. Complete data set

b. Expanded scale

Figure 3.19 Coefficient of RMS body axial (rolling) moment ("p" indicates propulsive scaling)
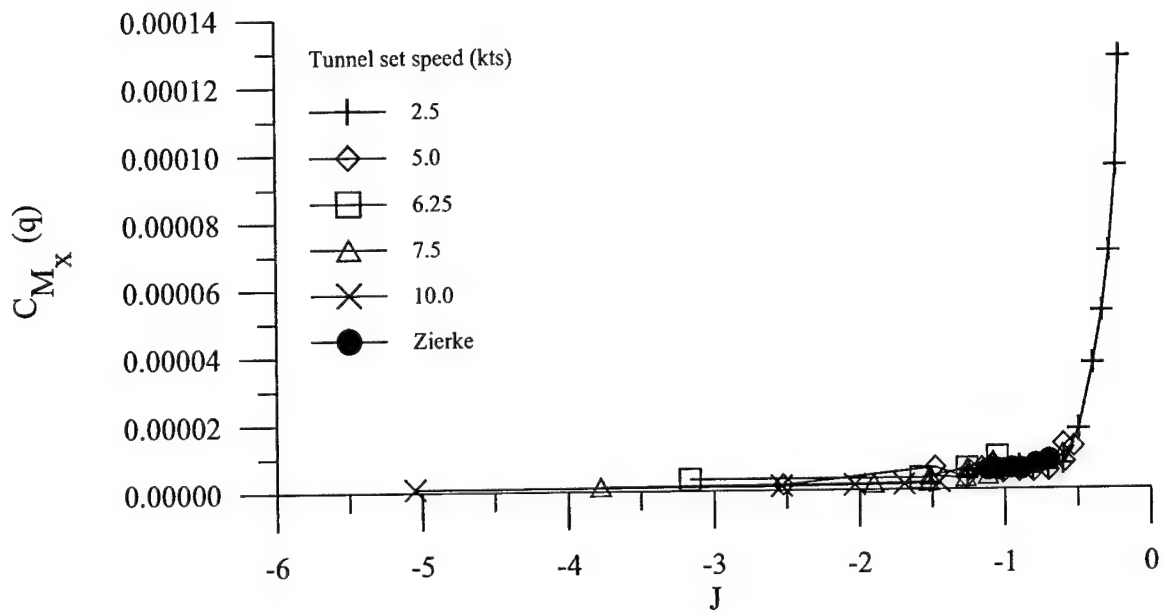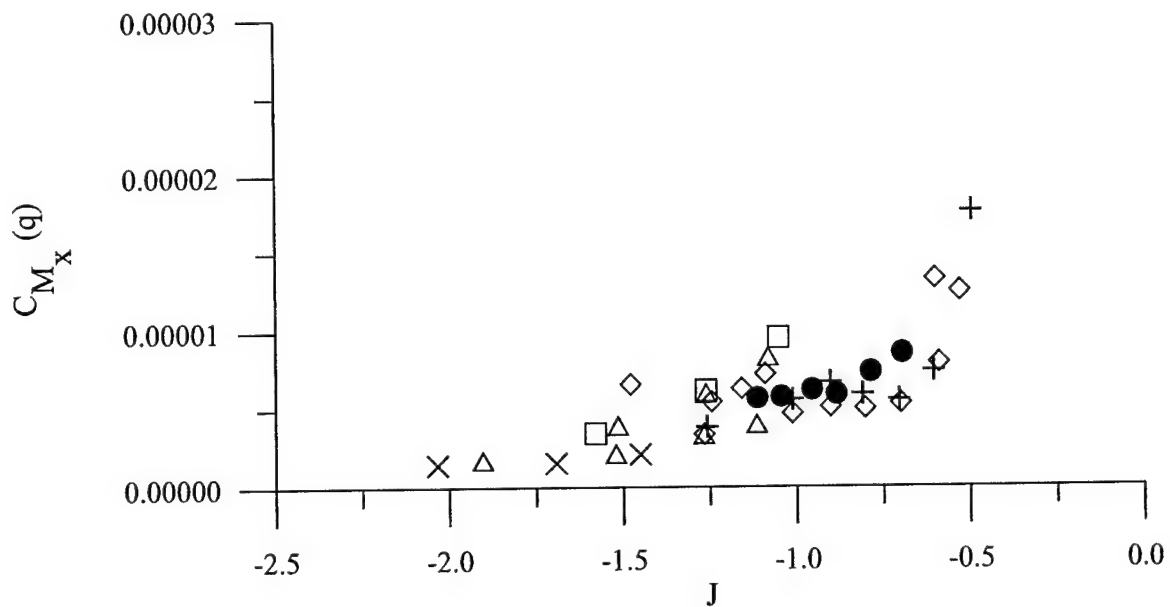
a. Complete data set

b. Expanded scale

Figure 3.20 Coefficient of RMS body axial (rolling) moment ("q" indicates dynamic pressure scaling)
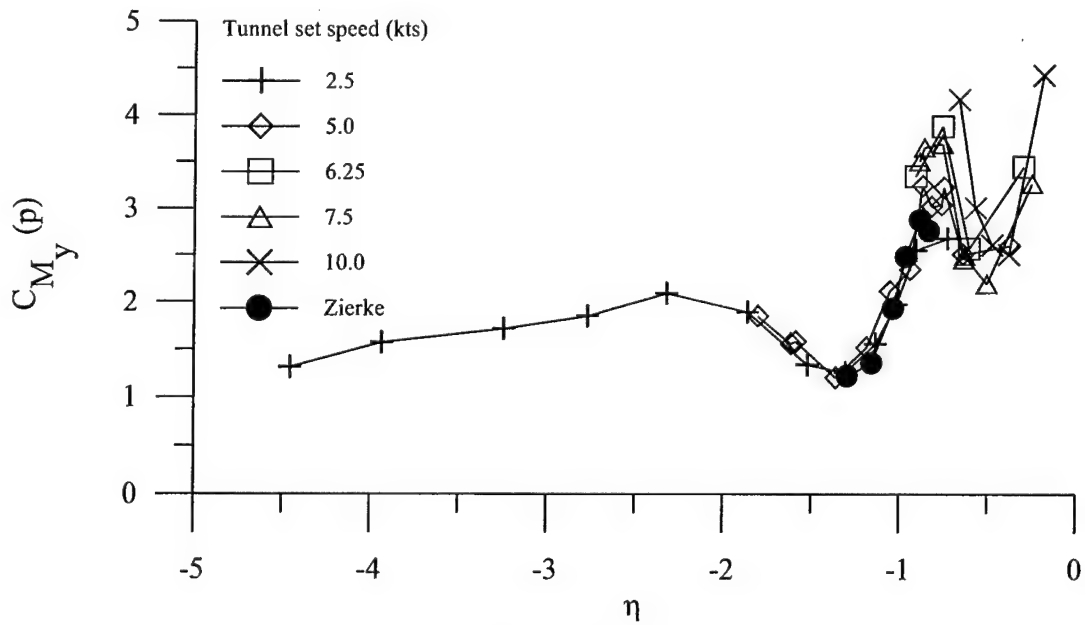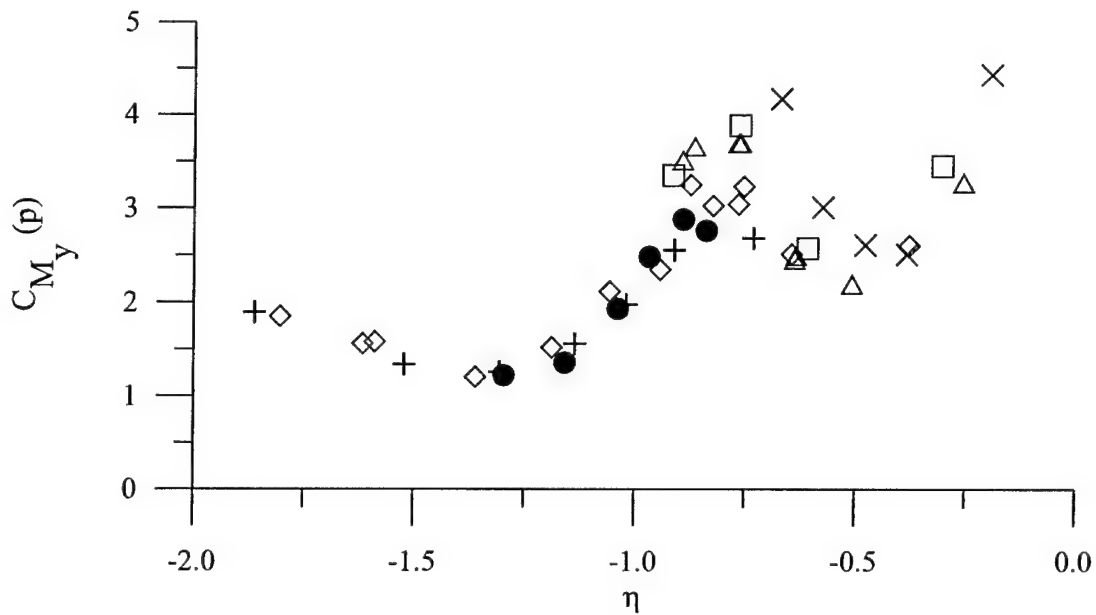
a. Complete data set

b. Expanded scale

Figure 3.21 Coefficient of body pitching moment ("p" indicates propulsive scaling)
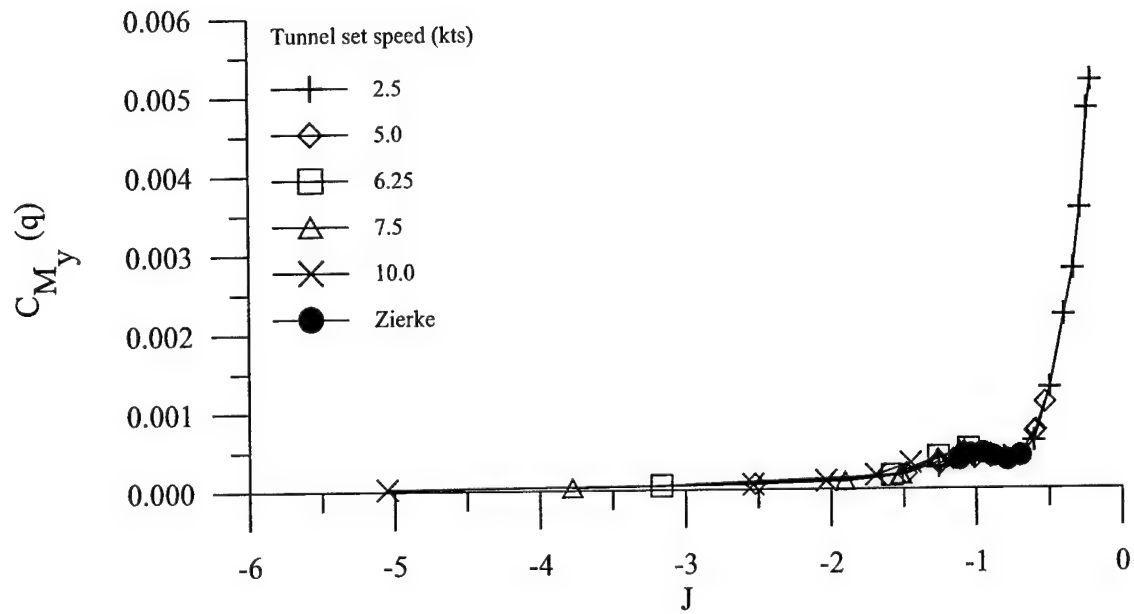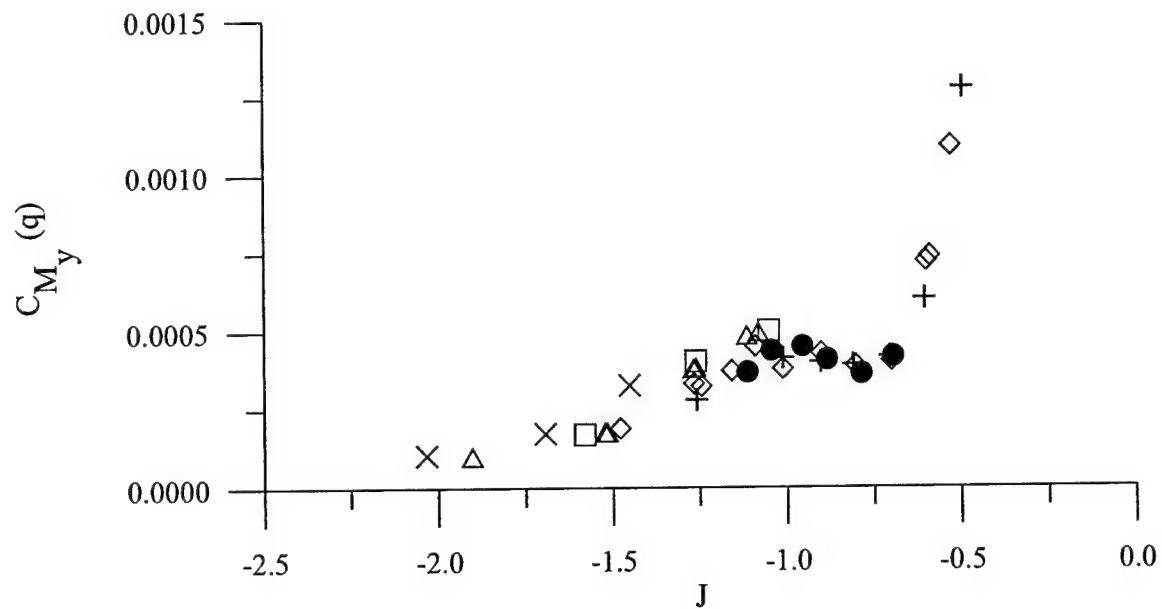
a. Complete data set

b. Expanded scale

Figure 3.22 Coefficient of RMS body pitching moment ("q" indicates dynamic pressure scaling)
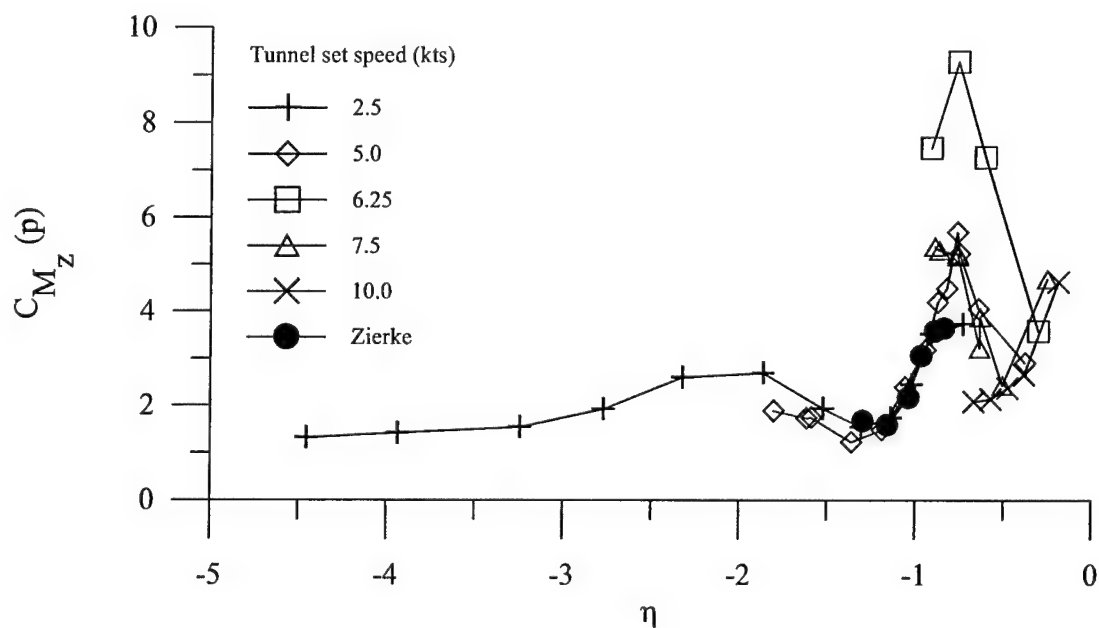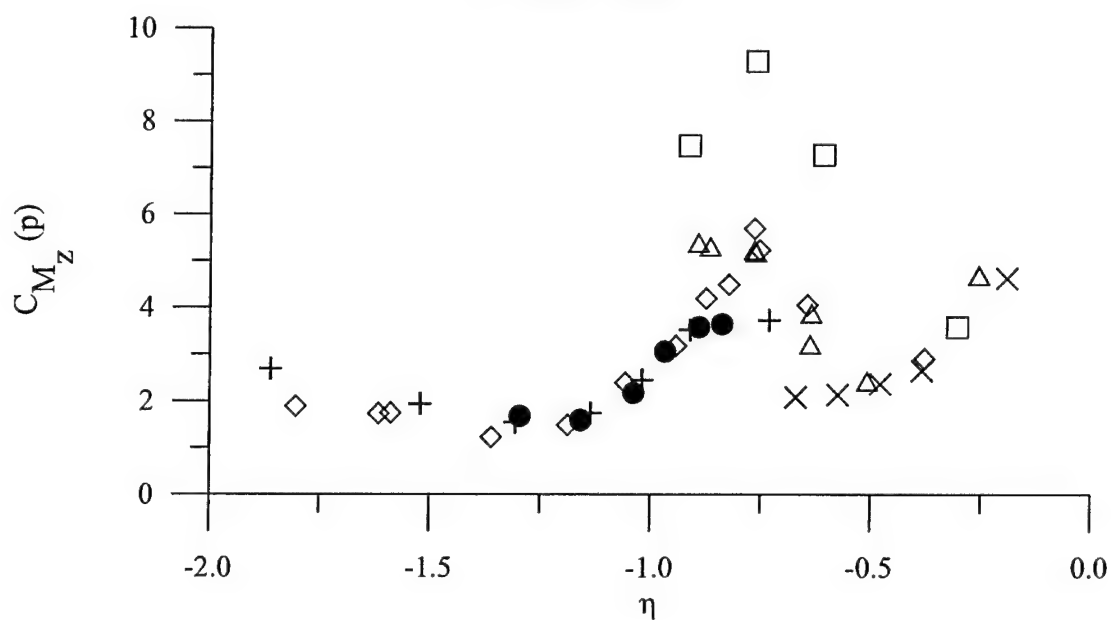
a. Complete data set

b. Expanded scale

Figure 3.23 Coefficient of RMS body yawing moment ("p" indicates propulsive scaling)
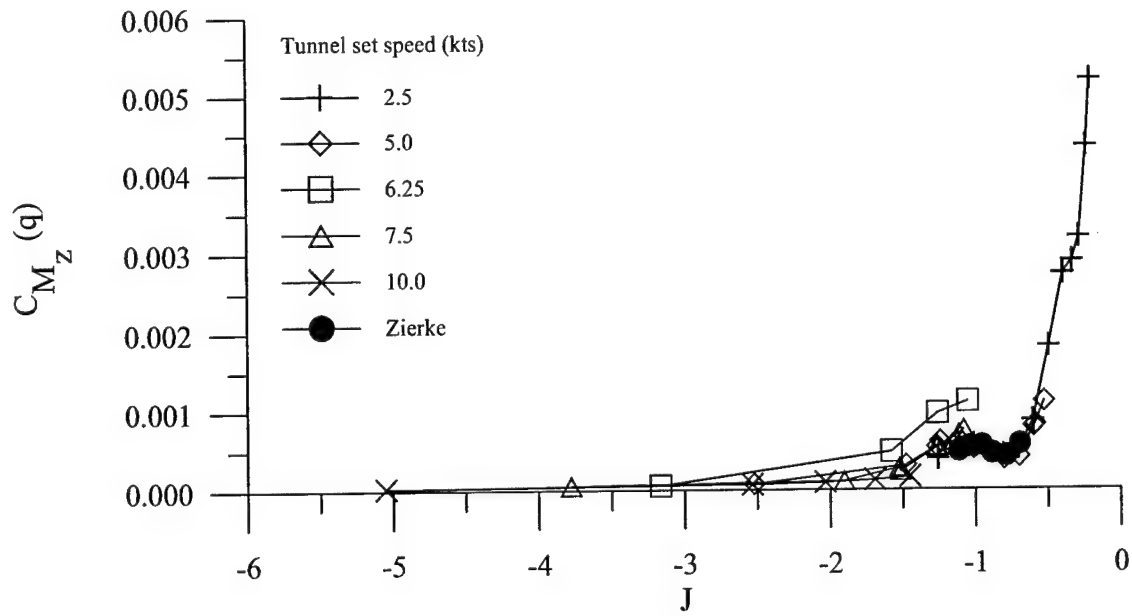
a. Complete data set
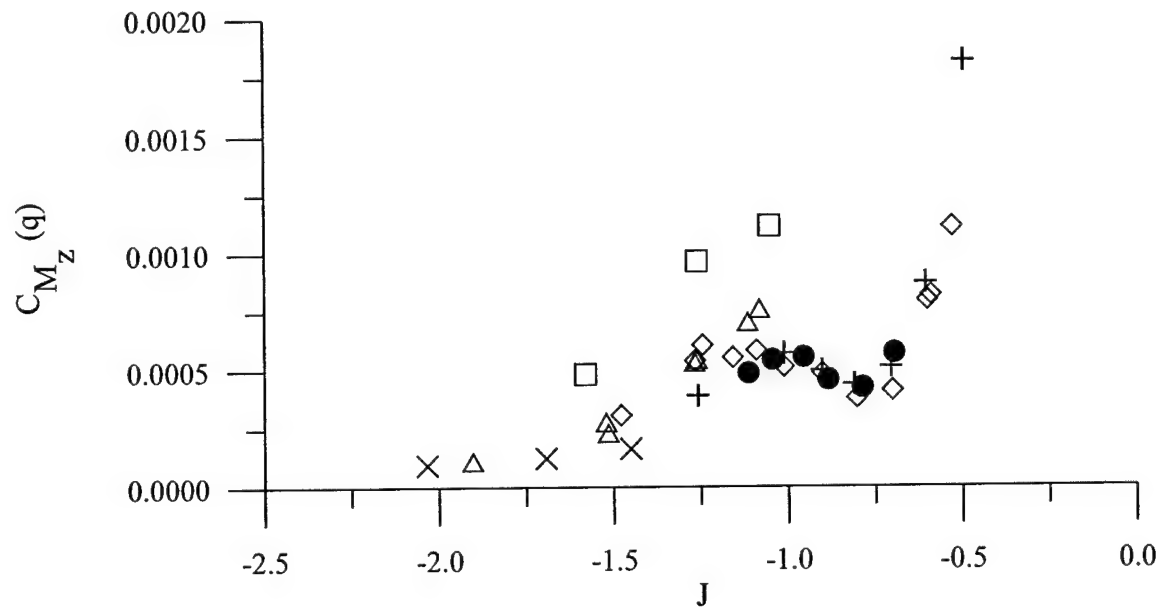
b. Expanded scale

Figure 3.24 Coefficient of RMS body yawing moment ("q" indicates dynamic pressure scaling)
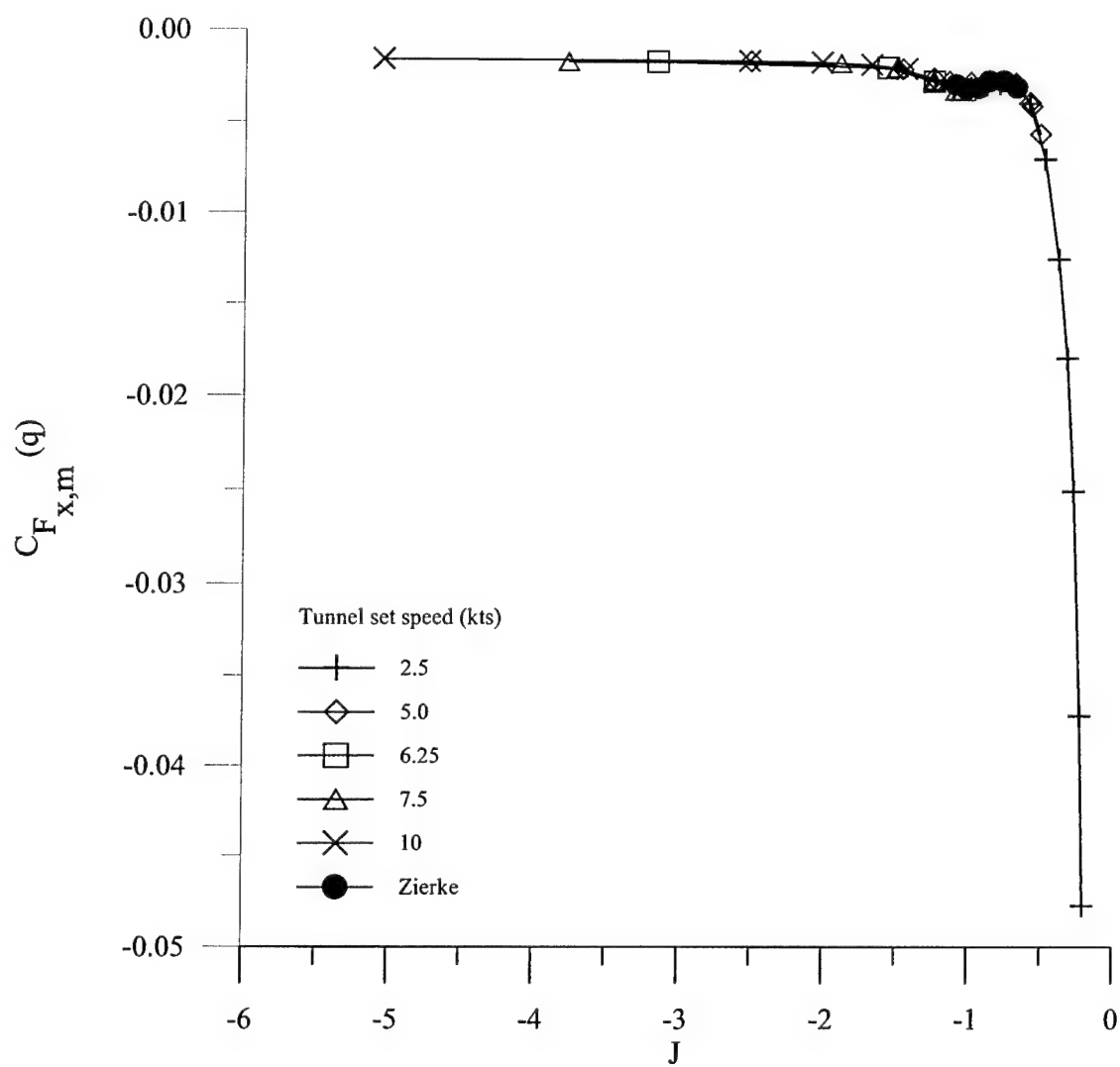
Figure 3.25 Coefficient of mean axial body force ("q" indicates dynamic pressure scaling)
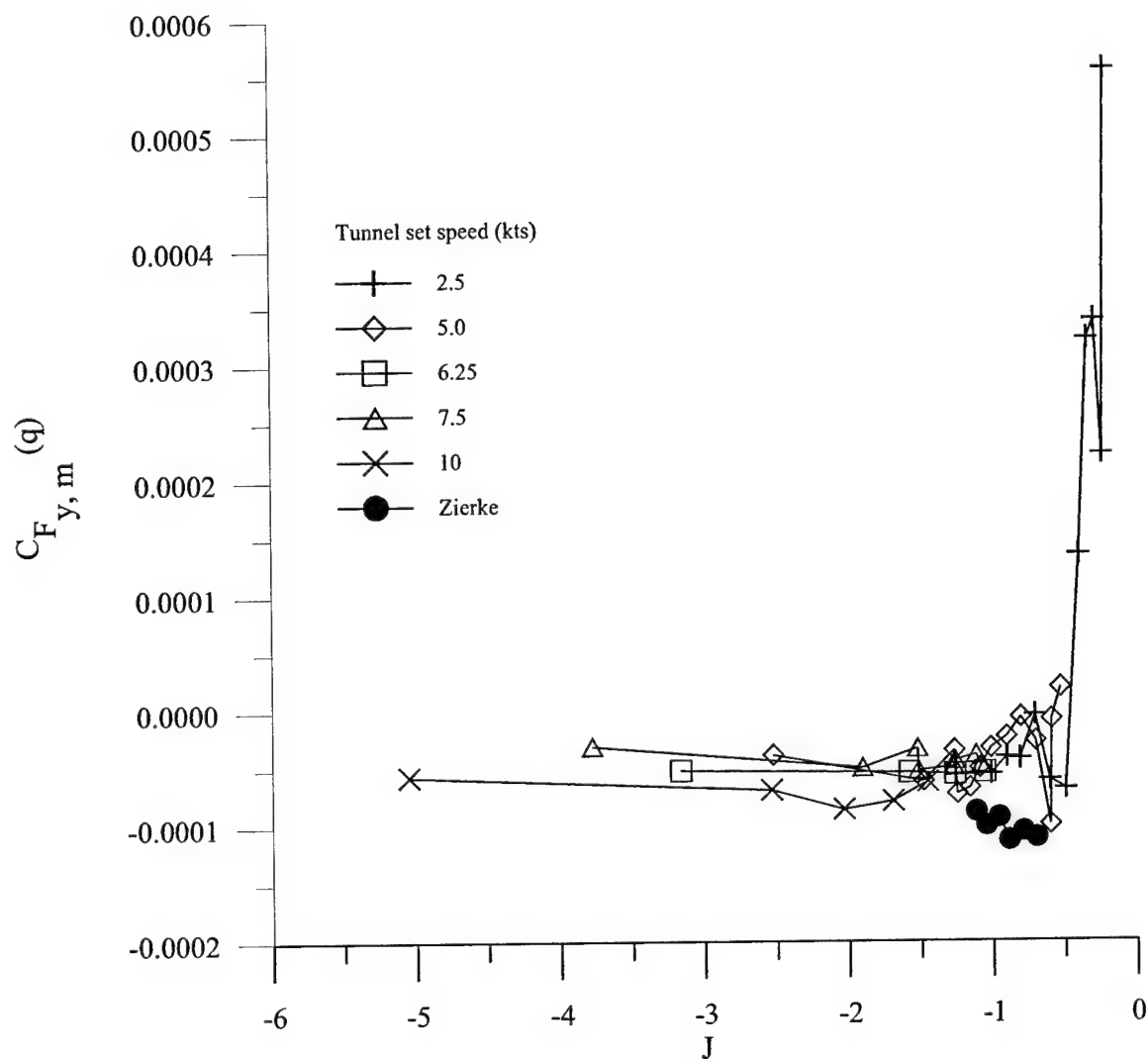
Figure 3.26 Coefficient of mean body side force ("q" indicates dynamic pressure scaling)
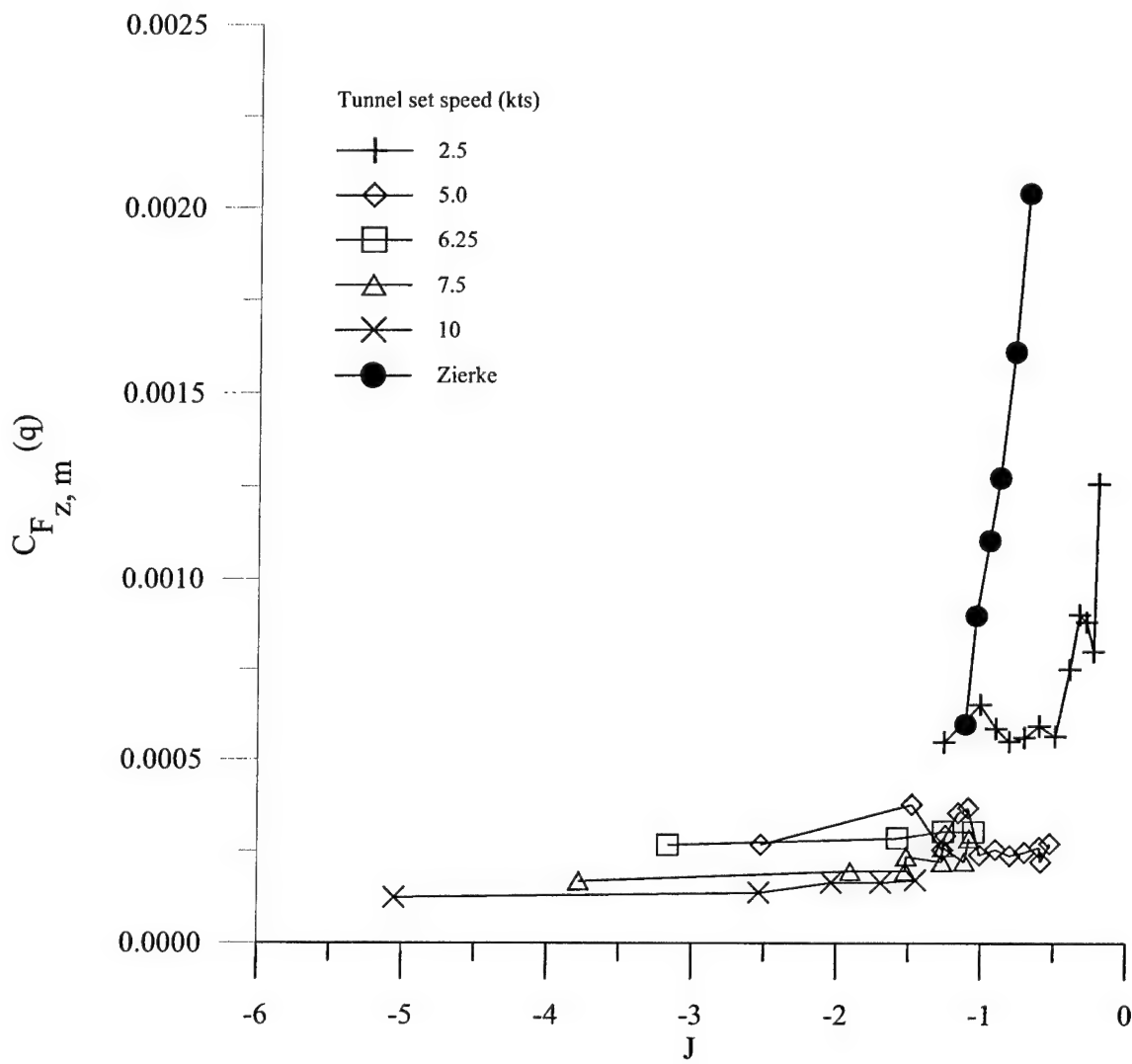
Figure 3.27 Coefficient of mean body vertical force ("q" indicates dynamic pressure scaling)
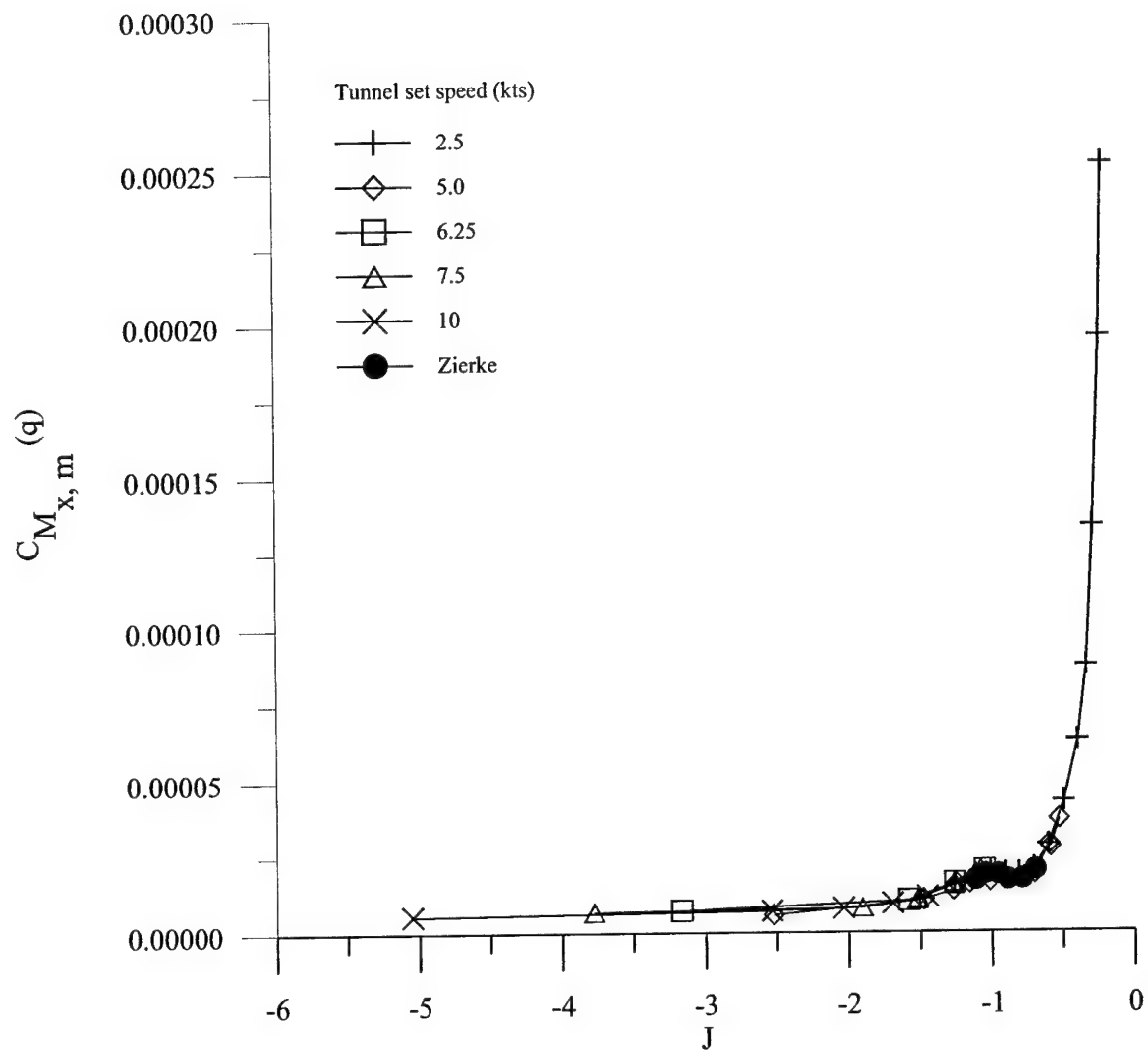
Figure 3.28 Coefficient of mean body axial (rolling) moment ("q" indicates dynamic pressure scaling)
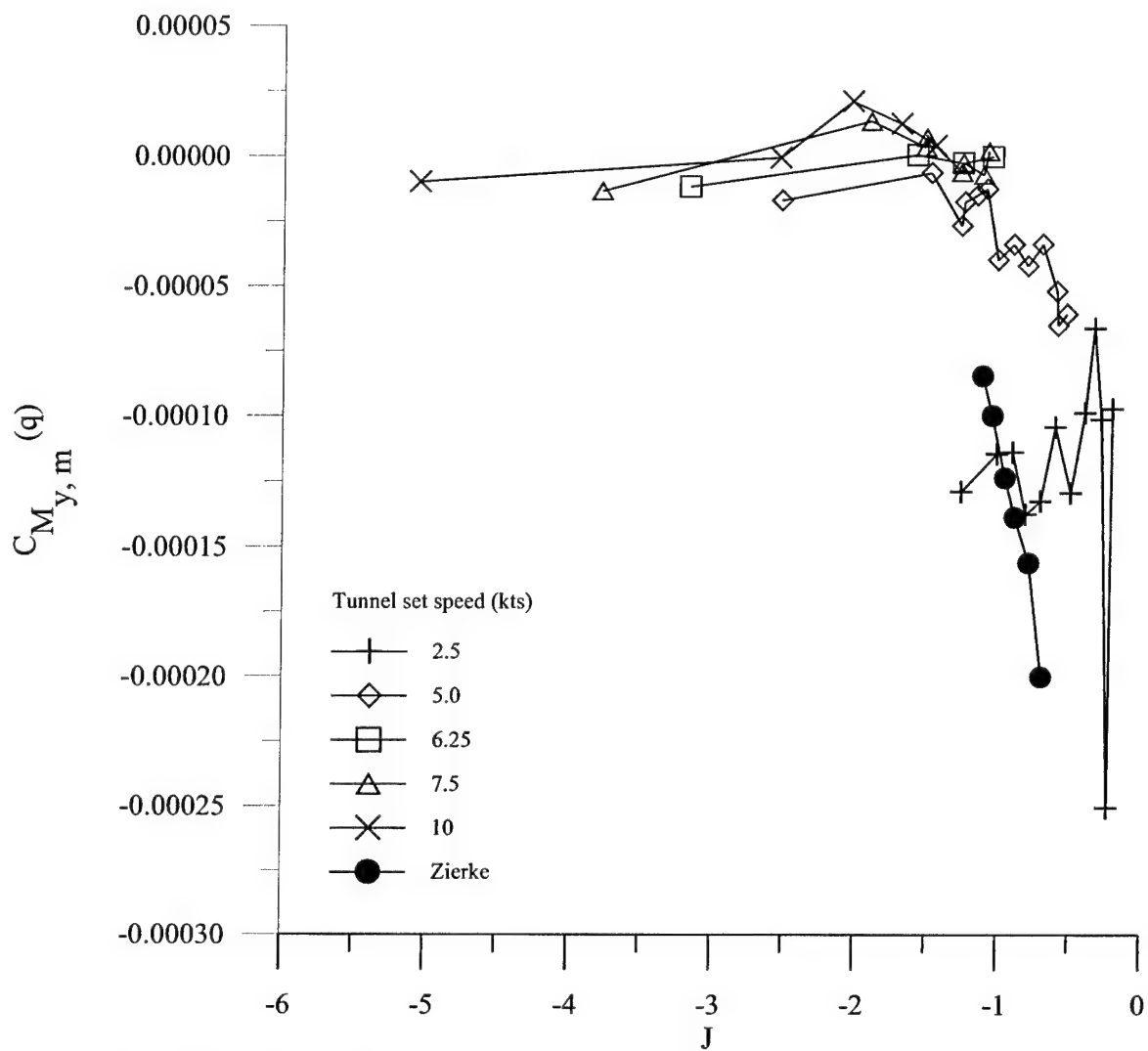
Figure 3.29 Coefficient of mean body pitching moment ("q" indicates dynamic pressure scaling)
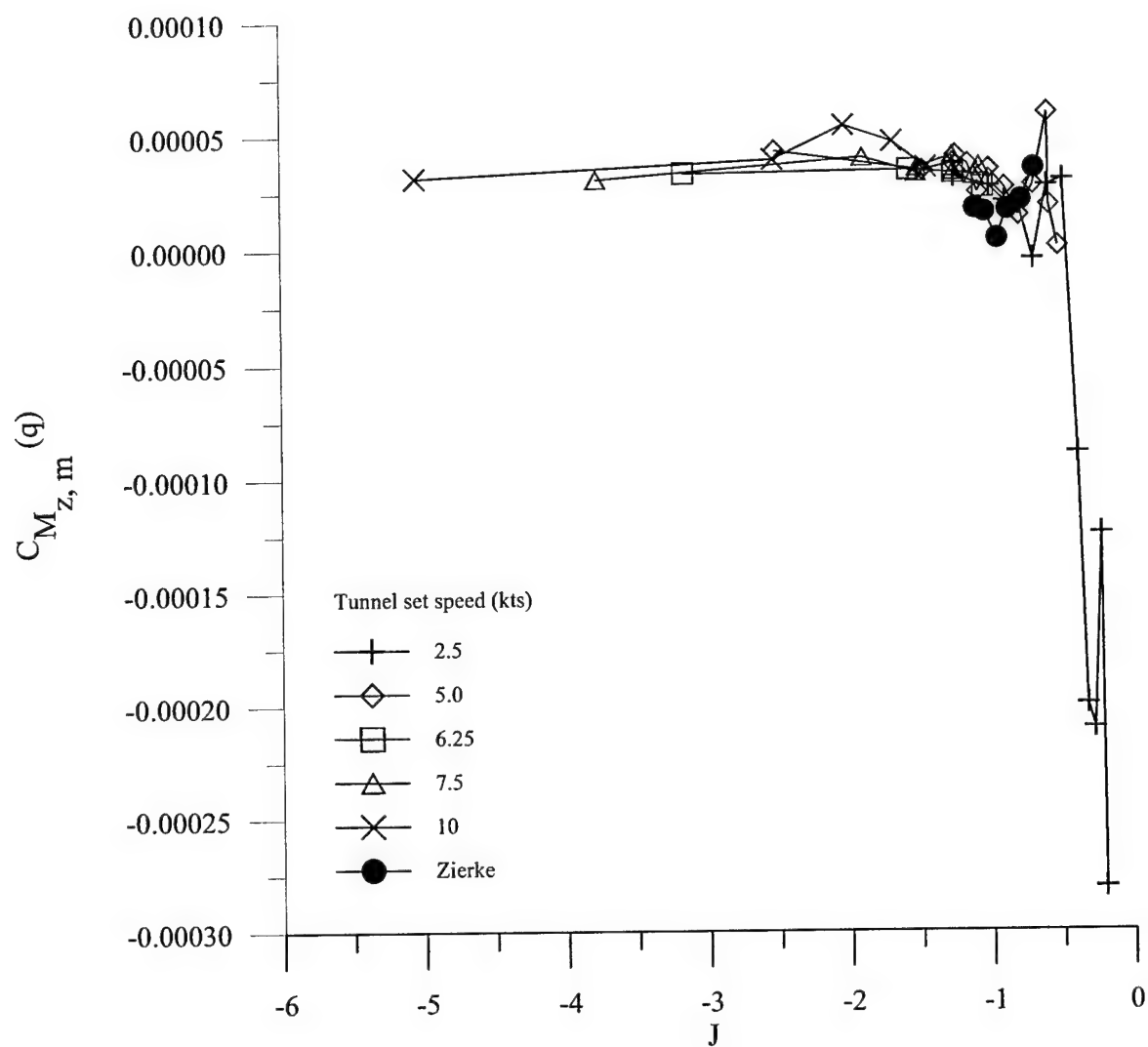
Figure 3.30 Coefficient of mean body yawing moment ("q" indicates dynamic pressure scaling)
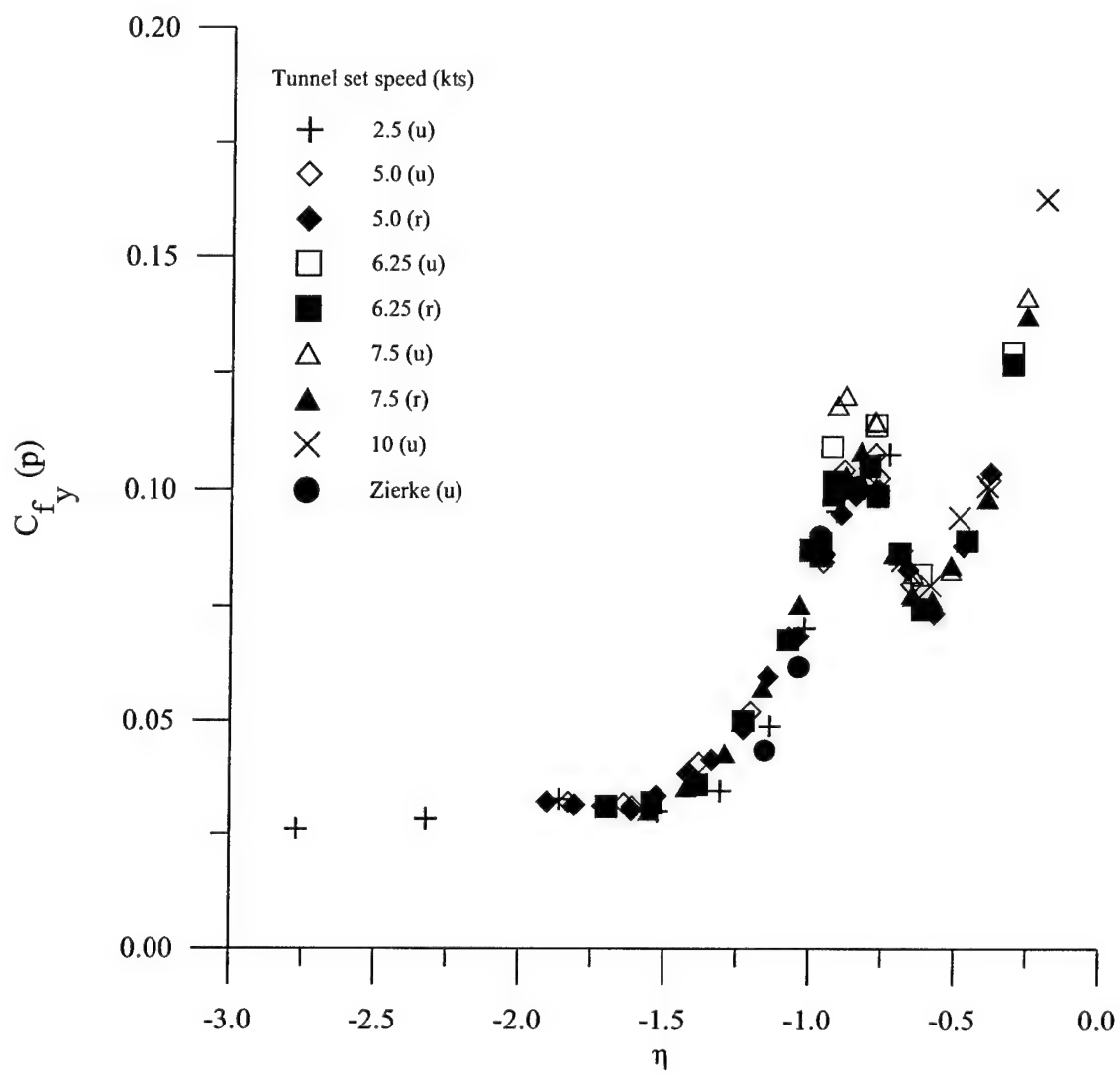
Figure 3.31 Coefficient of RMS propeller y force ("p" - propulsive scaling, "u" - model restraining strut off, "r" - model restraining strut on)
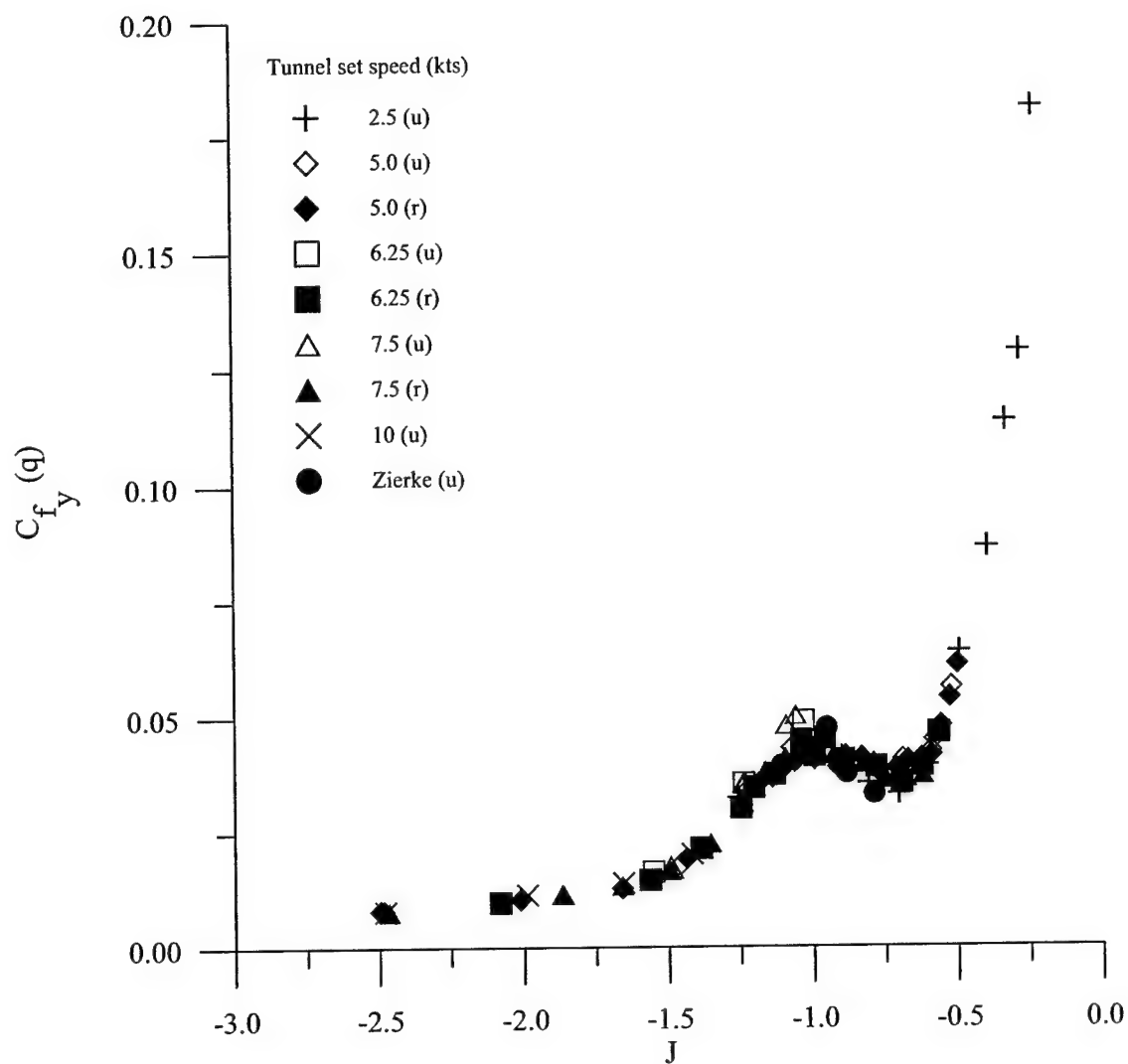
Figure 3.32 Coefficient of RMS propeller y force ("q" - dynamic pressure scaling, "u" - model restraining strut off, "r" - model restraining strut on)
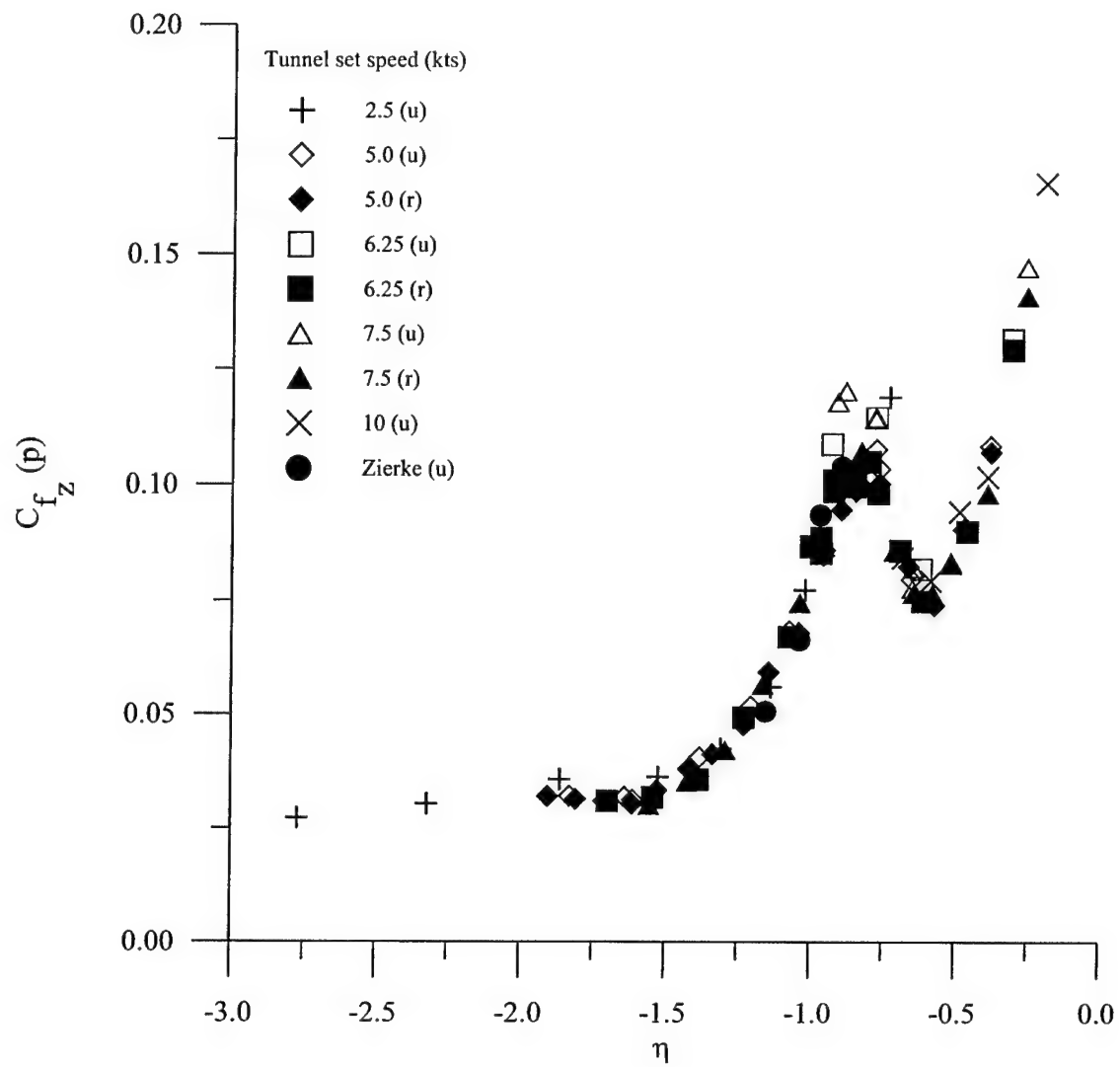
Figure 3.33 Coefficient of RMS propeller z-force ("p" - propulsive scaling, "u" - model restraining strut off, "r" - model restraining strut on)
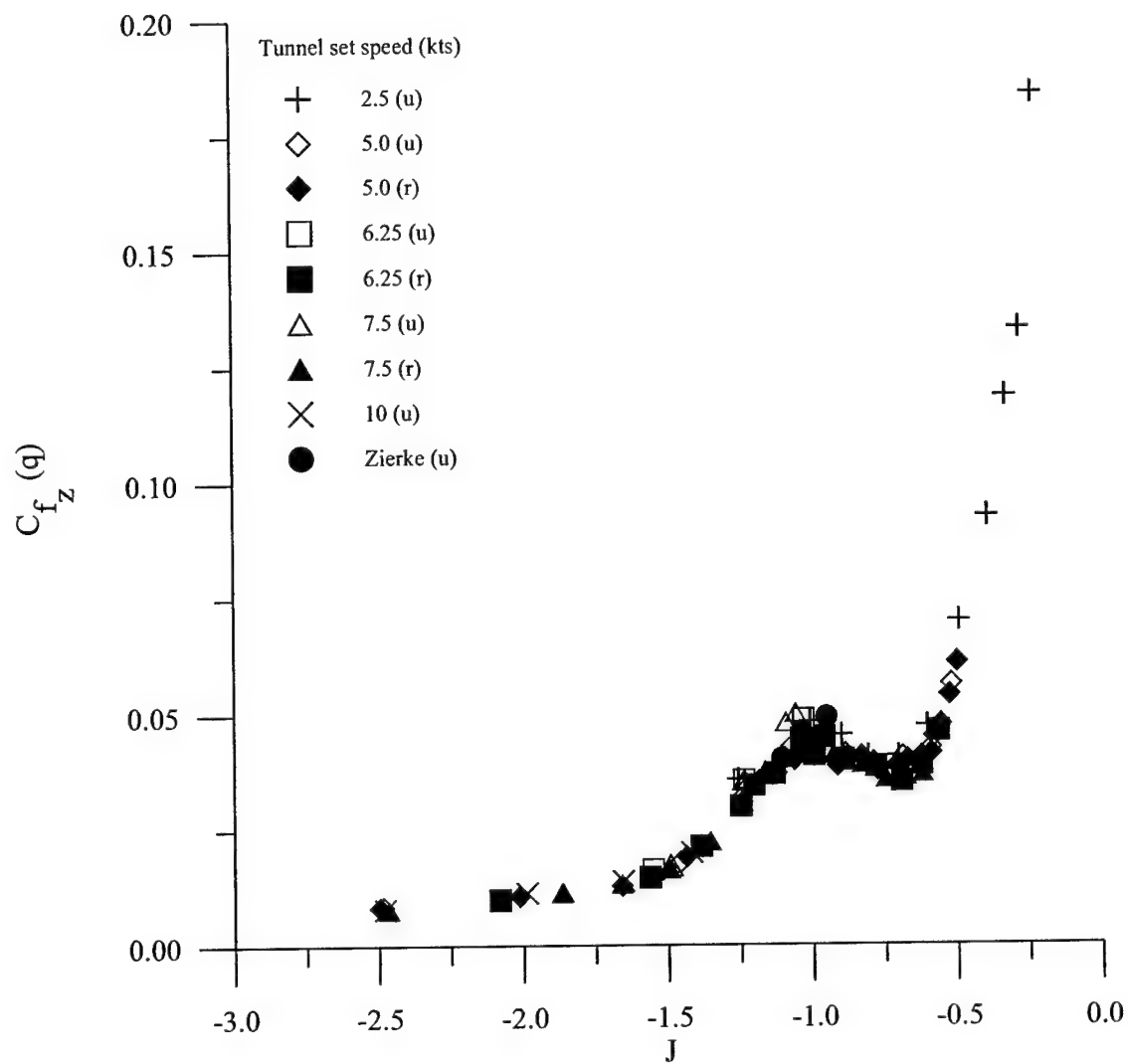
Figure 3.34 Coefficient of RMS propeller z force ("q" - dynamic pressure scaling, "u" - model restraining strut off, "r" - model restraining strut on)
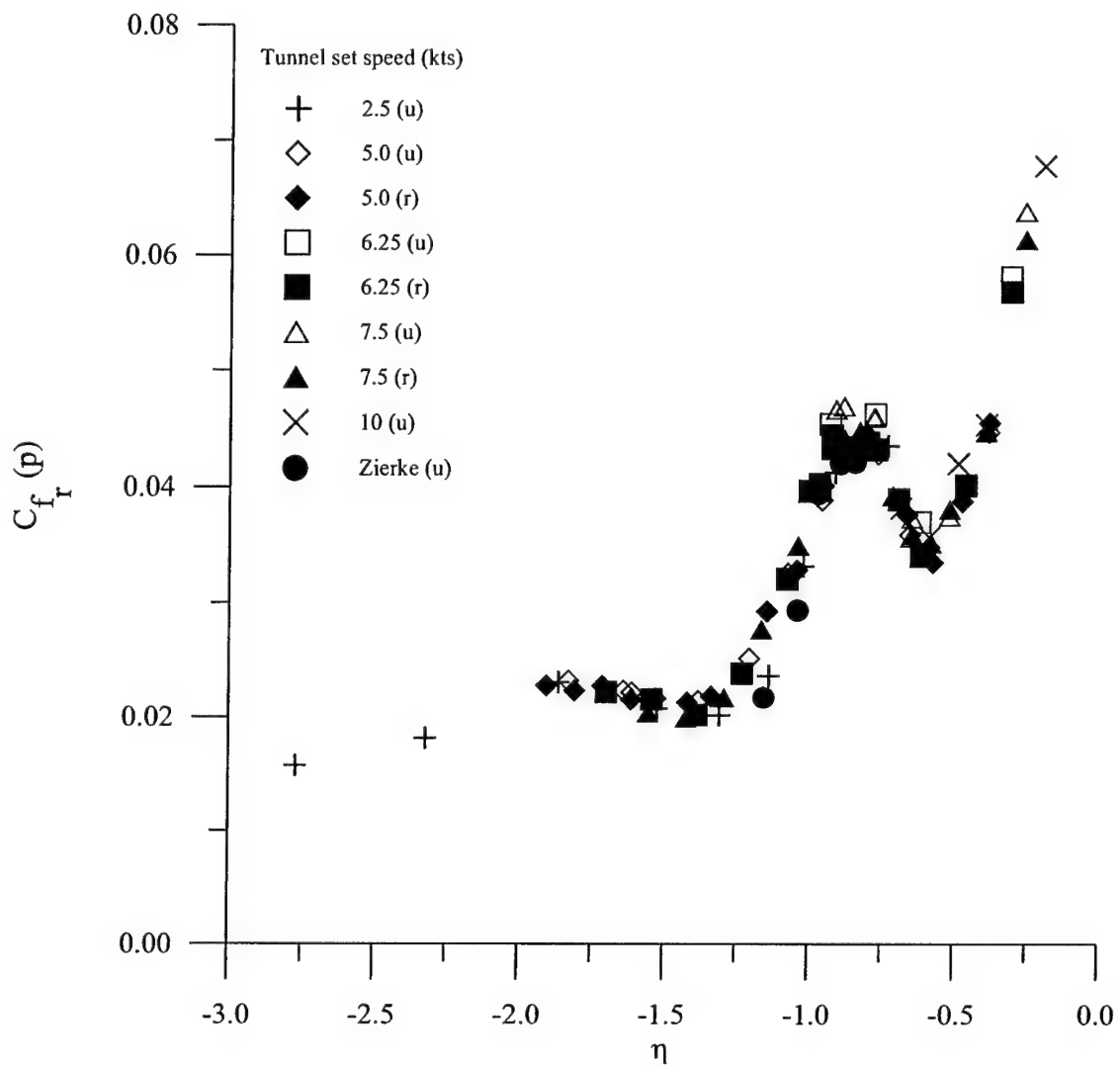
Figure 3.35 Coefficient of RMS propeller resultant off-axis force ("p" - propulsive scaling, "u" - model restraining strut off, "r" - model restraining strut on)
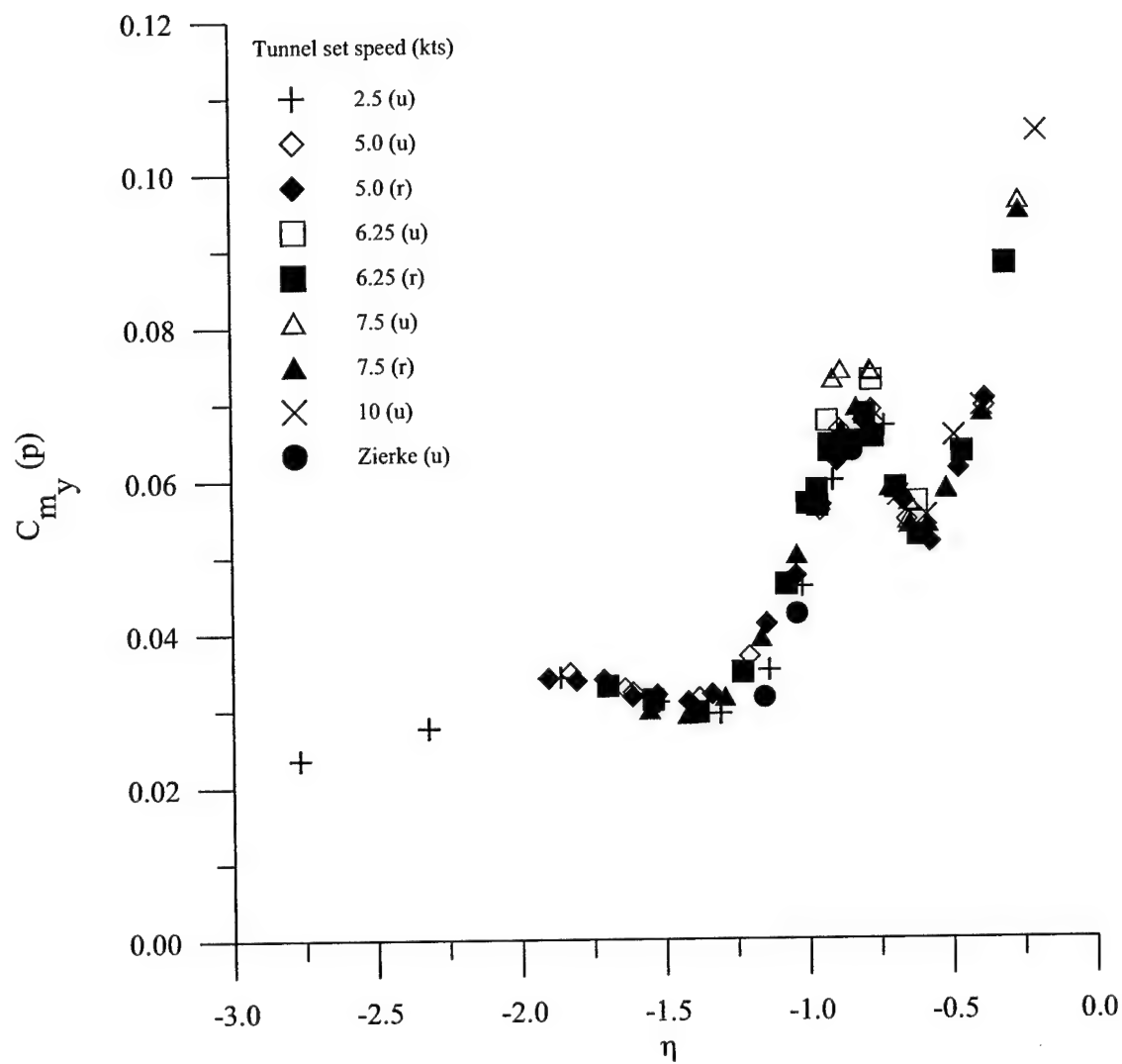
Figure 3.36 Coefficient of RMS propeller *y* moment ("p" - propulsive scaling, "u" - model restraining strut off, "r" - model restraining strut on)
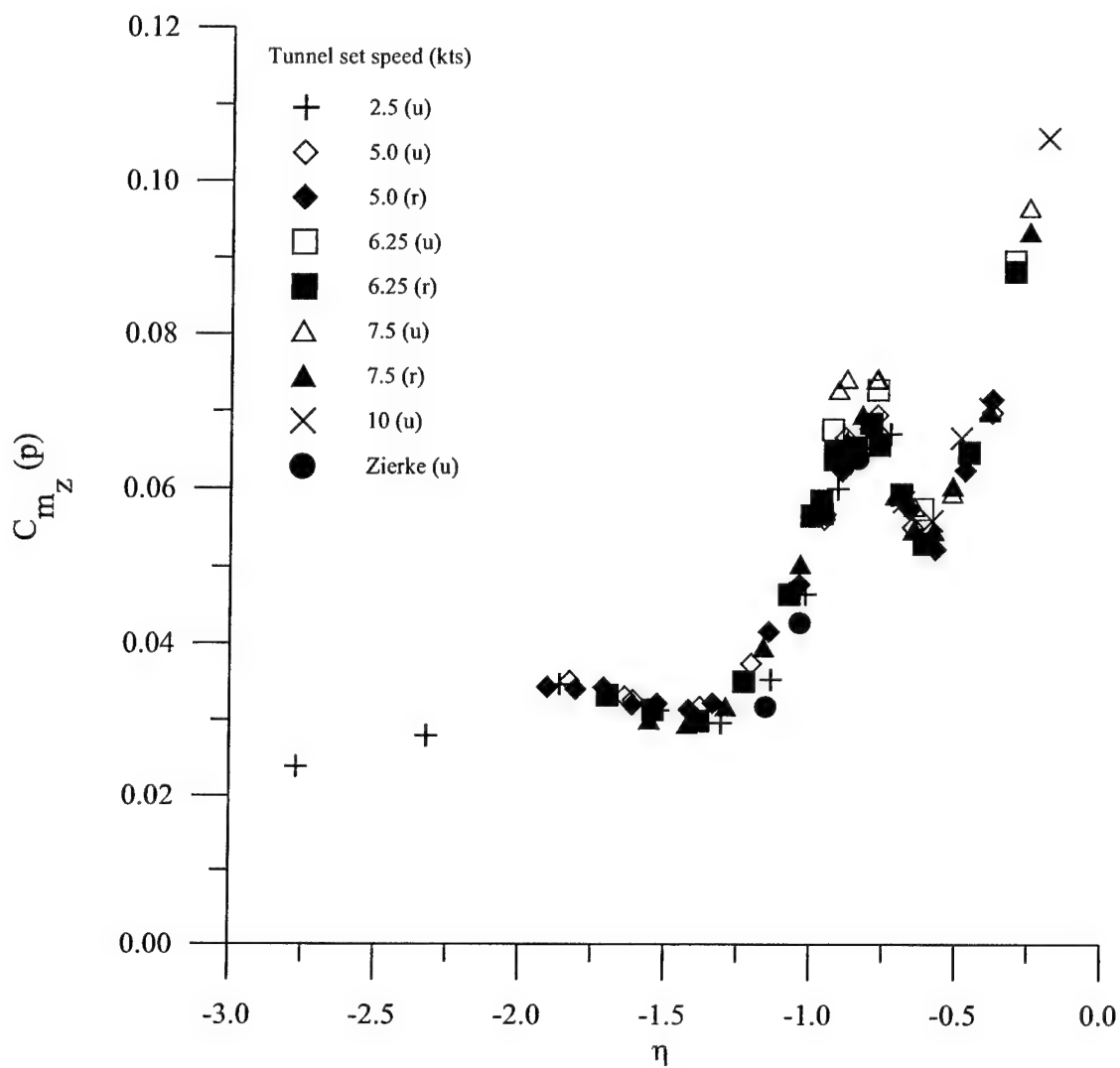
Figure 3.37 Coefficient of RMS propeller *z* moment ("p" - propulsive scaling, "u" - model restraining strut off, "r" - model restraining strut on)
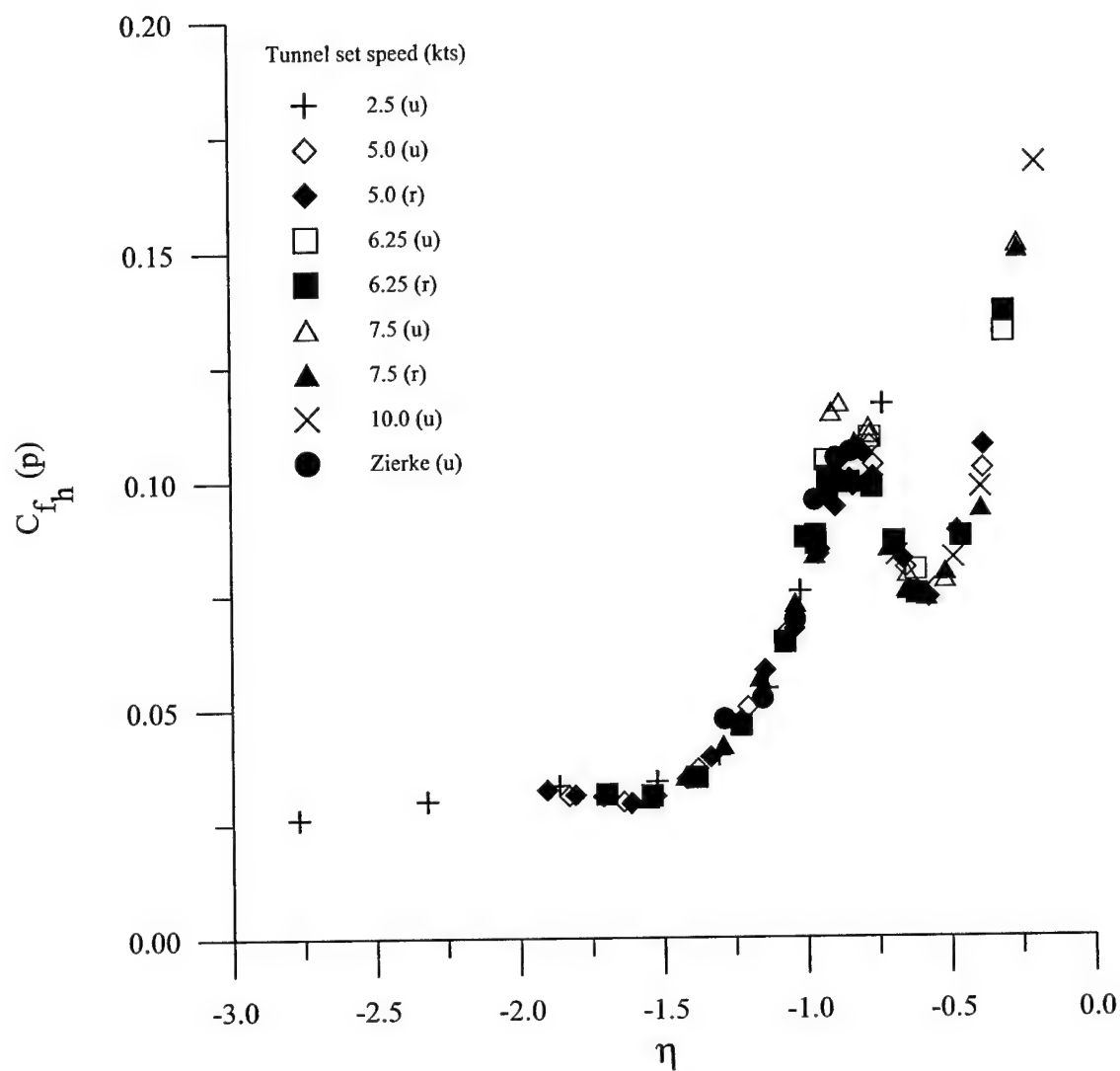
Figure 3.38 Coefficient of RMS propeller horizontal force ("p" - propulsive scaling, "u" - model restraining strut off, "r" - model restraining strut on)
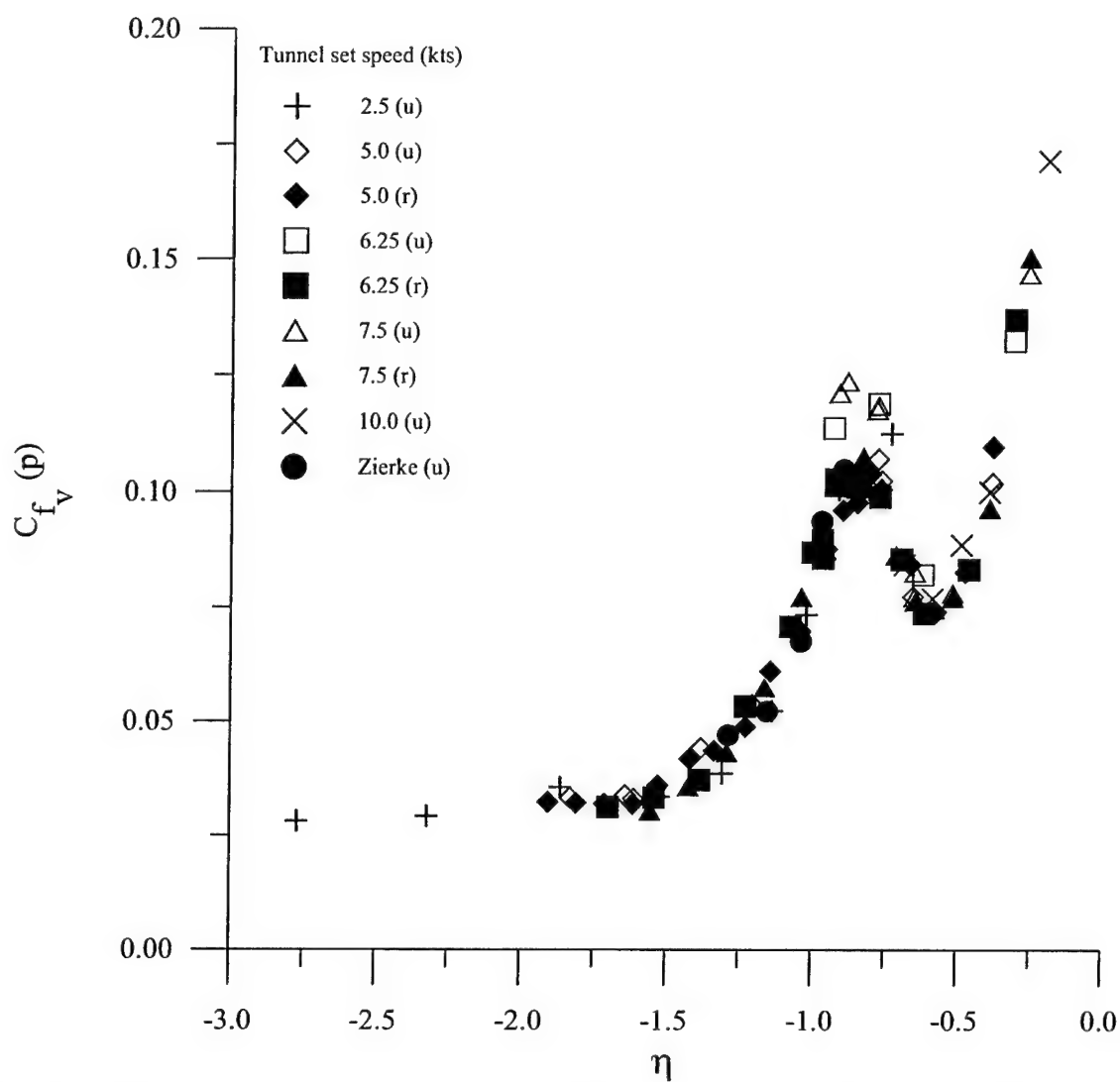
Figure 3.39 Coefficient of RMS propeller vertical force ("p" - propulsive scaling, "u" - model restraining strut off, "r" - model restraining strut on)
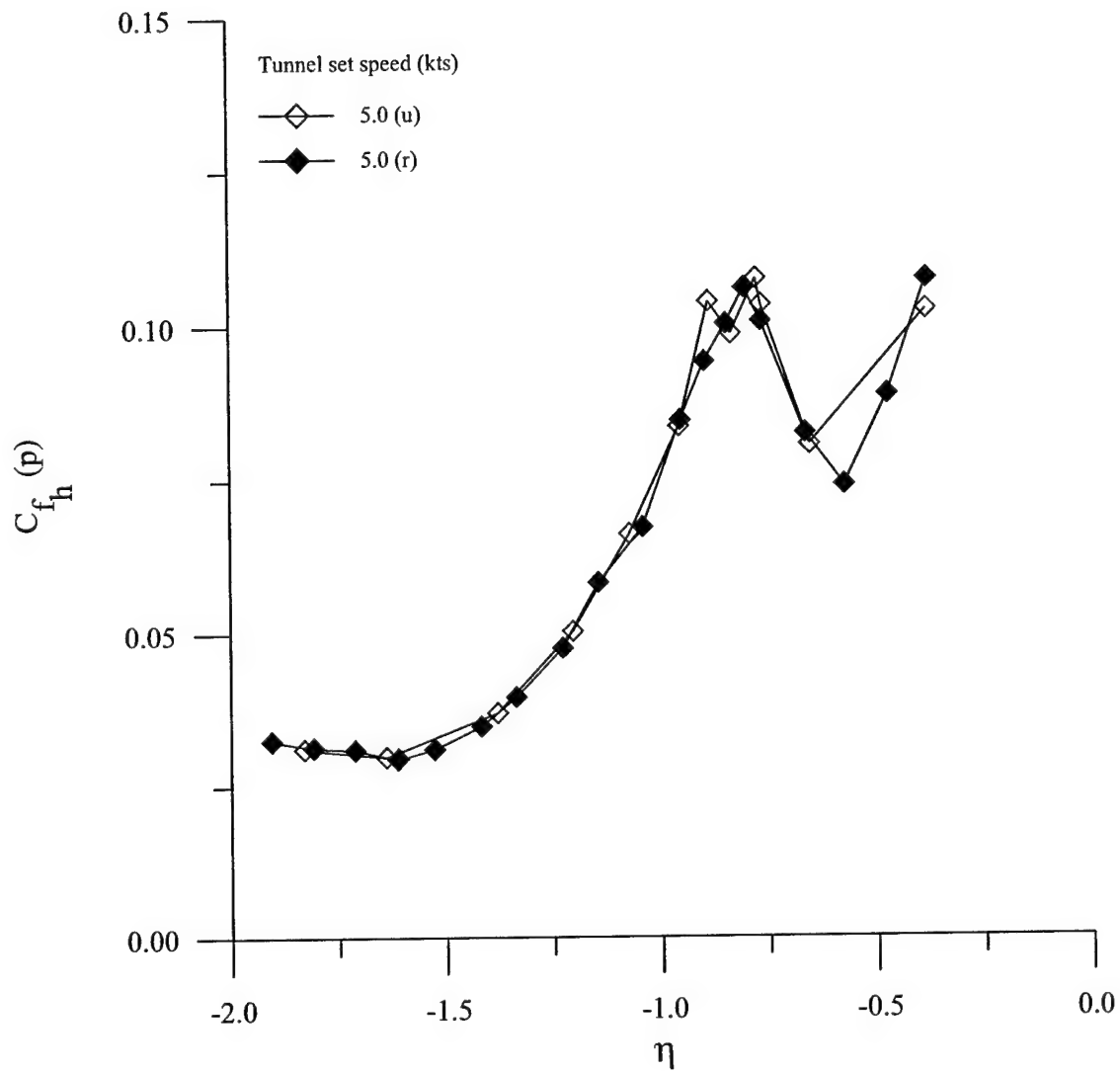
Figure 3.40 Comparison of coefficients of RMS propeller horizontal force for tests with model unrestrained ("u") and restrained ("r") ("p" - propulsive scaling)
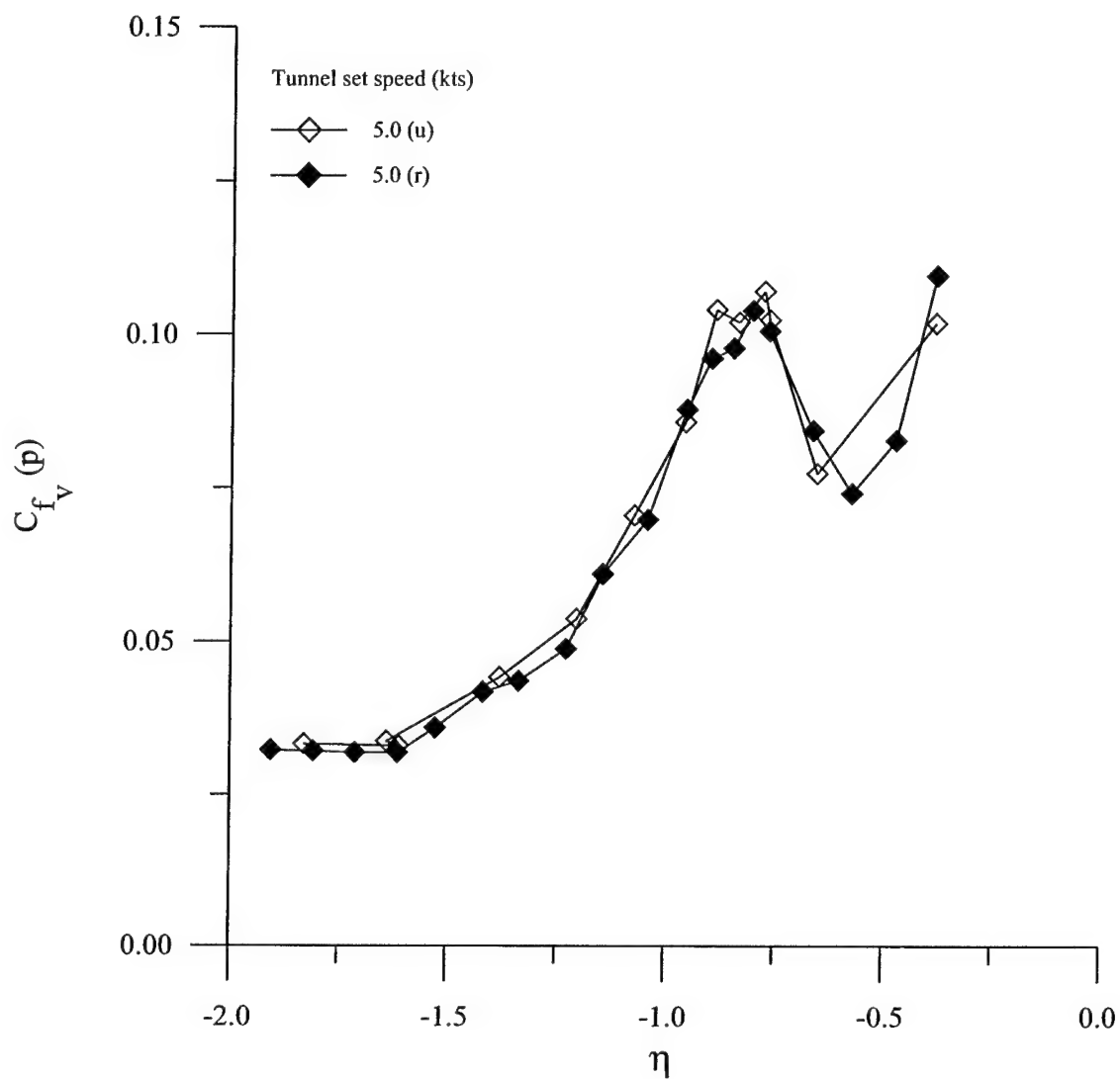
Figure 3.41 Comparison of coefficients of RMS propeller vertical force for tests with model unrestrained ("u") and restrained ("r") ("p" - propulsive scaling)
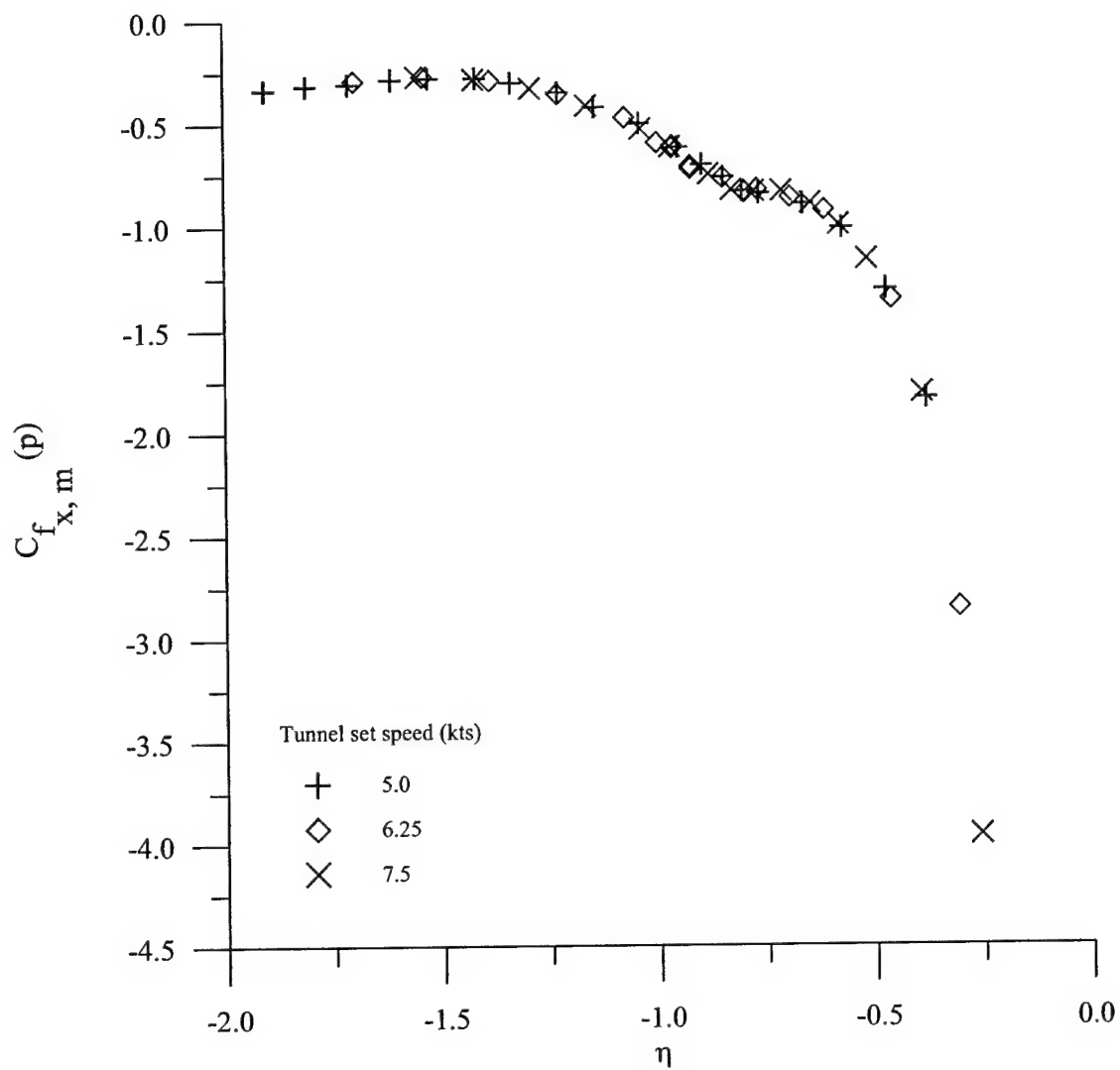
Figure 3.42 Coefficient of mean propeller axial force ("p" - propulsive scaling; all data for model with restraining strut on)
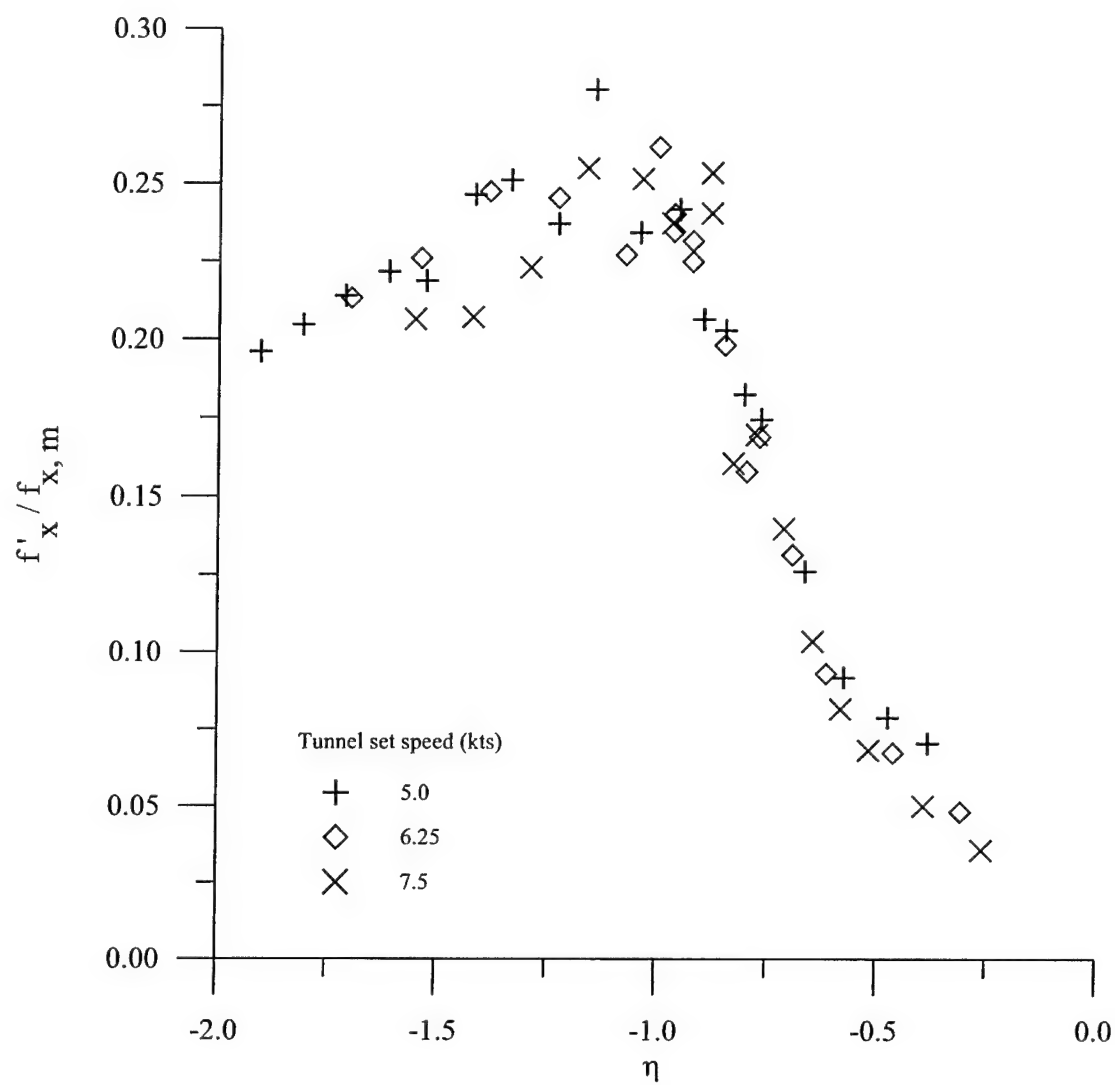
Figure 3.43 Propeller RMS axial force as a fraction of the mean propeller axial force (all data for model with restraining strut on)
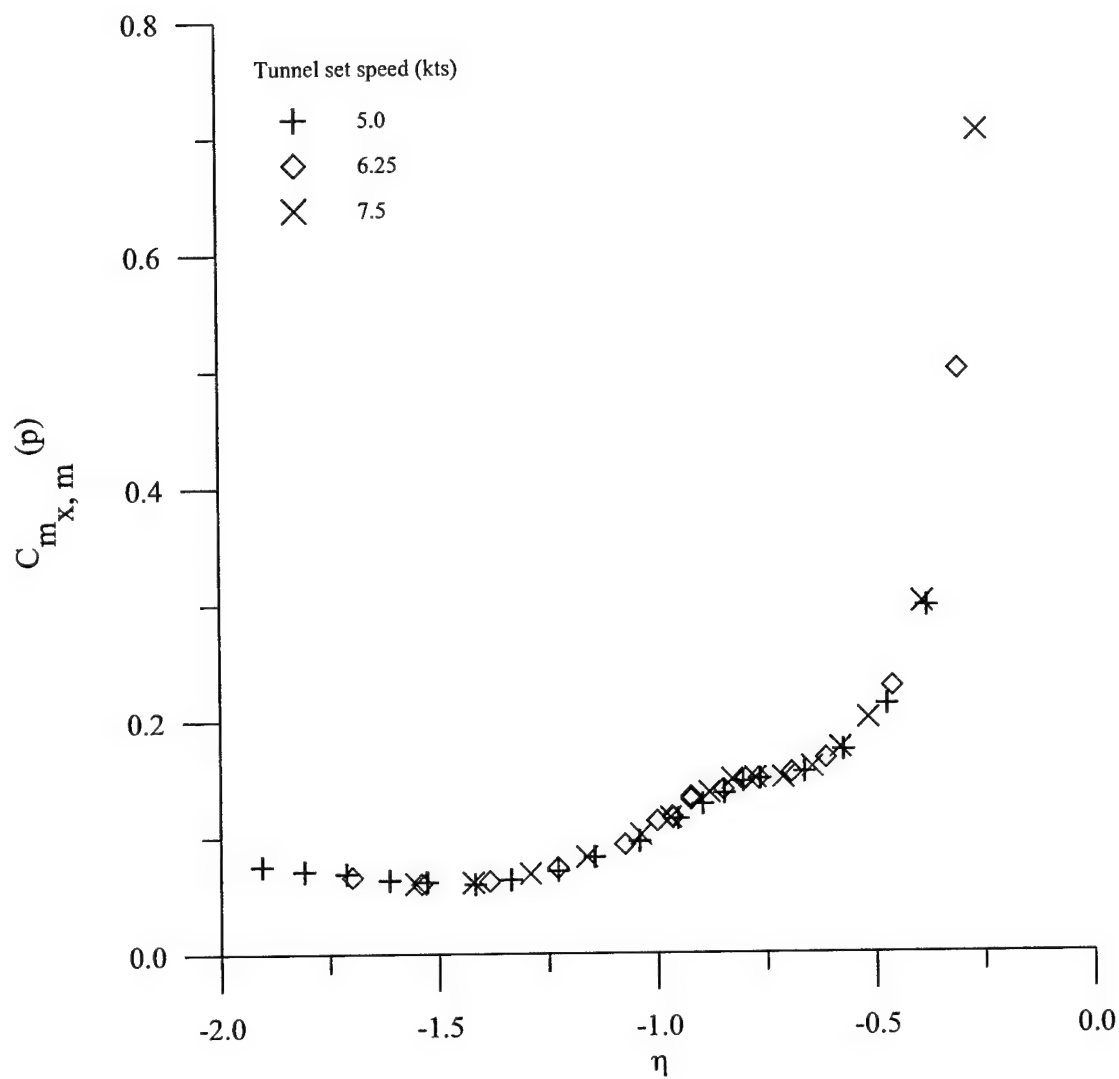
Figure 3.44 Coefficient of mean propeller axial moment (torque) ("p" - propulsive scaling; all data for model with restraining strut on)
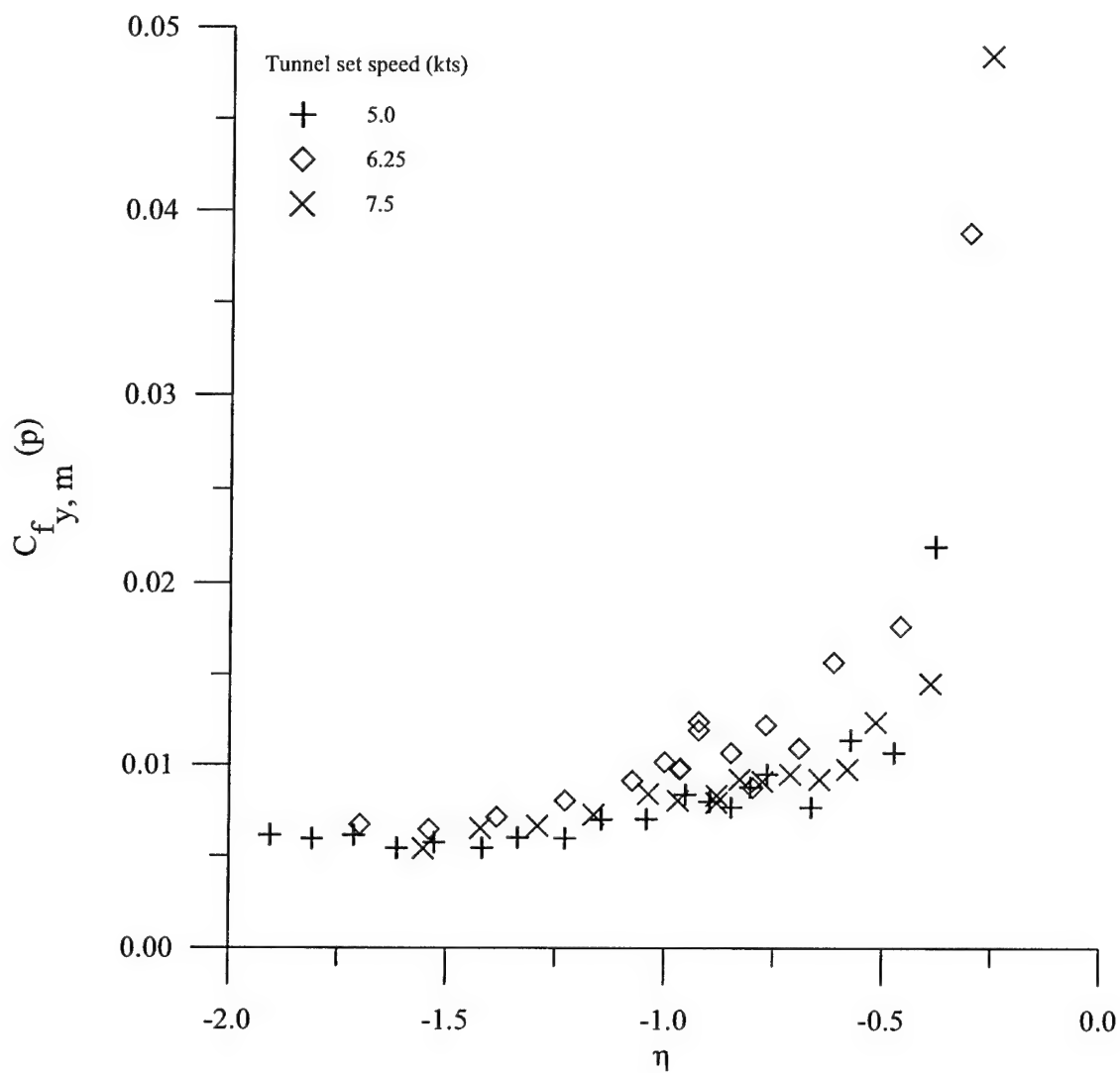
Figure 3.45 Coefficient of mean propeller *y* force ("p" - propulsive scaling, all data with model restraining strut on)
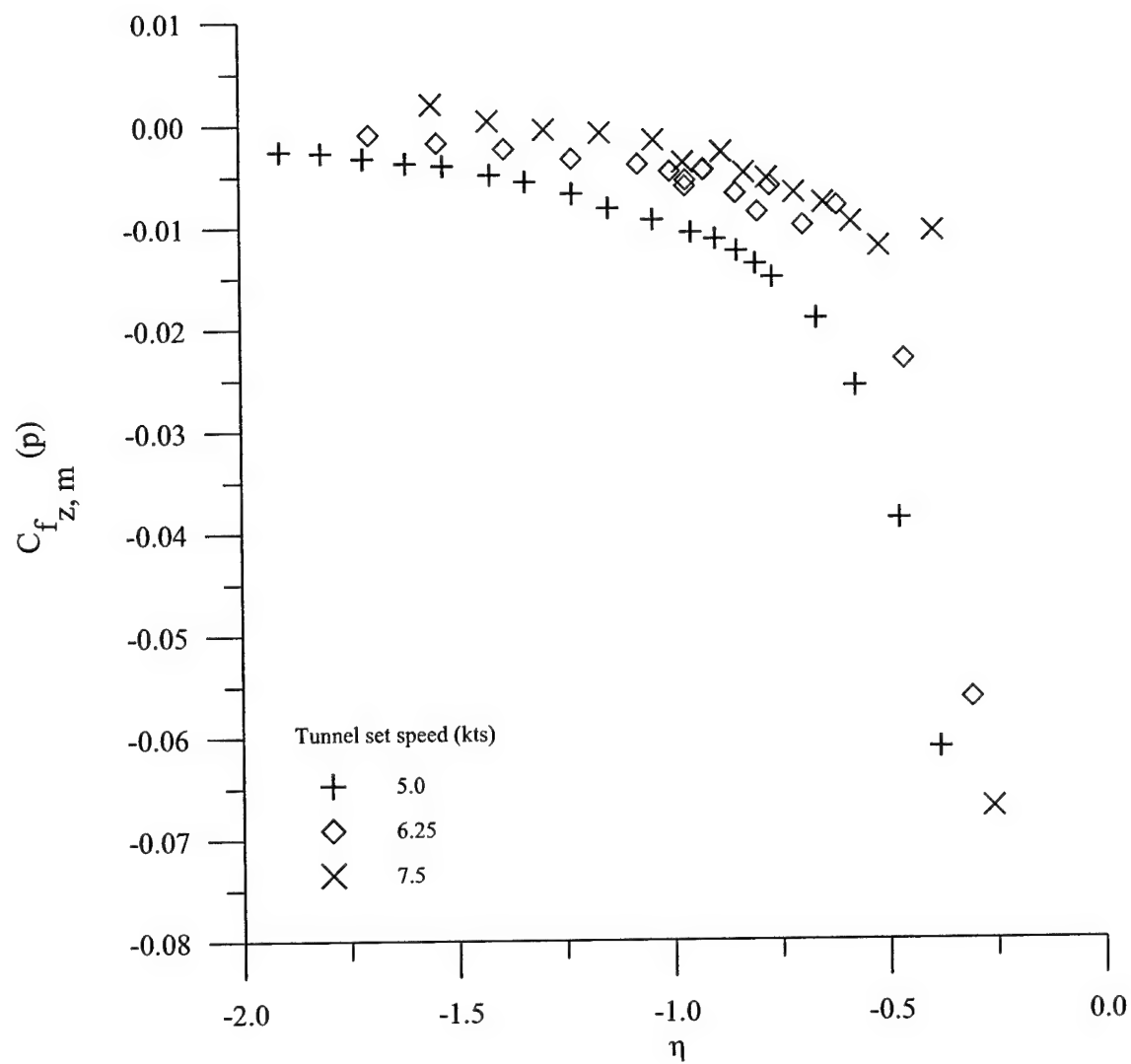
Figure 3.46 Coefficient of mean propeller *z* force ("p" - propulsive scaling; all data with model restraining strut on)
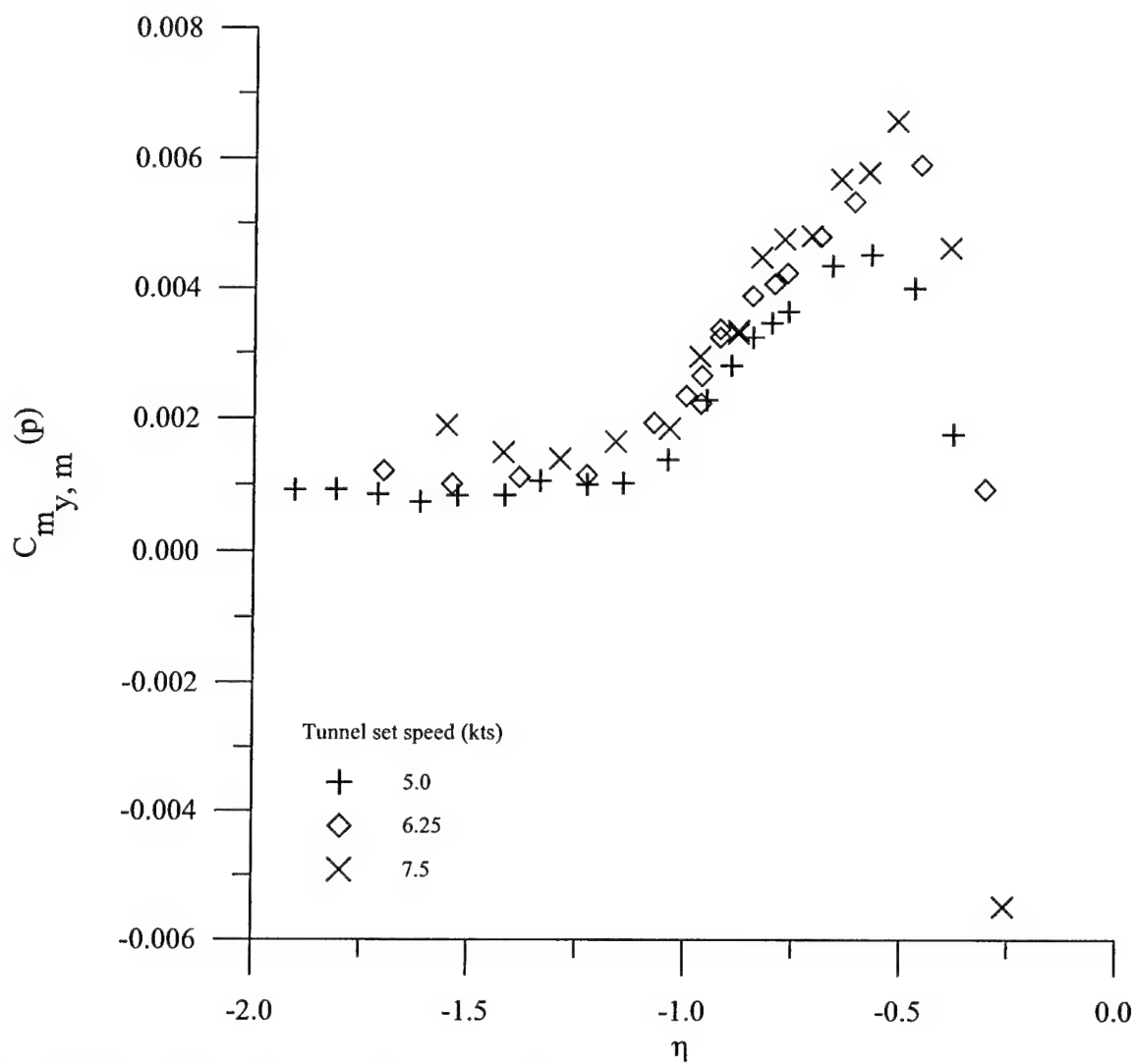
Figure 3.47 Coefficient of mean propeller y moment ("p" - propulsive scaling; all data with model restraining strut on)
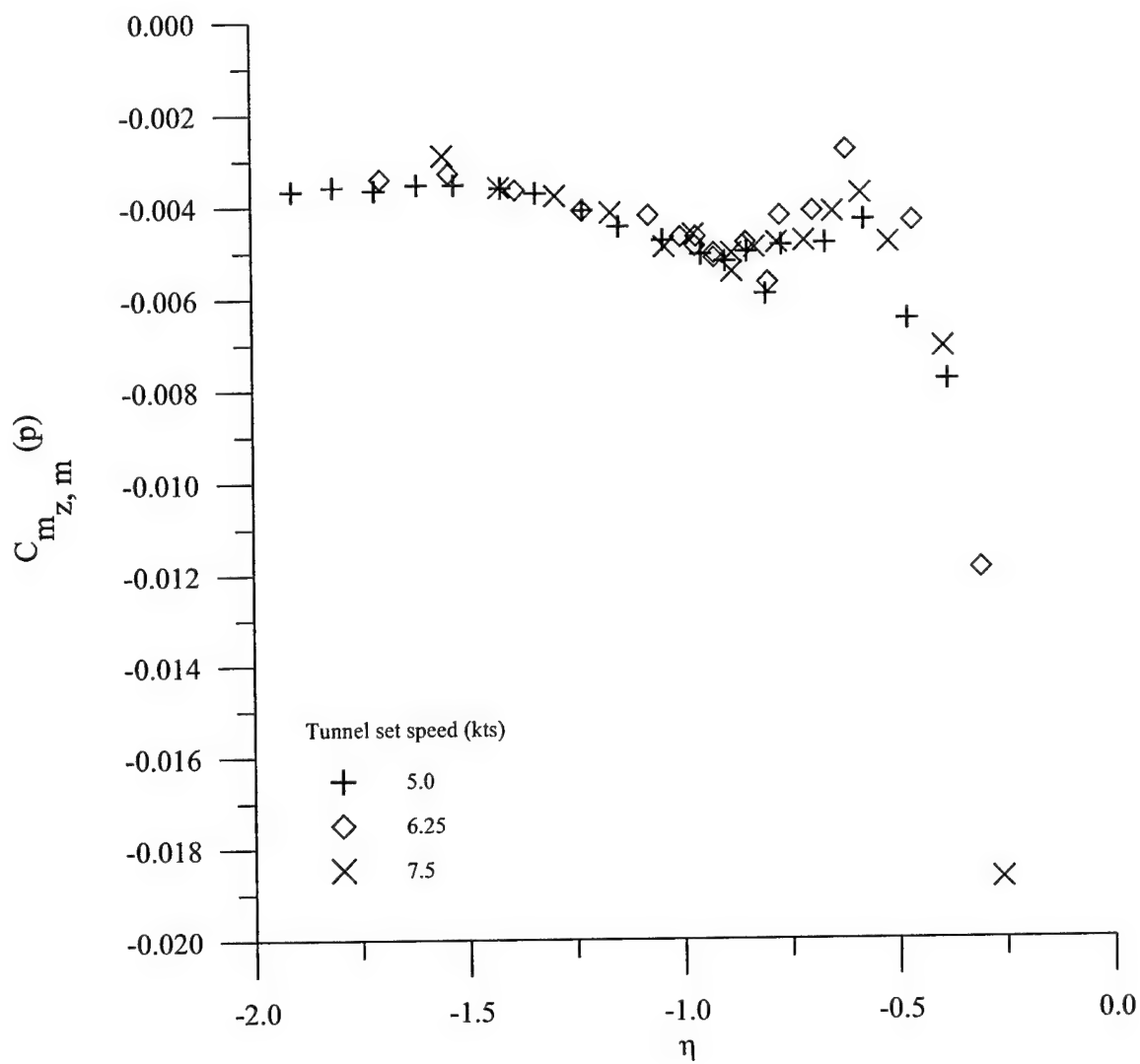
Figure 3.48 Coefficient of mean propeller z moment ("p" - propulsive scaling; all data with model restraining strut on)
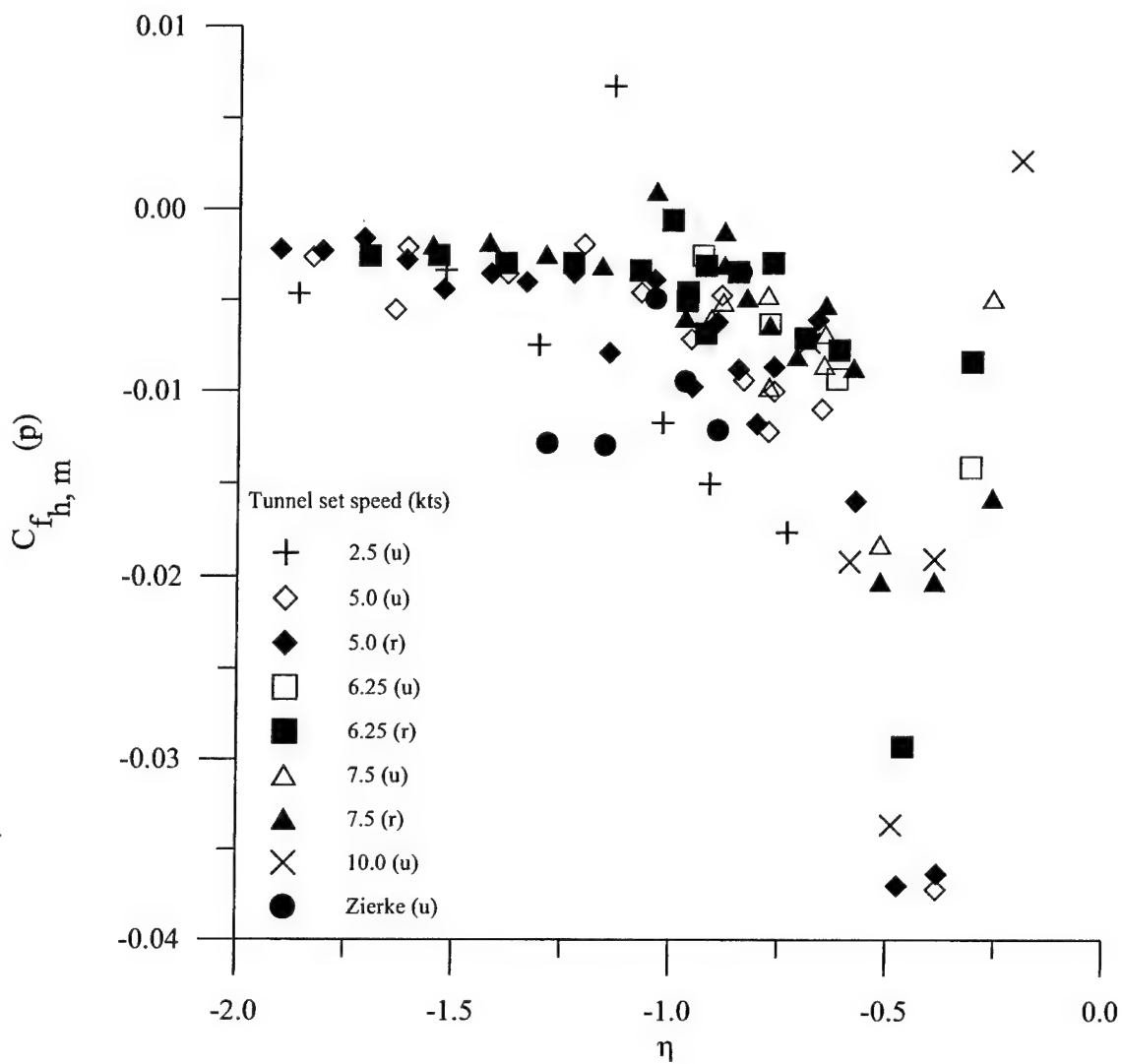
Figure 3.49 Coefficient of mean propeller horizontal force ("p" - propulsive scaling, "u" - model restraining strut off, "r" - model restraining strut on)
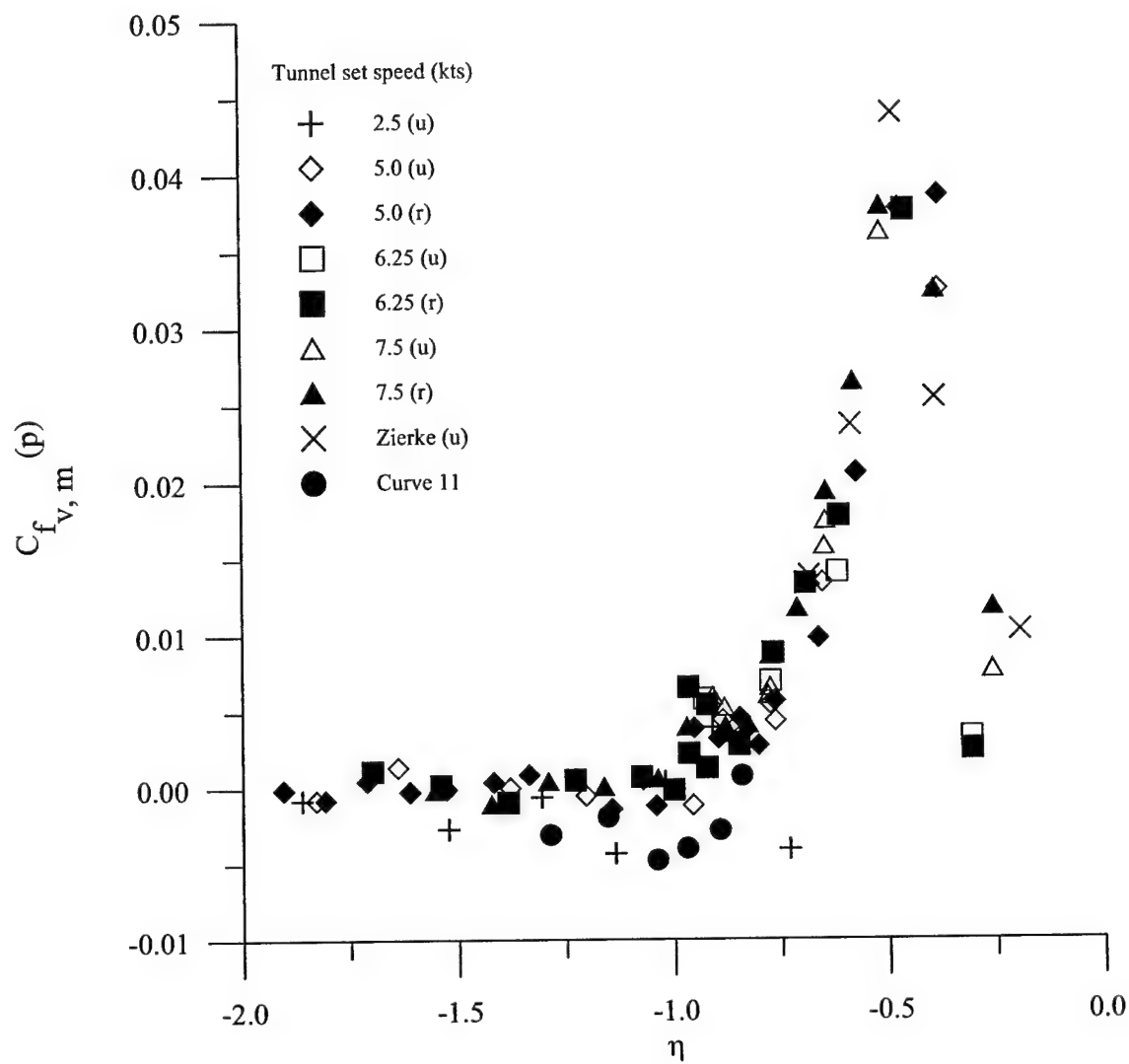
Figure 3.50 Coefficient of mean propeller vertical force ("p" - propulsive scaling, "u" - model restraining strut off, "r" - model restraining strut on)
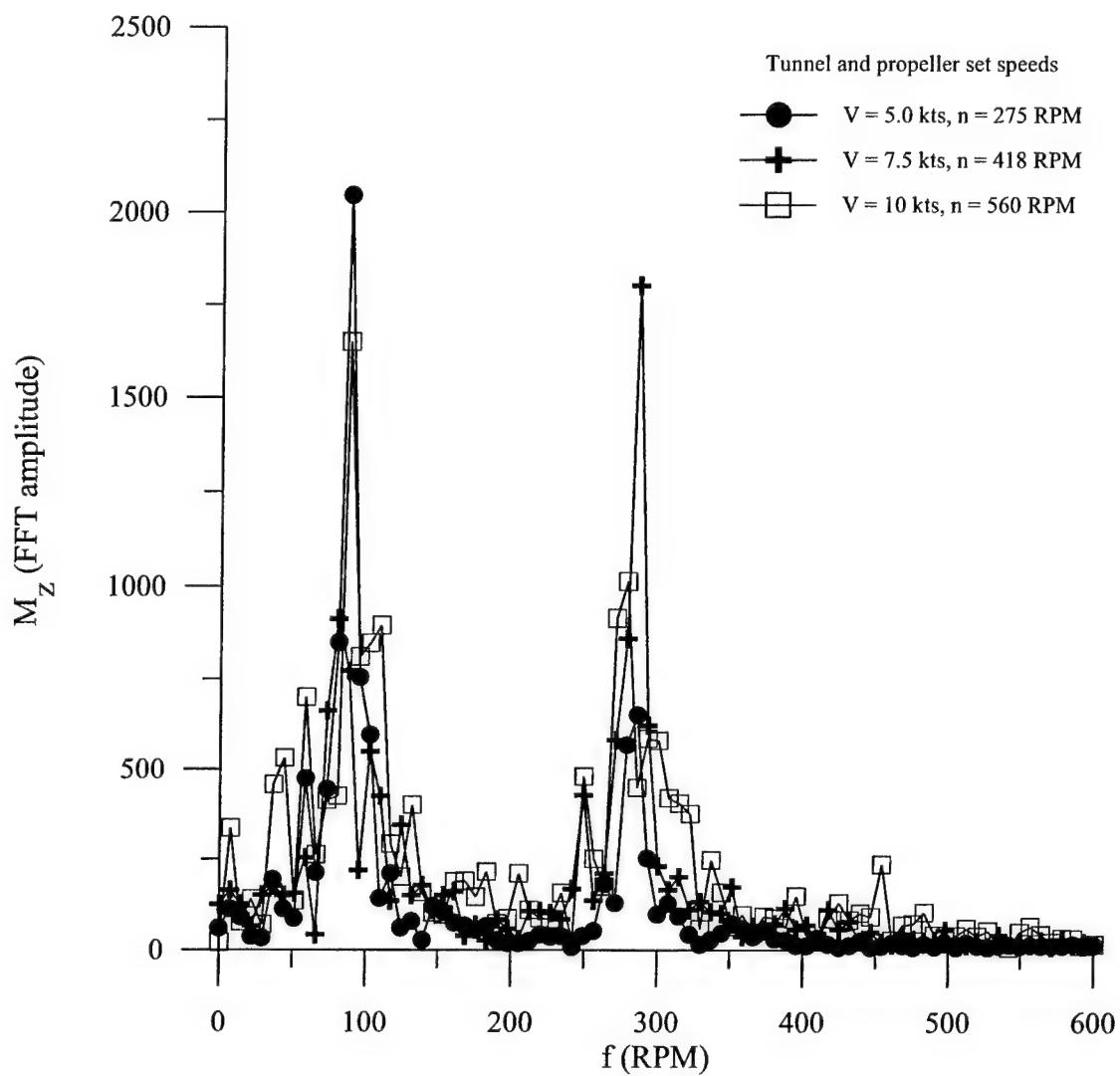
Figure 3.51 Frequency response curves for body yawing moment at zero propeller thrust conditions
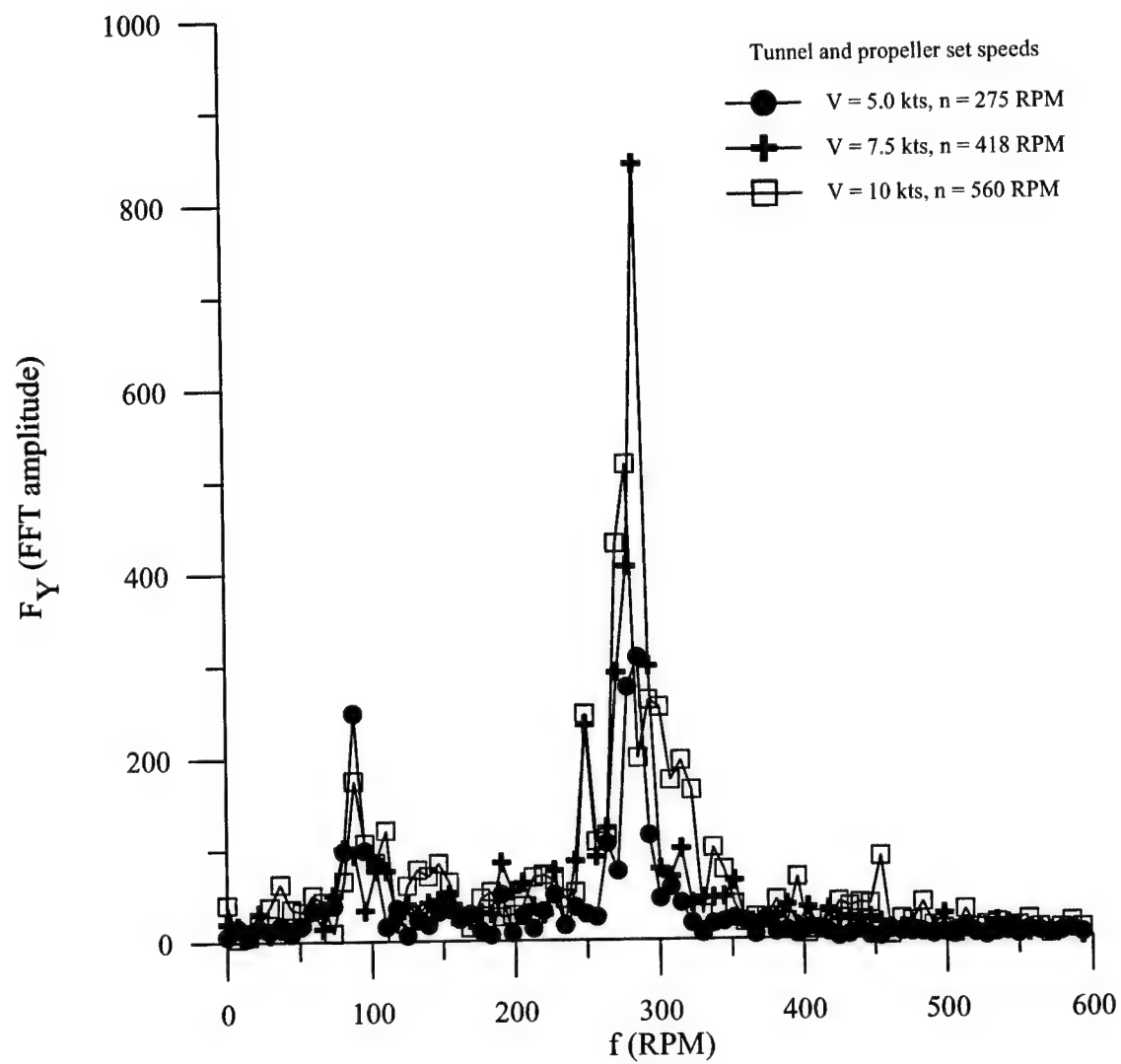
Figure 3.52 Frequency response curves for body side force at zero propeller thrust conditions
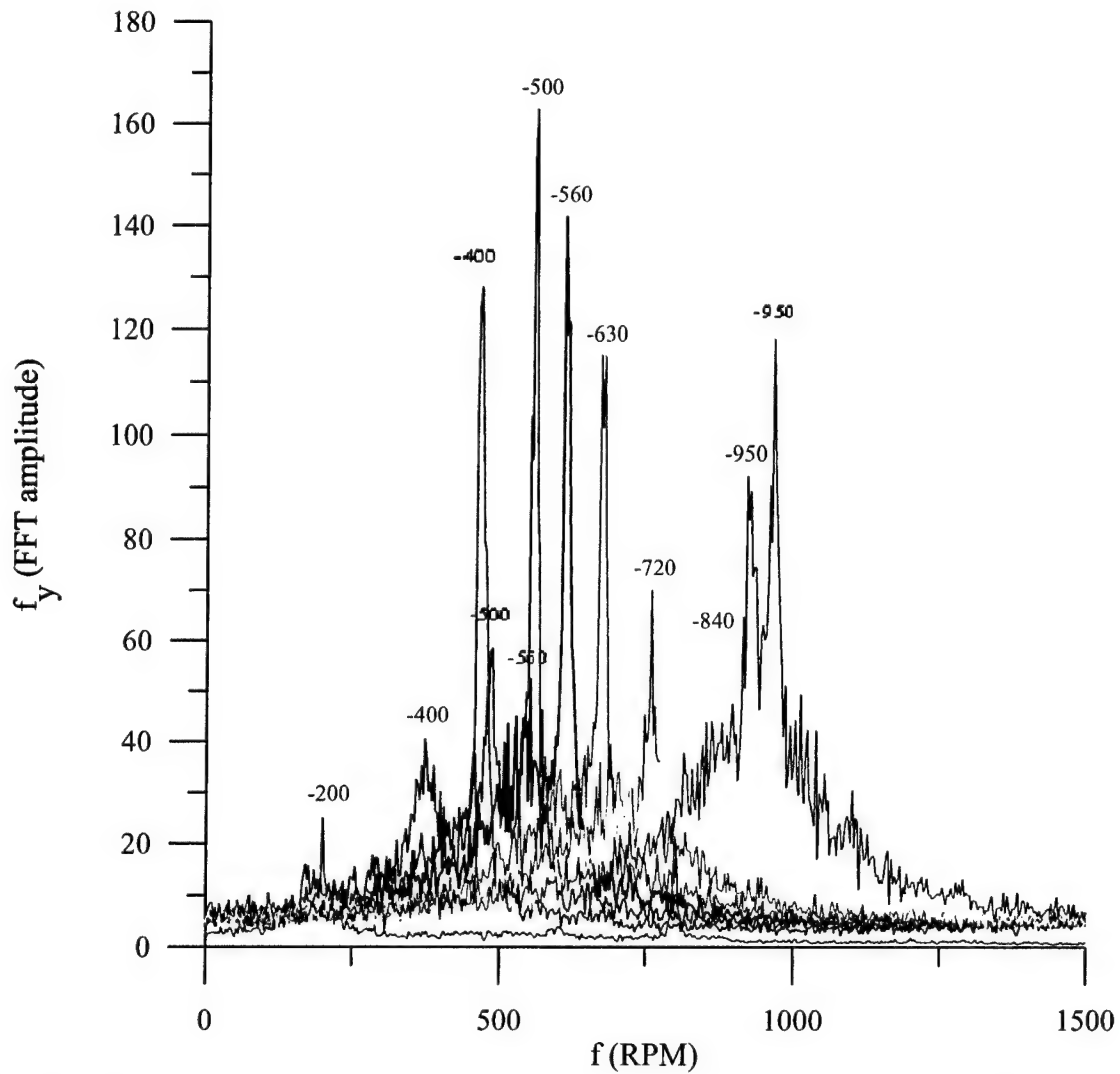
Figure 3.53 Frequency response curves of propeller y force (numbers indicate propeller speed for each response curve and are located at the peak(s) of each response curve)
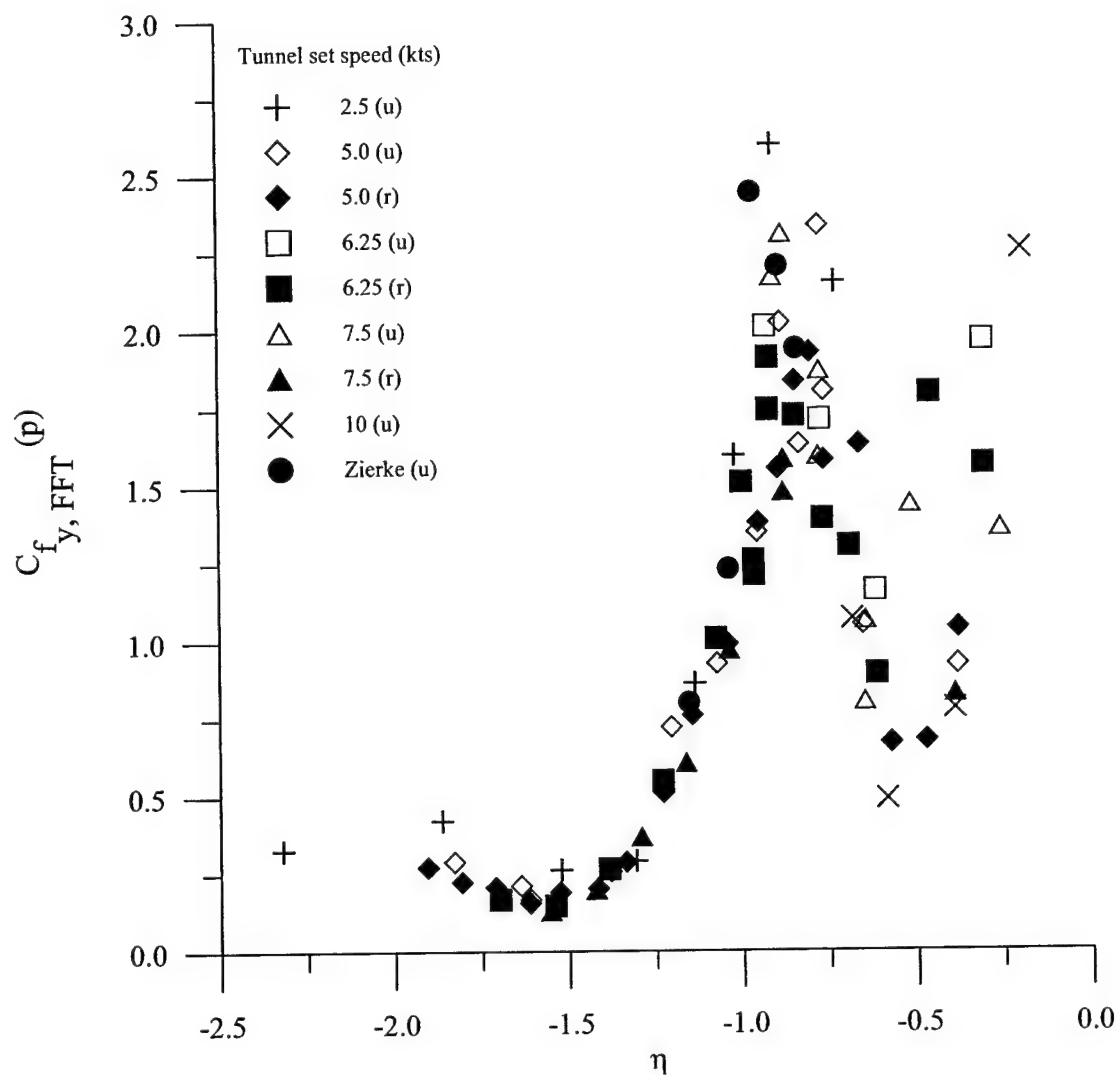
Figure 3.54 Coefficients of propeller y force formed from peak frequency response magnitudes ("p" - propulsive scaling, "u" - model restraining strut off, "r" - model restraining strut on)
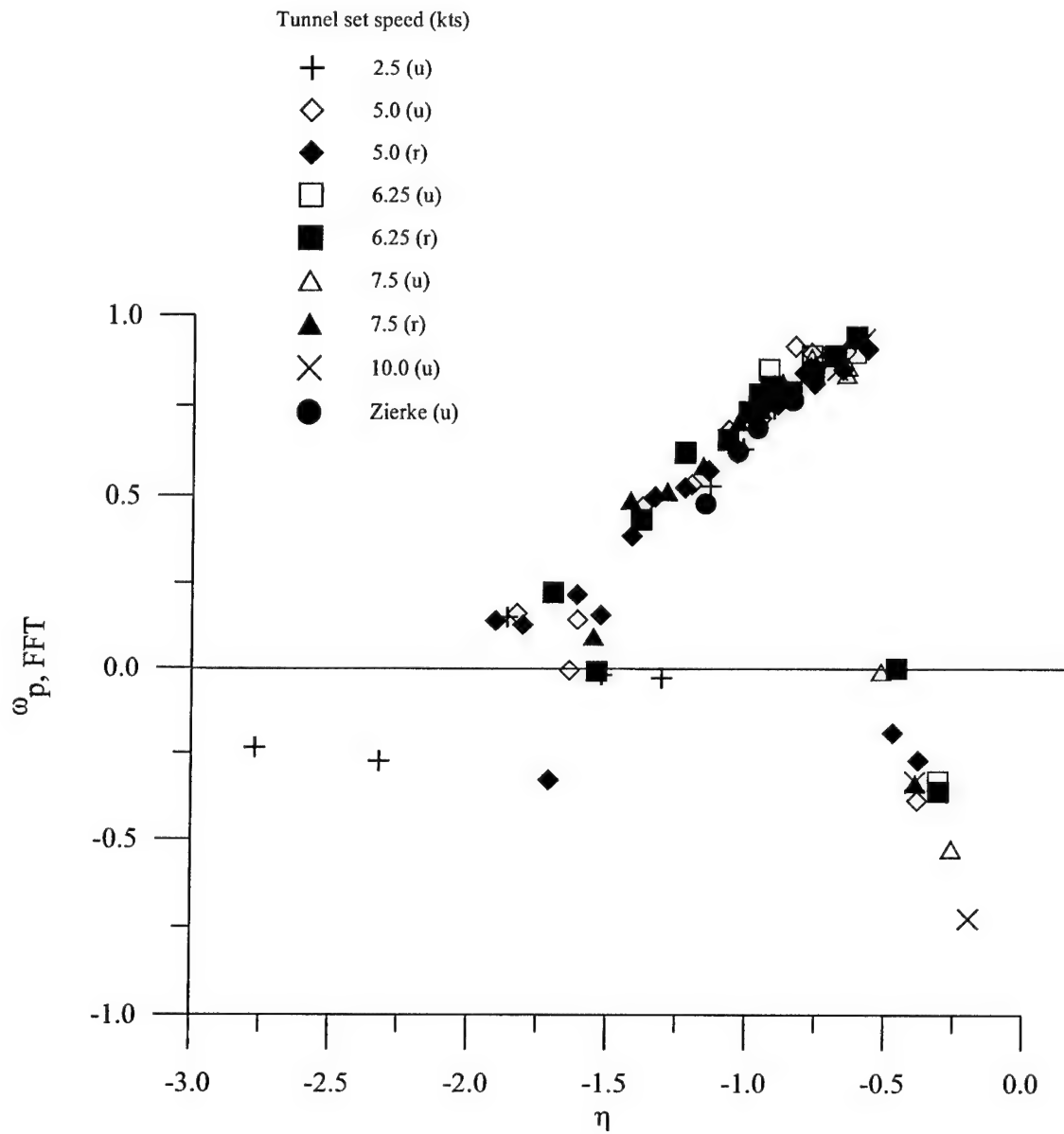
Figure 3.55 Dimensionless frequency of peak propeller *y* force amplitude ("u" - model restraining strut off, "r" - model restraining strut on)
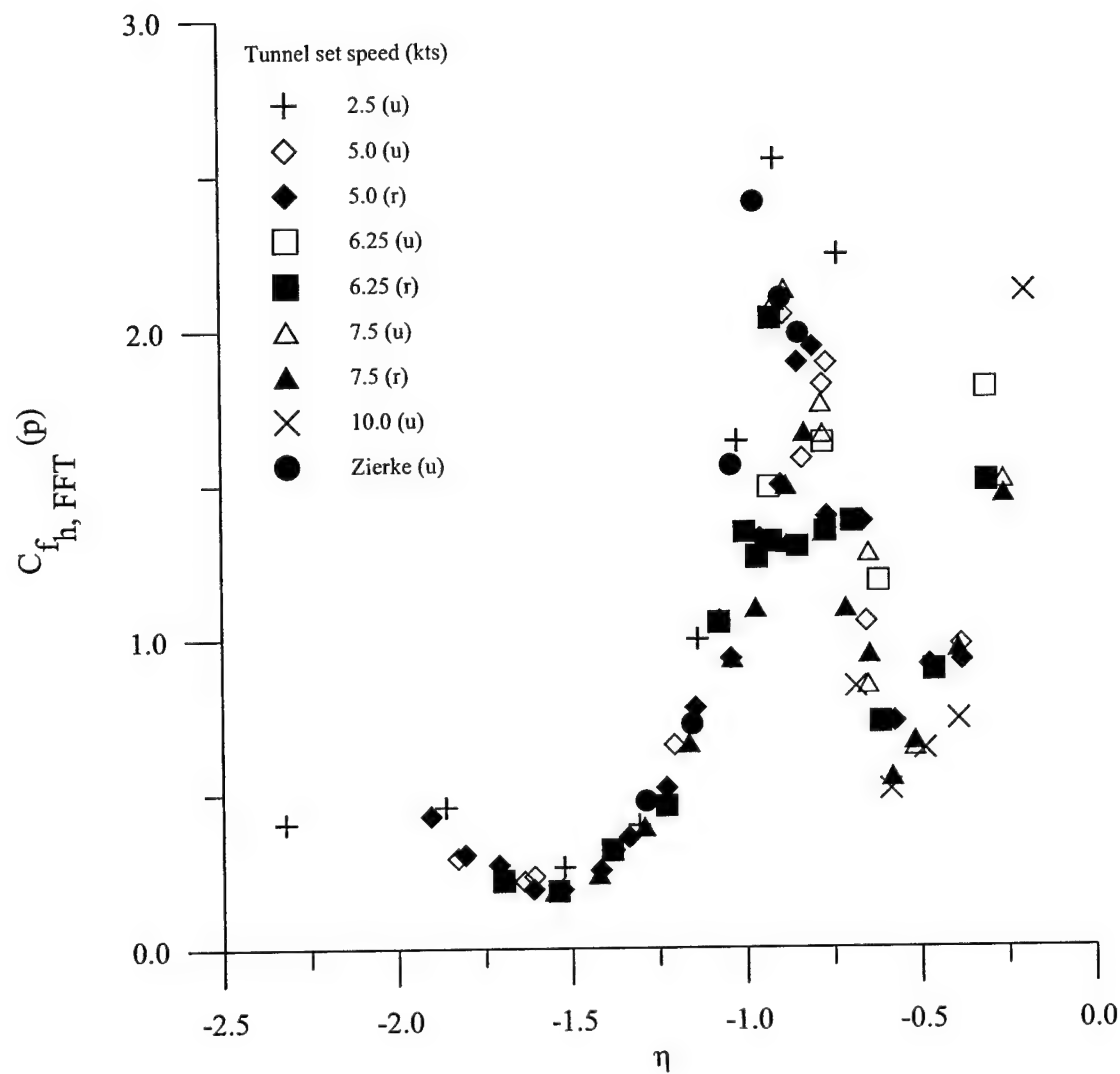
Figure 3.56 Coefficients of propeller horizontal force formed from peak frequency response magnitudes ("p" - propulsive scaling, "u" - model restraining strut off, "r" - model restraining strut on)
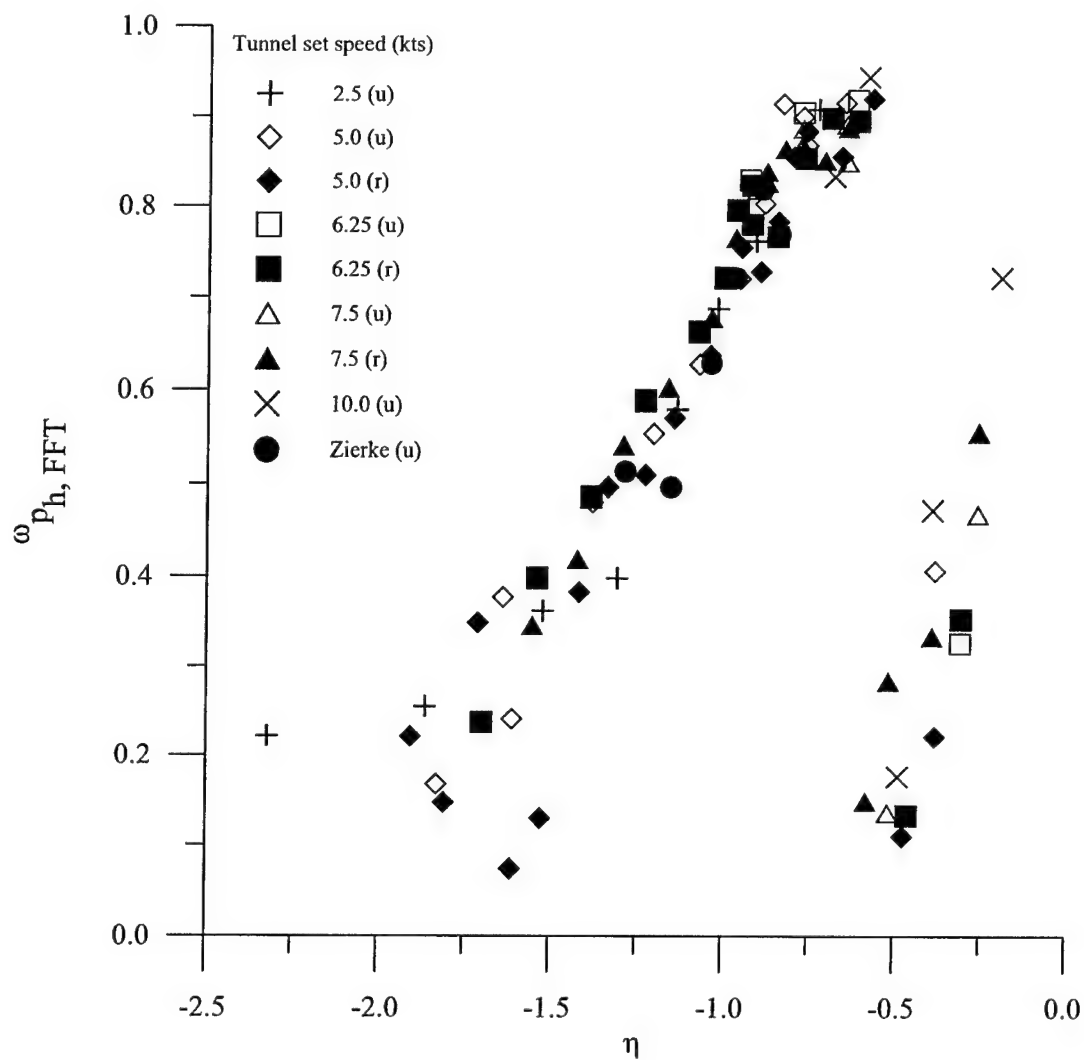
Figure 3.57 Dimensionless frequency of peak propeller horizontal force amplitude ("u" - model restraining strut off, "r" - model restraining strut on)
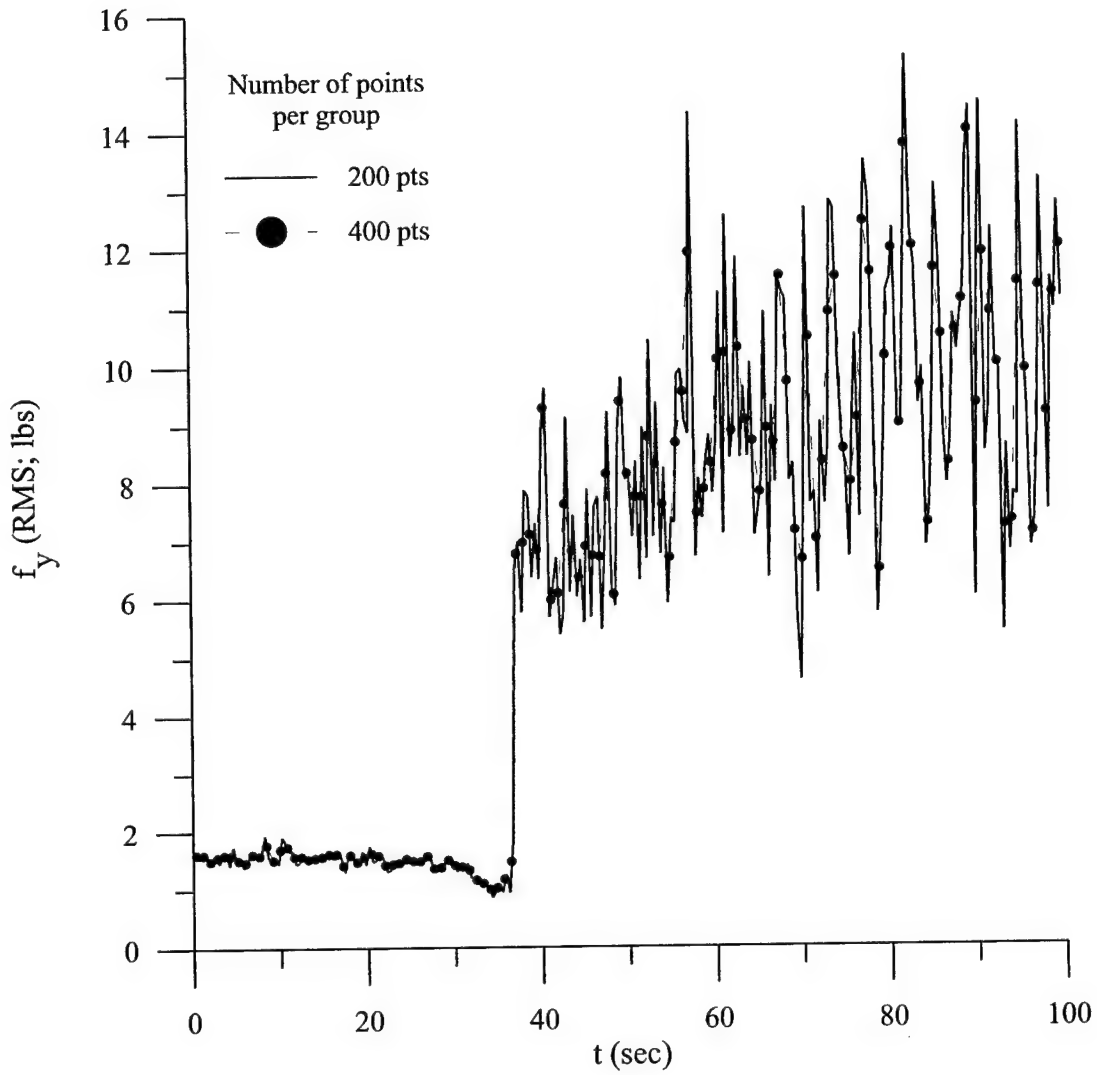
Figure 3.58 Effects of number of samples in each group on computation of time-varying RMS propeller y force (symbols only used to distinguish curves; not every data point is marked by a symbol)

104
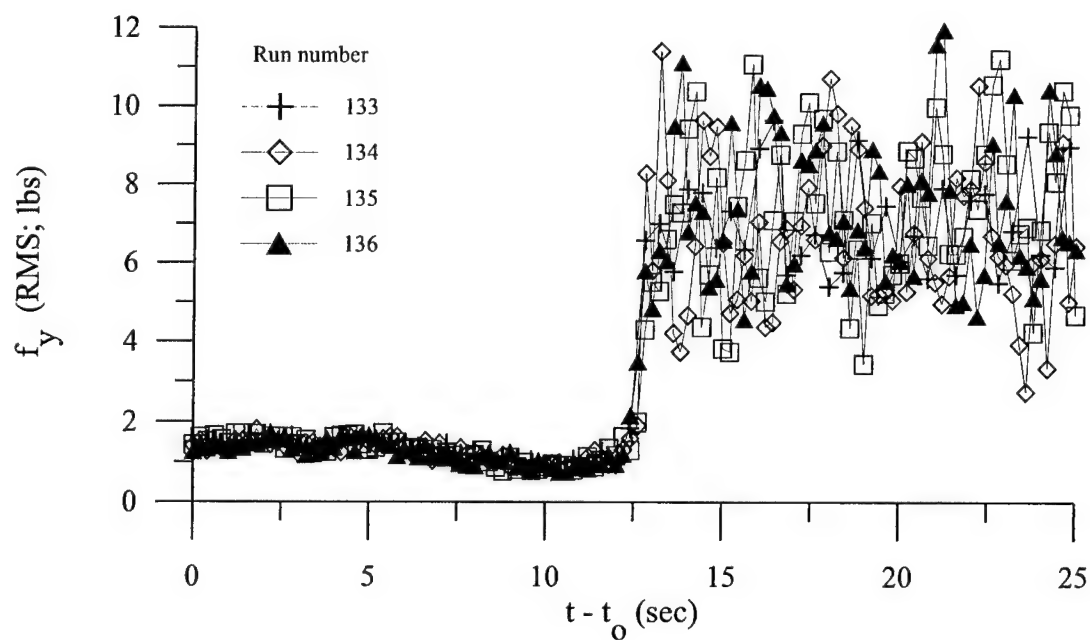
a. Extended data stream
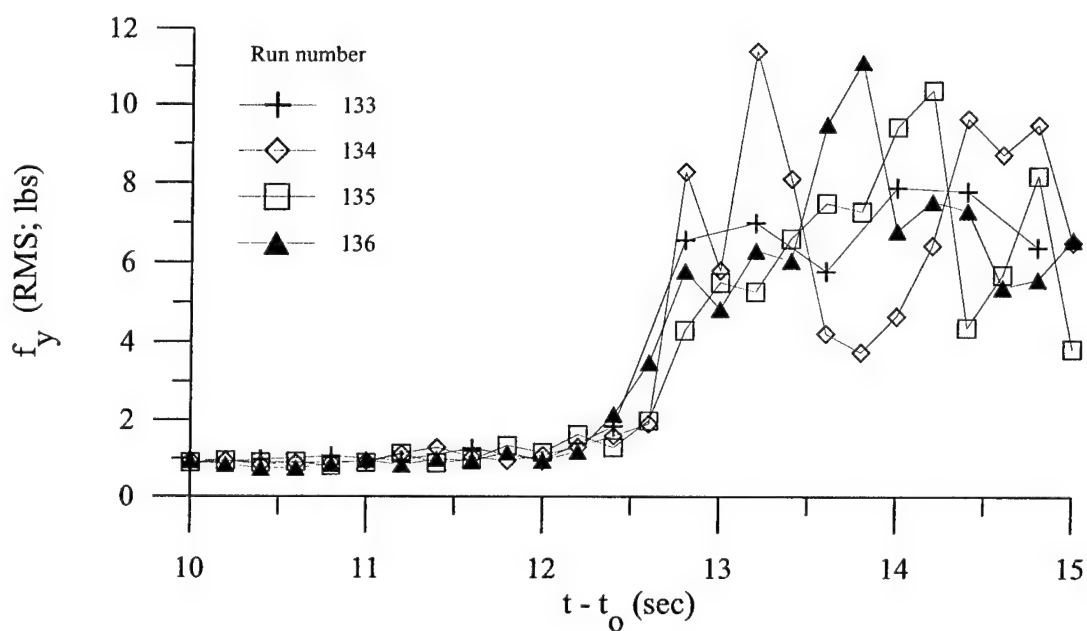
b. Expanded scale

Figure 3.59 RMS propeller side force development for constant tunnel speed, ramped propeller speed simulation of unsteady crashback maneuver
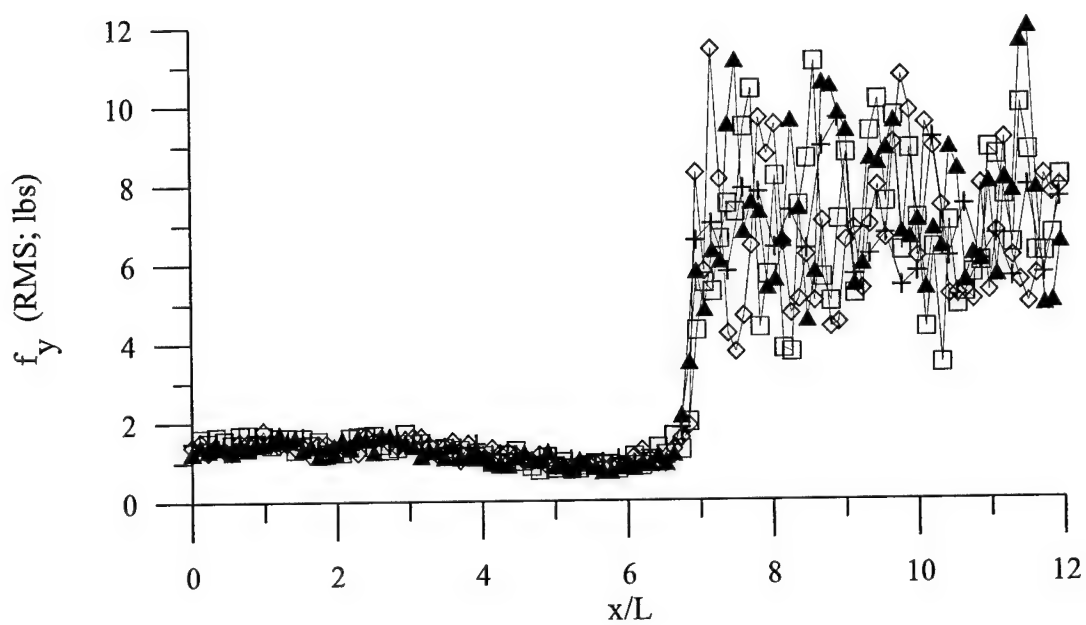
a. Extended data stream
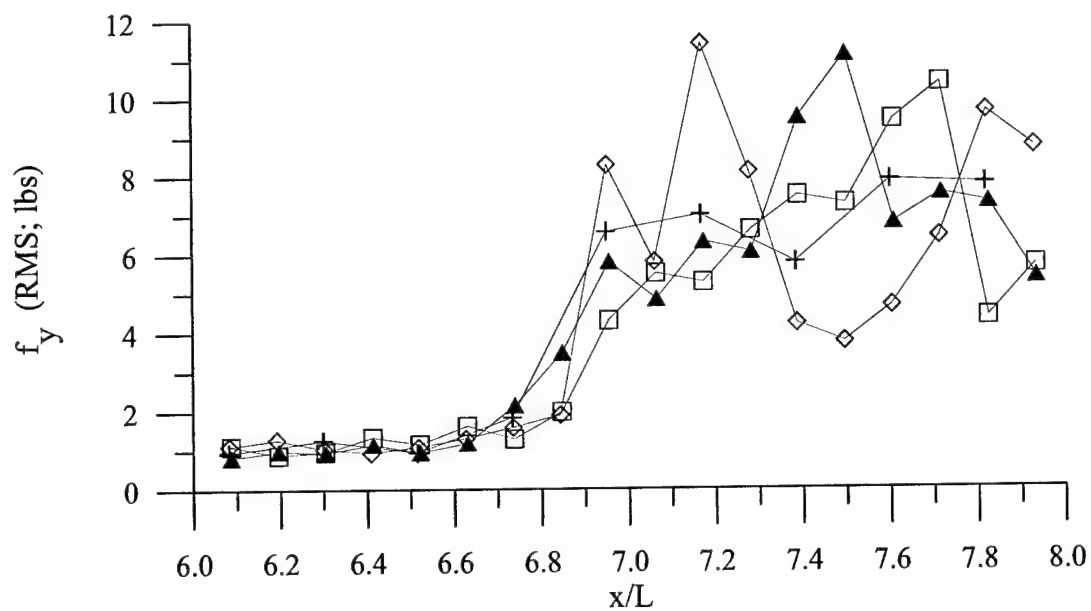
b. Expanded scale

Figure 3.60 RMS propeller side force development for constant tunnel speed, ramped propeller speed simulation of unsteady crashback maneuver, against body position coordinate
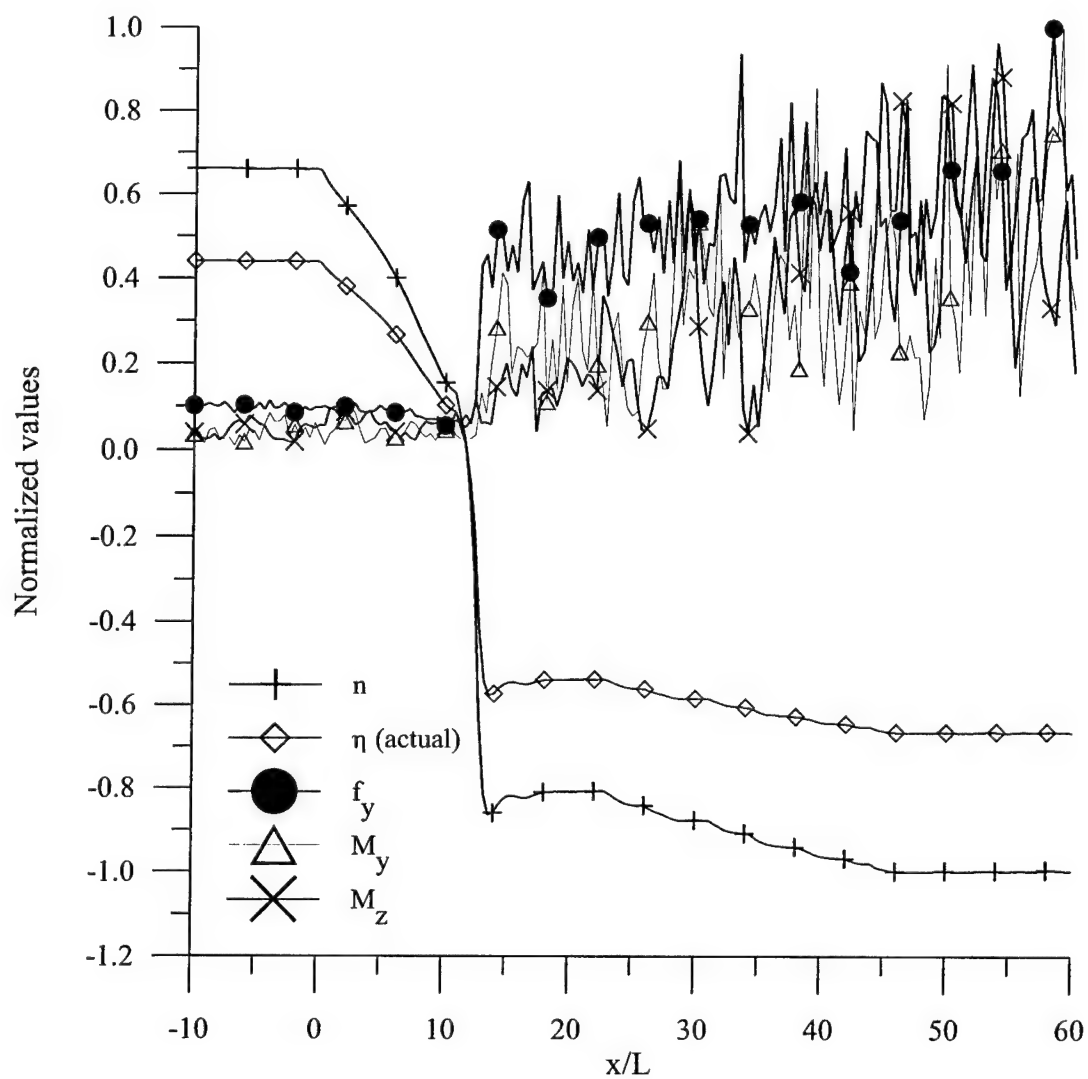
Figure 3.61 Development of RMS propeller y force and RMS body pitching and yawing moments during constant tunnel velocity, ramped propeller speed simulation of unsteady crashback maneuver (run 133; values normalized by maximum data value in each set)
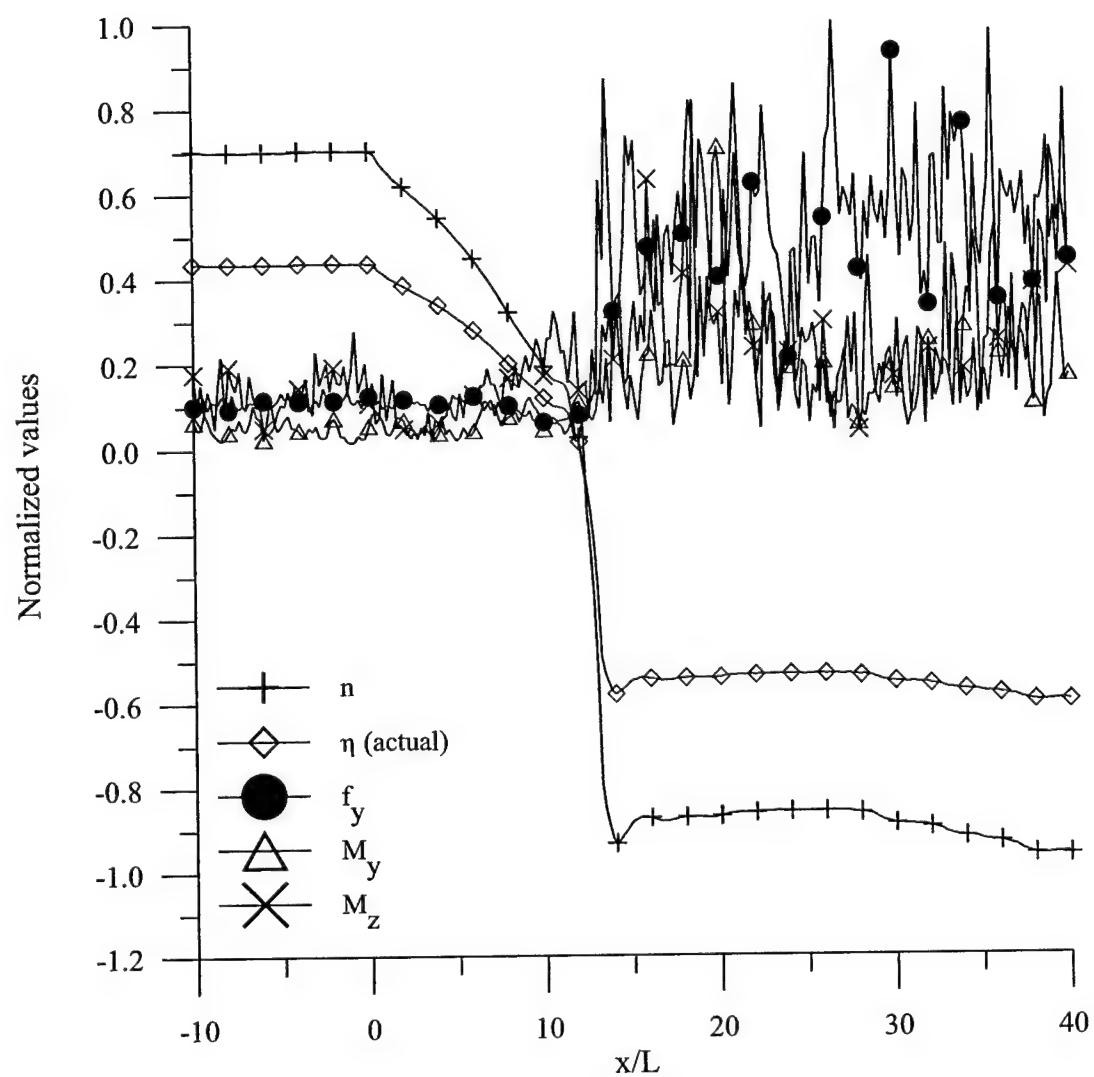
Figure 3.62 Development of RMS propeller y force and RMS body pitching and yawing moments during constant tunnel velocity, ramped propeller speed simulation of unsteady crashback maneuver (run 134; values normalized by maximum data value in each set)
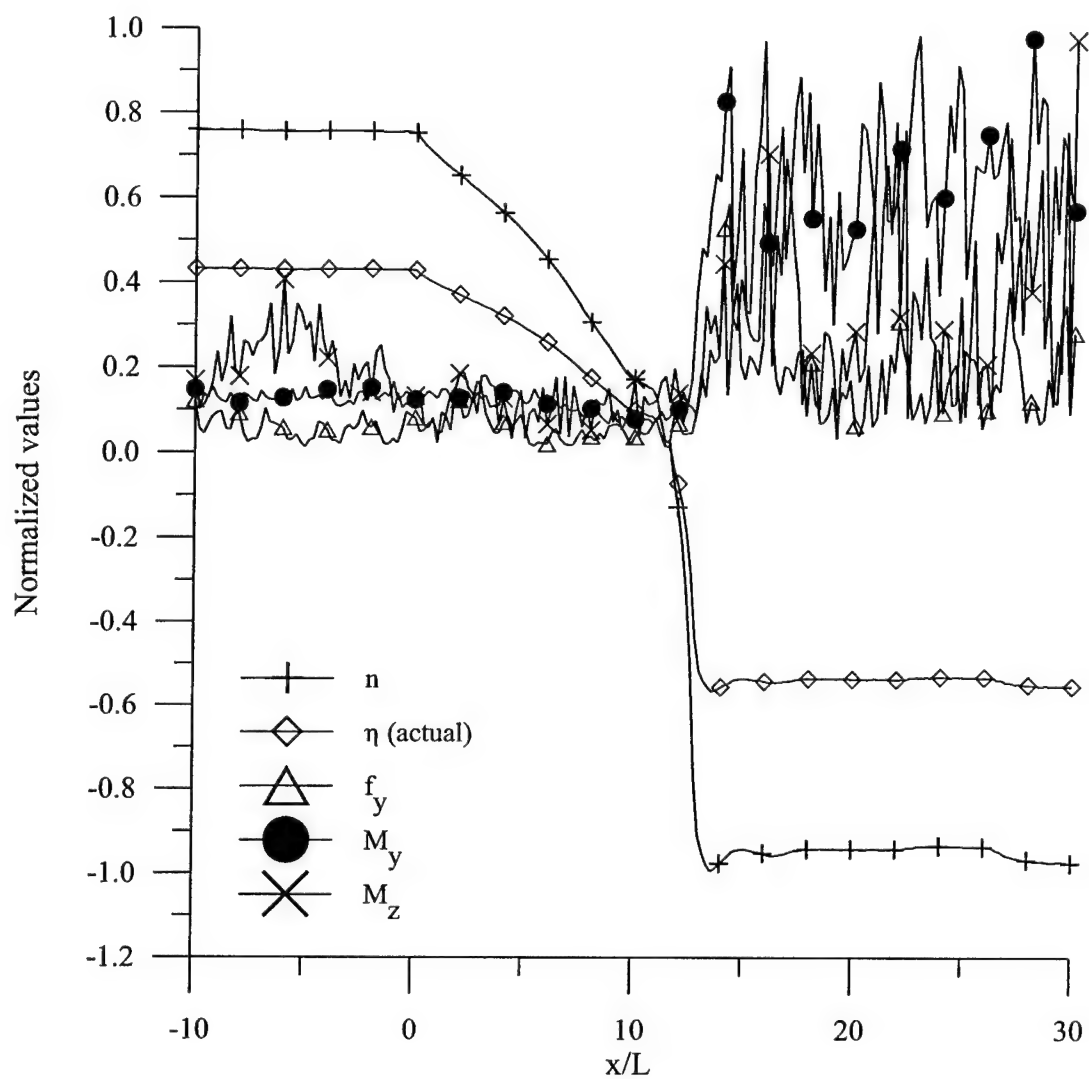
Figure 3.63 Development of RMS propeller y force and RMS body pitching and yawing moments during constant tunnel velocity, ramped propeller speed simulation of unsteady crashback maneuver (run 135; values normalized by maximum data value in each set)
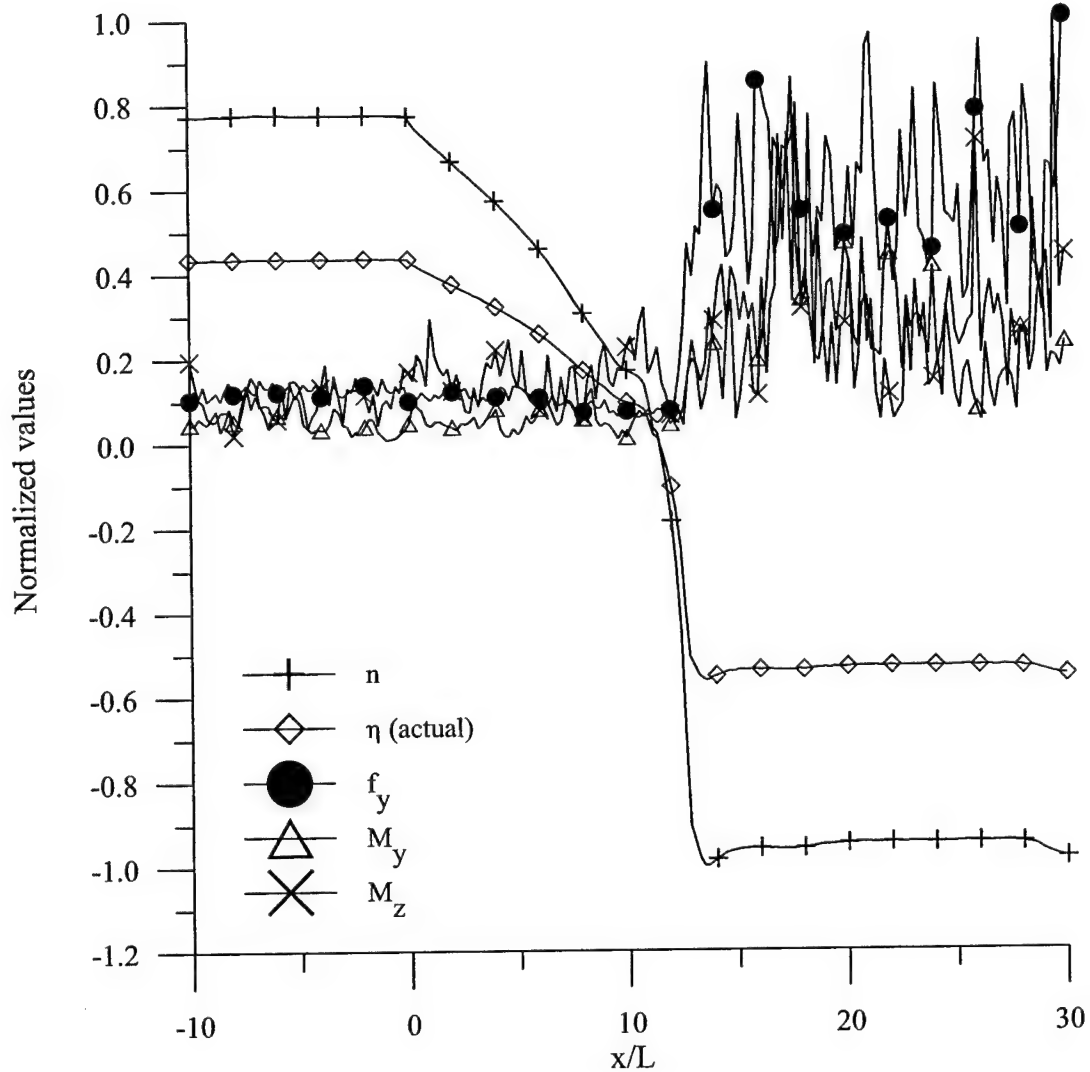
Figure 3.64 Development of RMS propeller y force and RMS body pitching and yawing moments during constant tunnel velocity, ramped propeller speed simulation of unsteady crashback maneuver (run 136; values normalized by maximum data value in each set)
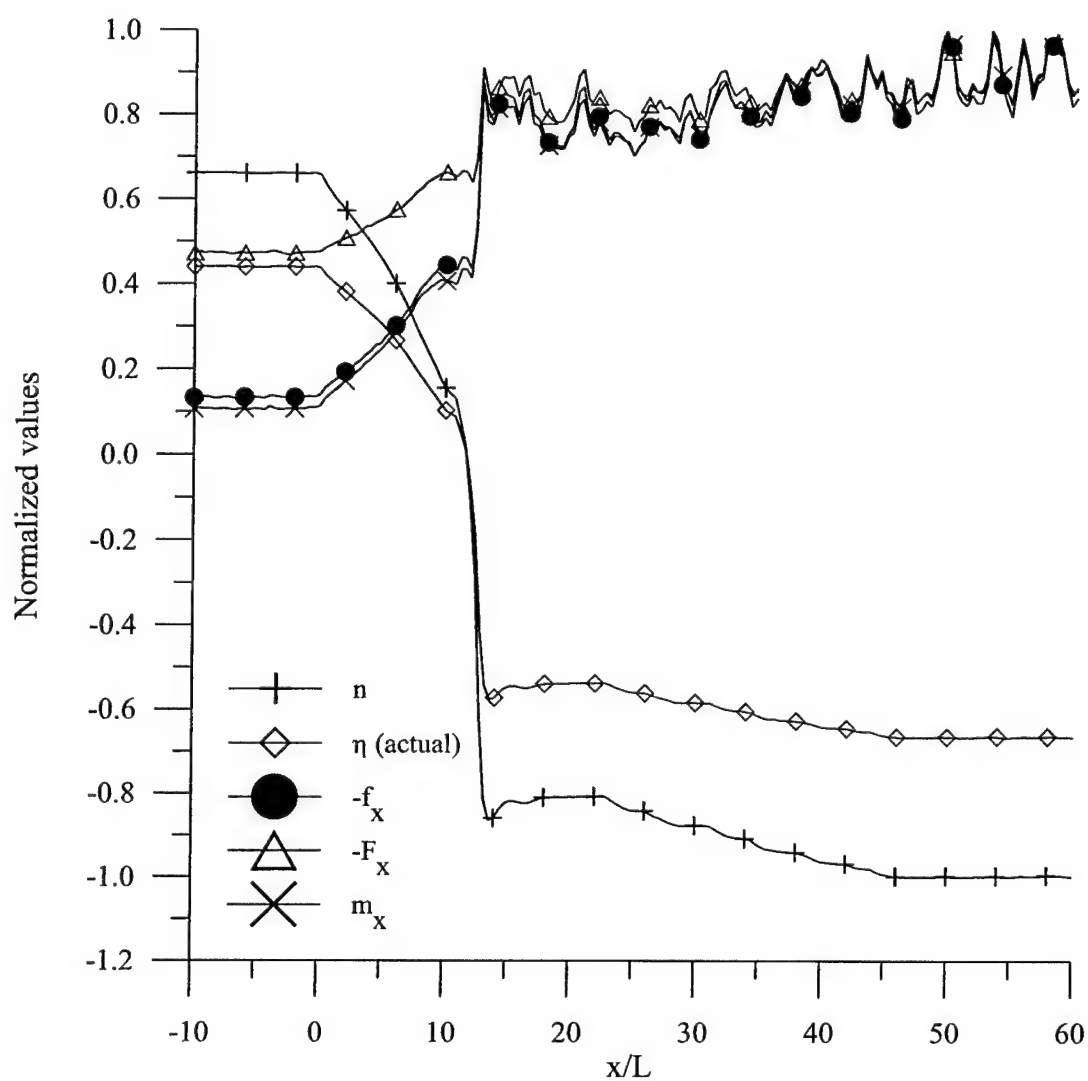
Figure 3.65 Development of RMS propeller axial force, RMS body axial force and RMS propeller axial moment (torque) during constant tunnel velocity, ramped propeller speed simulation of unsteady crashback maneuver (run 133; values normalized by maximum data value in each set)
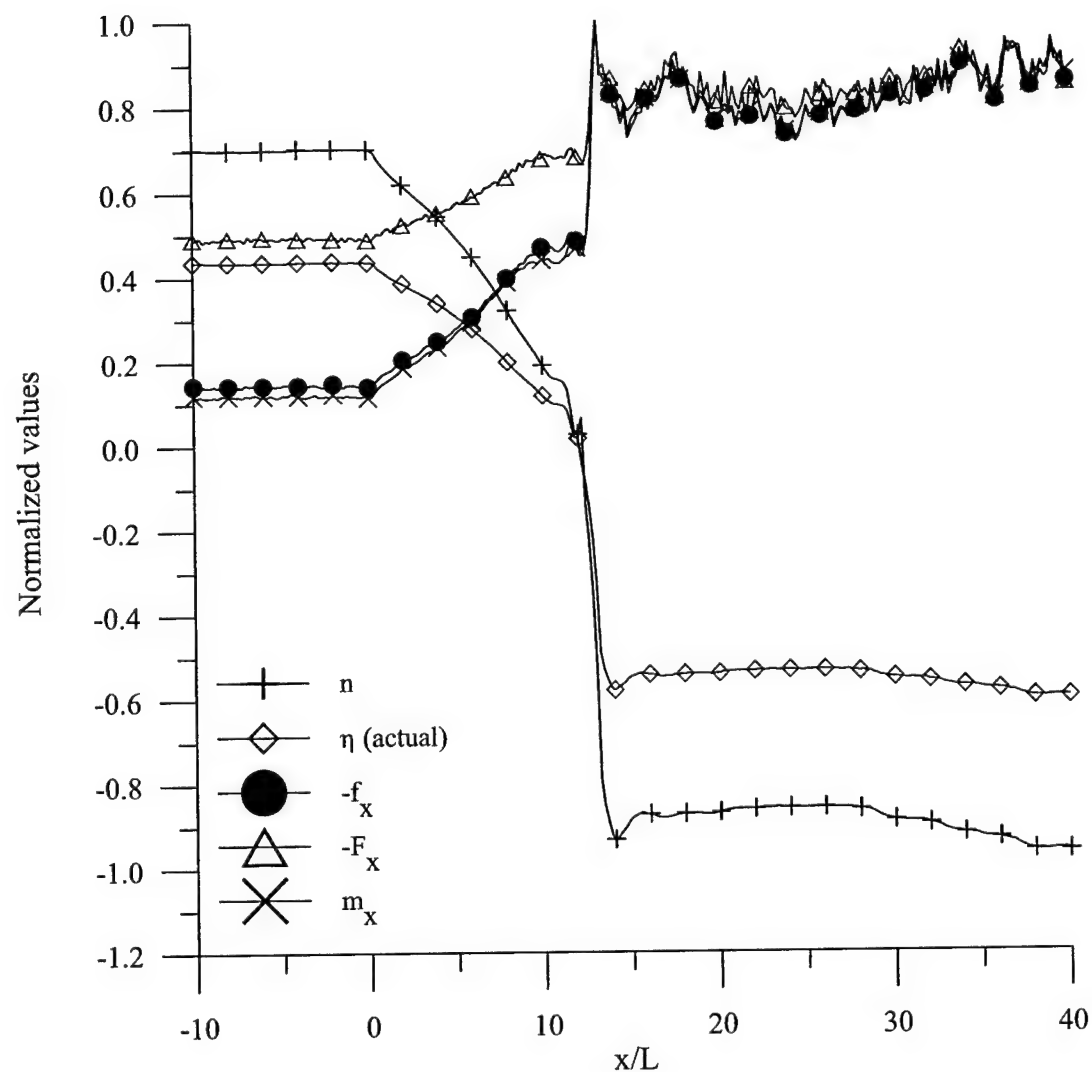
Figure 3.66 Development of RMS propeller axial force, RMS body axial force and RMS propeller axial moment (torque) during constant tunnel velocity, ramped propeller speed simulation of unsteady crashback maneuver (run 134; values normalized by maximum data value in each set)
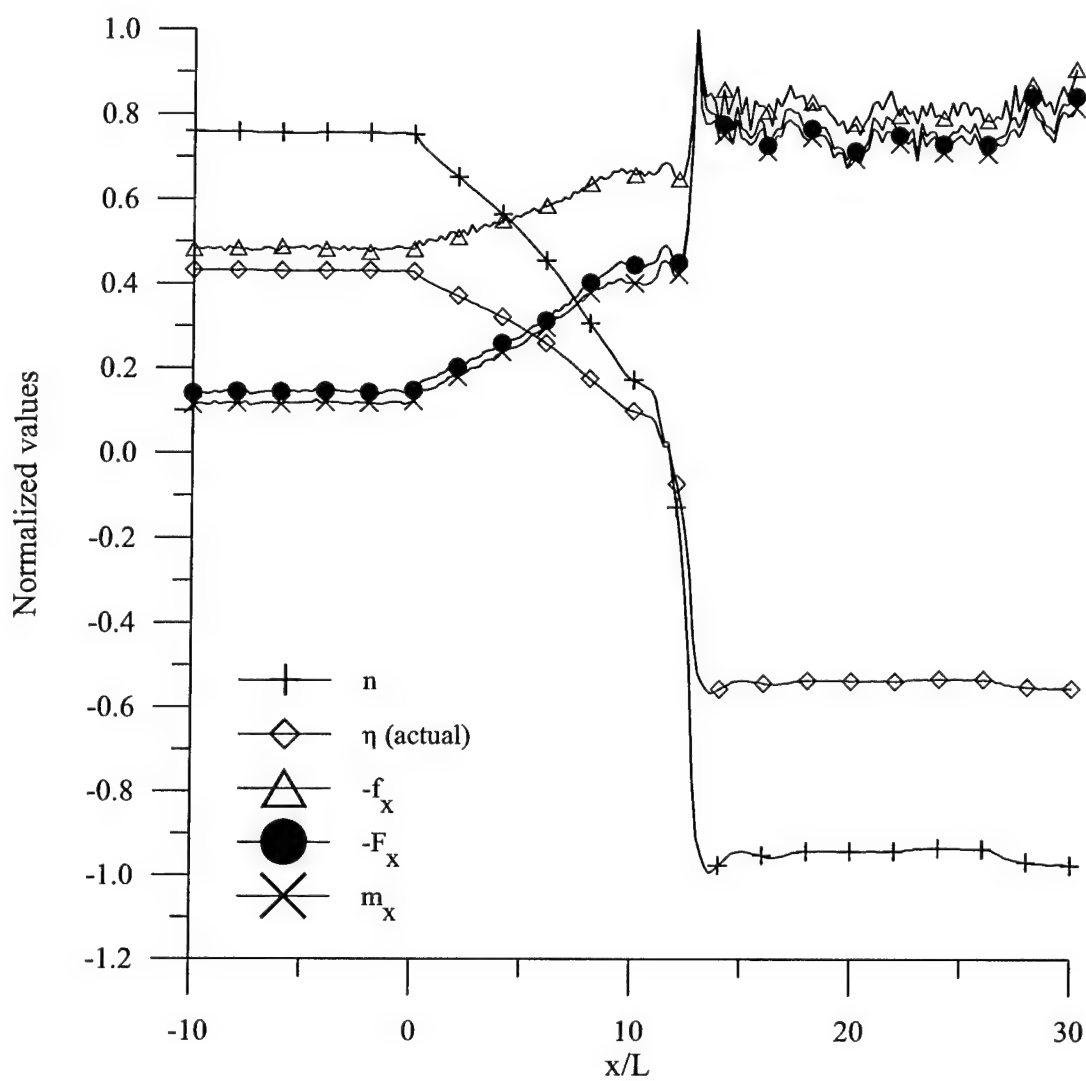
Figure 3.67 Development of RMS propeller axial force, RMS body axial force and RMS propeller axial moment (torque) during constant tunnel velocity, ramped propeller speed simulation of unsteady crashback maneuver (run 135; values normalized by maximum data value in each set)
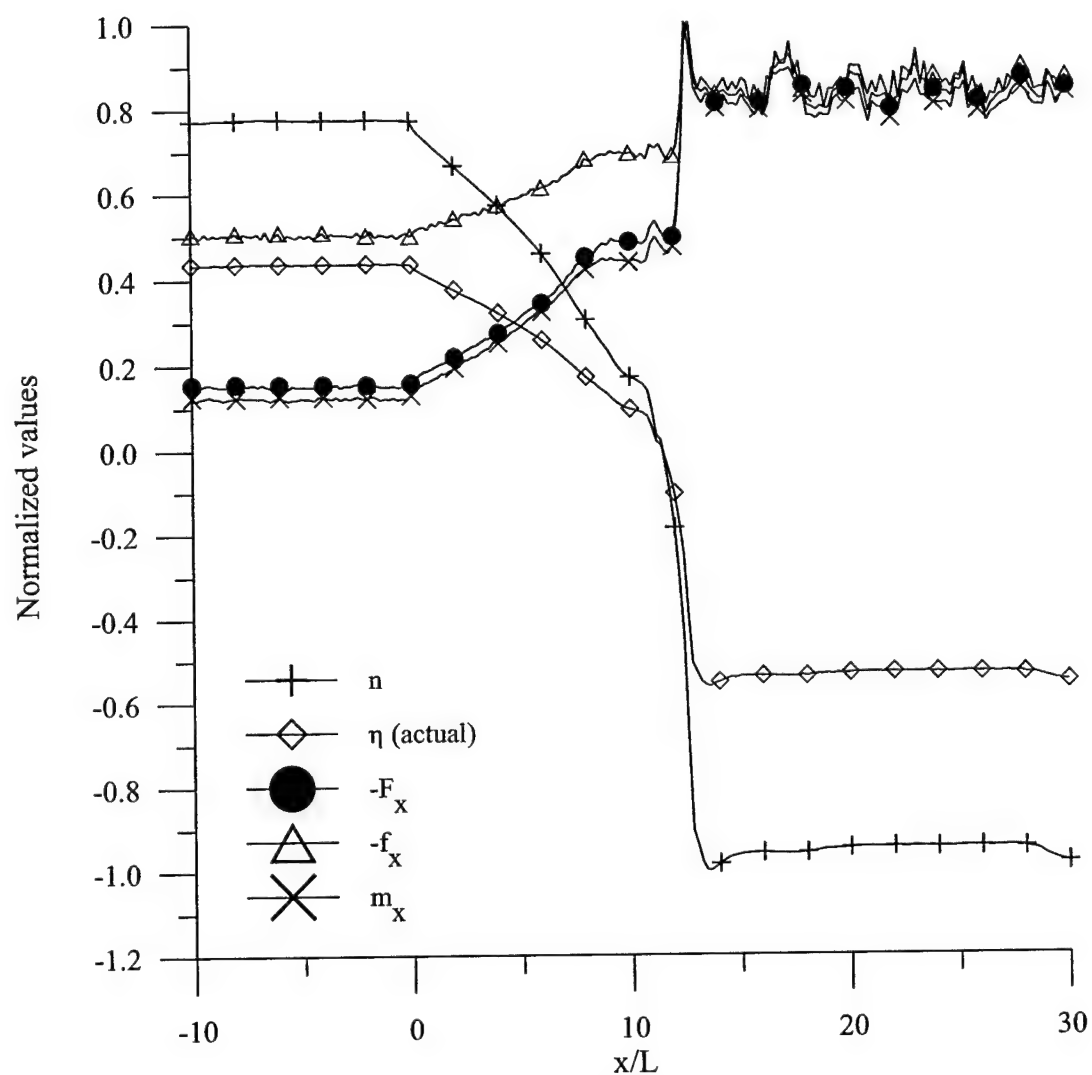
Figure 3.68 Development of RMS propeller axial force, RMS body axial force and RMS propeller axial moment (torque) during constant tunnel velocity, ramped propeller speed simulation of unsteady crashback maneuver (run 136; values normalized by maximum data value in each set)

114
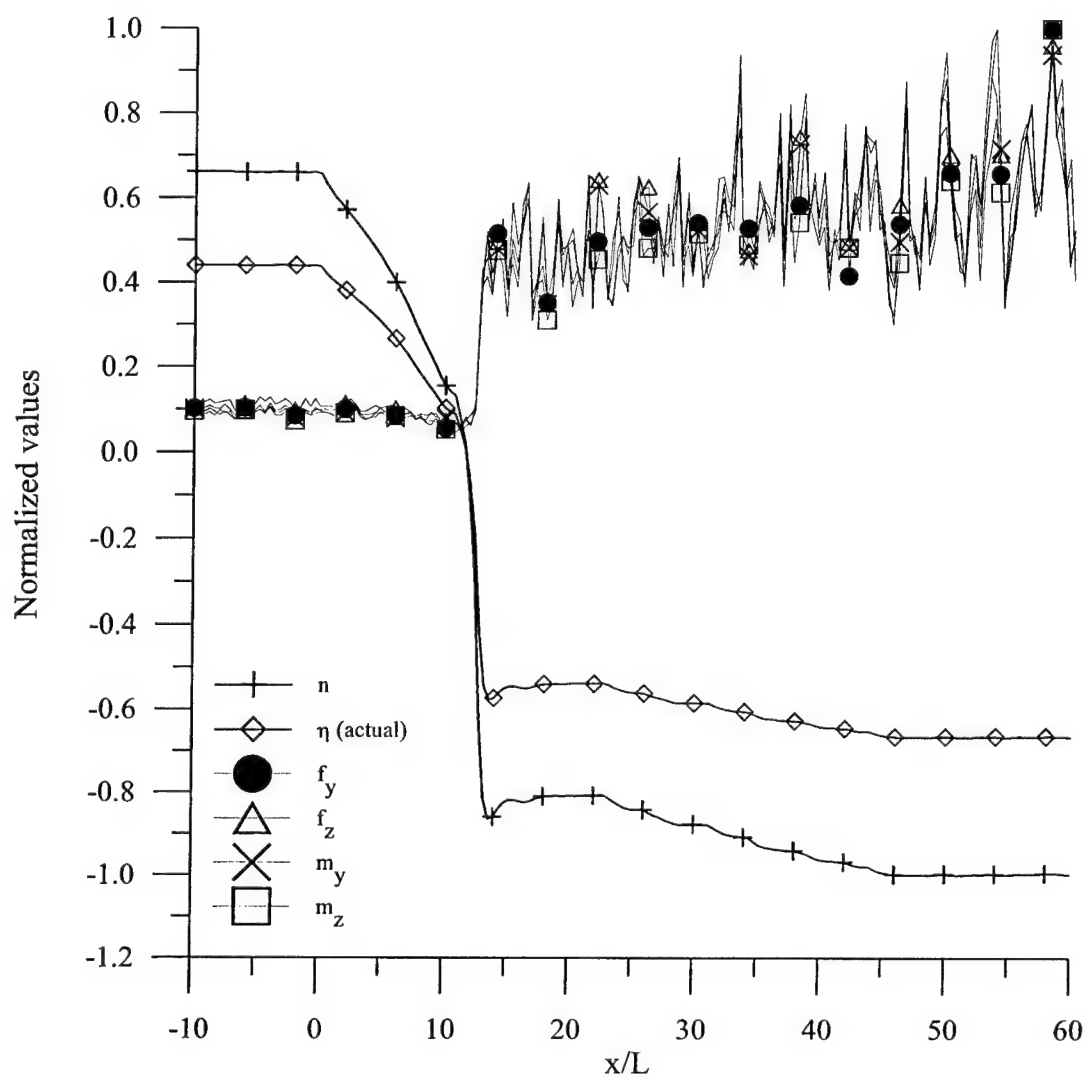
Figure 3.69 Development of RMS propeller off-axis forces and moments during constant tunnel velocity, ramped propeller speed simulation of unsteady crashback maneuver (run 133; values normalized by maximum data value in each set)
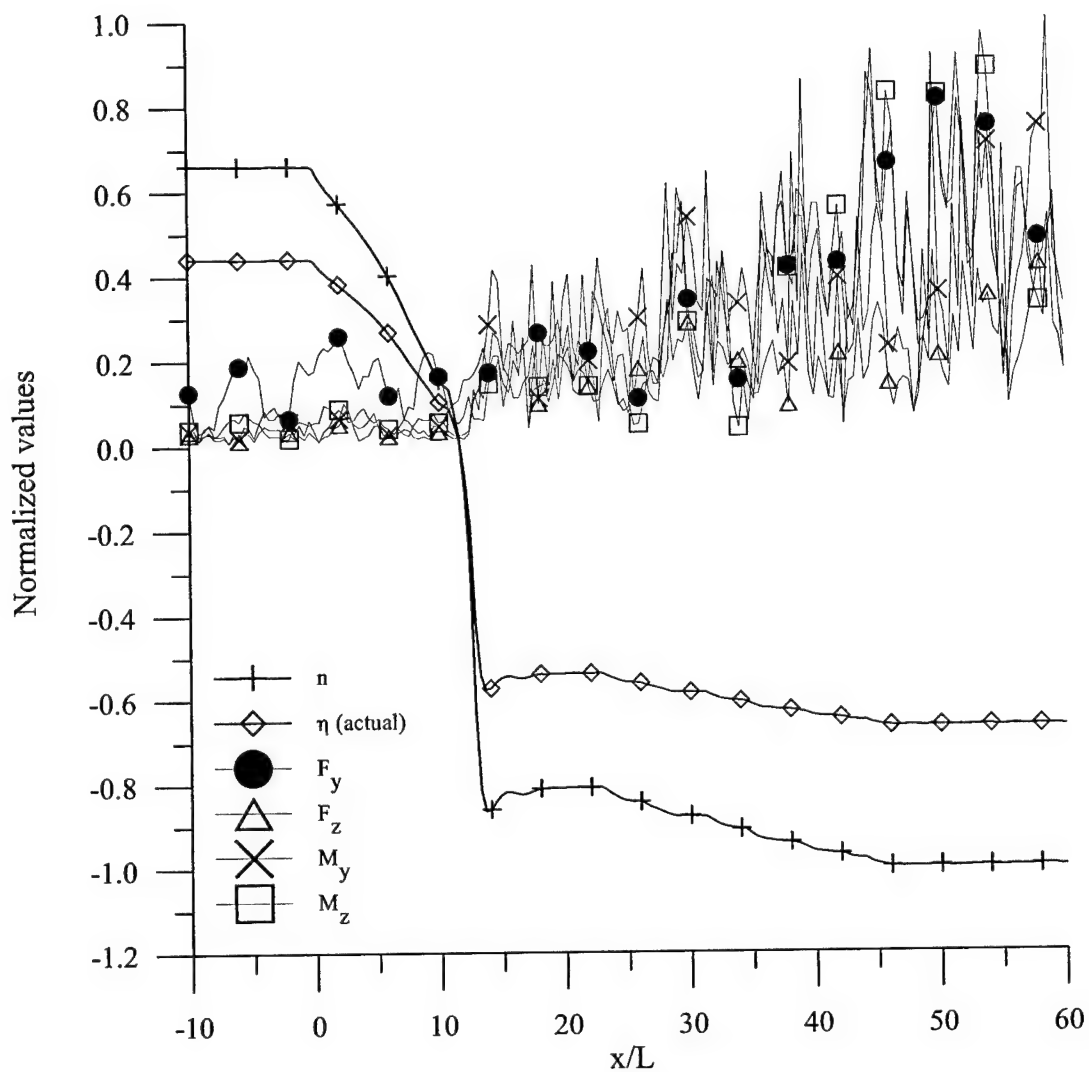
Figure 3.70 Development of RMS body off-axis forces and moments during constant tunnel velocity, ramped propeller speed simulation of unsteady crashback maneuver (run 133; values normalized by maximum data value in each set)
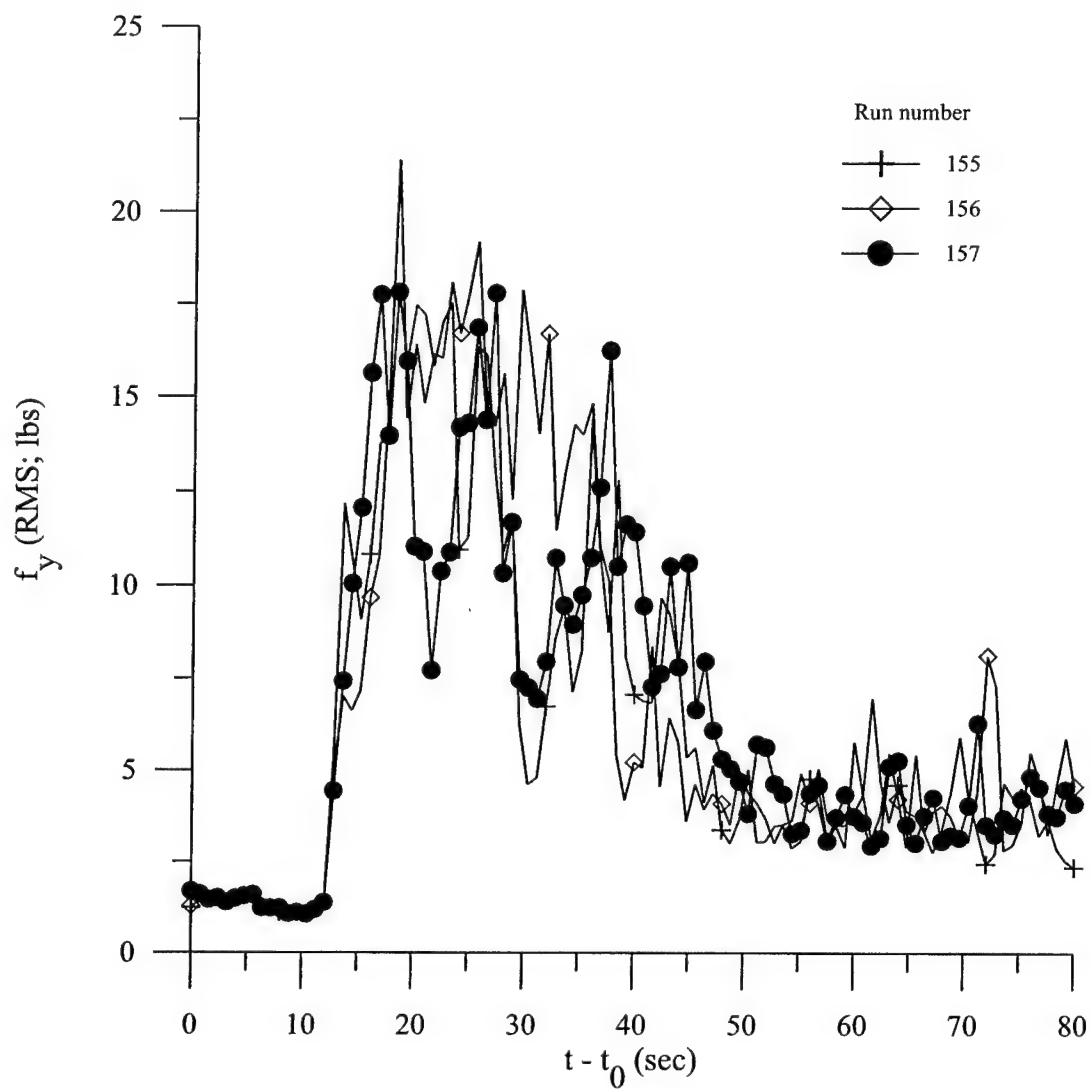
Figure 3.71 Development of RMS propeller *y* force during ramped tunnel velocity, ramped propeller speed simulation of unsteady crashback maneuver, against time
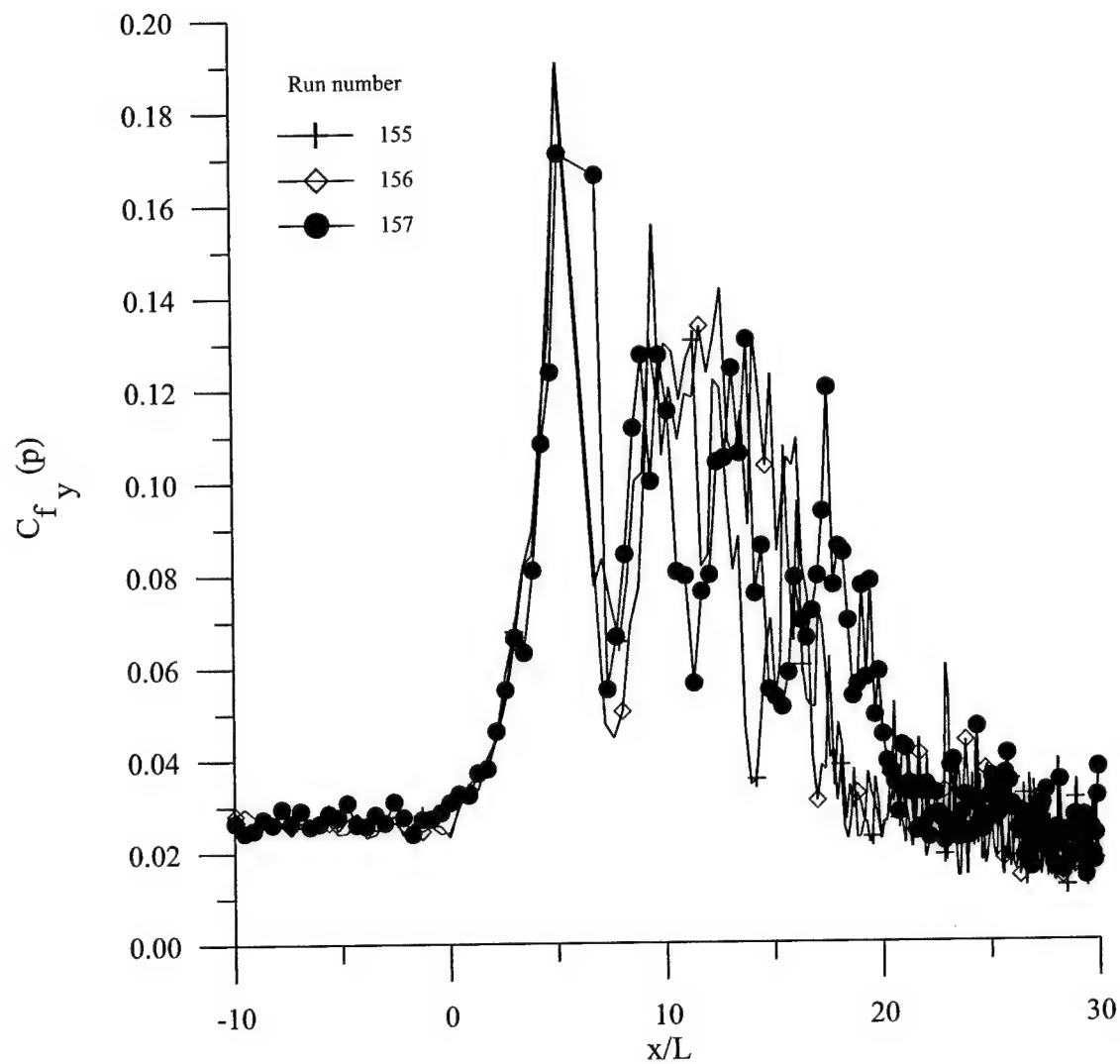
Figure 3.72 Development of coefficient of propeller *y* force during ramped tunnel velocity, ramped propeller speed simulation of unsteady crashback maneuver ("p" - propulsive scaling)
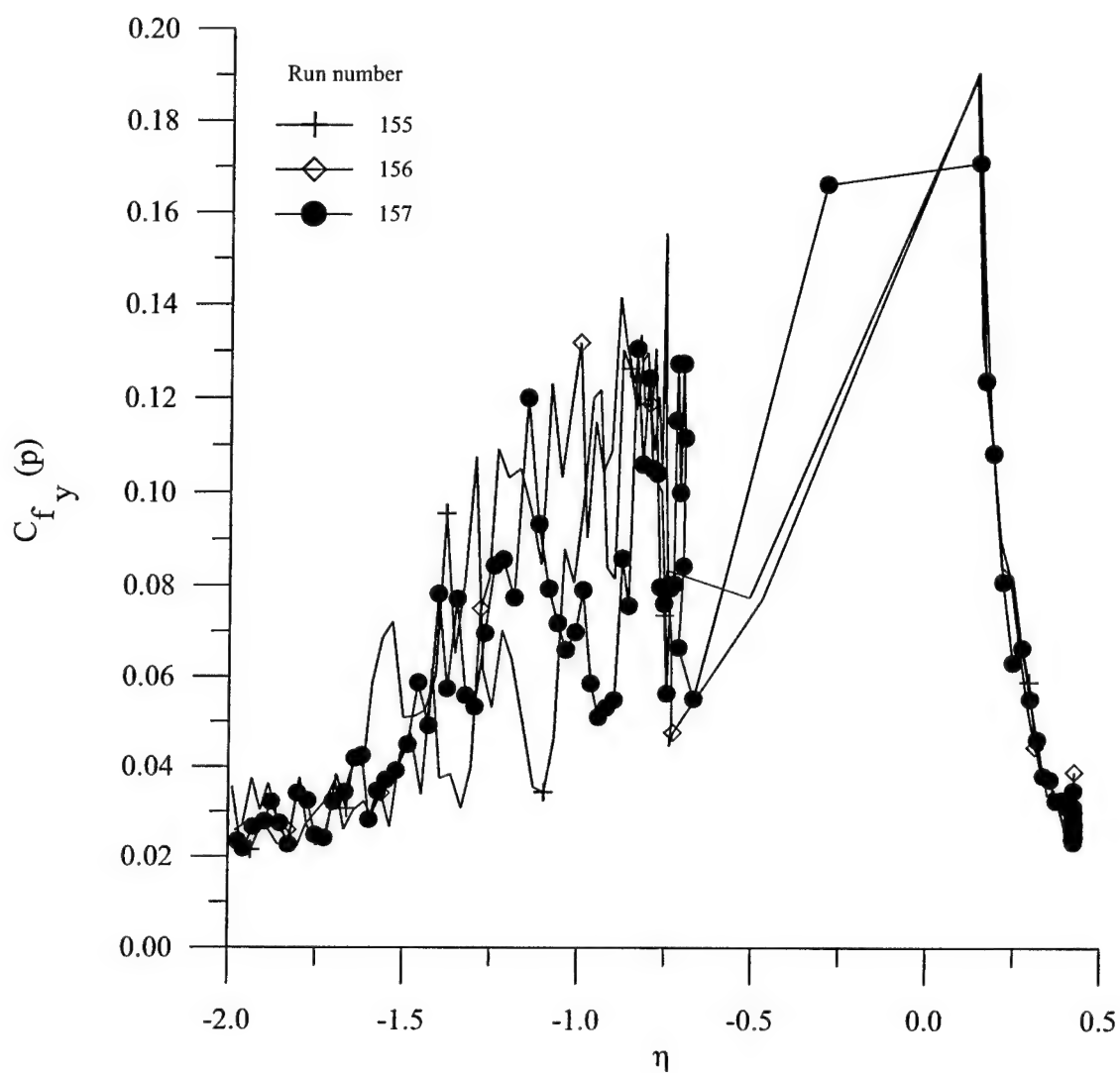
Figure 3.73 Coefficient of RMS propeller *y* force coefficient against instantaneous values of η during ramped tunnel velocity, ramped propeller speed simulation of unsteady crashback maneuver ("p" - propulsive scaling)
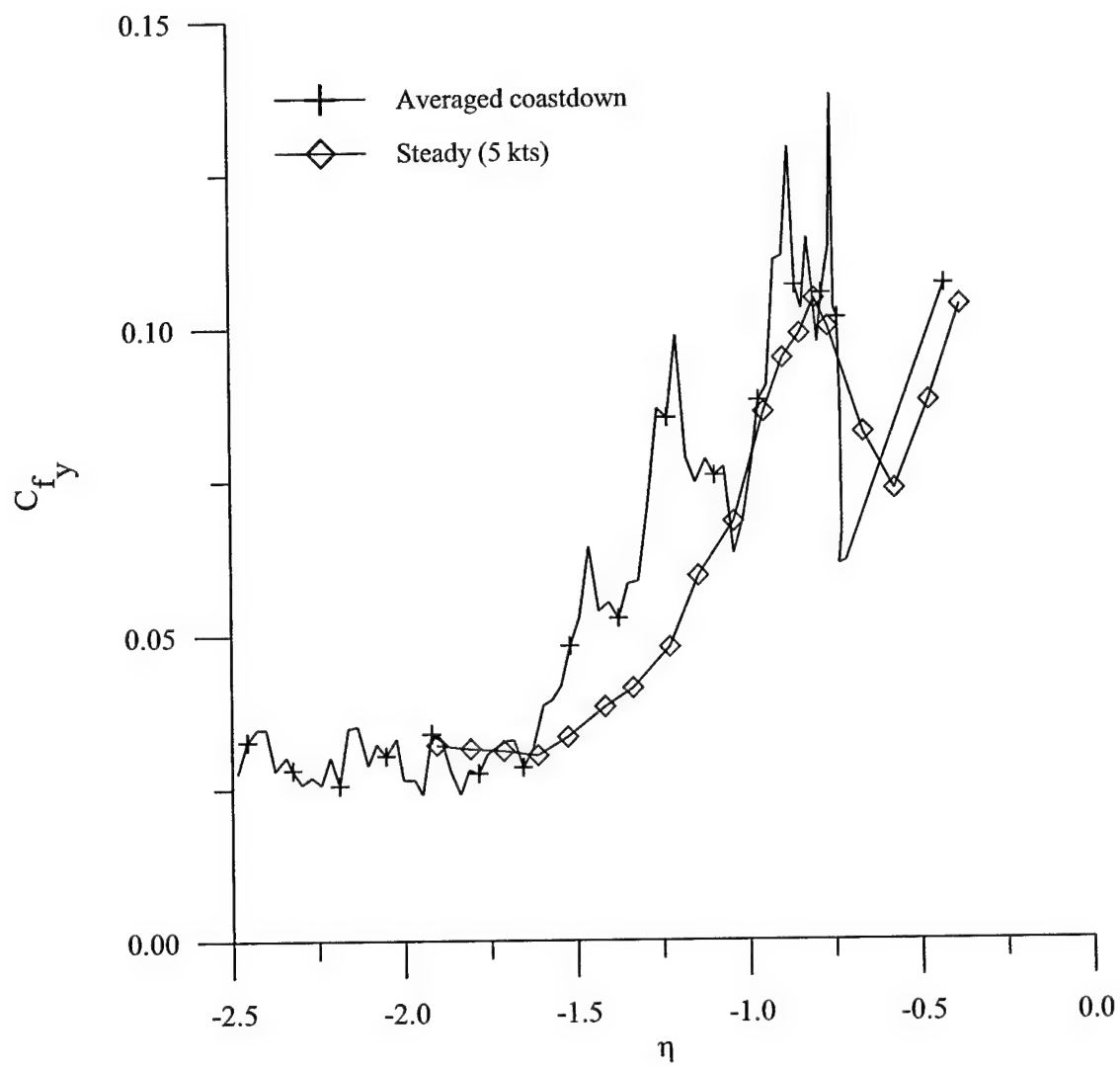
Figure 3.74 Comparison of coefficients of RMS propeller y force between steady crashback conditions and the averaged values of the three ramped tunnel velocity, ramped propeller speed simulations of the unsteady crashback maneuver
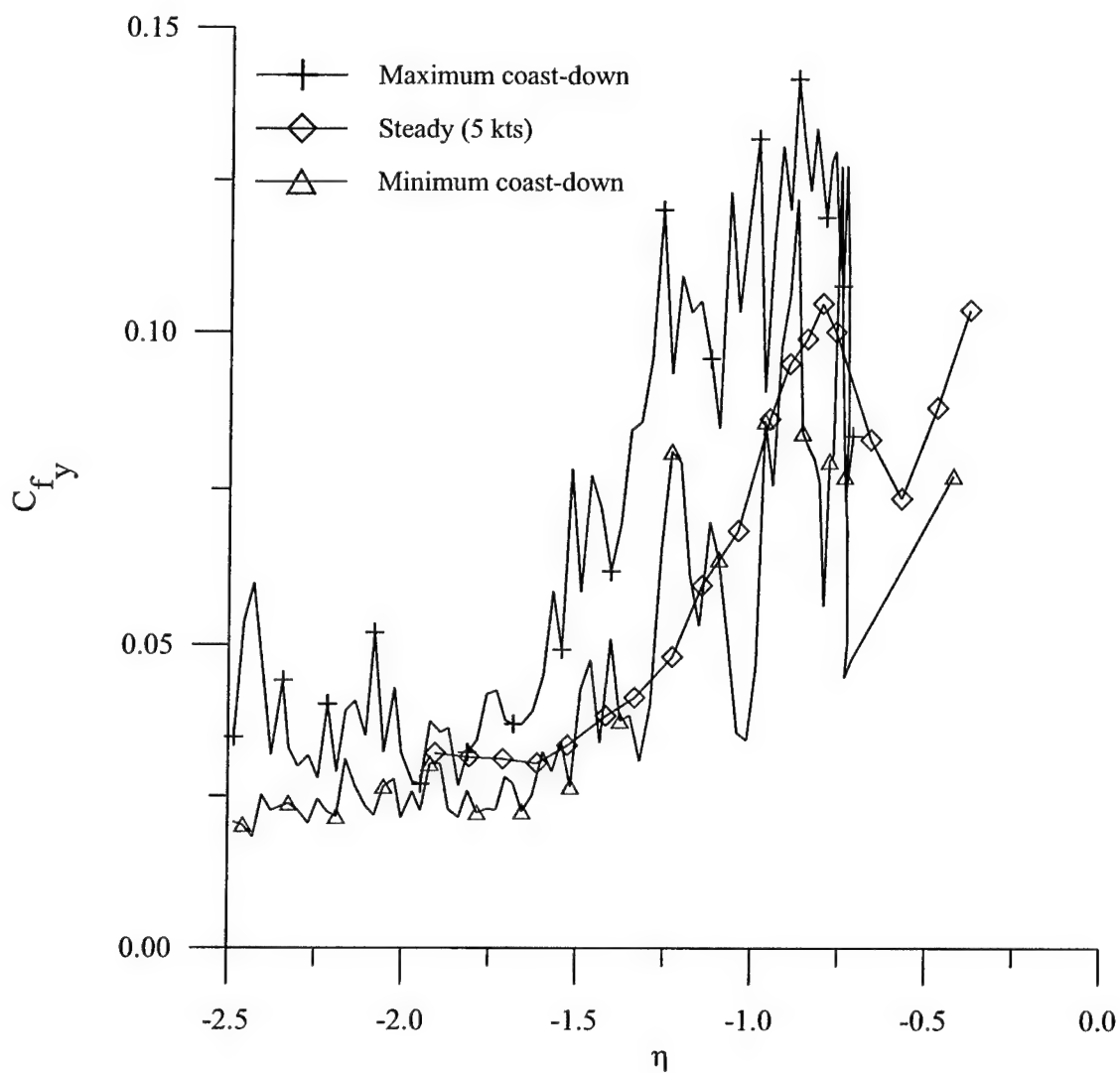
Figure 3.75 Comparison of coefficients of RMS propeller *y* force between steady crashback conditions and the minimum and maximum values of the three ramped tunnel velocity, ramped propeller speed simulations of the unsteady crashback maneuver
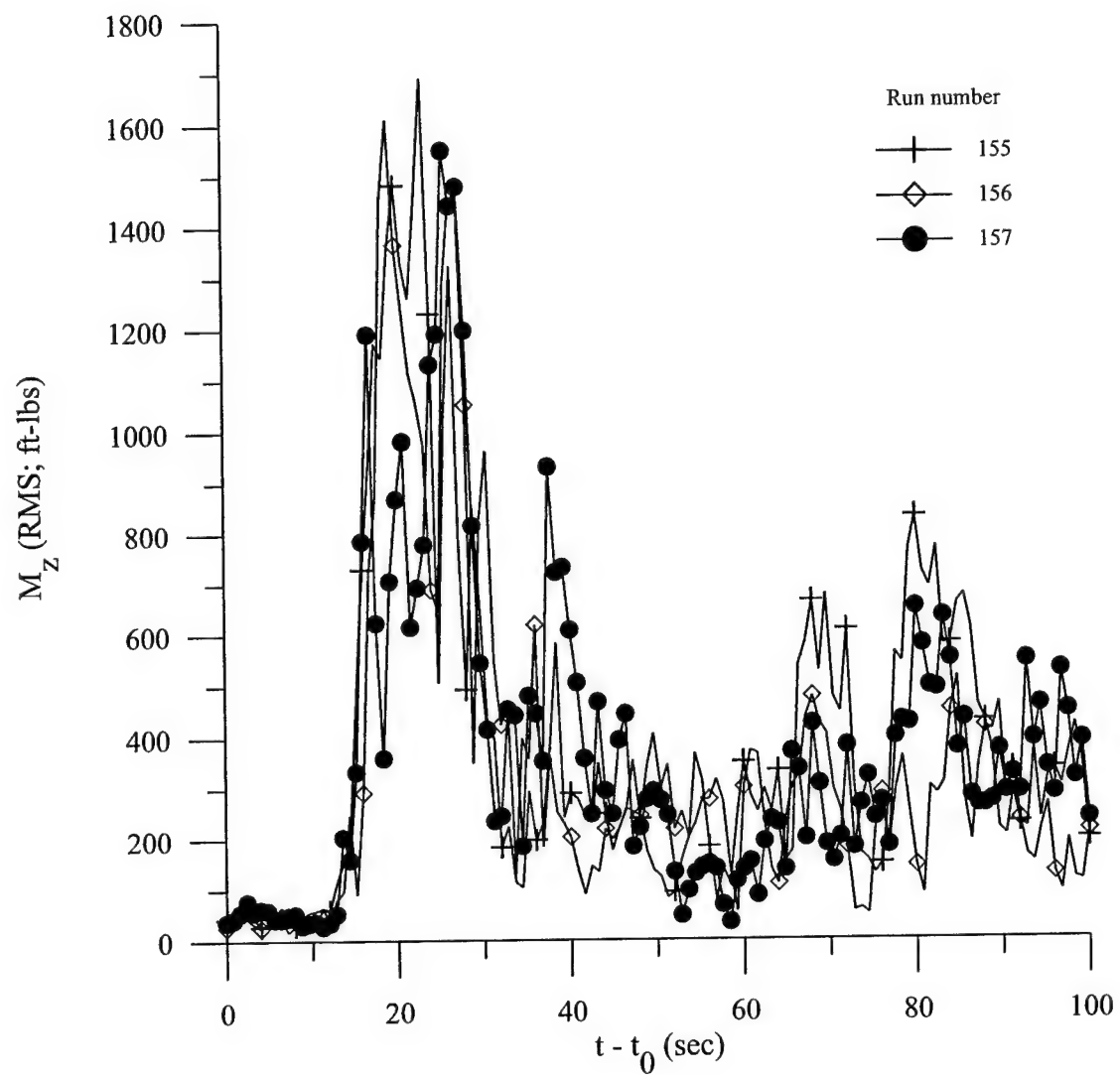
Figure 3.76 Development of the RMS body yawing moment during the ramped tunnel velocity, ramped propeller speed simulations of the unsteady crashback maneuver
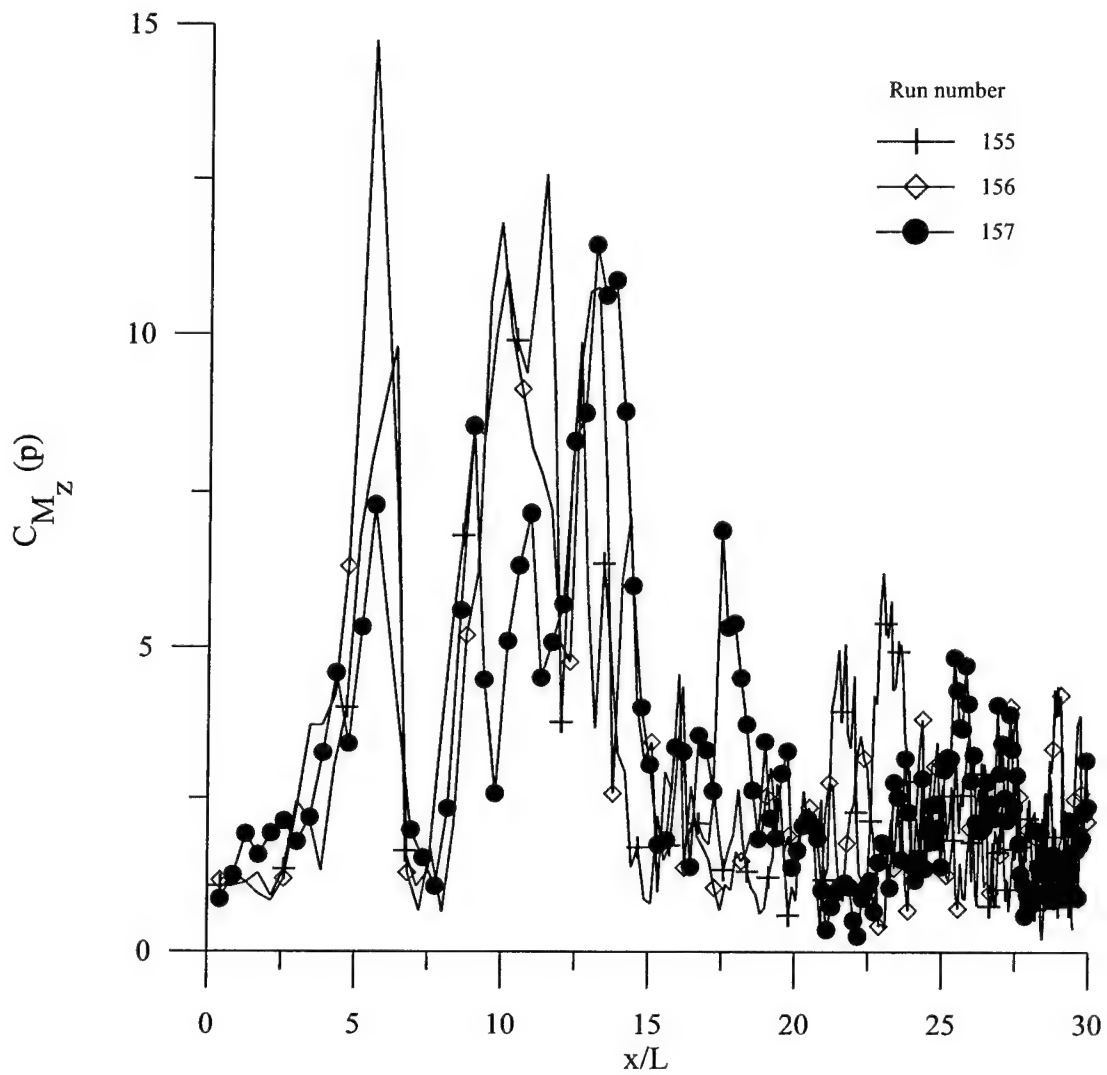
Figure 3.77 Development of the coefficient of RMS body yawing moment during the ramped tunnel velocity, ramped propeller speed simulations of the unsteady crashback maneuver ("p" - propulsive scaling)
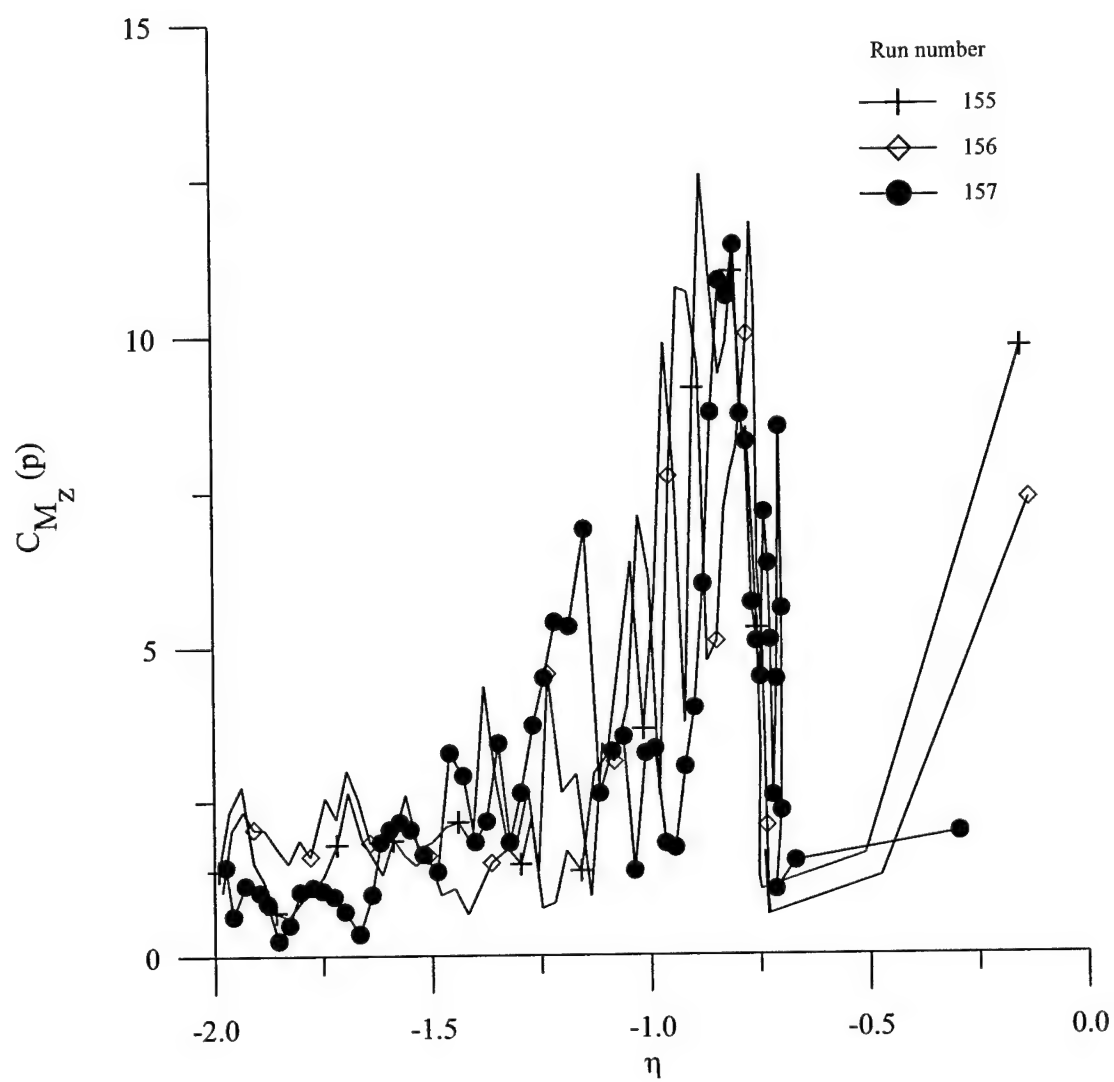
Figure 3.78 Coefficient of RMS body yawing moment coefficient against instantaneous values of η during ramped tunnel velocity, ramped propeller speed simulation of unsteady crashback maneuver ("p" - propulsive scaling)
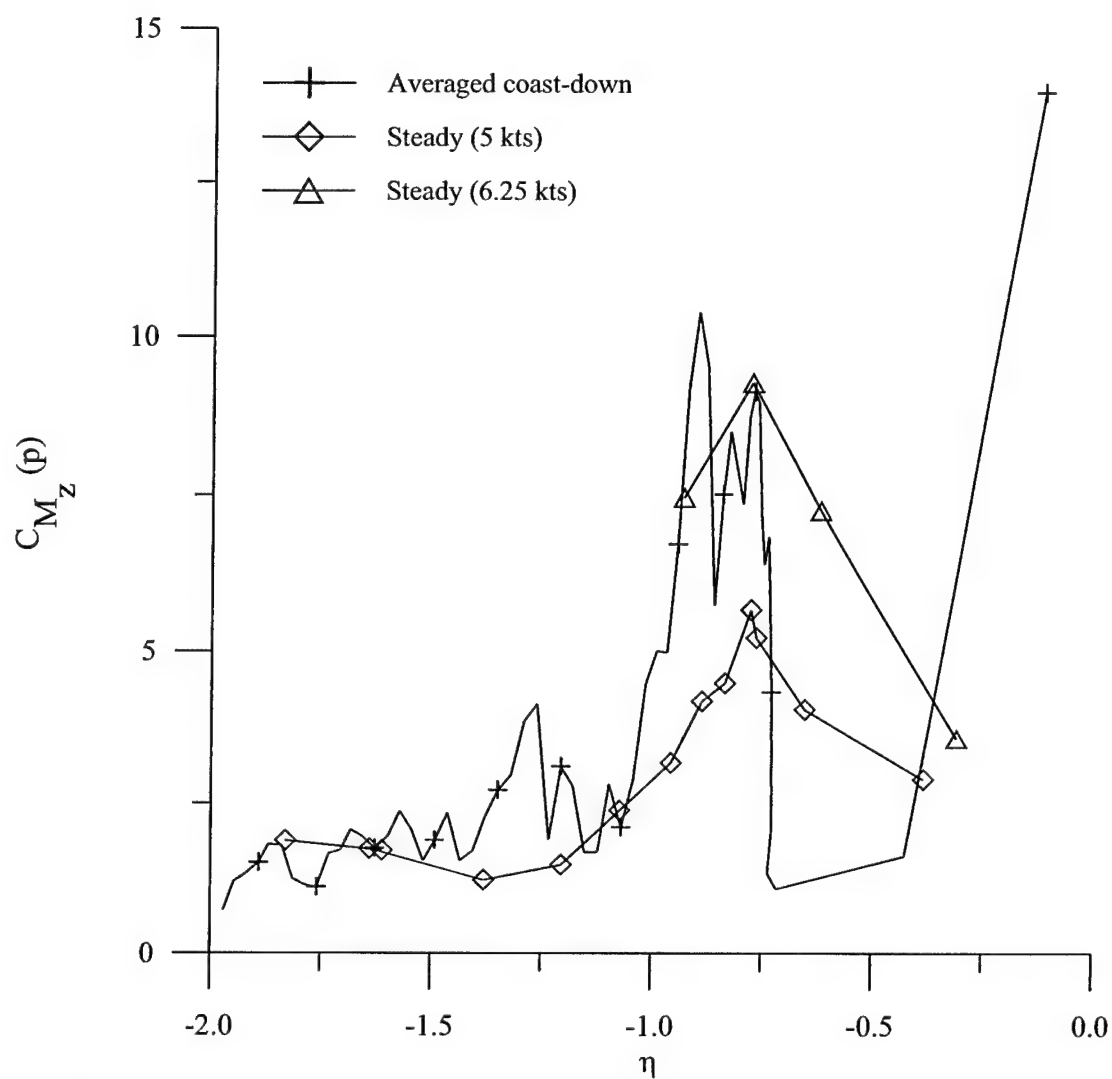
Figure 3.79 Comparison of coefficients of RMS yawing moment between steady crashback conditions and the averaged values of the three ramped tunnel velocity, ramped propeller speed simulations of the unsteady crashback maneuver
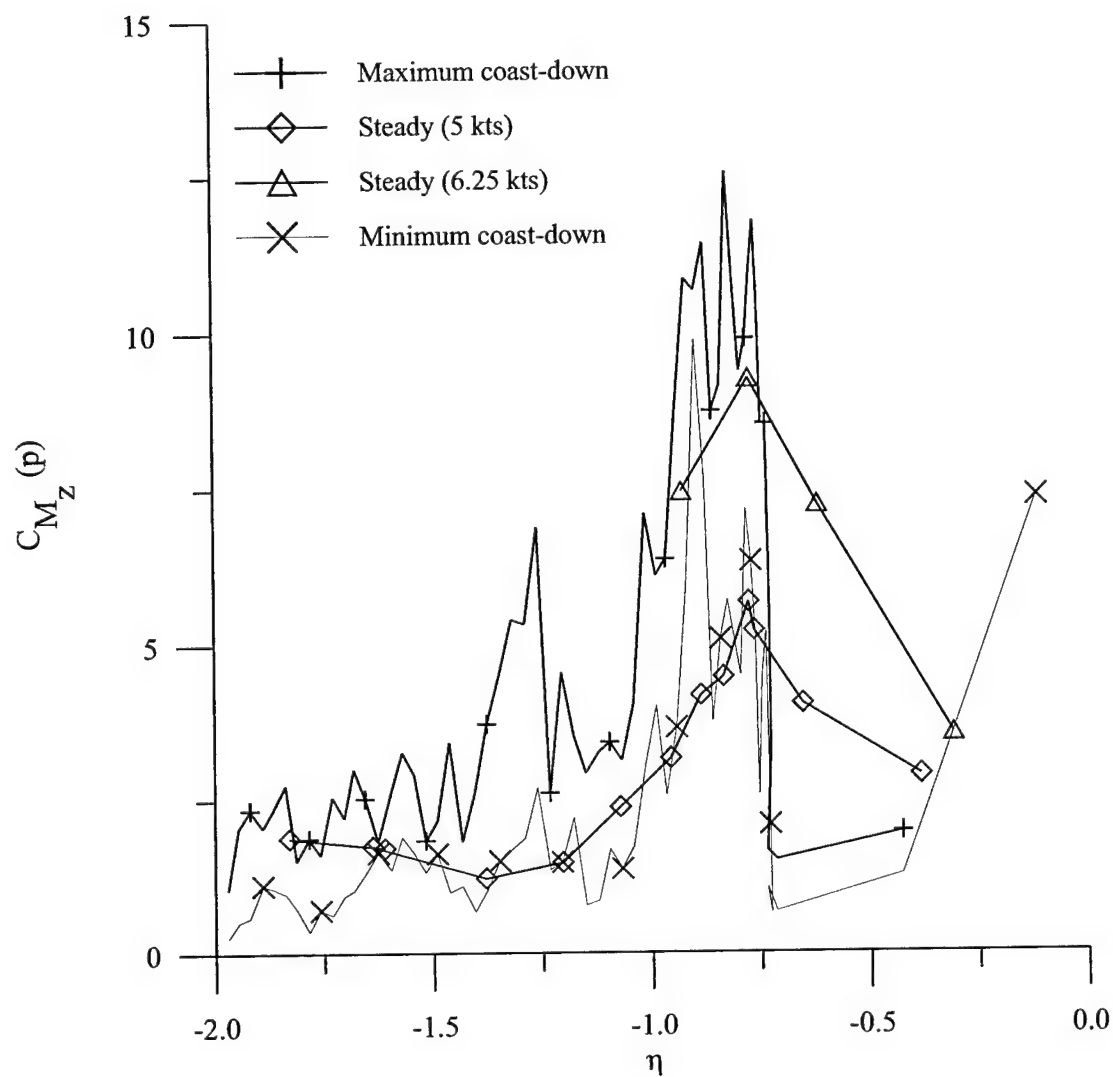
Figure 3.80 Comparison of coefficients of RMS body yawing moment between steady crashback conditions and the minimum and maximum values of the three ramped tunnel velocity, ramped propeller speed simulations of the unsteady crashback maneuver

126
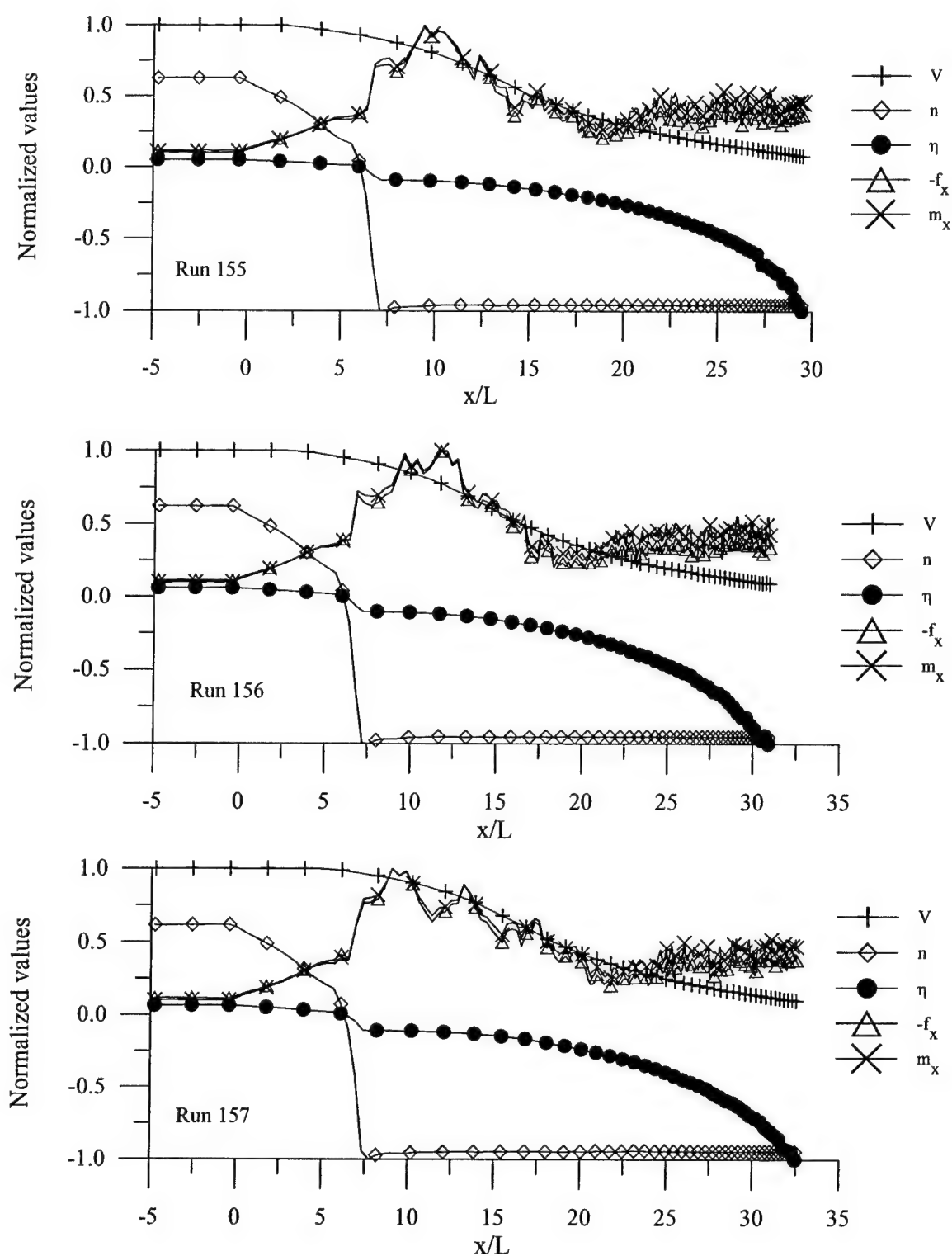
Figure 3.81 Development of RMS propeller axial force and moment during unsteady crashback maneuver simulation (extended data stream)
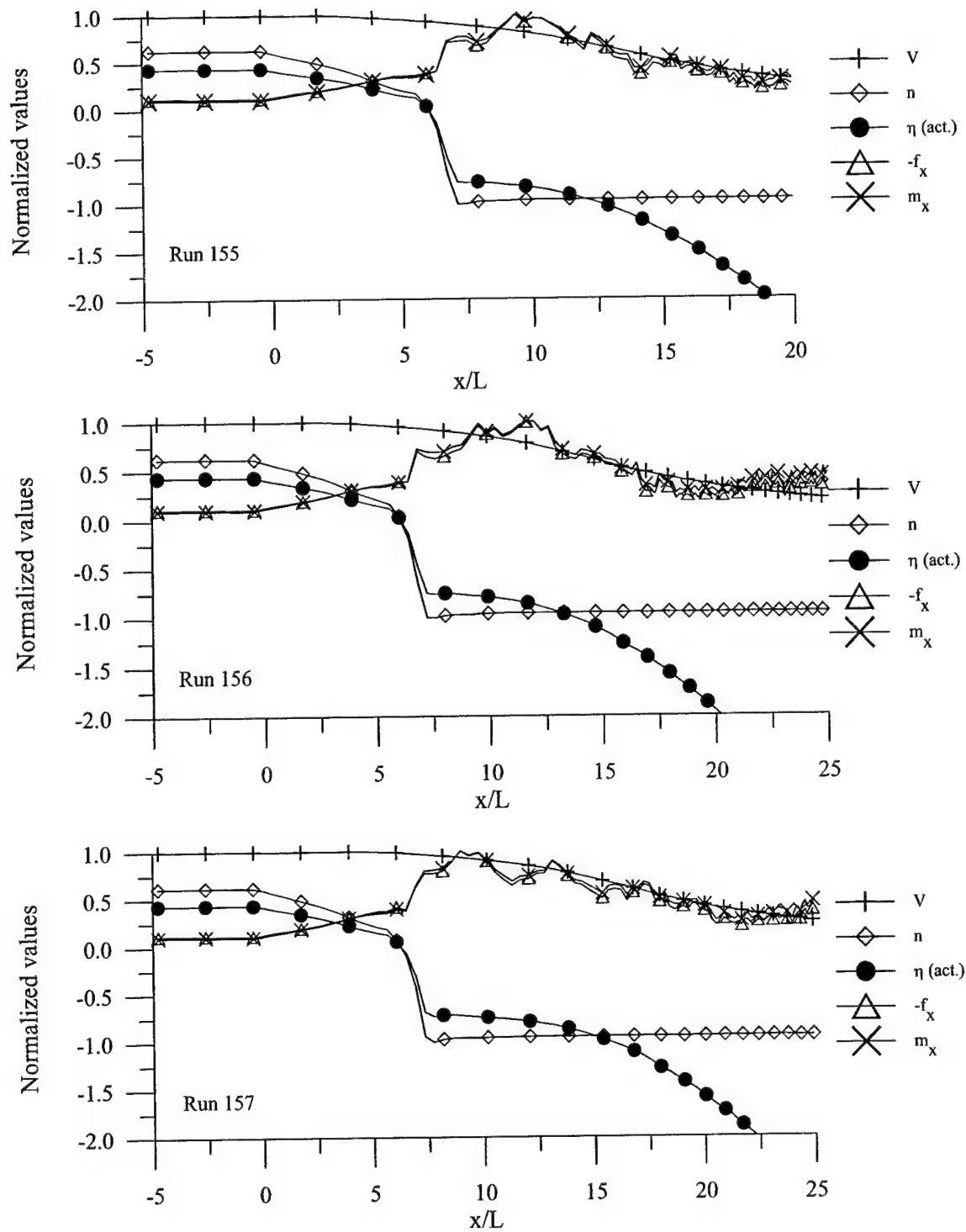
Figure 3.81 (continued) Expanded scale

128
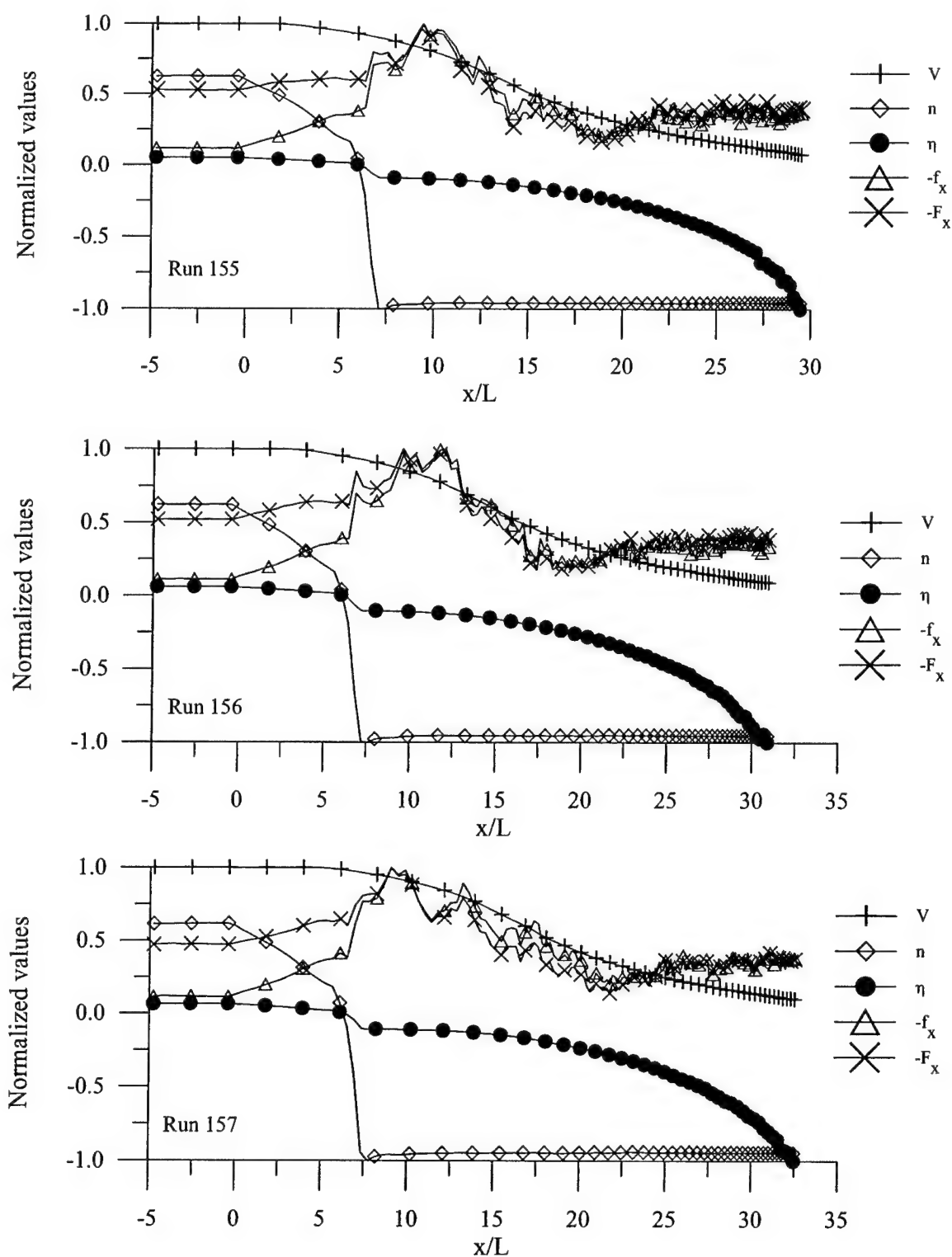
Figure 3.82 Development of RMS body axial force and moment during unsteady crashback maneuver simulation (extended data stream)
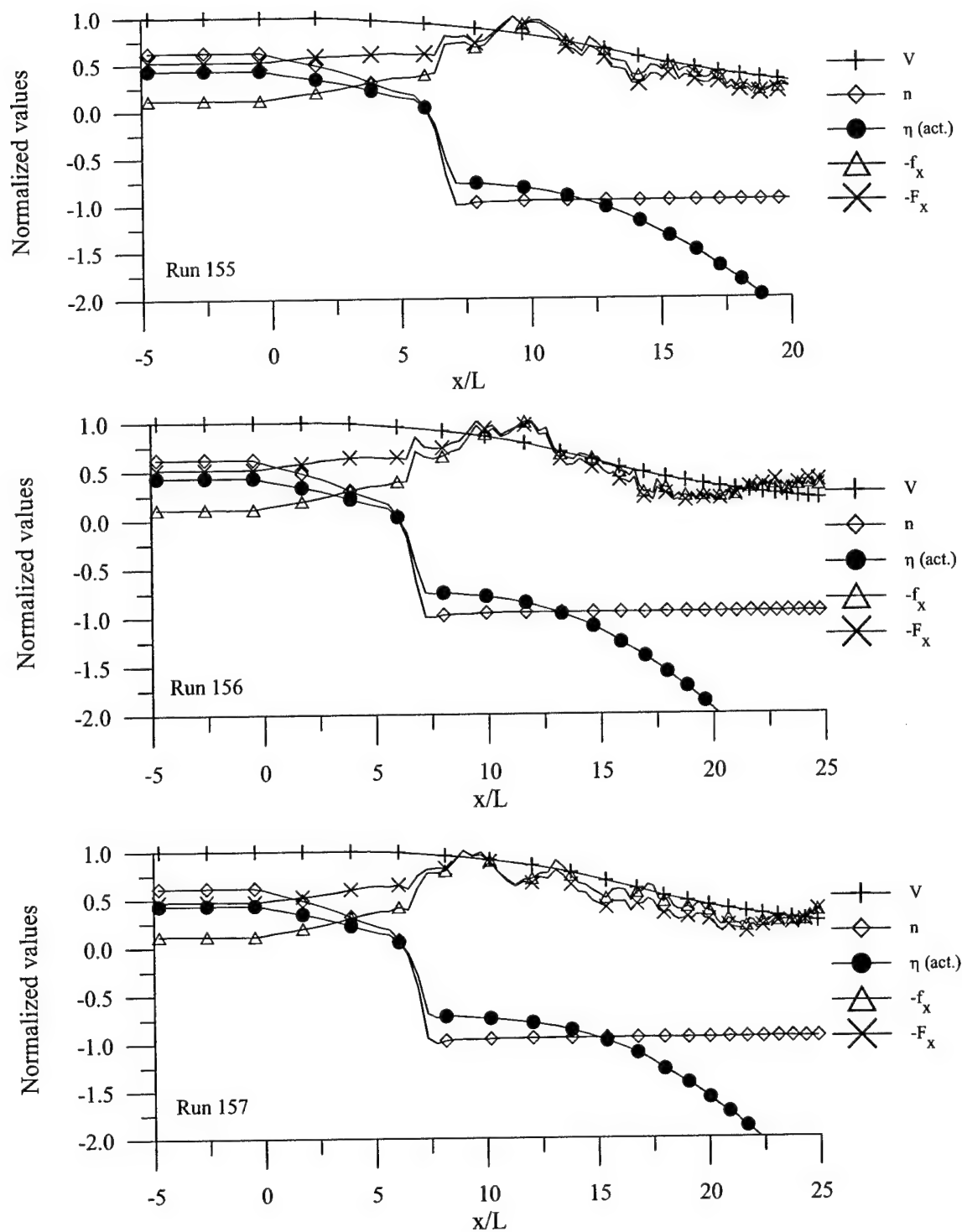
Figure 3.82 (continued) Expanded scale
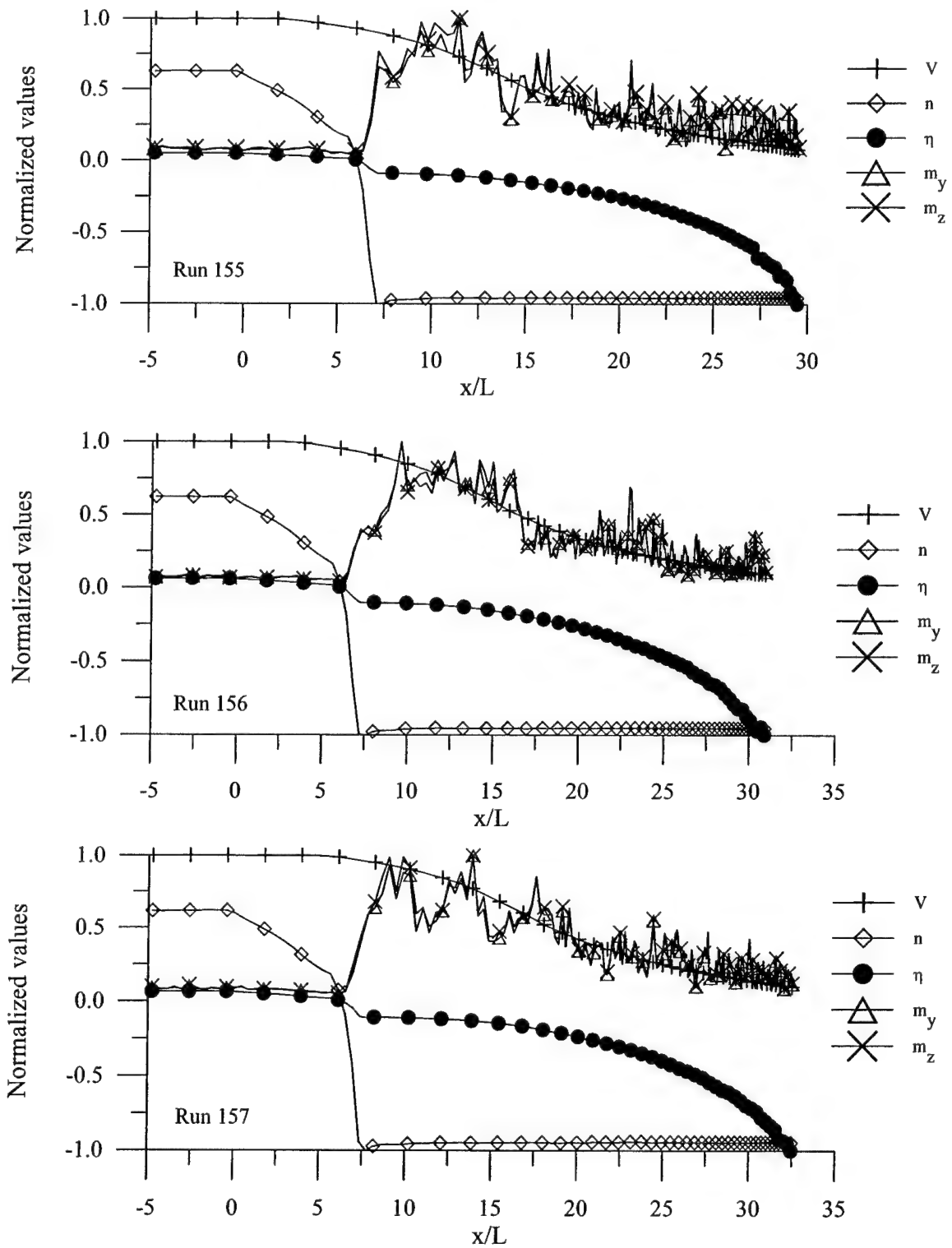
Figure 3.83 Development of RMS propeller off-axis moments during unsteady crashback maneuver simulation (extended data stream)
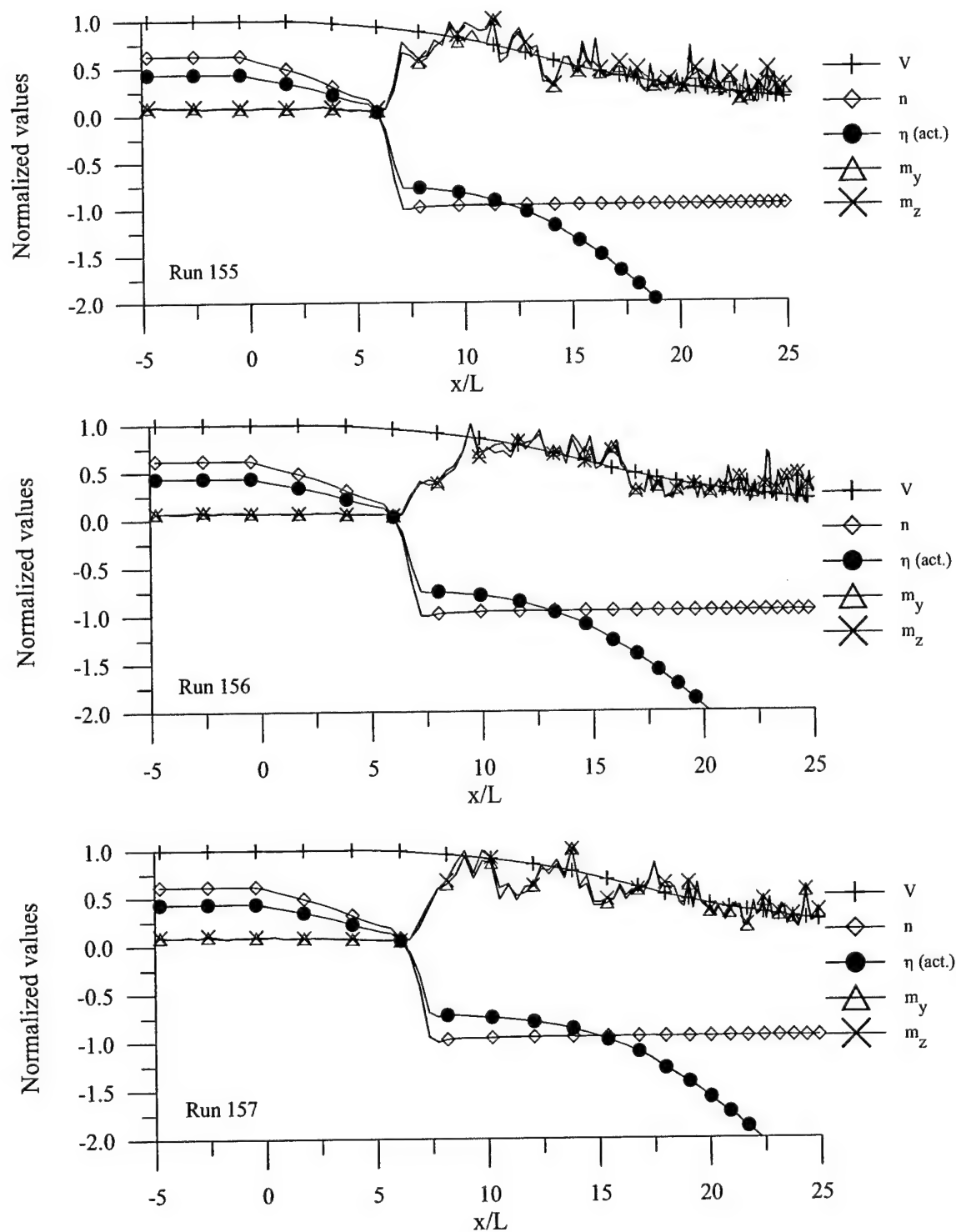
Figure 3.83 (continued) Expanded scale
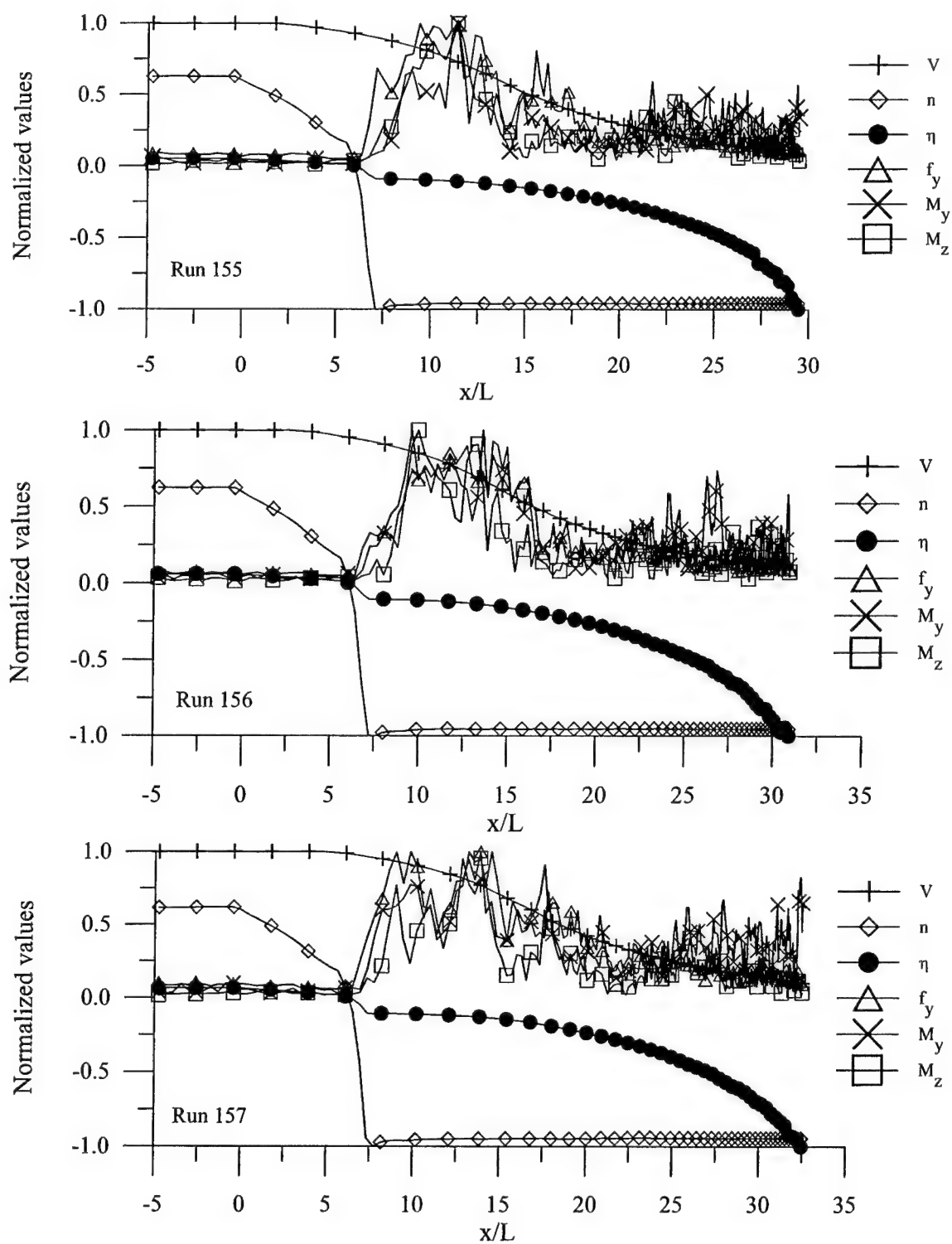
Figure 3.84 Development of RMS propeller y force and RMS body pitching and yawing moments during unsteady crashback maneuver simulation (extended data stream)

133
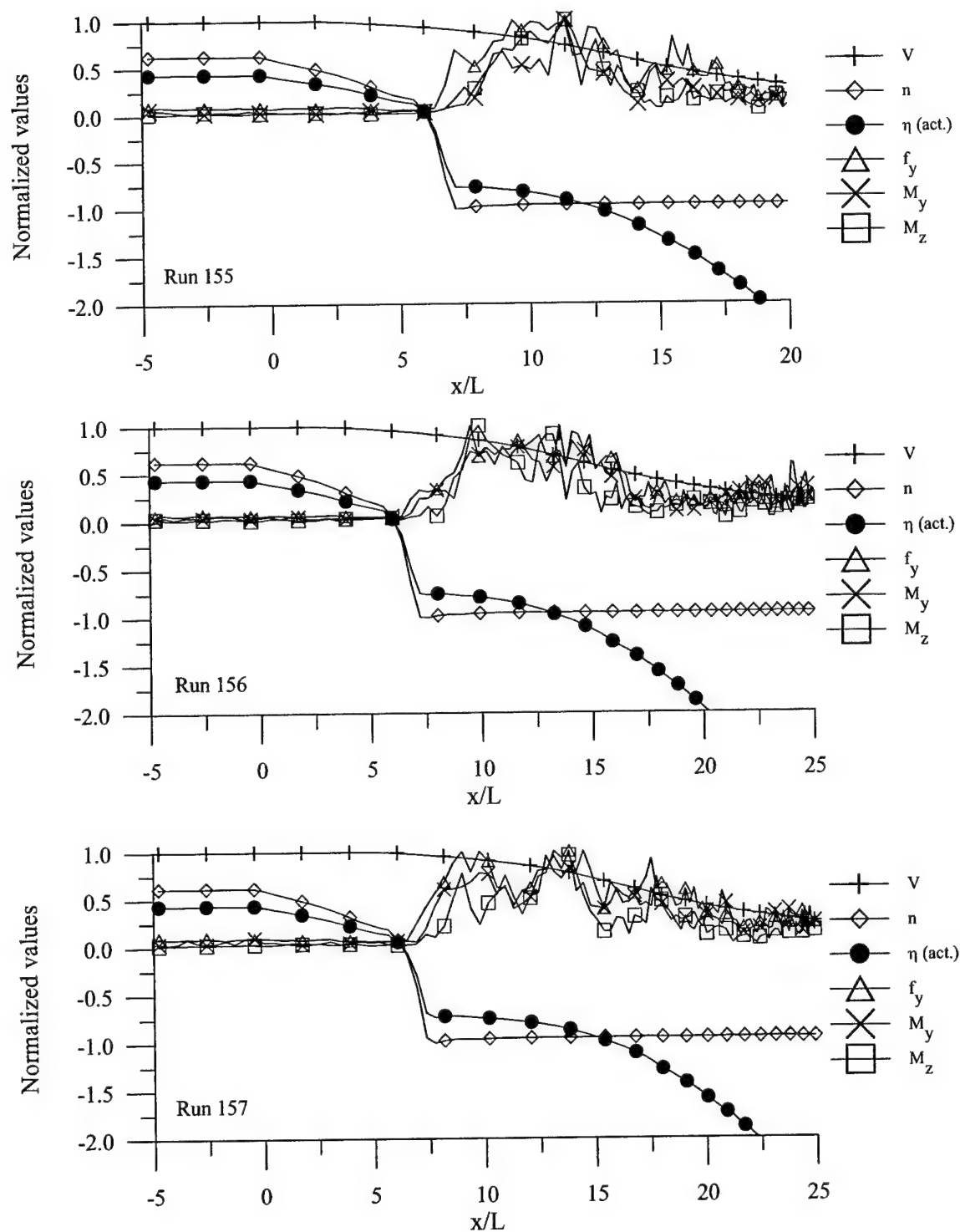
Figure 3.84 (continued) Expanded scale
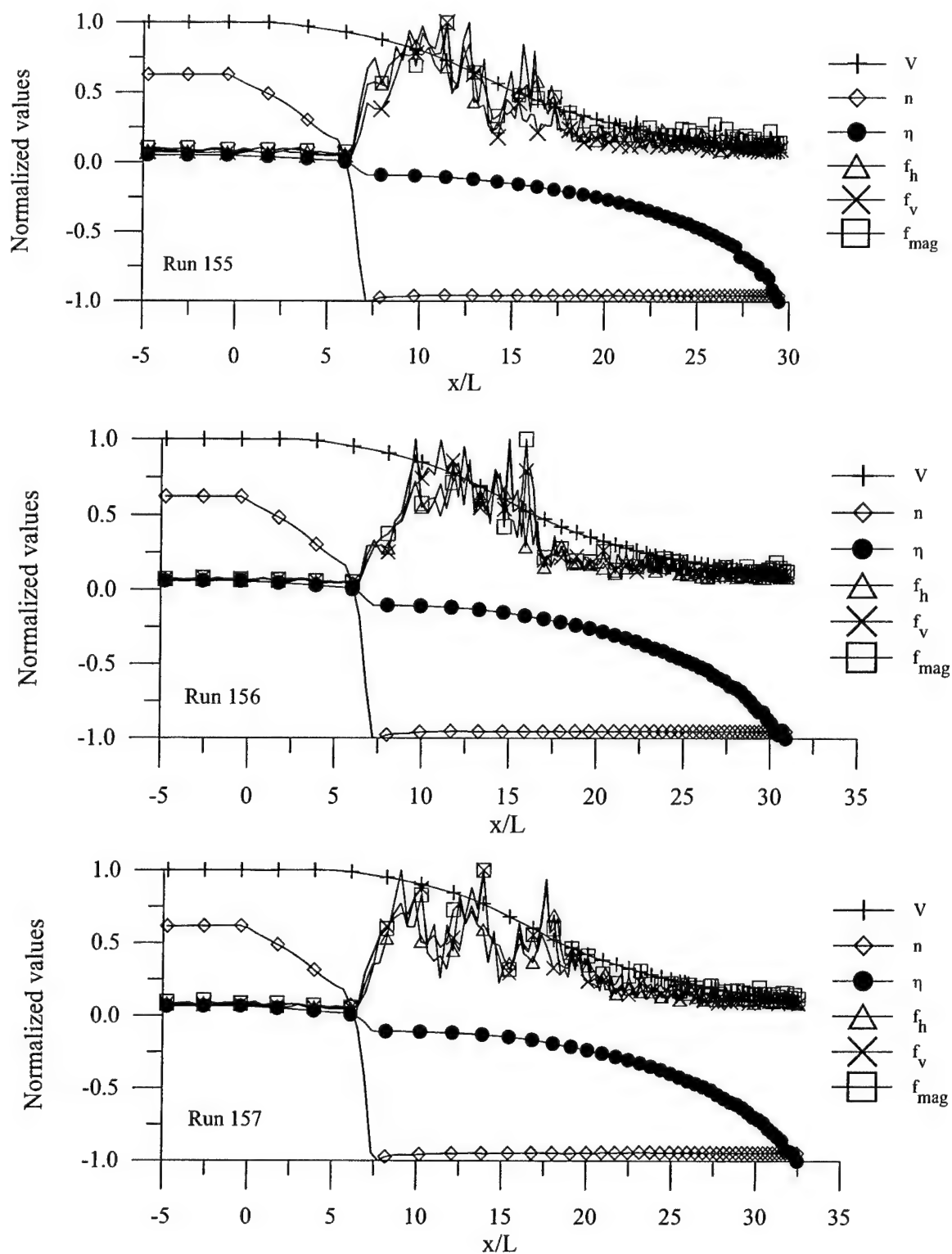
Figure 3.85 Development of RMS propeller horizontal and vertical forces and RMS propeller force magnitude during unsteady crashback maneuver simulation (extended data stream)
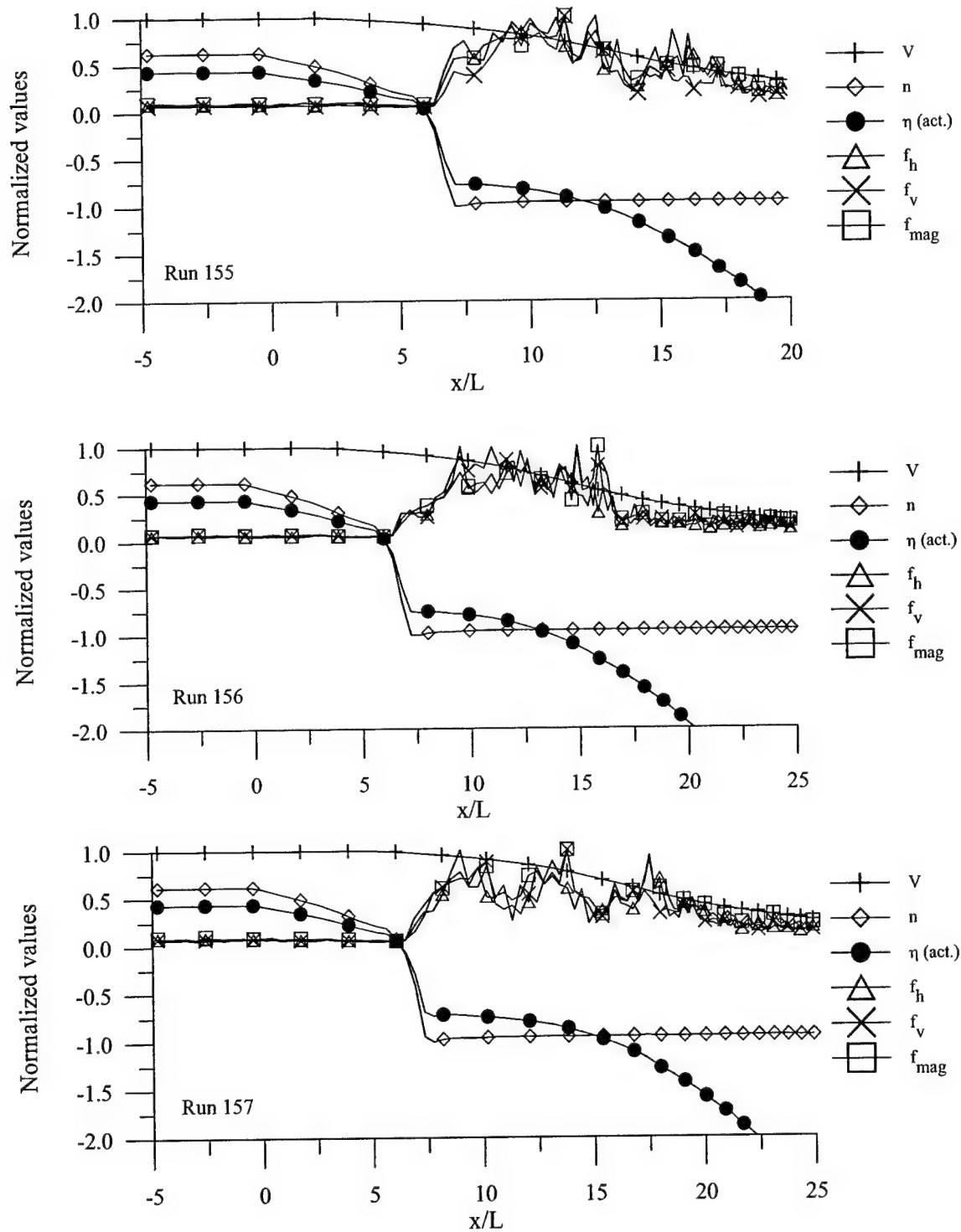
Figure 3.85 (continued) Expanded scale
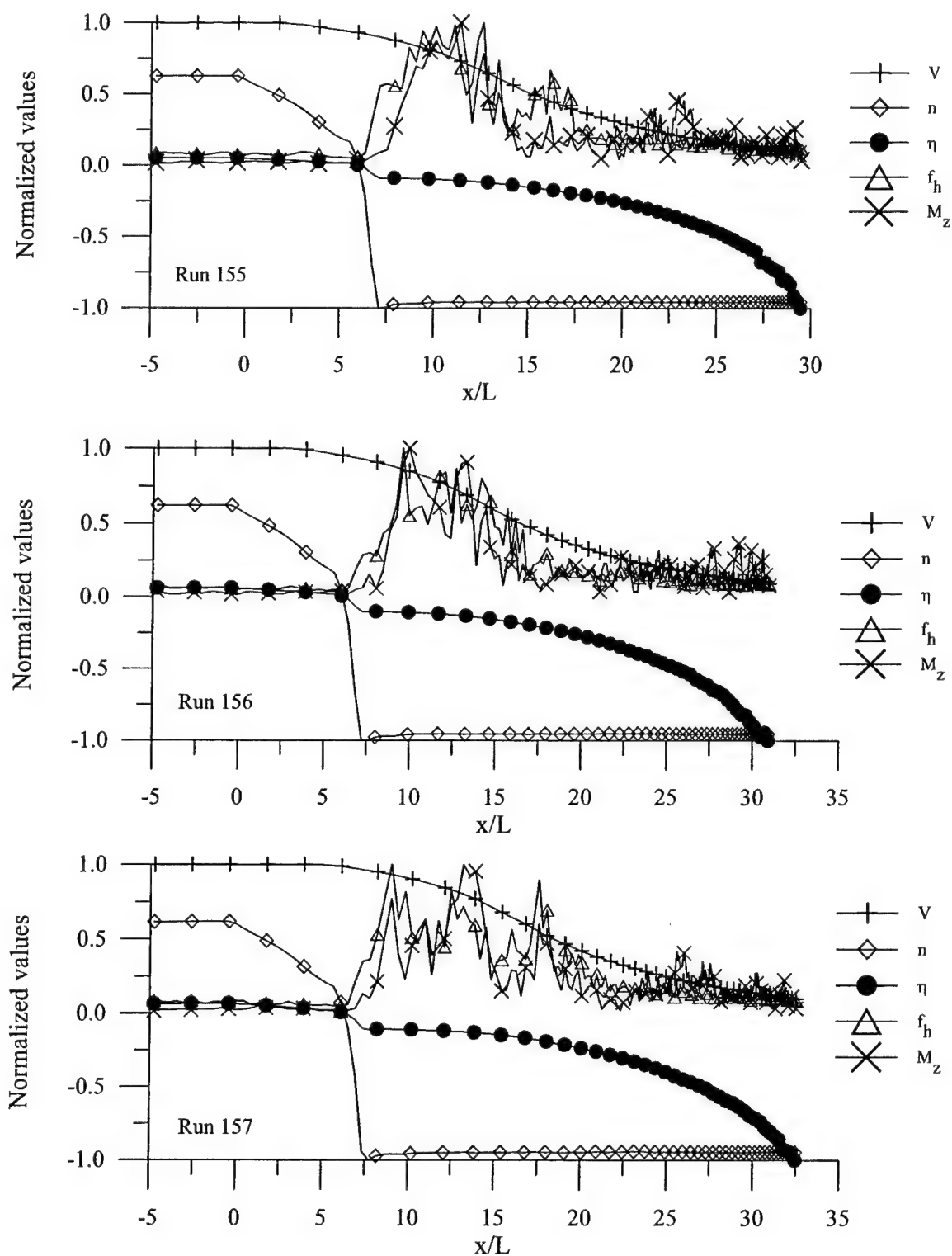
Figure 3.86 Development of RMS propeller horizontal force and RMS body yawing moment during unsteady crashback maneuver simulation (extended data stream)
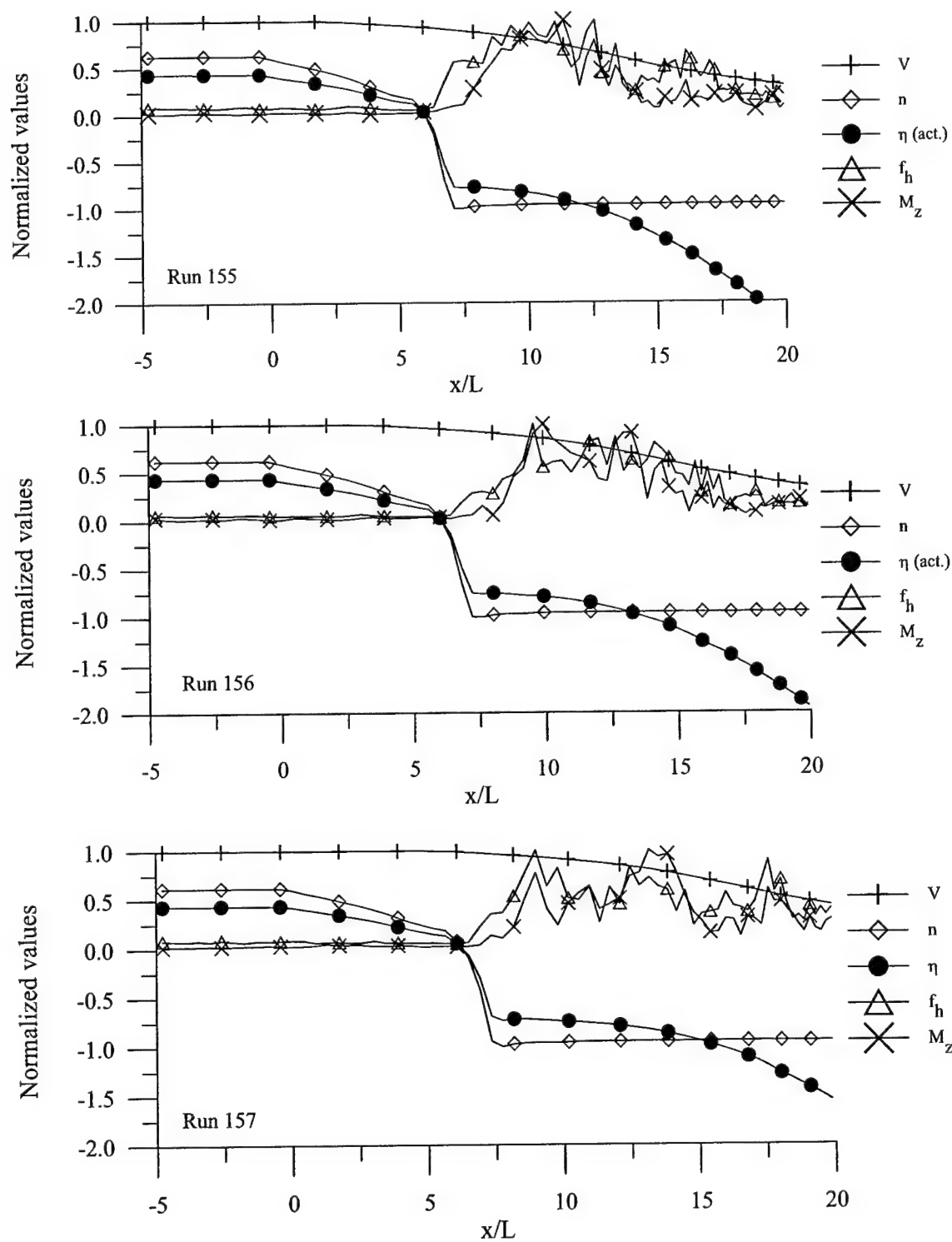
Figure 3.86 (continued) Expanded scale
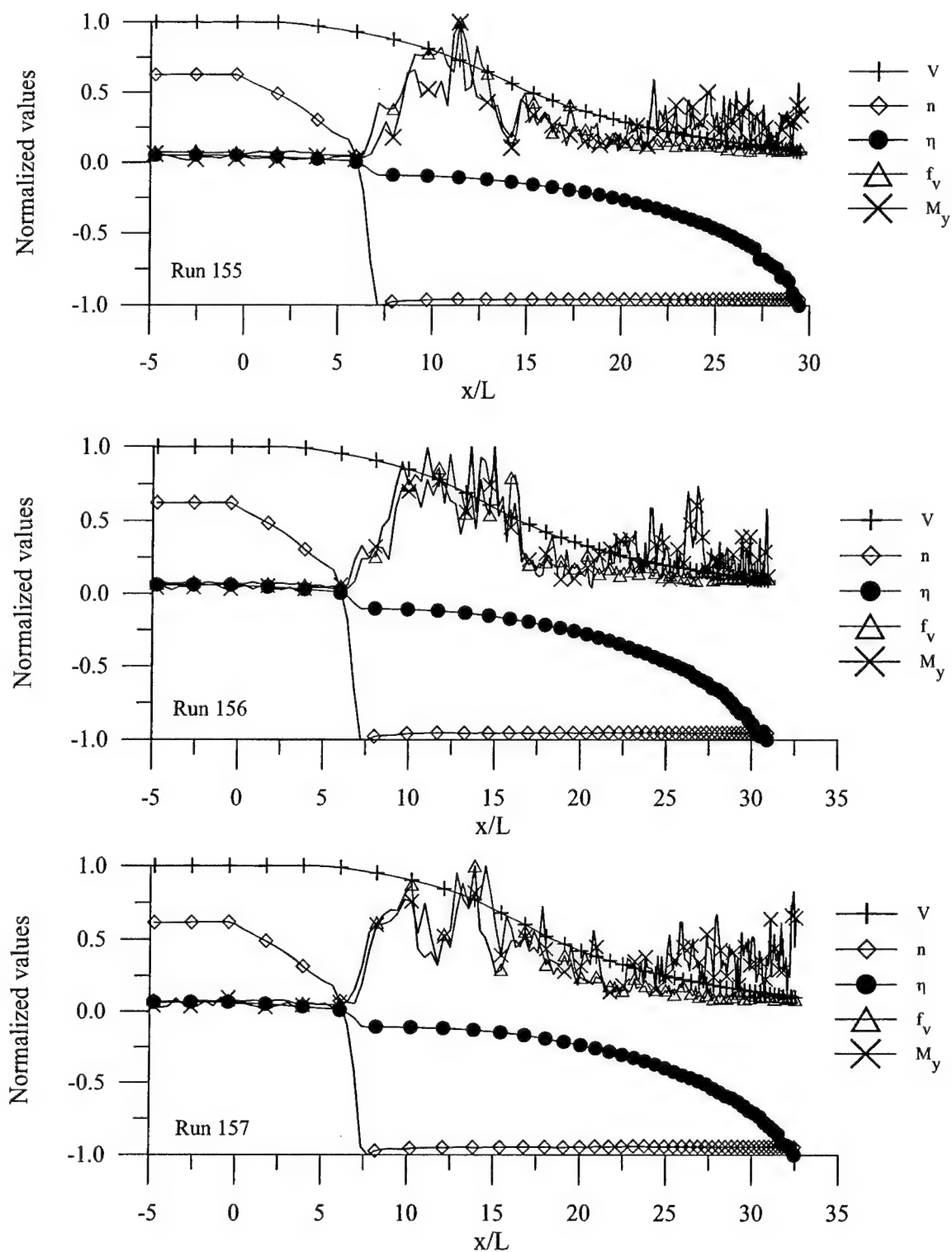
Figure 3.87 Development of RMS propeller vertical force and RMS body pitching moment during unsteady crashback maneuver simulation (extended data stream)
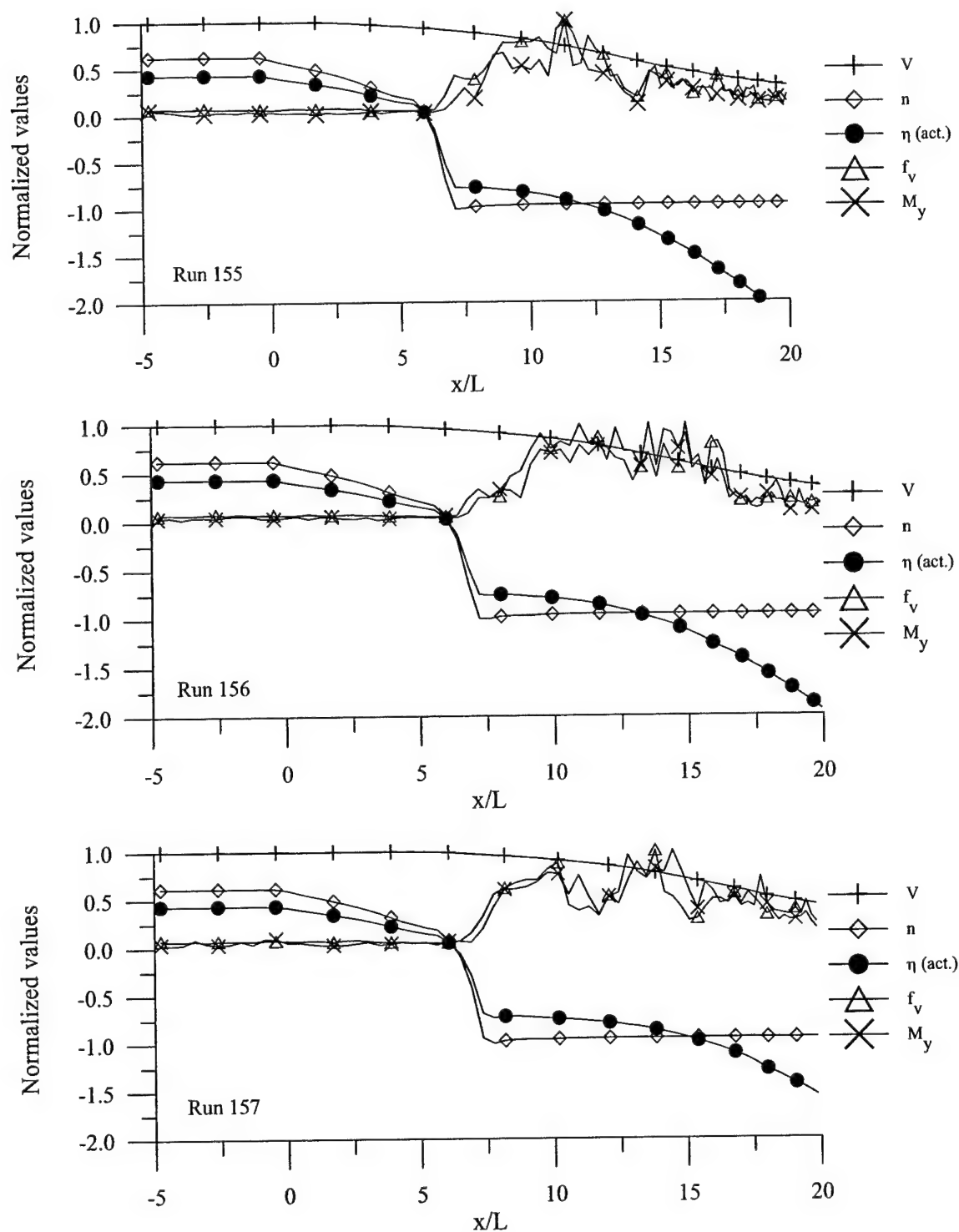
Figure 3.87 (continued) Expanded scale
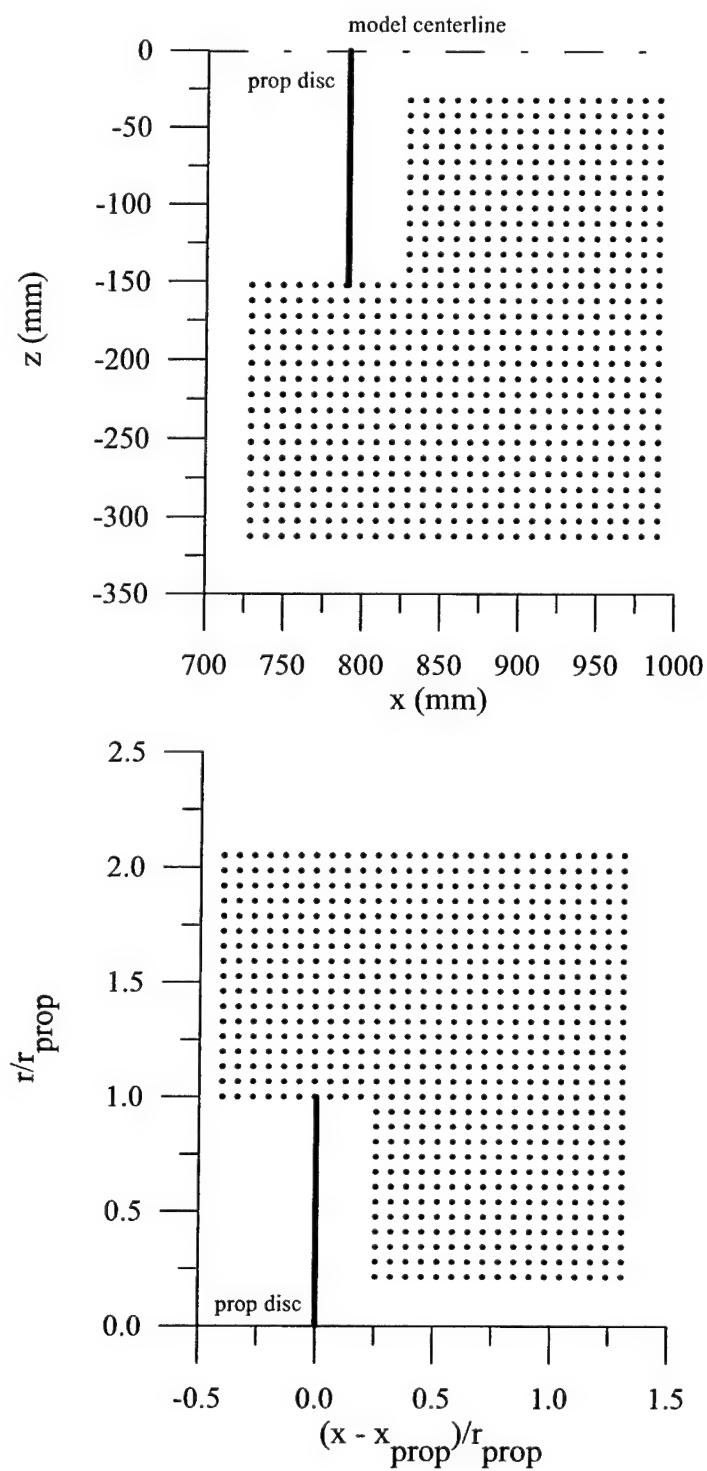
Figure 4.1 Measurement grids for LDV velocity field surveys

141

**MSU/ONR Crashback
Model 5495-3, Prop. 4381
Prop Speed -200 rpm**

x/L = 1
Umodel = 2.56 m/s
Ulocal = 2.56 m/s*
CB5200.tec
4/13/00
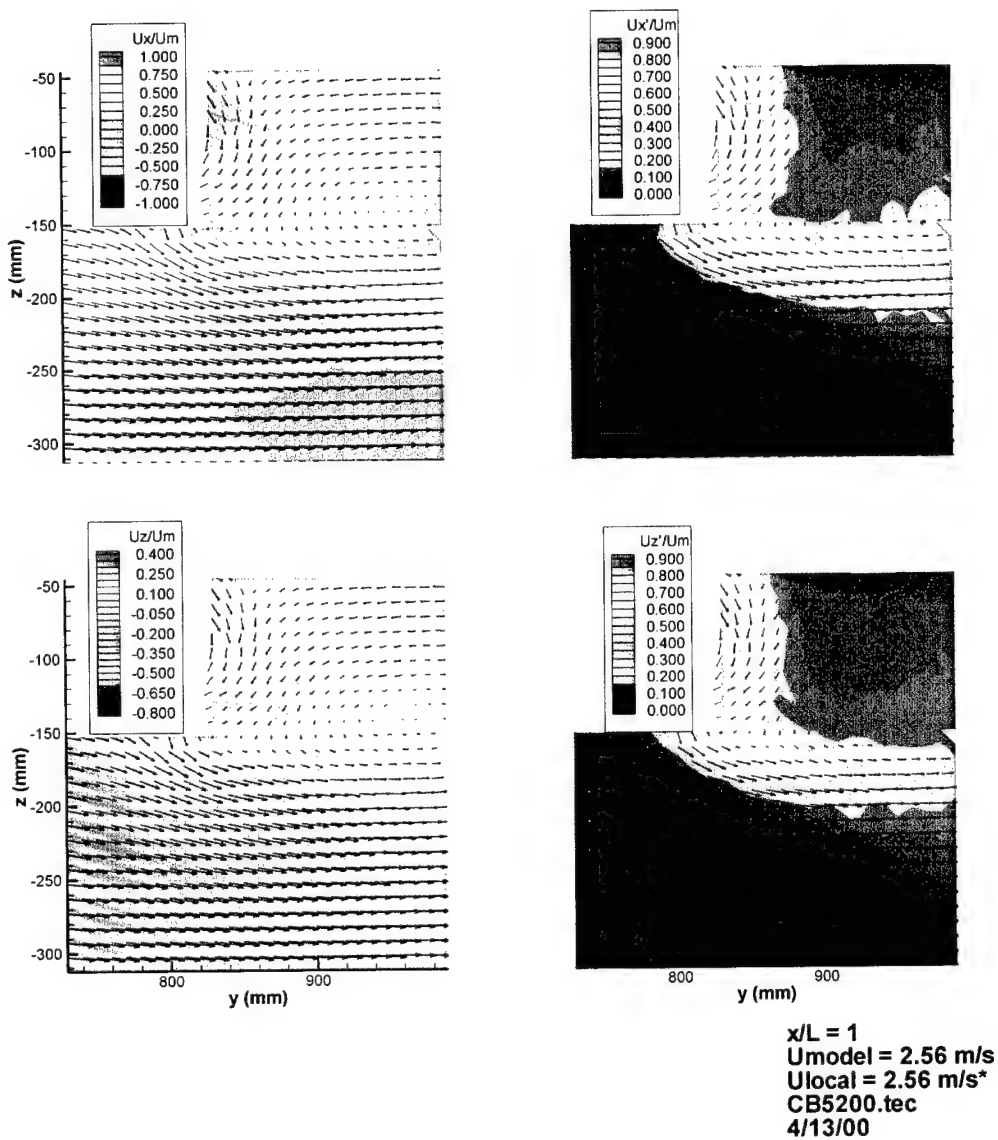
Figure 4.2 Summary of LDV velocity field surveys for η = - 0.382 (Propeller plane located at y = 809.2 mm; propeller radius = 152.4 mm; mean velocity vectors superimposed on contours)

MSU/ONR Crashback
Model 5495-3, Prop. 4381
Prop Speed -200 rpm

x/L = 1
Umodel = 2.56 m/s
Ulocal = 2.56 m/s*
CB5200.tec
4/13/00
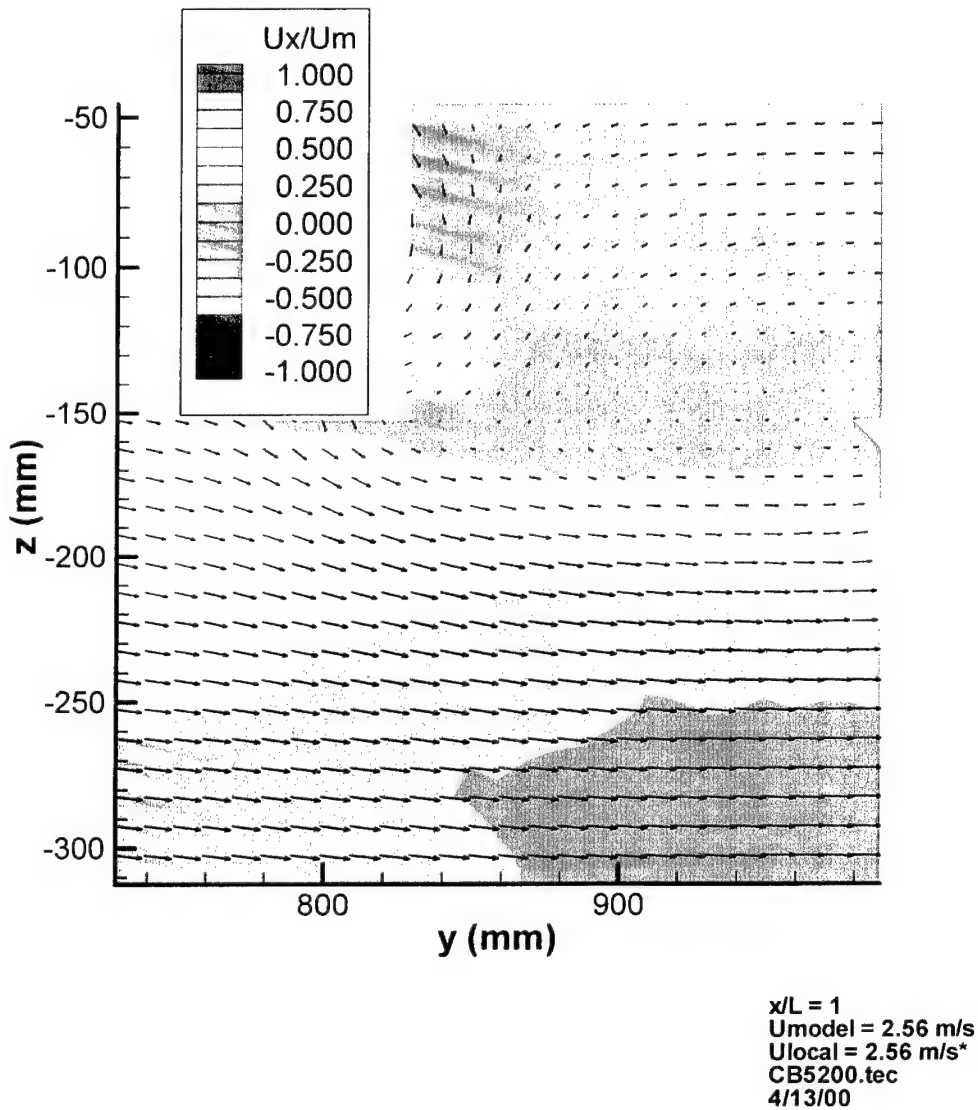
Figure 4.3   LDV survey of mean streamwise velocity component for η = -0.382 (mean velocity vectors overlaid; propeller plane located at y = 809.2 mm; propeller radius = 152.4 mm)

MSU/ONR Crashback
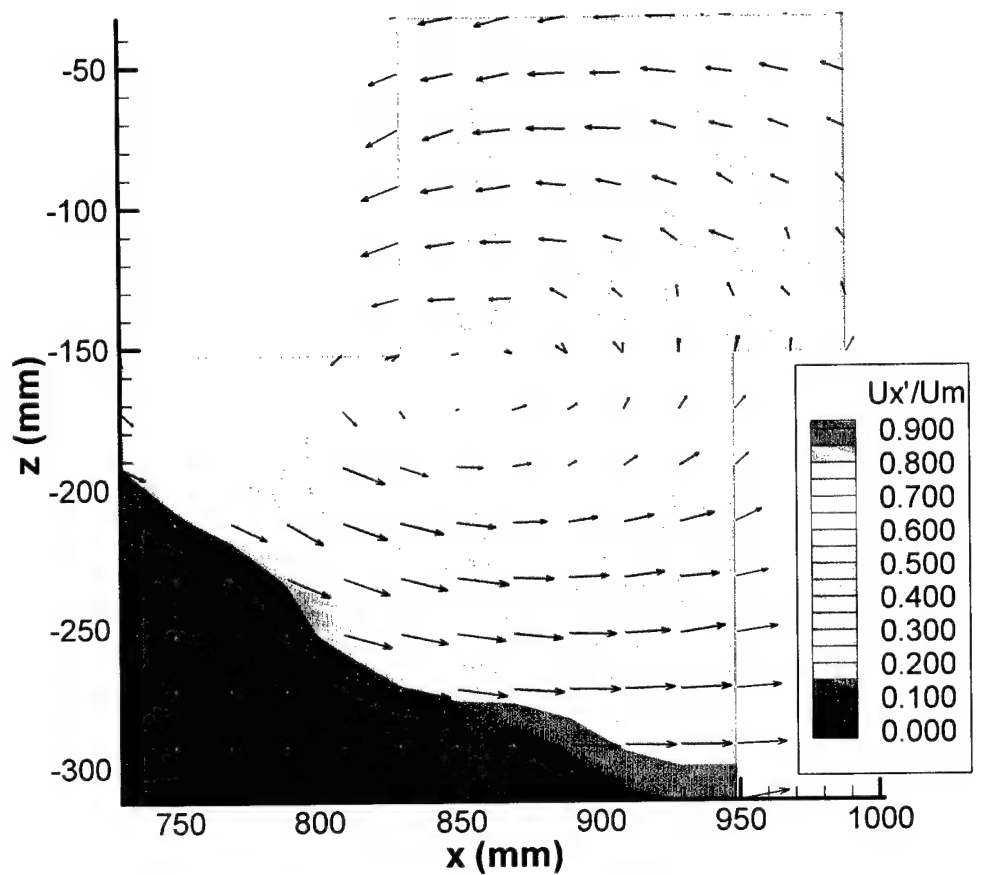**Model 5495-3, Prop. 4381**
Prop Speed -200 rpm

Figure 4.4   LDV survey of RMS streamwise velocity component for η = -0.382 (mean velocity vectors overlaid; propeller plane located at y = 809.2 mm; propeller radius = 152.4 mm)

MSU/ONR Crashback
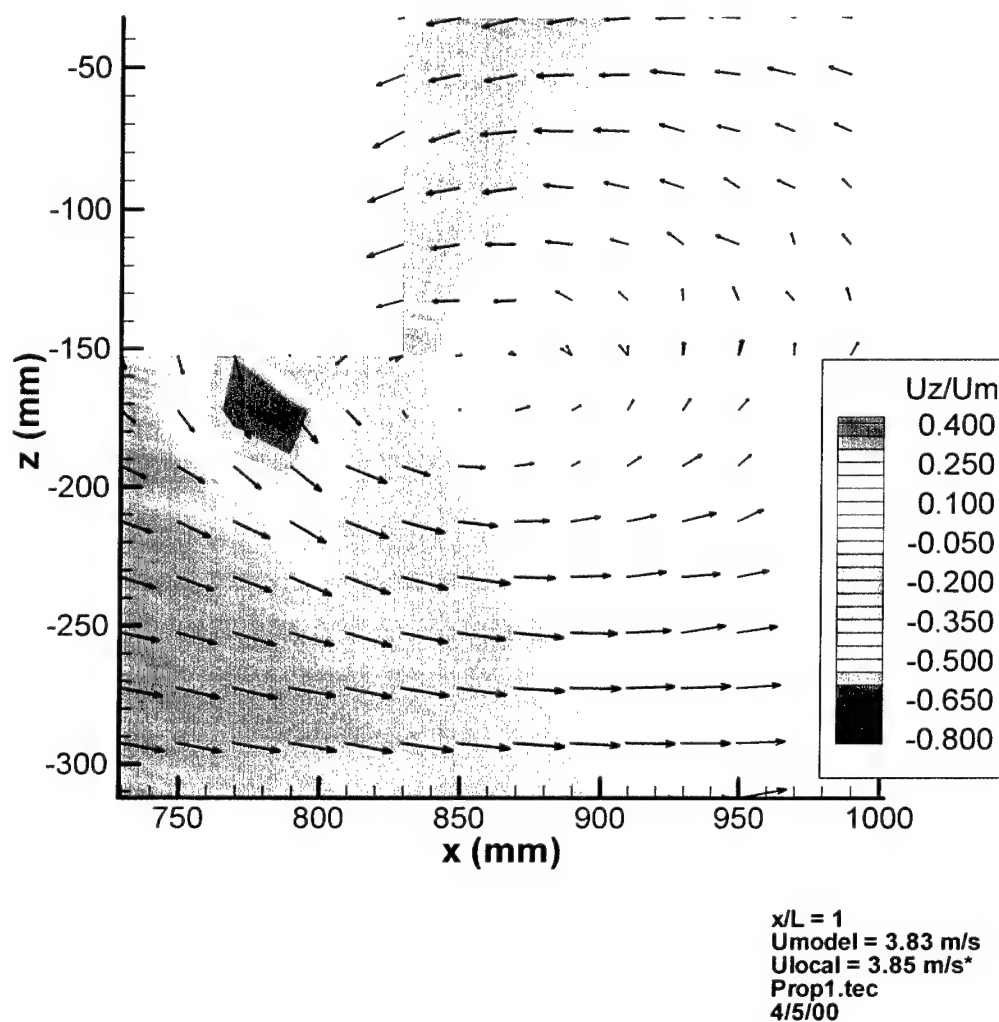# Model 5495-3, Prop. 4381
Prop Speed -200 rpm

x/L = 1
Umodel = 2.56 m/s
Ulocal = 2.56 m/s*
CB5200.tec
4/13/00

Figure 4.5 LDV survey of mean transverse velocity component for η = -0.382 (mean velocity vectors overlaid; propeller plane located at y = 809.2 mm; propeller radius = 152.4 mm)

**MSU/ONR Crashback
Model 5495-3, Prop. 4381
Prop Speed -200 rpm**

x/L = 1
Umodel = 2.56 m/s
Ulocal = 2.56 m/s*
CB5200.tec
4/13/00

Figure 4.6 LDV survey of RMS transverse velocity component for $\eta = -0.382$ (mean velocity vectors overlaid; propeller plane located at $y = 809.2$ mm; propeller radius = 152.4 mm)

MSU/ONR Crashback Test
Model 5495, Prop 4381
Prop Speed -300 rpm
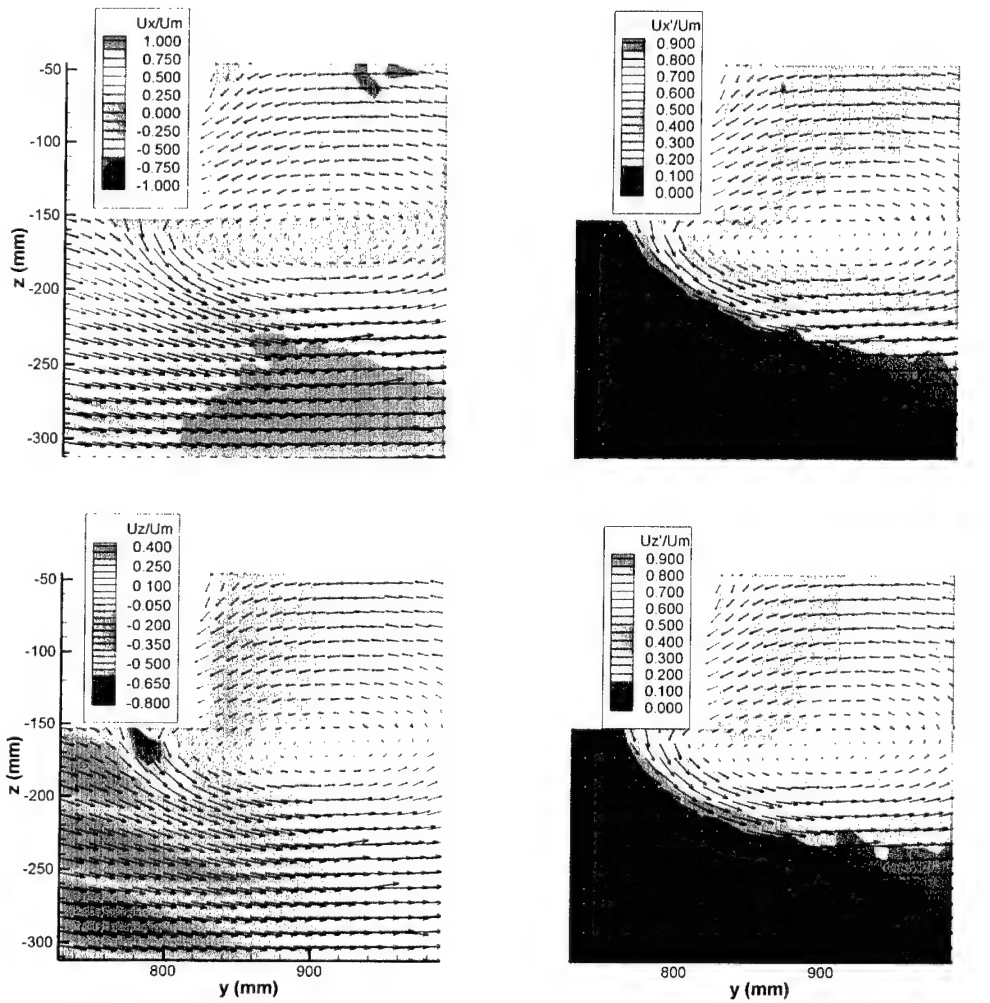
x/L = 1
Umodel = 2.56 m/s
Ulocal = 2.56 m/s*
CB5300.tec
4/12/00

Figure 4.7 Summary of LDV velocity field surveys for $\eta = -0.565$ (Propeller plane located at $y = 809.2$ mm; propeller radius = 152.4 mm)

**MSU/ONR Crashback Test
Model 5495, Prop 4381
Prop Speed -300 rpm**

x/L = 1
Umodel = 2.56 m/s
Ulocal = 2.56 m/s*
CB5300.tec
4/12/00
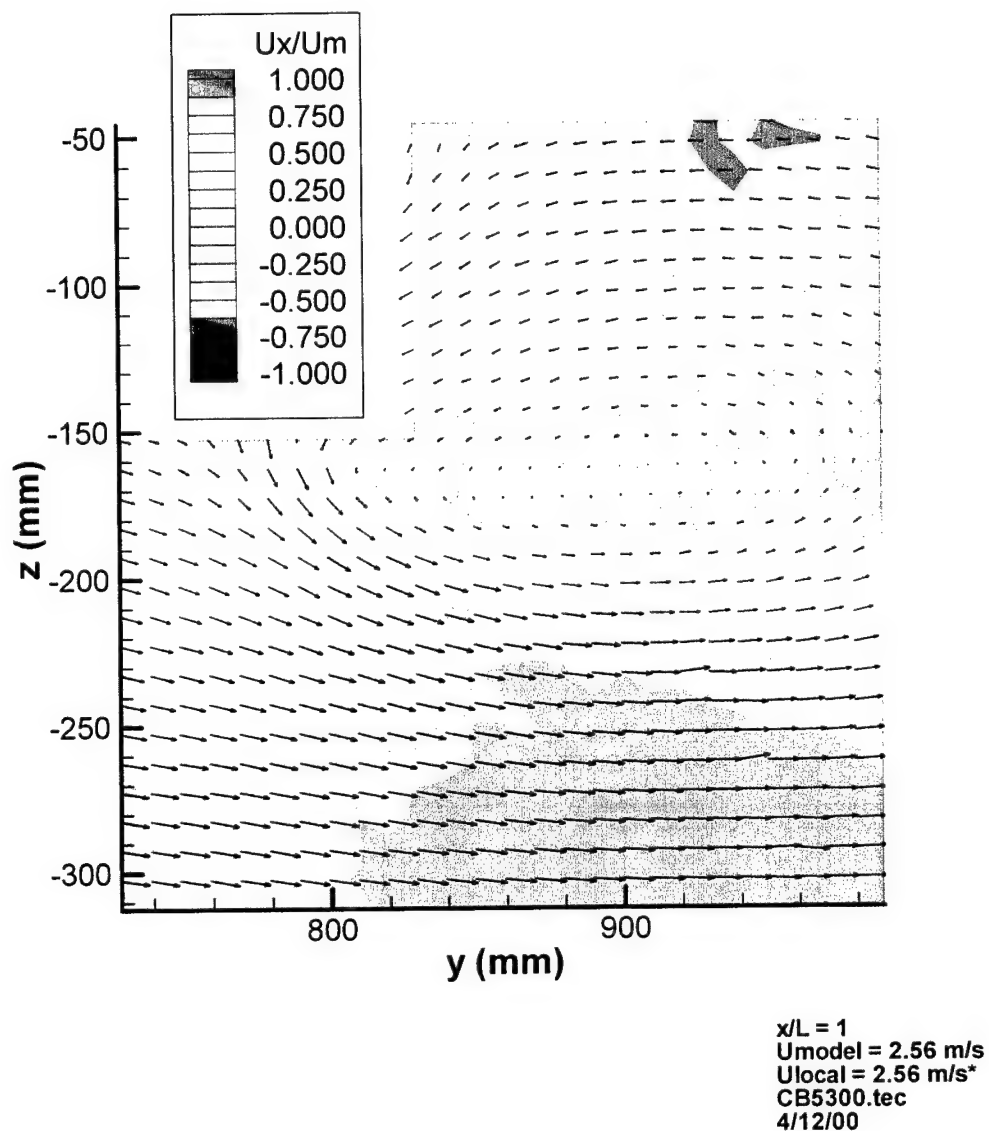
Figure 4.8   LDV survey of mean streamwise velocity component for η = -0.565 (mean velocity vectors overlaid; propeller plane located at y = 809.2 mm; propeller radius = 152.4 mm)

MSU/ONR Crashback Test
Model 5495, Prop 4381
Prop Speed -300 rpm

x/L = 1
Umodel = 2.56 m/s
Ulocal = 2.56 m/s*
CB5300.tec
4/12/00
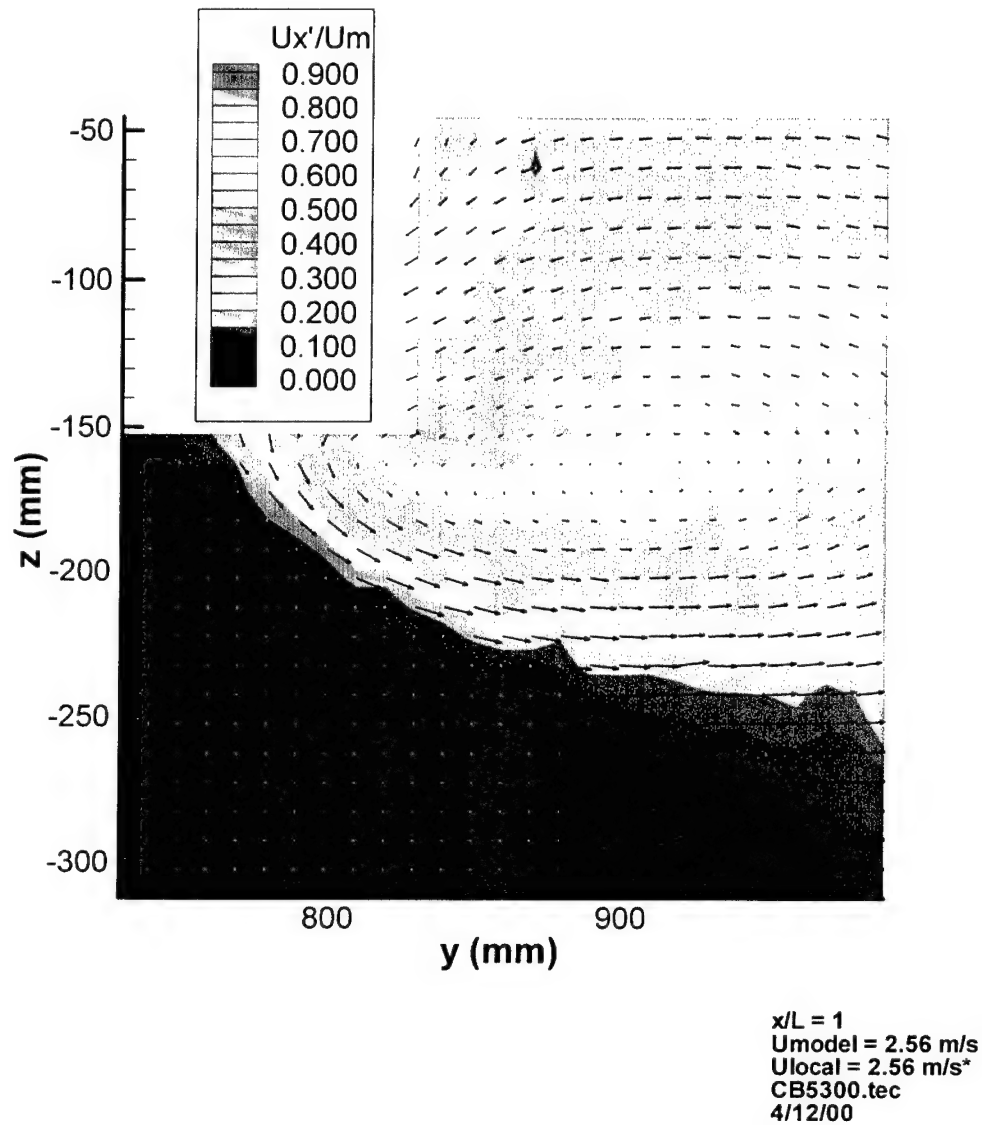
Figure 4.9 LDV survey of RMS streamwise velocity component for η = -0.565 (mean velocity vectors overlaid; propeller plane located at y = 809.2 mm; propeller radius = 152.4 mm)

**MSU/ONR Crashback Test
Model 5495, Prop 4381
Prop Speed -300 rpm**
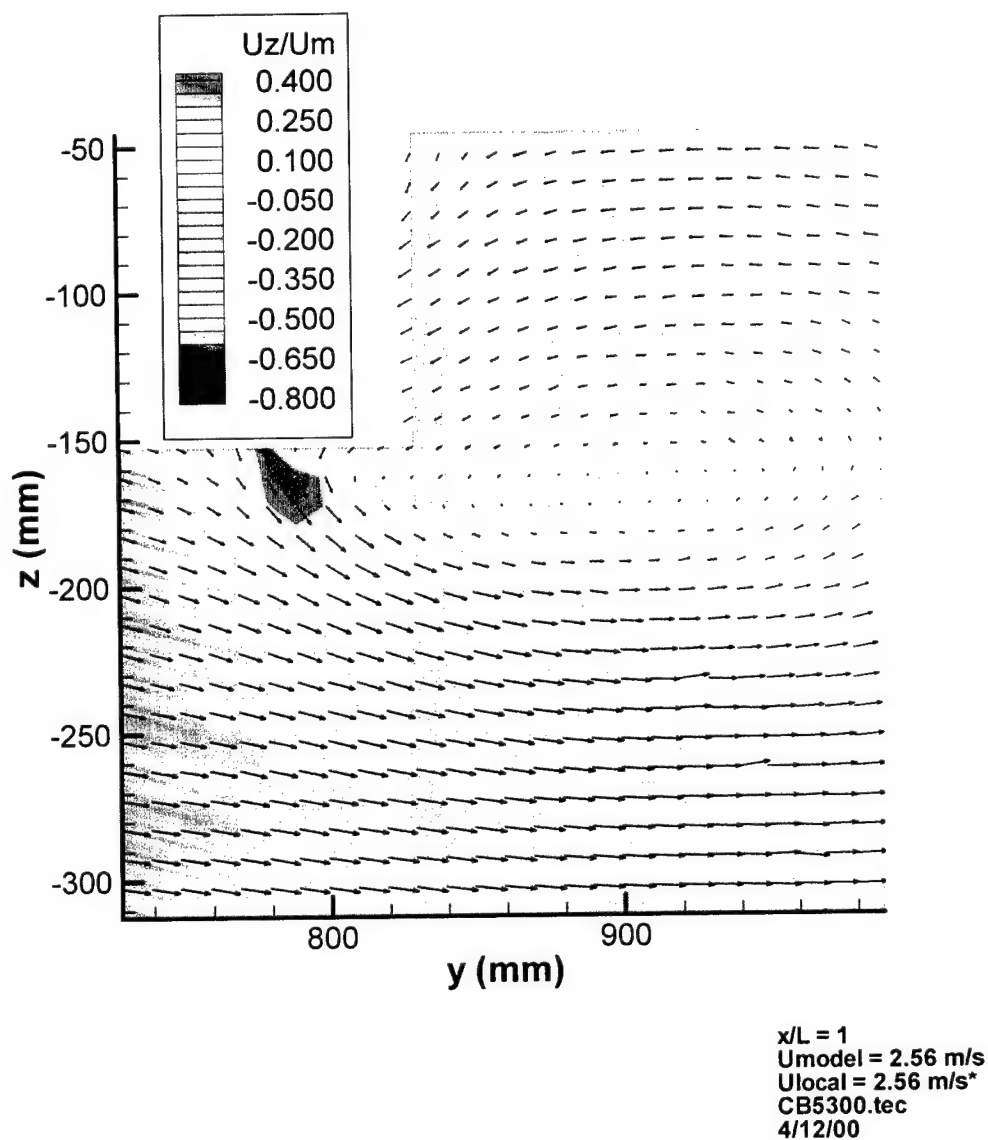
Figure 4.10 LDV survey of mean transverse velocity component for η = -0.565 (mean velocity vectors overlaid; propeller plane located at y = 809.2 mm; propeller radius = 152.4 mm)

MSU/ONR Crashback Test
Model 5495, Prop 4381
Prop Speed -300 rpm

x/L = 1
Umodel = 2.56 m/s
Ulocal = 2.56 m/s*
CB5300.tec
4/12/00
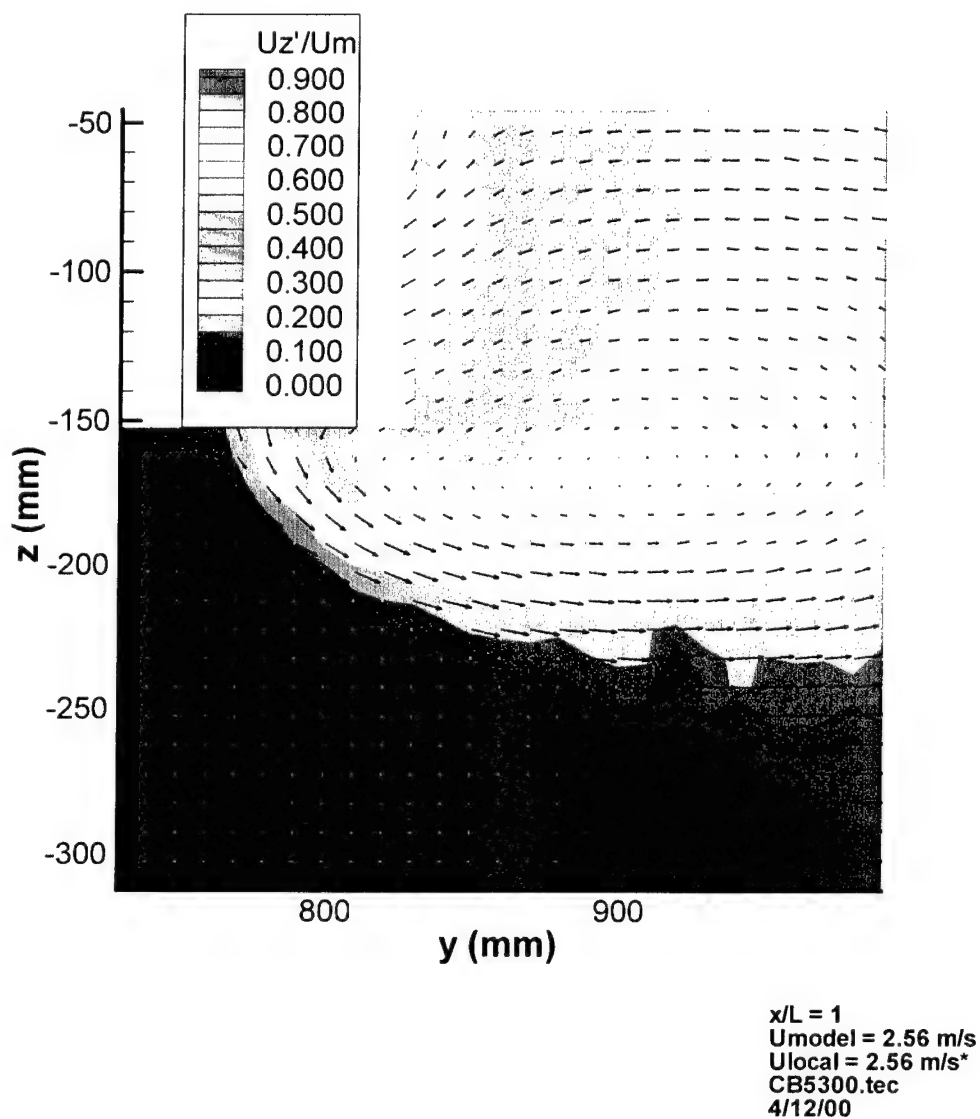
Figure 4.11 LDV survey of RMS transverse velocity component for η = -0.565 (mean velocity vectors overlaid; propeller plane located at y = 809.2 mm; propeller radius = 152.4 mm)

MSU/ONR Crashback Test
Model 5495, Prop 4381
Prop Speed -426 rpm
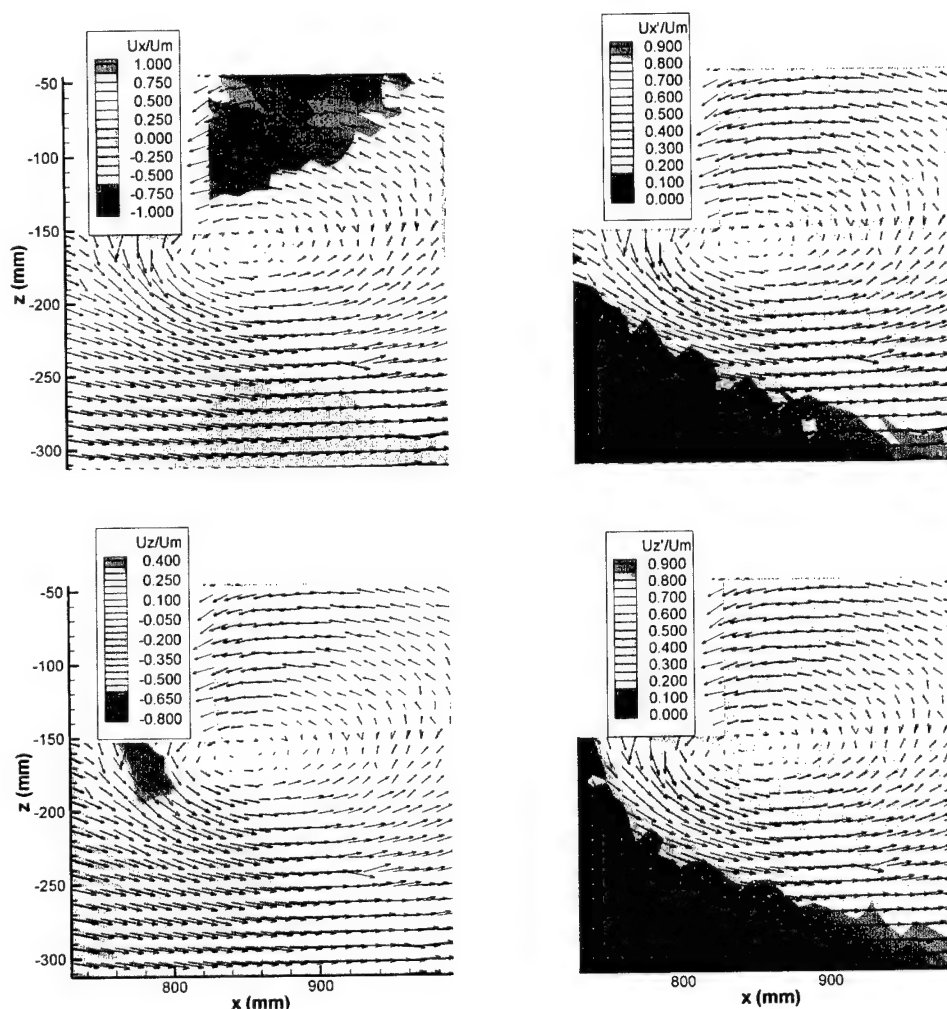
x/L = 1
Umodel = 2.57 m/s
Ulocal = 2.58 m/s*
Prop2.tec
04/07/2000

Figure 4.12 Summary of LDV velocity field surveys for η = -0.801 (Propeller plane located at y = 809.2 mm; propeller radius = 152.4 mm)

MSU/ONR Crashback Test
Model 5495, Prop 4381
Prop Speed -426 rpm

x/L = 1
Umodel = 2.57 m/s
Ulocal = 2.58 m/s*
Prop2.tec
04/07/2000
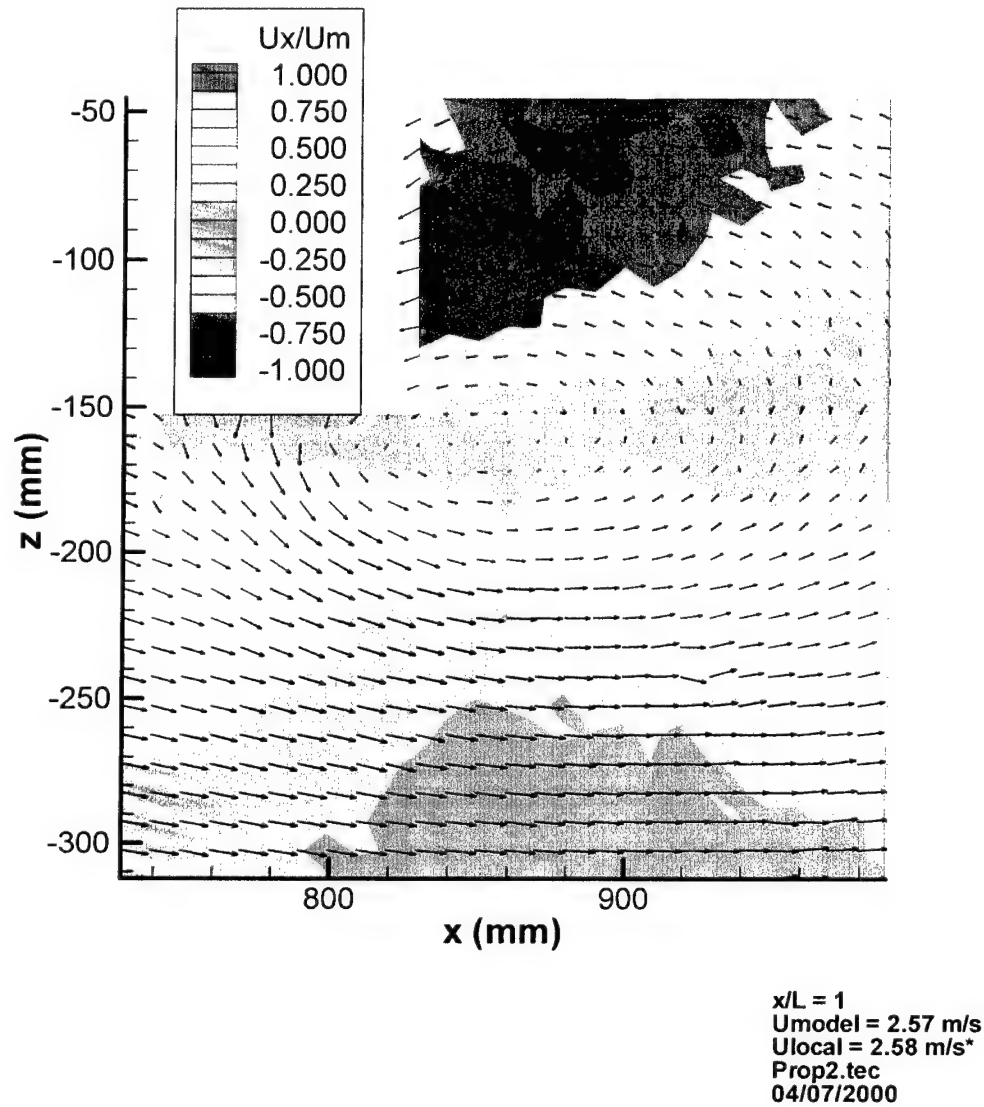
Figure 4.13 LDV survey of mean streamwise velocity component for η = -0.801 (mean velocity vectors overlaid; propeller plane located at x = 809.2 mm; propeller radius = 152.4 mm)

MSU/ONR Crashback Test
Model 5495, Prop 4381
Prop Speed -426 rpm

x/L = 1
Umodel = 2.57 m/s
Ulocal = 2.58 m/s*
Prop2.tec
04/07/2000
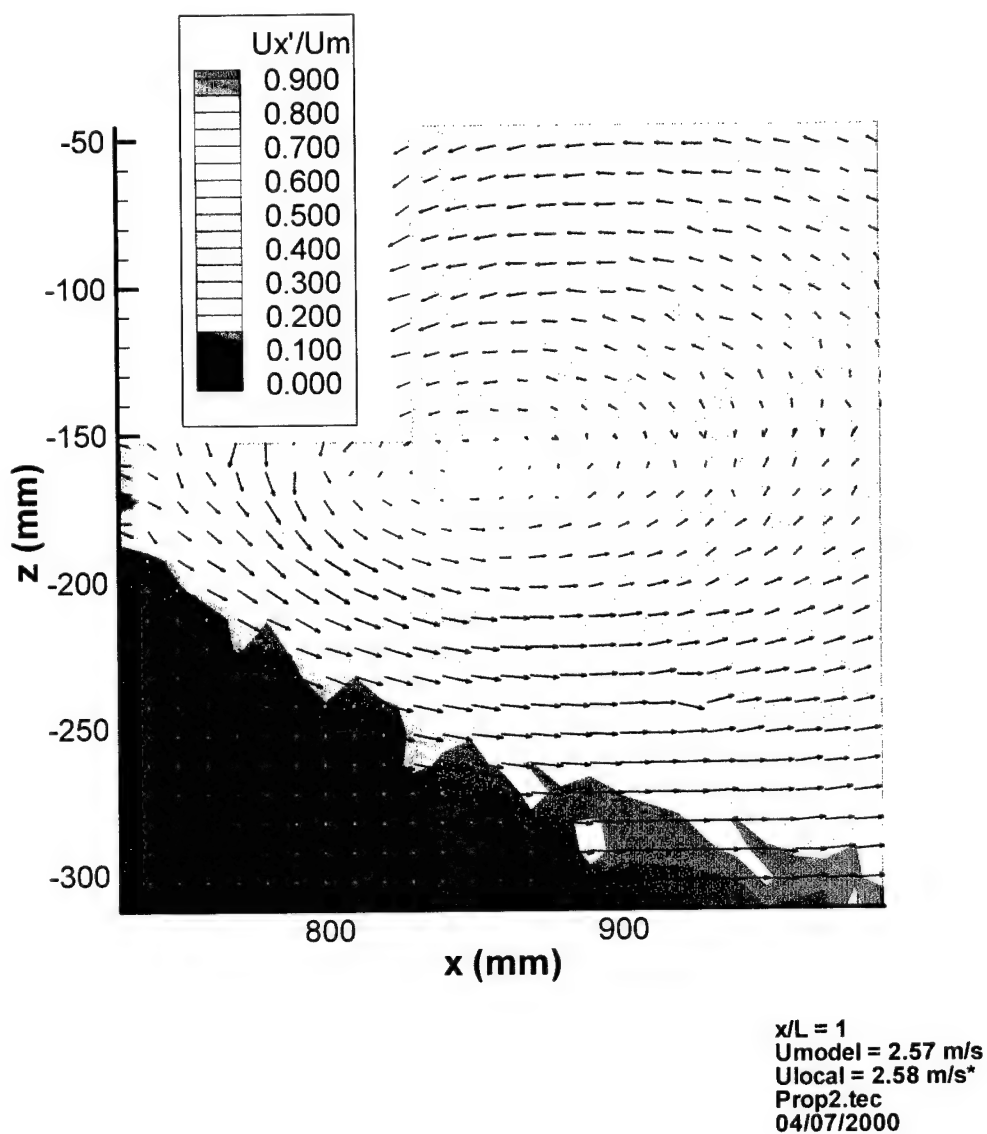
Figure 4.14 LDV survey of RMS streamwise velocity component for η = -0.801 (mean velocity vectors overlaid; propeller plane located at x = 809.2 mm; propeller radius = 152.4 mm)

MSU/ONR Crashback Test
Model 5495, Prop 4381
Prop Speed -426 rpm
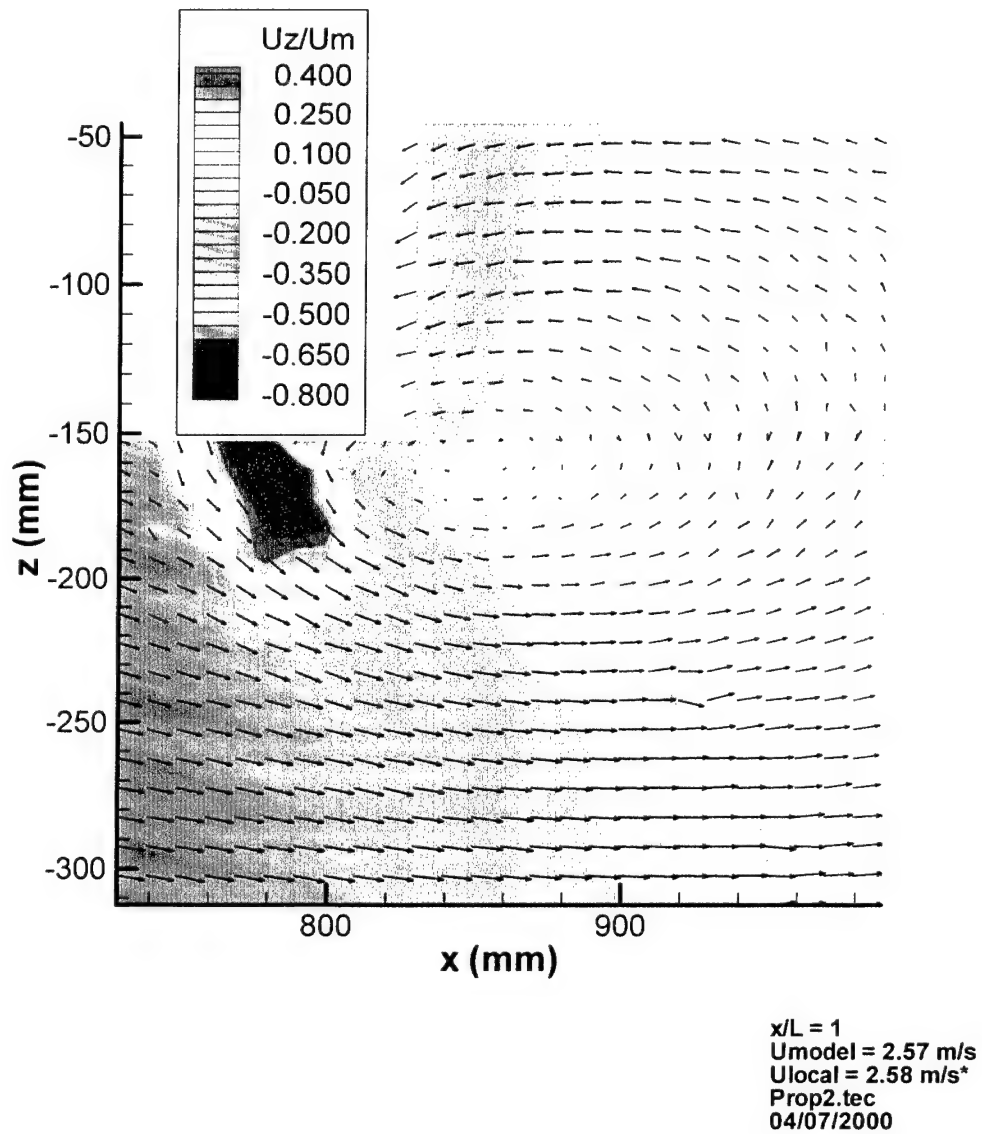
Figure 4.15 LDV survey of mean transverse velocity component for η = -0.801 (mean velocity vectors overlaid; propeller plane located at x = 809.2 mm; propeller radius = 152.4 mm)

MSU/ONR Crashback Test
Model 5495, Prop 4381
Prop Speed -426 rpm

x/L = 1
Umodel = 2.57 m/s
Ulocal = 2.58 m/s*
Prop2.tec
04/07/2000
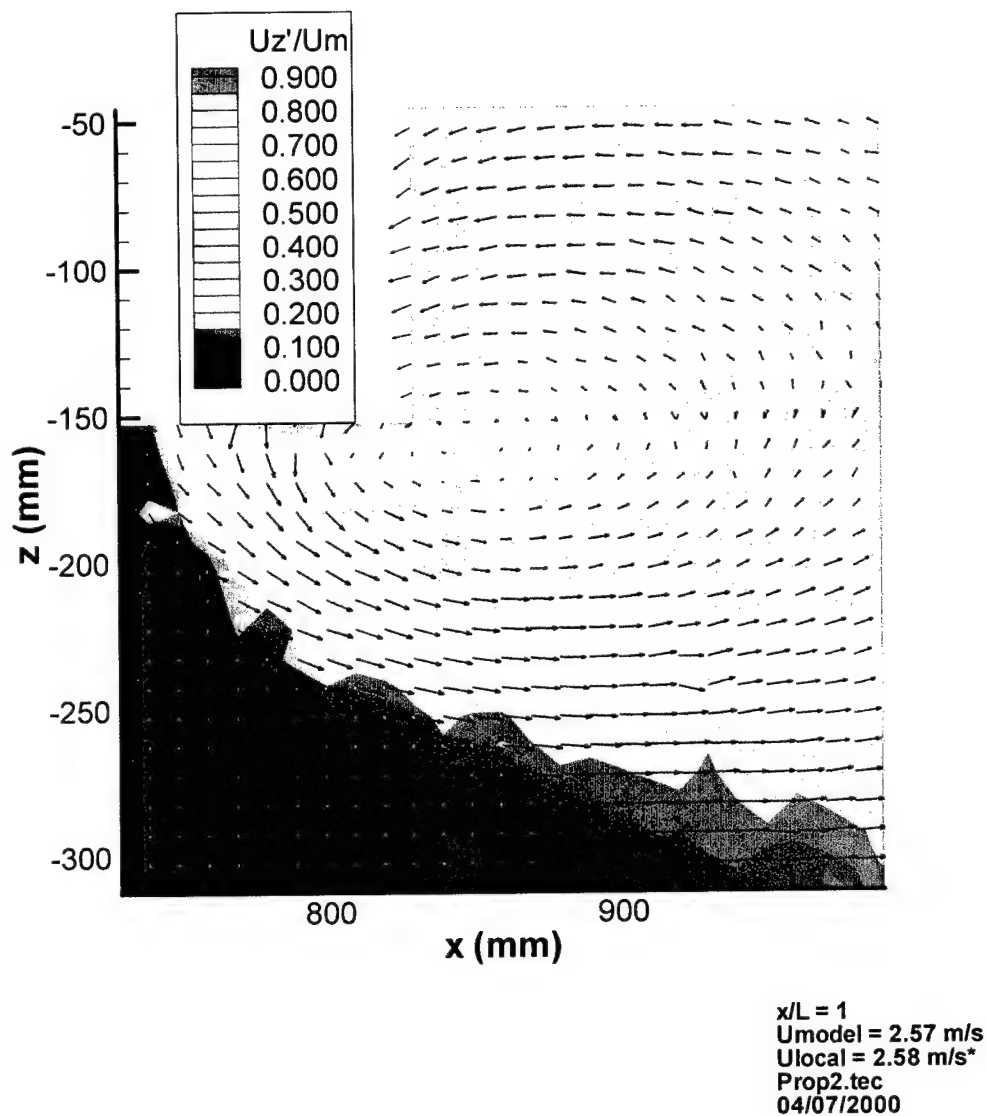
Figure 4.16 LDV survey of RMS transverse velocity component for η = -0.801(mean velocity vectors overlaid); propeller plane located at x = 809.2 mm; propeller radius = 152.4 mm)

MSU/ONR Crashback
Model 5495-3, Prop. 4381
Prop Speed -600 rpm

x/L = 1
Umodel = 2.55 m/s
Ulocal = 2.55 m/s*
CB5600.tec
4/12/00
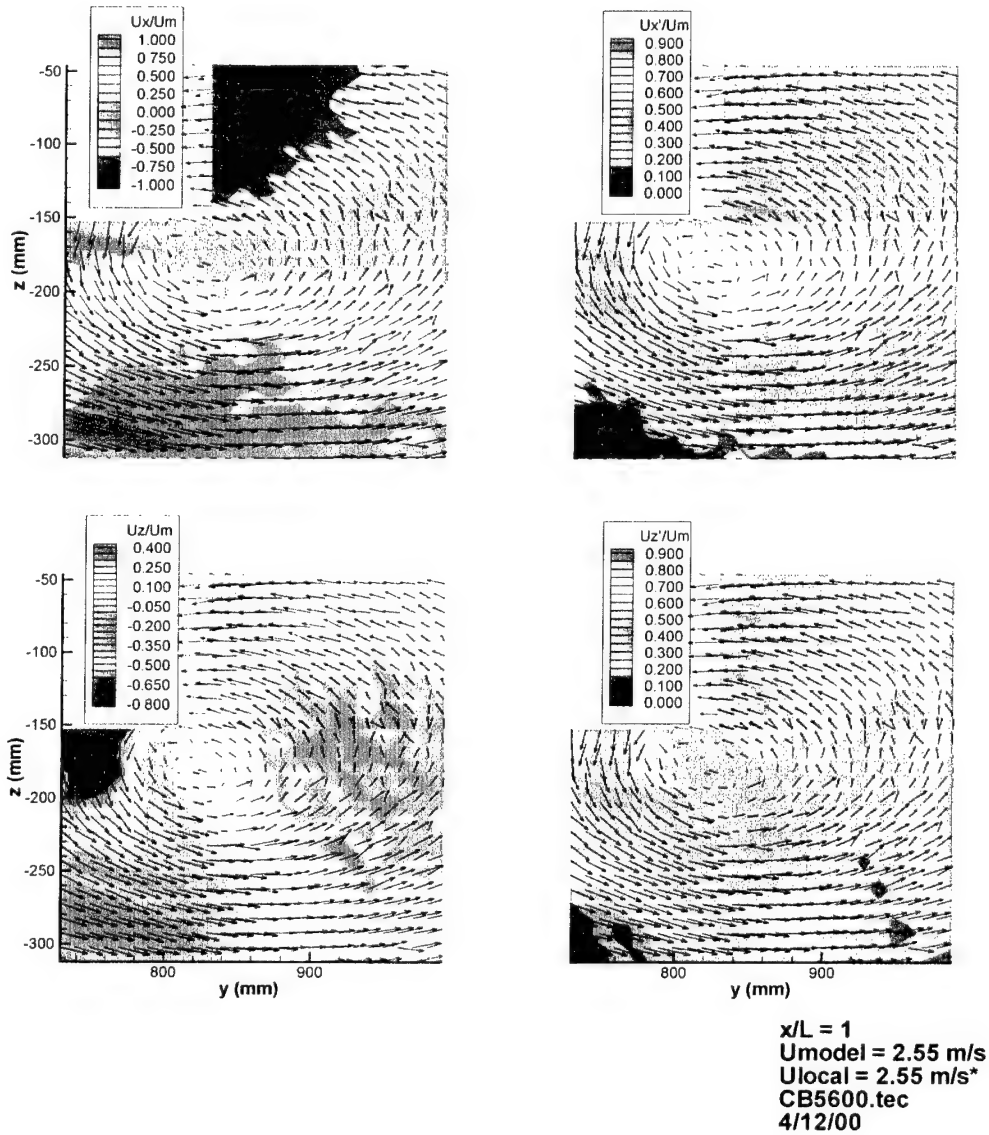
Figure 4.17 Summary of LDV velocity field surveys for $\eta = -1.15$ (Propeller plane located at $y = 809.2$ mm; propeller radius = 152.4 mm)

**MSU/ONR Crashback
Model 5495-3, Prop. 4381
Prop Speed -600 rpm**

Ux/Um
1.000
0.750
0.500
0.250
0.000
-0.250
-0.500
-0.750
-1.000

x/L = 1
Umodel = 2.55 m/s
Ulocal = 2.55 m/s*
CB5600.tec
4/12/00
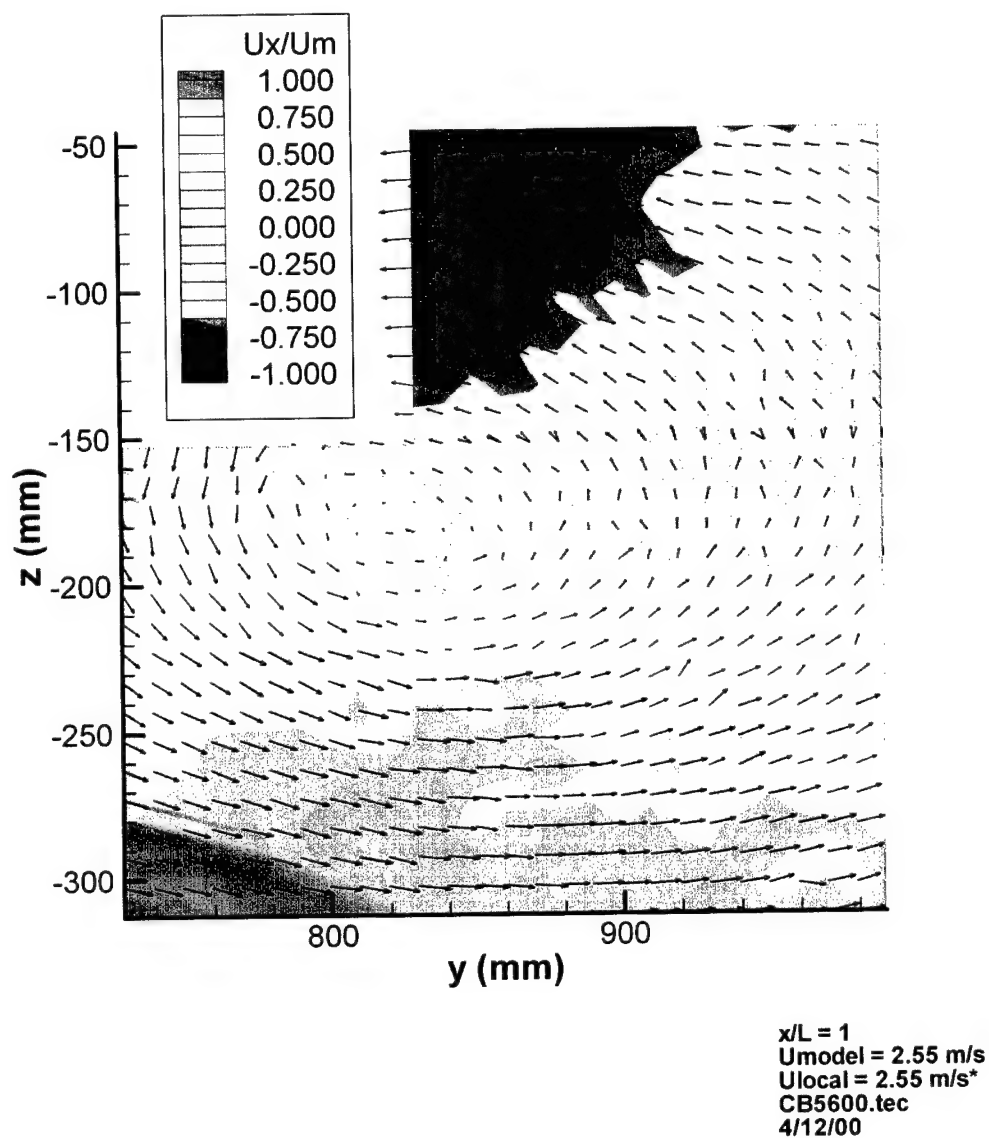
Figure 4.18 LDV survey of mean streamwise velocity component for $\eta = -1.15$ (mean velocity vectors overlaid; propeller plane located at $y = 809.2$ mm; propeller radius = 152.4 mm)

158

MSU/ONR Crashback
Model 5495-3, Prop. 4381
Prop Speed -600 rpm

x/L = 1
Umodel = 2.55 m/s
Ulocal = 2.55 m/s*
CB5600.tec
4/12/00
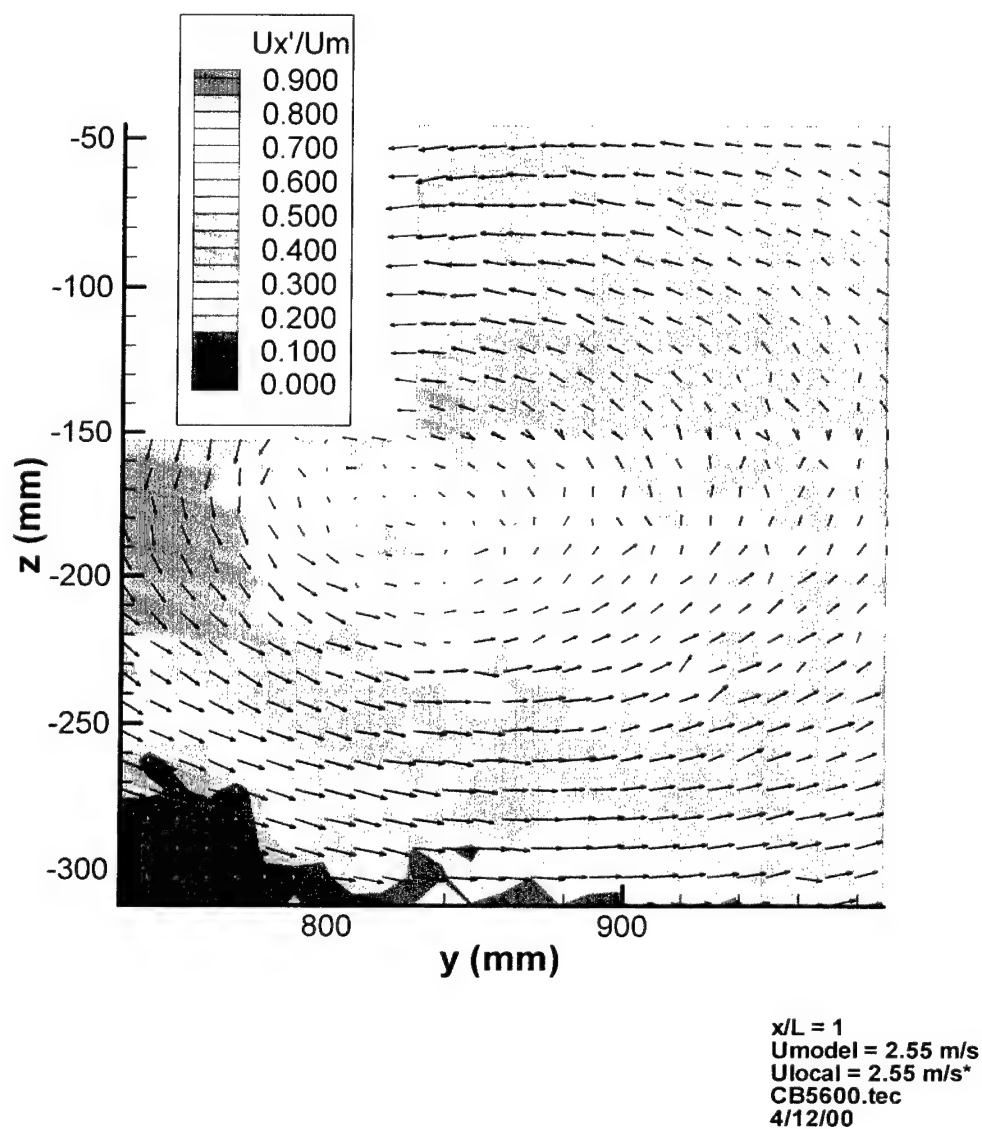
Figure 4.19 LDV survey of RMS streamwise velocity component for η = -1.15 (mean velocity vectors overlaid; propeller plane located at y = 809.2 mm; propeller radius = 152.4 mm)

MSU/ONR Crashback
Model 5495-3, Prop. 4381
Prop Speed -600 rpm
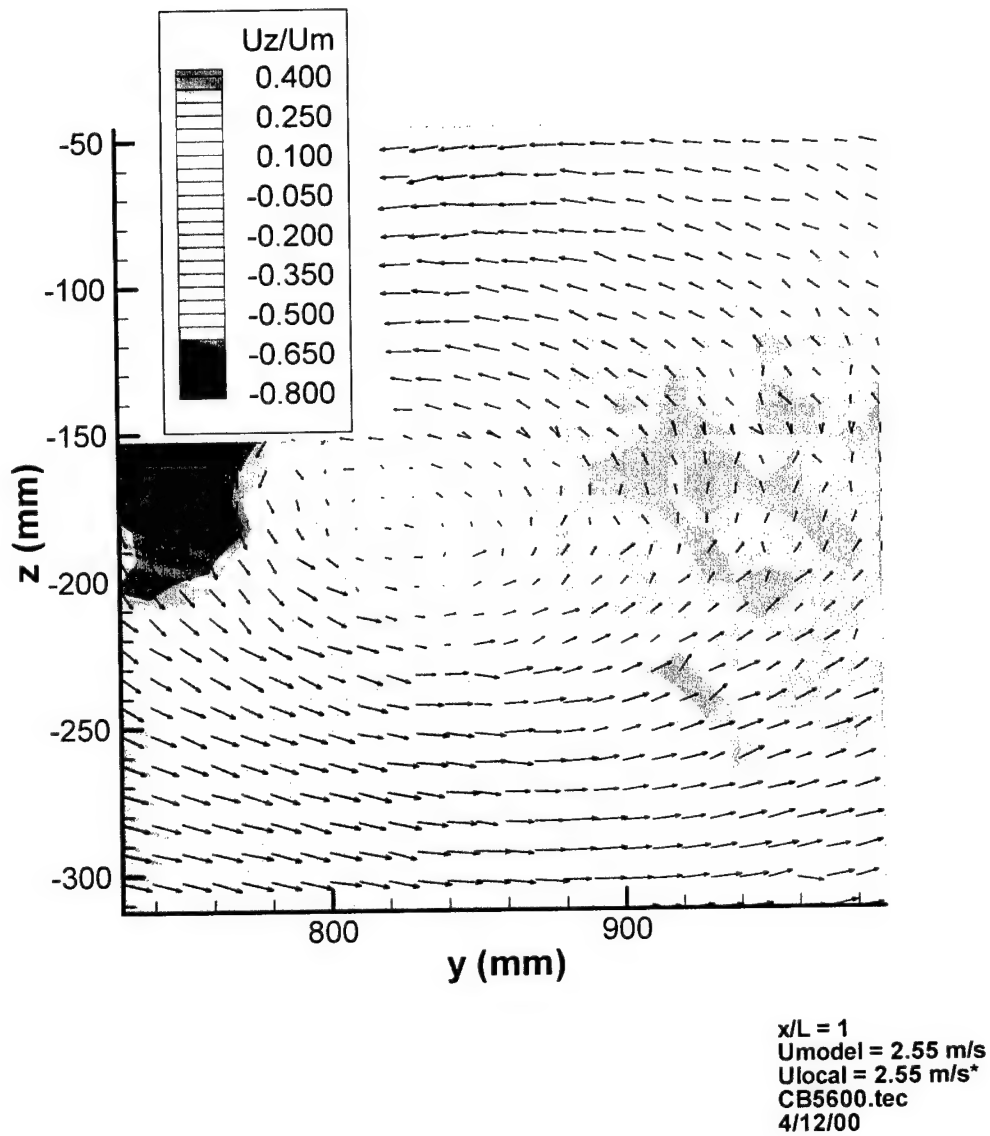
Figure 4.20 LDV survey of mean transverse velocity component for $\eta = -1.15$ (mean velocity vectors overlaid; propeller plane located at $y = 809.2$ mm; propeller radius = 152.4 mm)

MSU/ONR Crashback
Model 5495-3, Prop. 4381
Prop Speed -600 rpm

x/L = 1
Umodel = 2.55 m/s
Ulocal = 2.55 m/s*
CB5600.tec
4/12/00
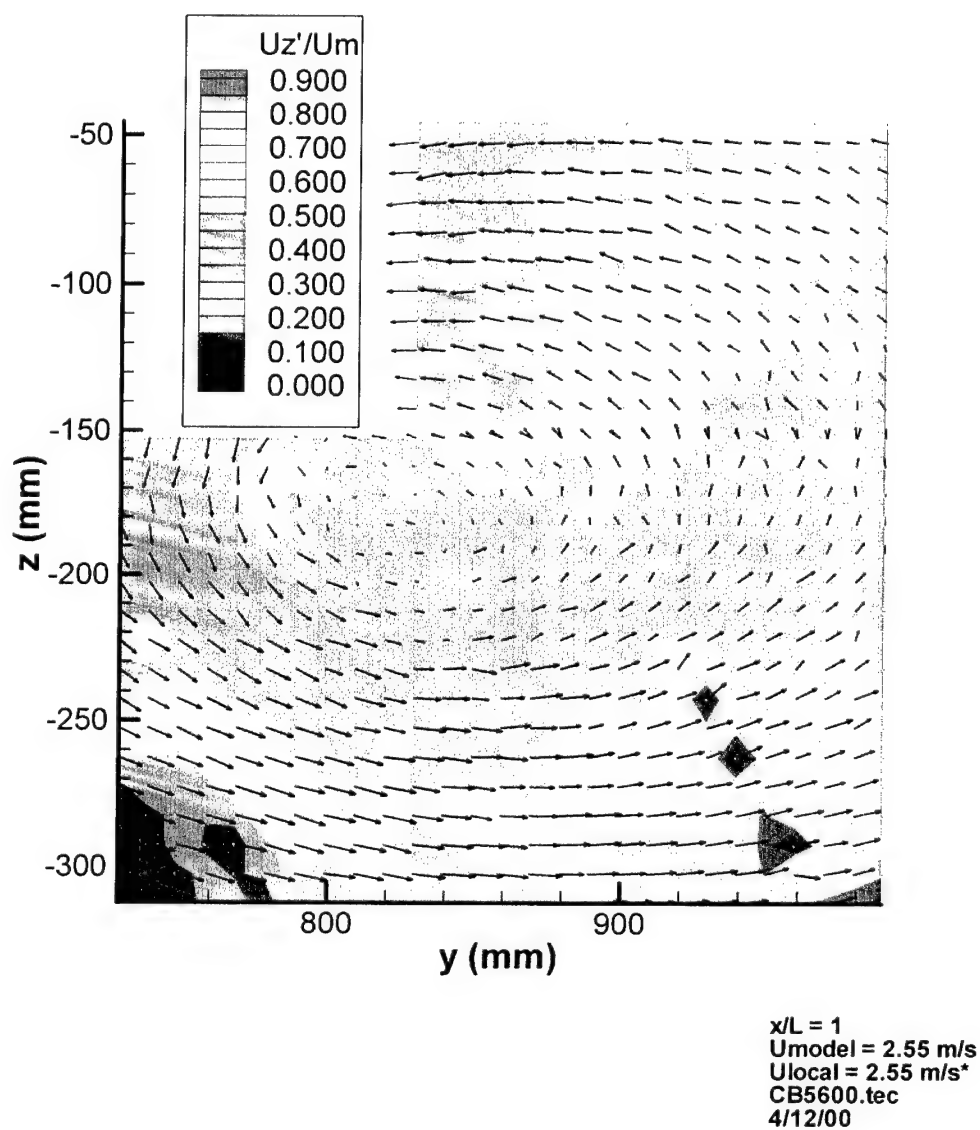
Figure 4.21 LDV survey of RMS transverse velocity component for η = -1.15 (mean velocity vectors overlaid; propeller plane located at y = 809.2 mm; propeller radius = 152.4 mm)

MSU/ONR Crashback Test
Model 5495, Prop 4381
Prop Speed -680 rpm

x/L = 1
Umodel = 3.83 m/s
Ulocal = 3.85 m/s*
Prop1.tec
4/5/00
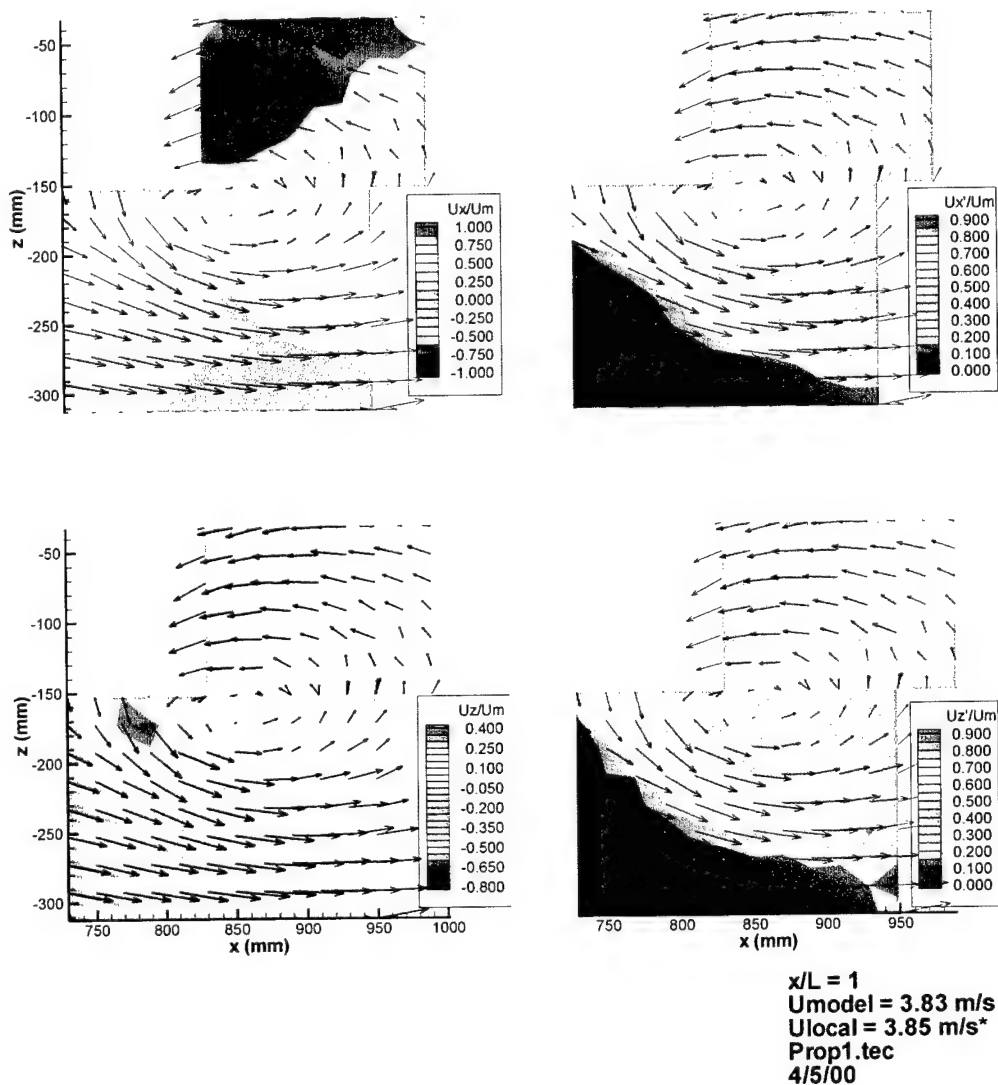
Figure 4.22 Summary of LDV velocity field surveys for η = -0.877 and tunnel set speed of 7.5 kts (Propeller plane located at x = 809.2 mm; propeller radius = 152.4 mm)

MSU/ONR Crashback Test
Model 5495, Prop 4381
Prop Speed -680 rpm

x/L = 1
Umodel = 3.83 m/s
Ulocal = 3.85 m/s*
Prop1.tec
4/5/00
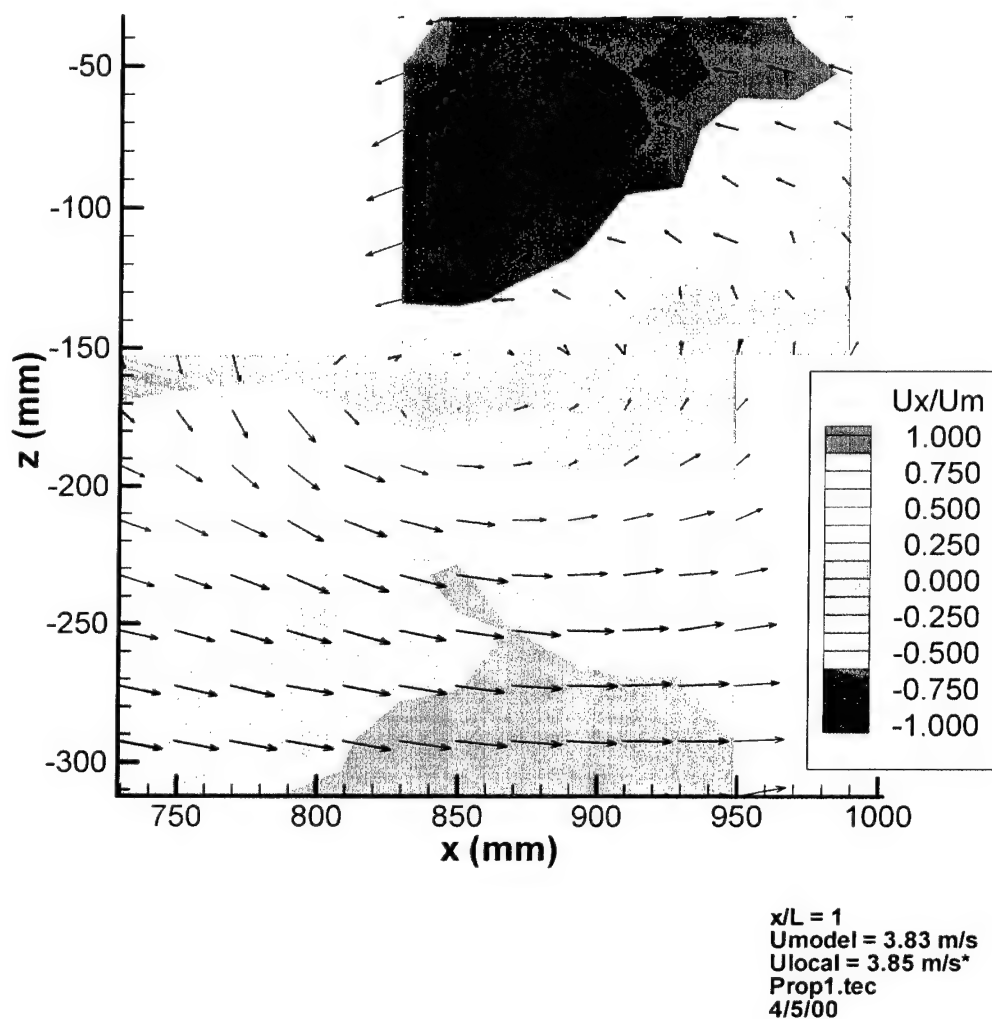
Figure 4.23 LDV survey of mean streamwise velocity component for η = -0.877 and tunnel set speed of 7.5 kts (mean velocity vectors overlaid; propeller plane located at x = 809.2 mm; propeller radius = 152.4 mm)

Figure 4.24 LDV survey of RMS streamwise velocity component for η = -0.877 and tunnel set speed of 7.5 kts (mean velocity vectors overlaid; propeller plane located at x = 809.2 mm; propeller radius = 152.4 mm)

MSU/ONR Crashback Test
Model 5495, Prop 4381
Prop Speed -680 rpm

Figure 4.25 LDV survey of mean transverse velocity component for η = -0.877 and tunnel set speed of 7.5 kts (mean velocity vectors overlaid; propeller plane located at x = 809.2 mm; propeller radius = 152.4 mm)

MSU/ONR Crashback Test
Model 5495, Prop 4381
Prop Speed -680 rpm
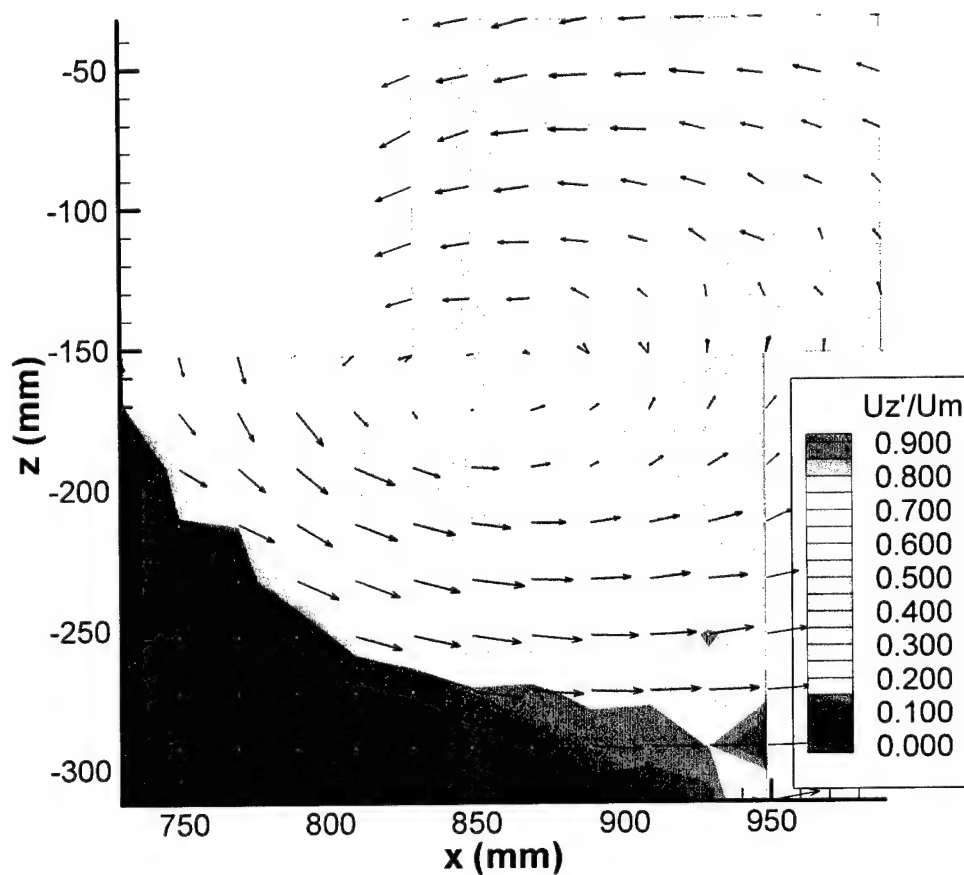
x/L = 1
Umodel = 3.83 m/s
Ulocal = 3.85 m/s*
Prop1.tec
4/5/00

Figure 4.26 LDV survey of RMS transverse velocity component for η = -0.877 and tunnel set speed of 7.5 kts (mean velocity vectors overlaid; propeller plane located at x = 809.2 mm; propeller radius = 152.4 mm)
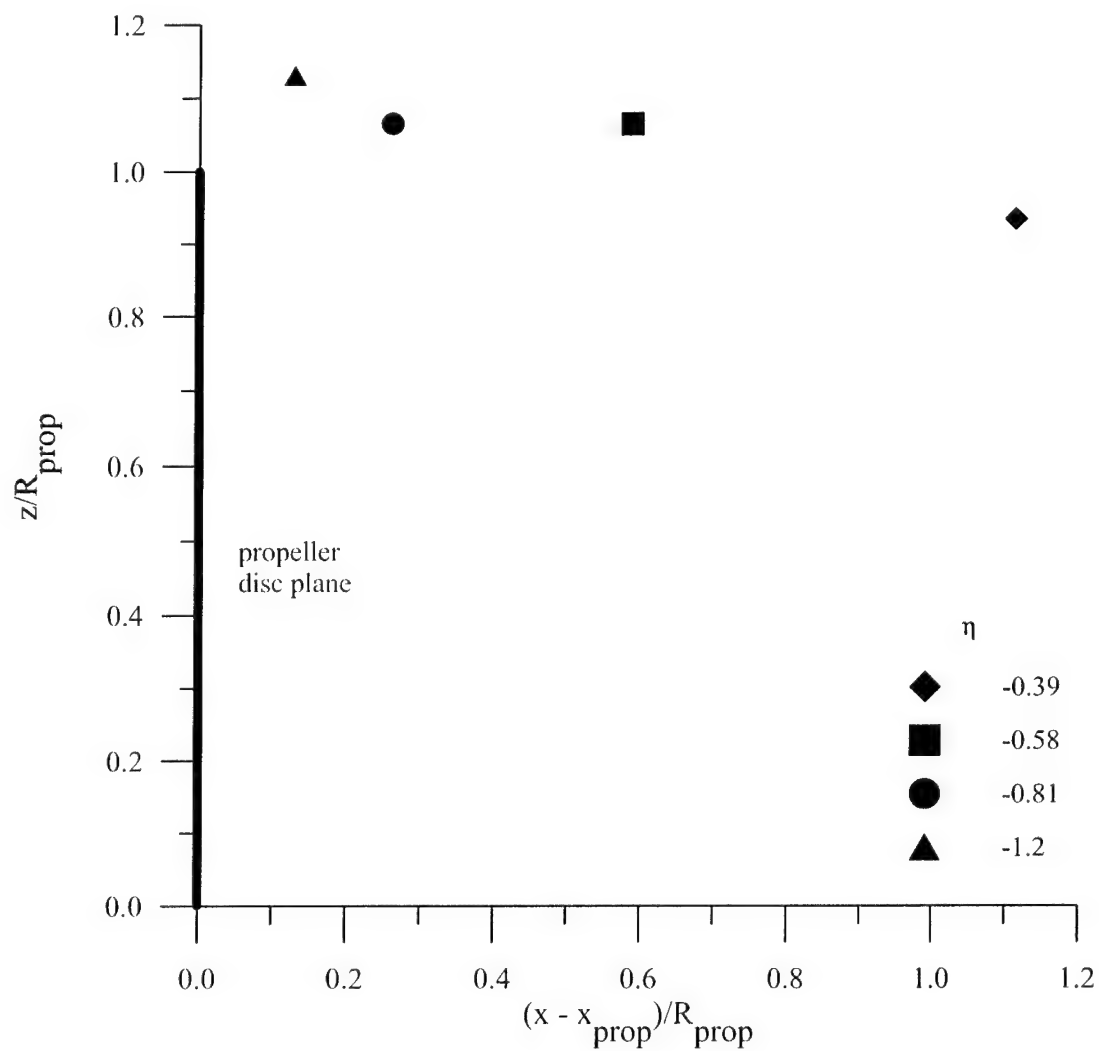
Figure 4.27 Vortex center positions estimated from LDV measurements
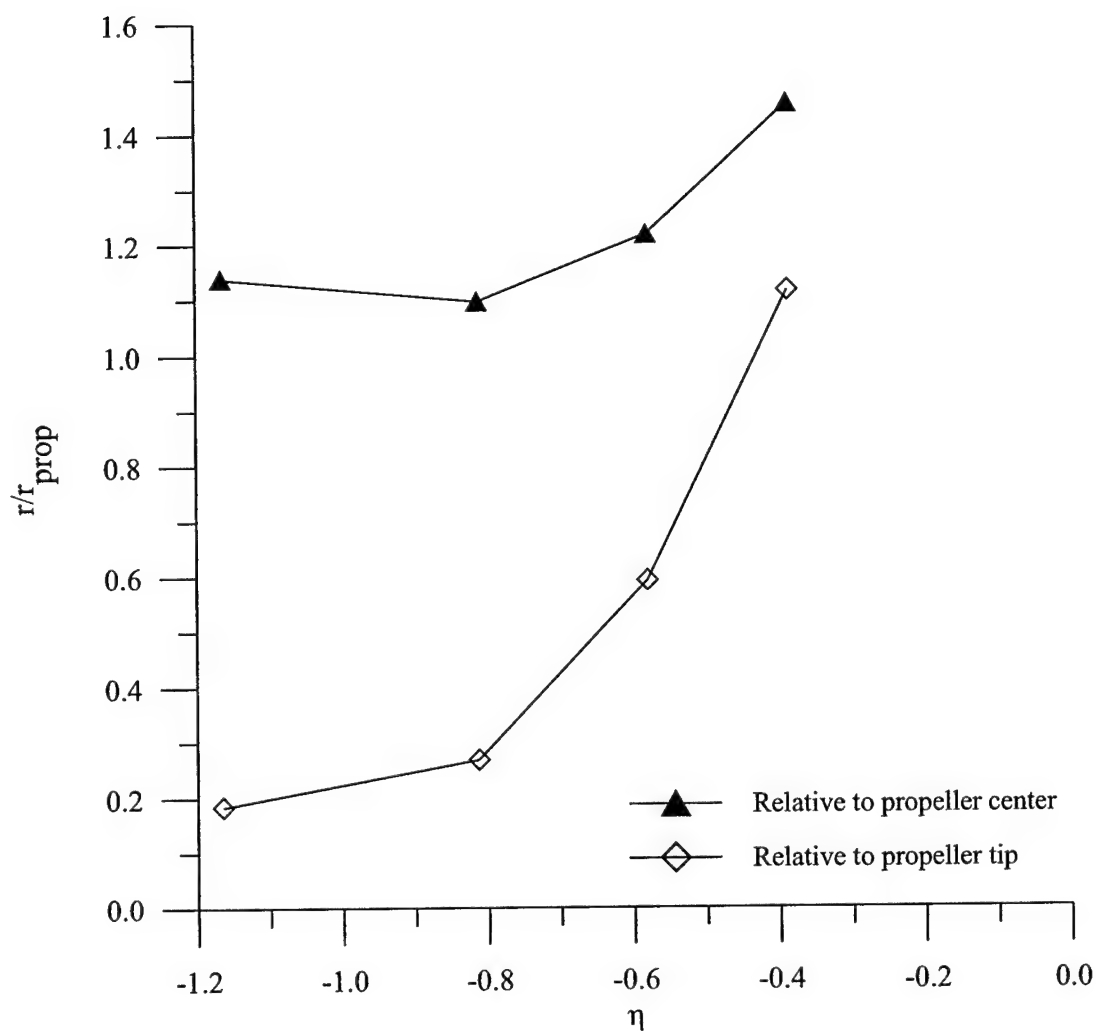
Figure 4.28 Vortex center distances normalized by the propeller radius
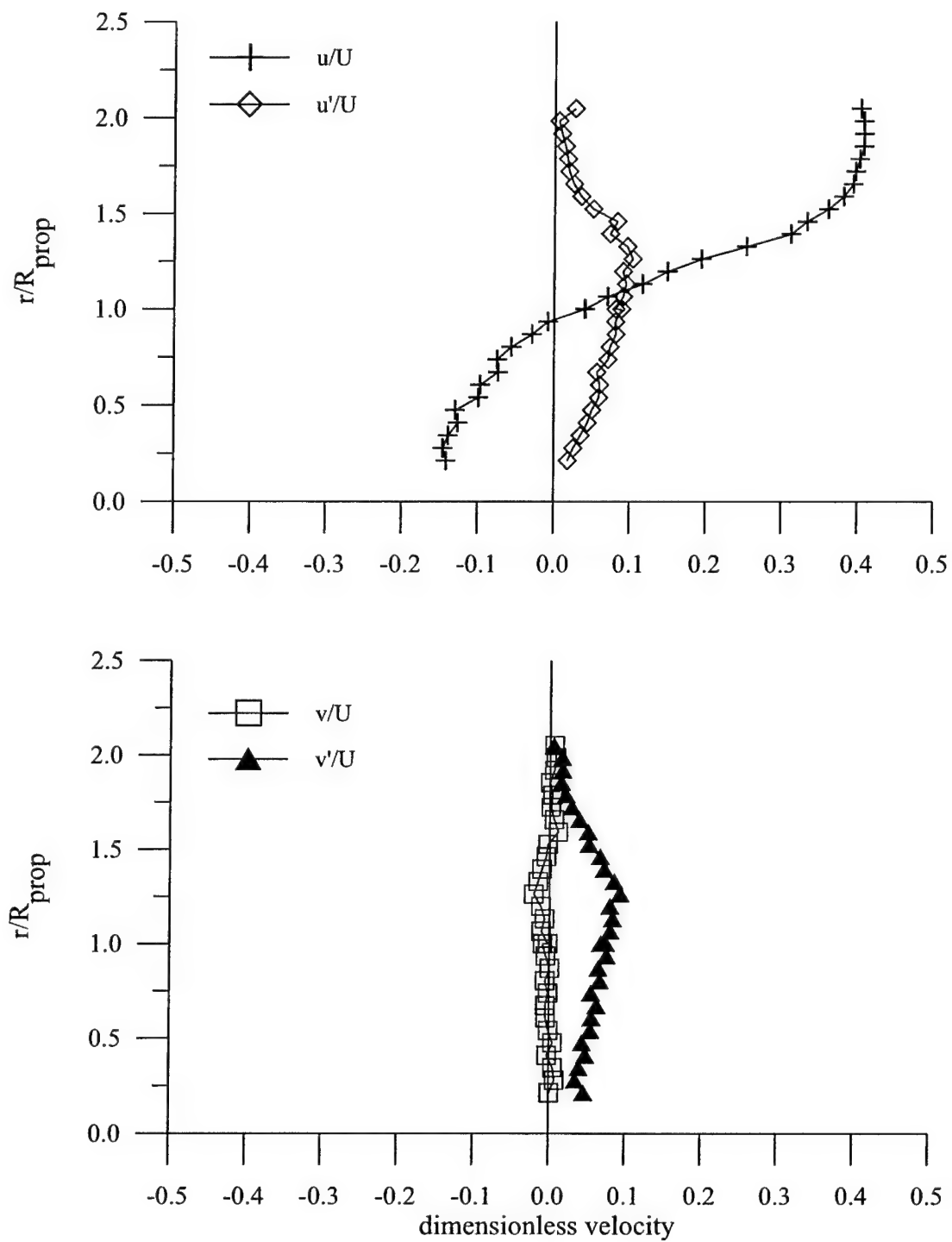
Figure 4.29 Velocity components at nominal vortex core position $(x - x_{prop})/R_{prop} = 1.1$ for $\eta = -0.38$
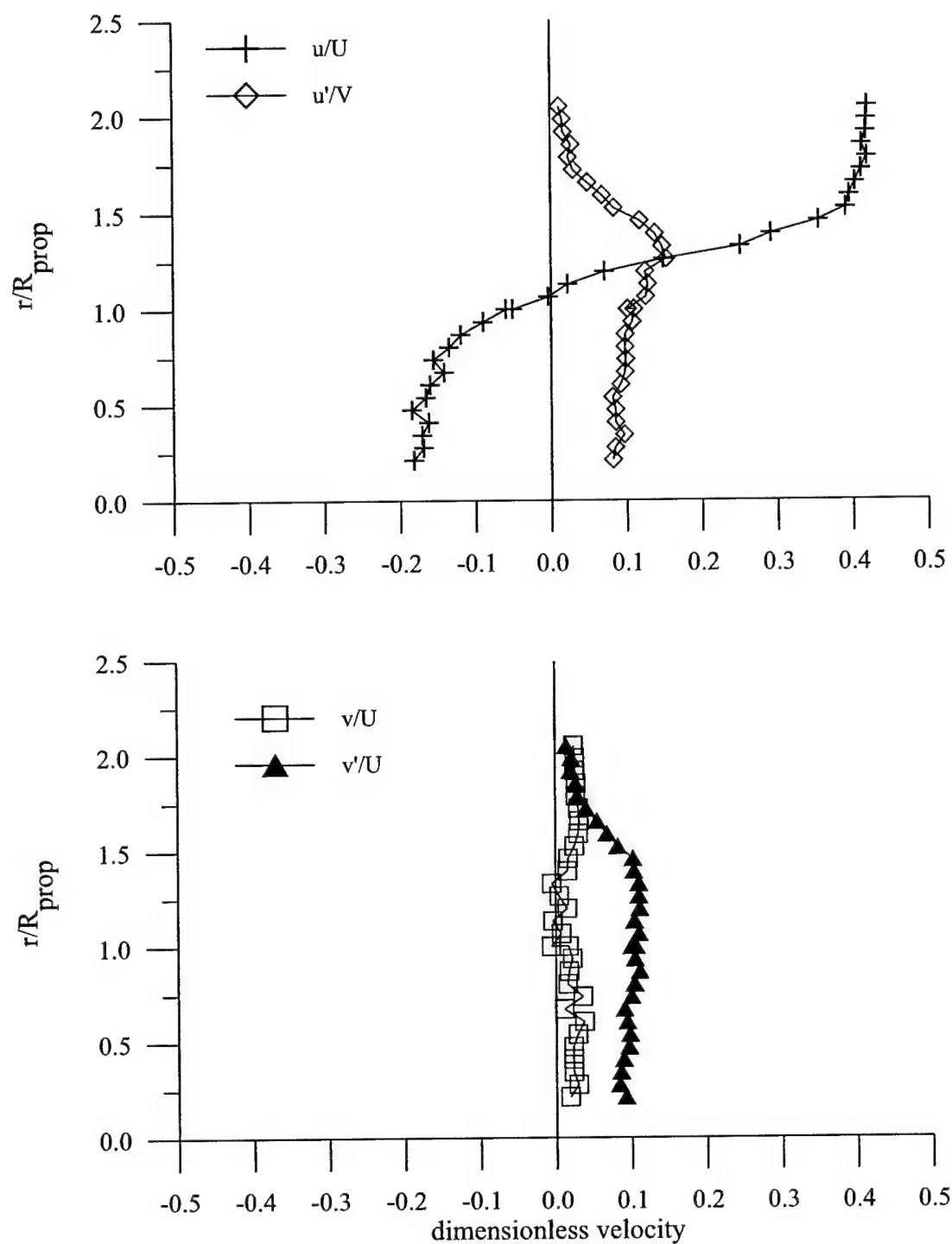
Figure 4.30 Velocity components at nominal vortex core position $(x - x_{prop})/R_{prop} = 0.59$ for $\eta = -0.57$
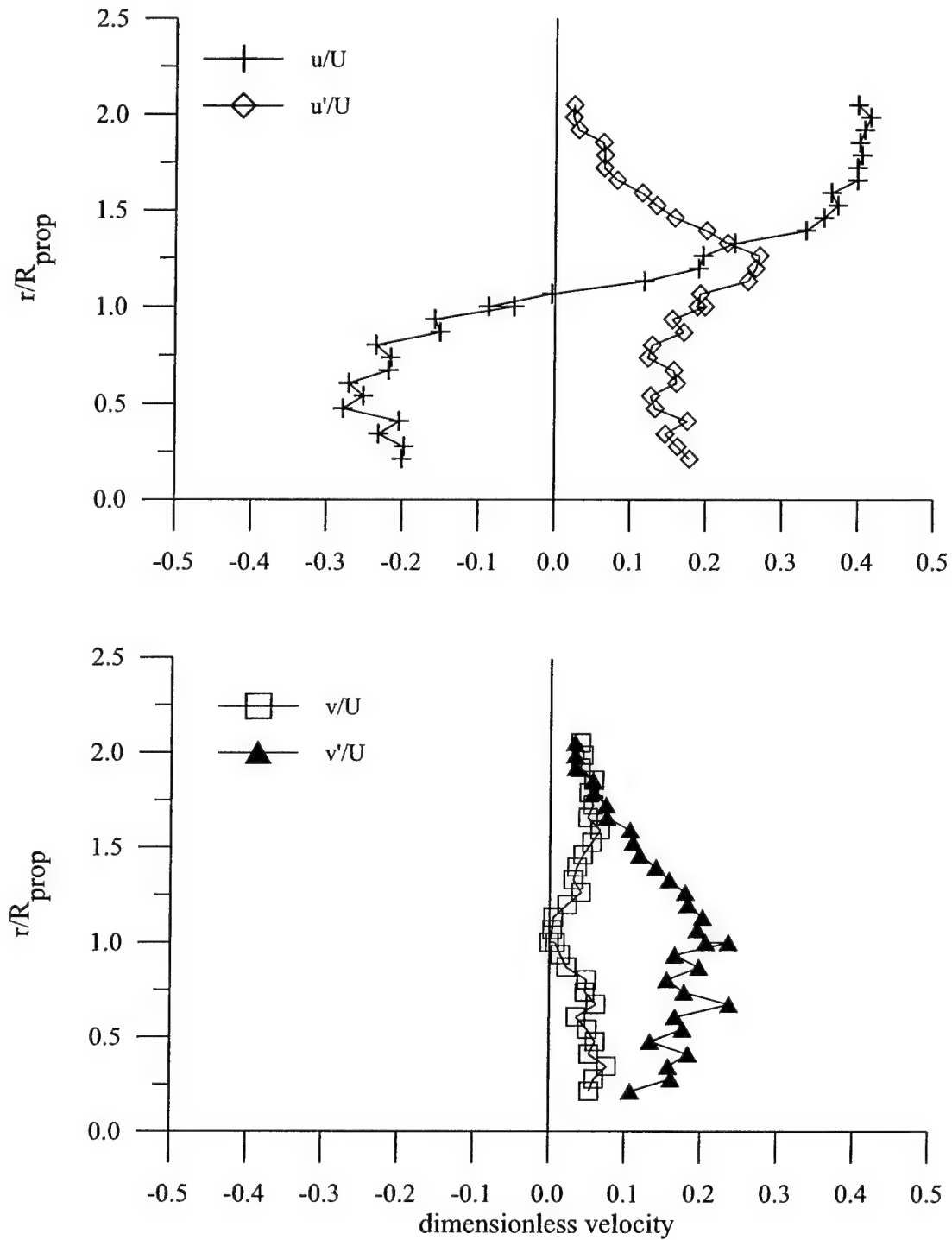
Figure 4.31 Velocity components at nominal vortex core position $(x - x_{prop})/R_{prop} = 0.26$ for $\eta = -0.80$
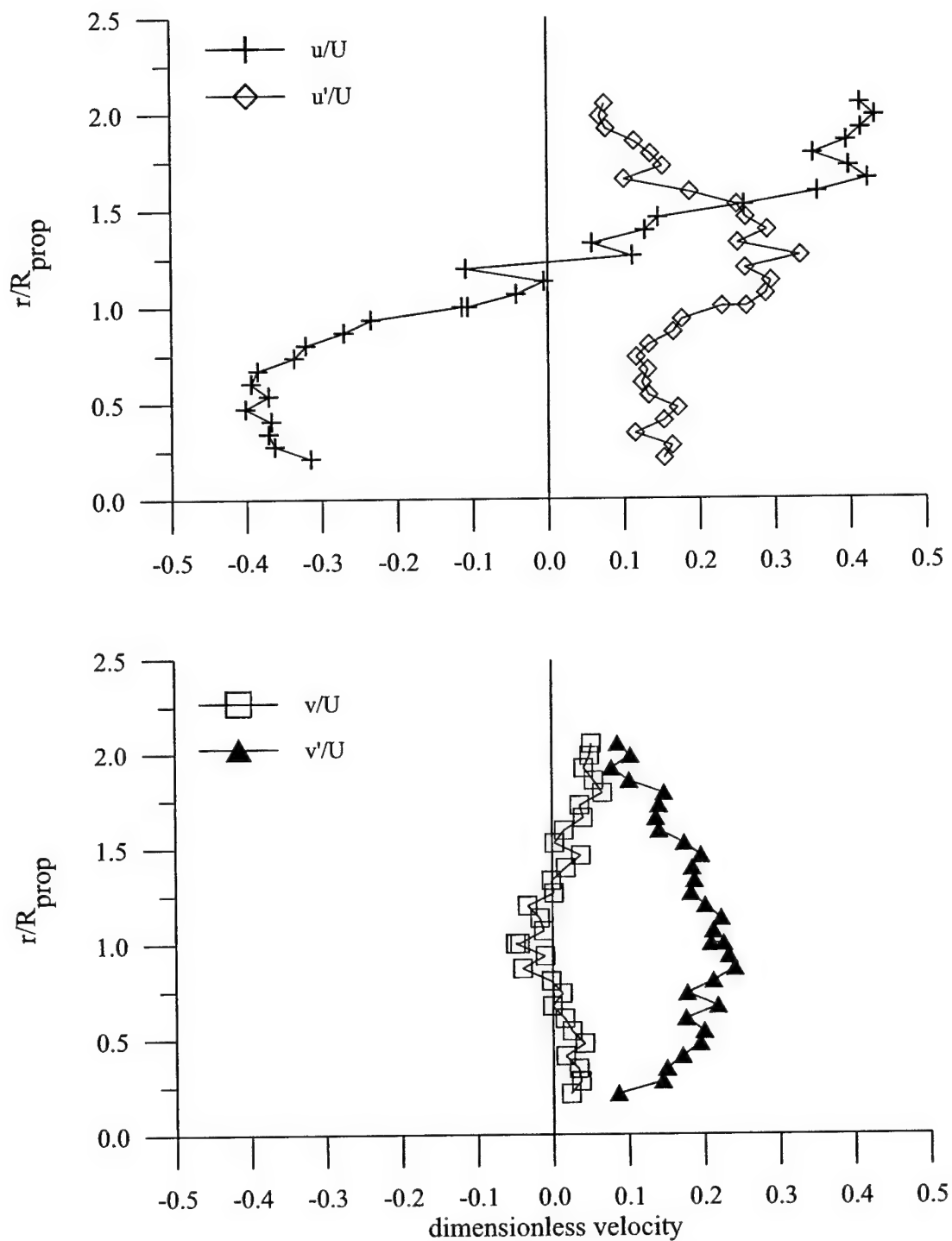
Figure 4.32 Velocity components at nominal vortex core position $(x - x_{prop})/R_{prop} = 0.13$ for $\eta = -1.2$
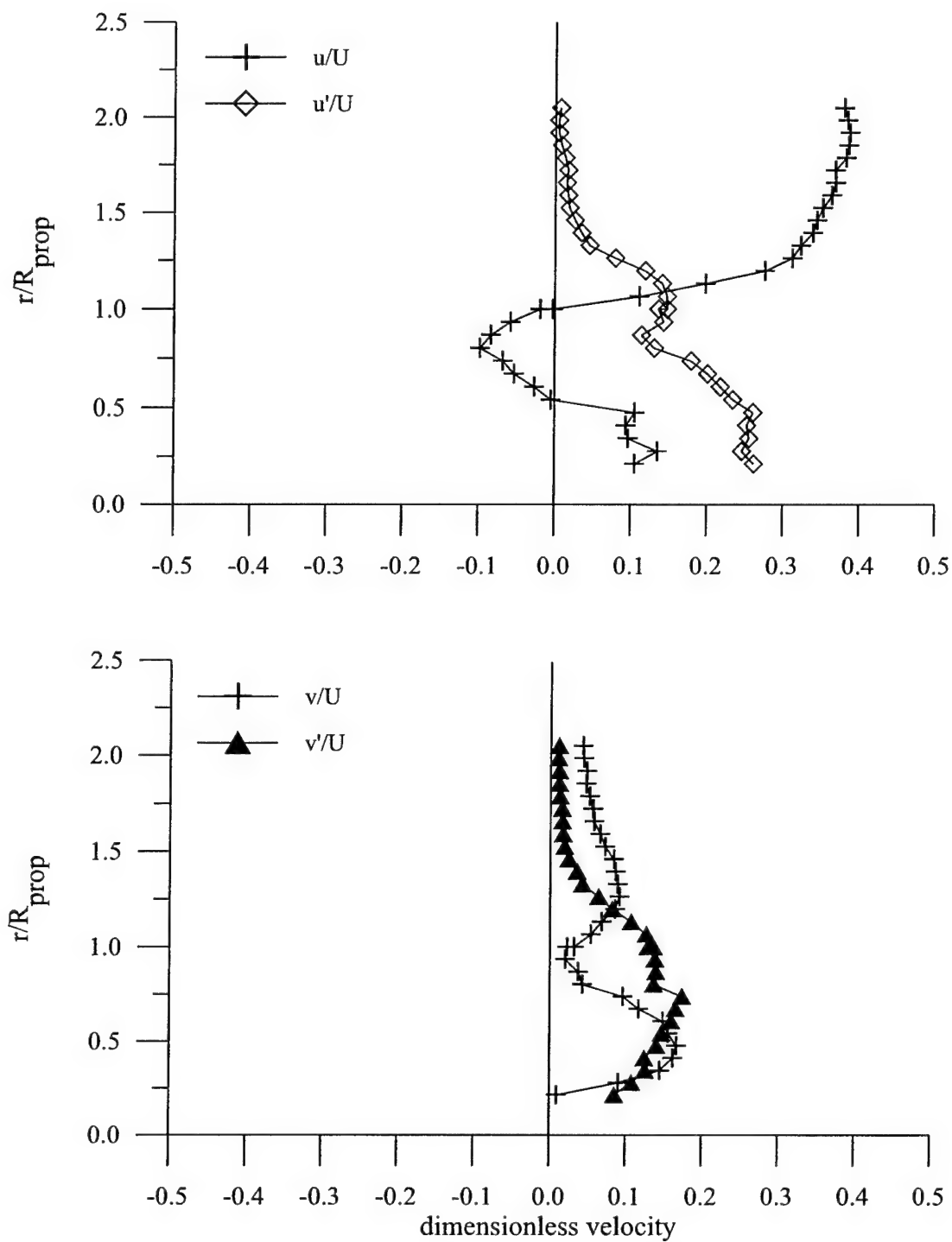
Figure 4.33 Velocity components at complete survey position nearest propeller for η = -0.38
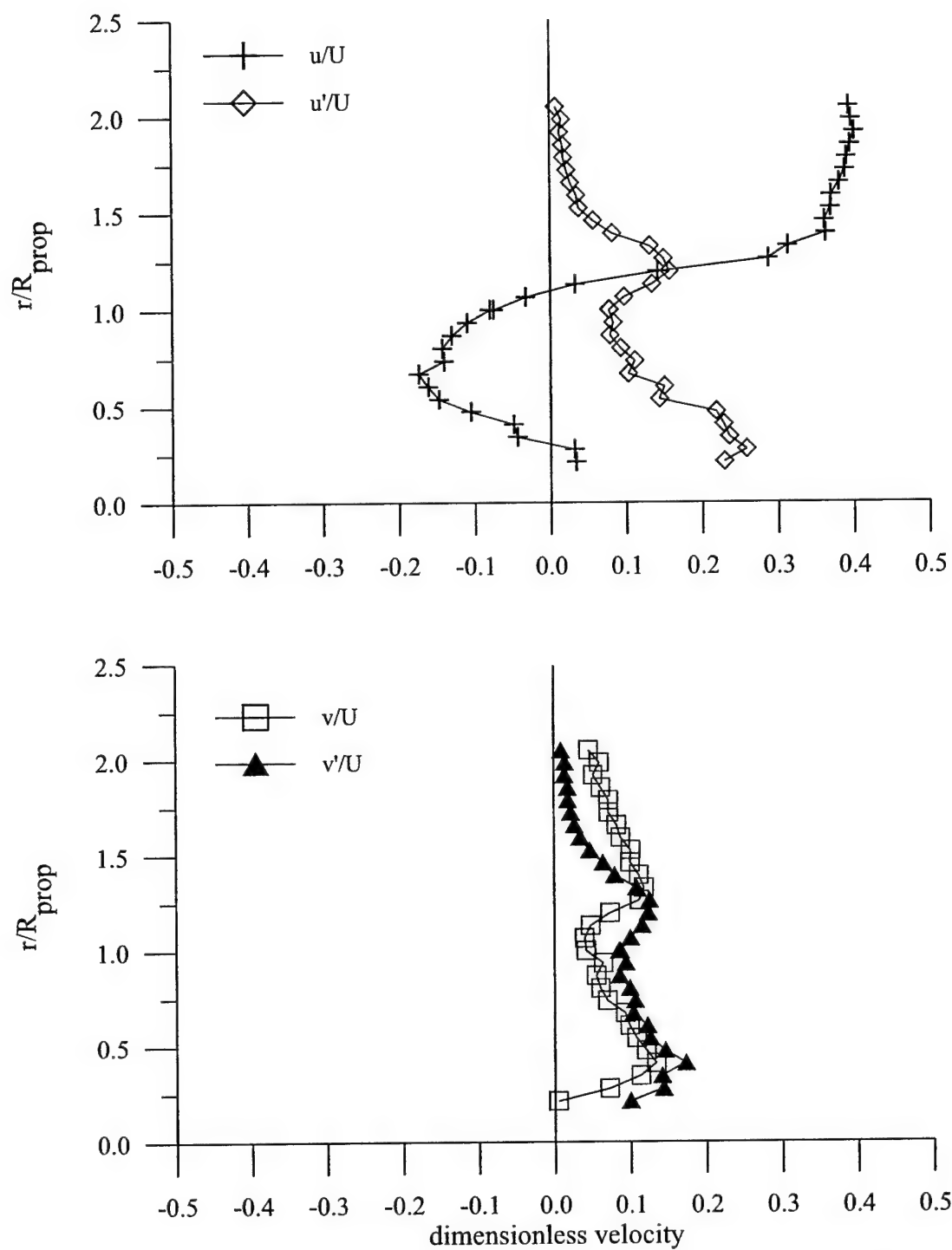
Figure 4.34 Velocity components at complete survey position nearest propeller for η = -0.57
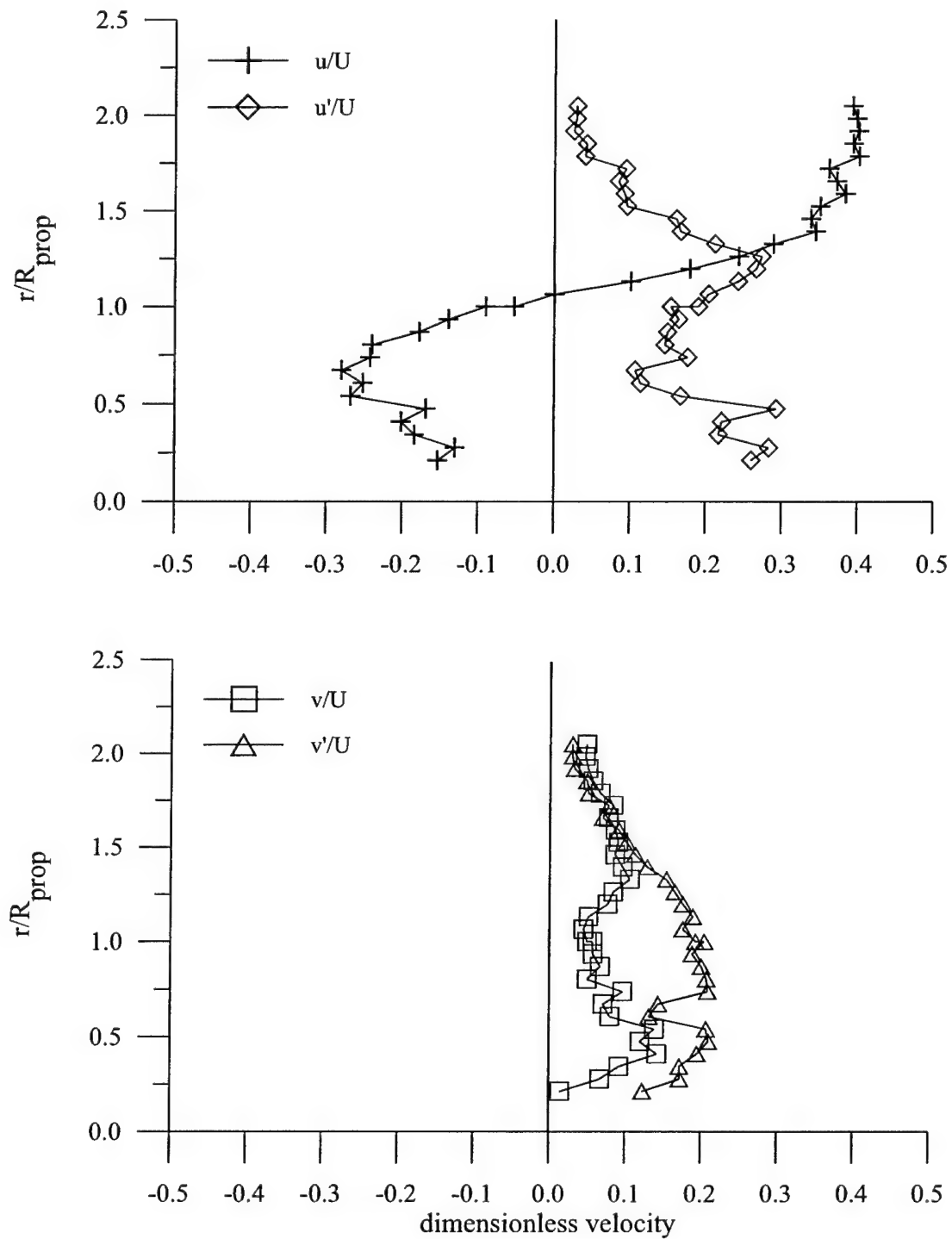
Figure 4.35 Velocity components at complete survey position nearest propeller for $\eta = -0.80$
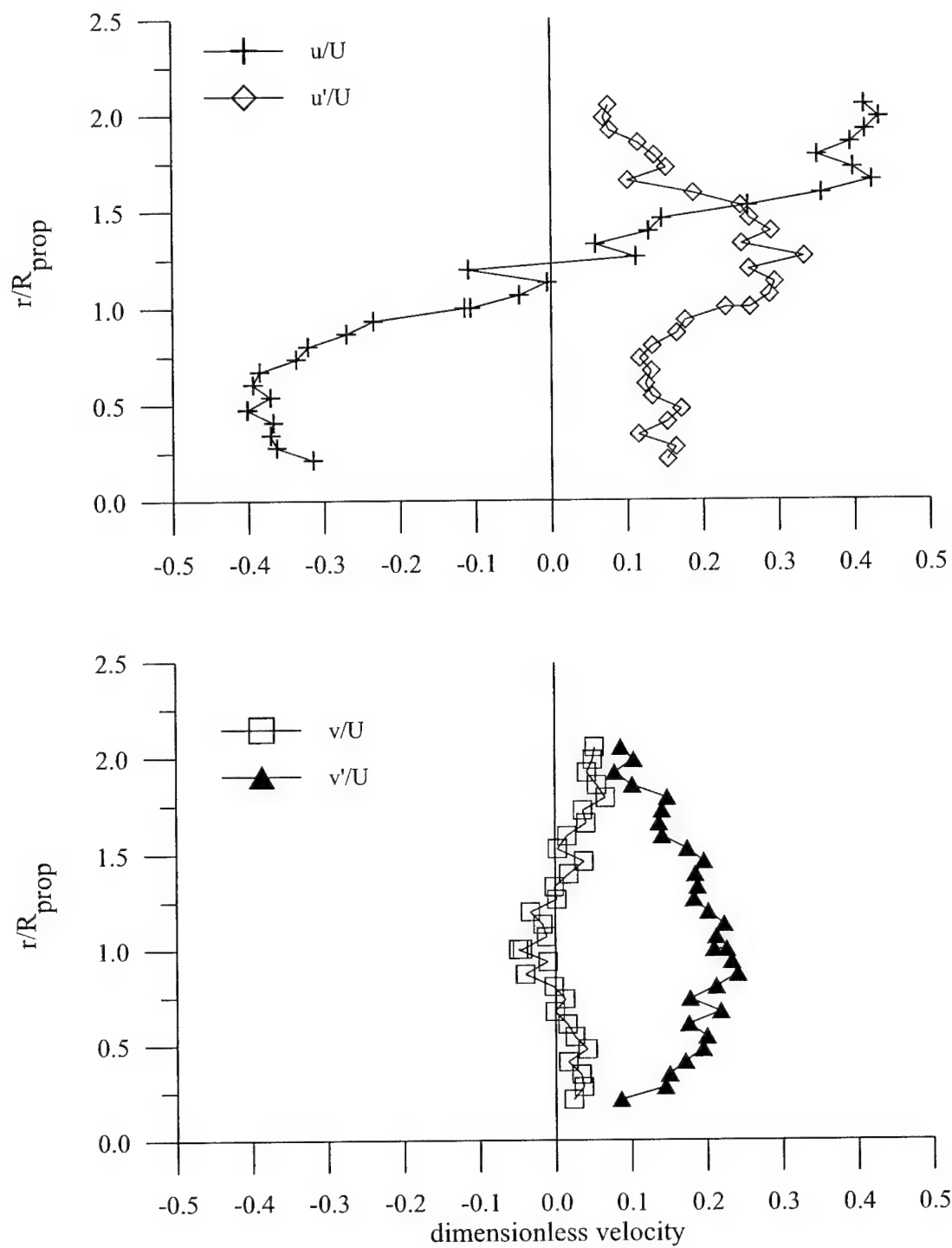
Figure 4.36 Velocity components at complete survey position nearest propeller for $\eta = -1.2$

(a) V = 5 kts, n = 200 RPM, η = -0.380

(b) V = 5 kts, n = 200 RPM, η = -0.380
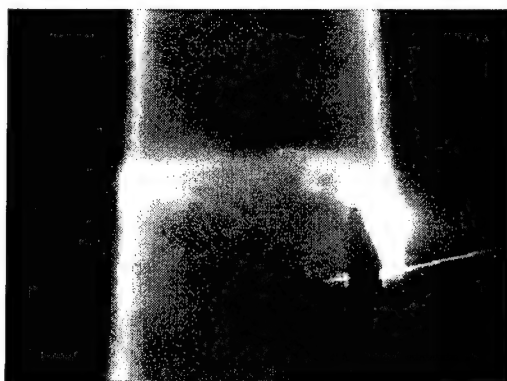
(c) V = 7.5 kts, n = 300 RPM, η = -0.387
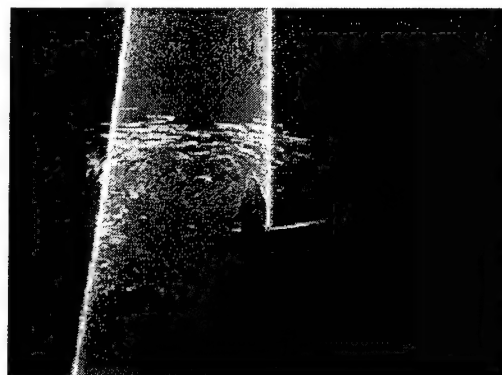

(d) V = 7.5 kts, n = 300 RPM, η = -0.387
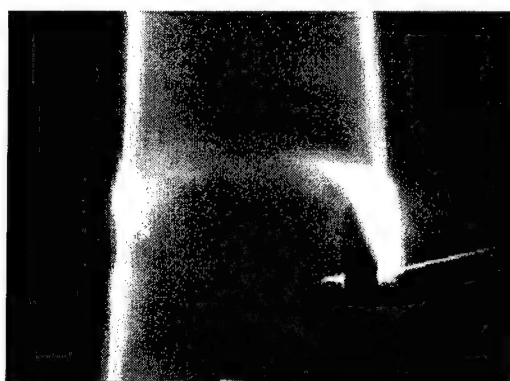
(e) V = 10 kts, n = 400 RPM, η = -0.390

Figure 4.37 Flow visualization results for $\eta \approx$ -0.4
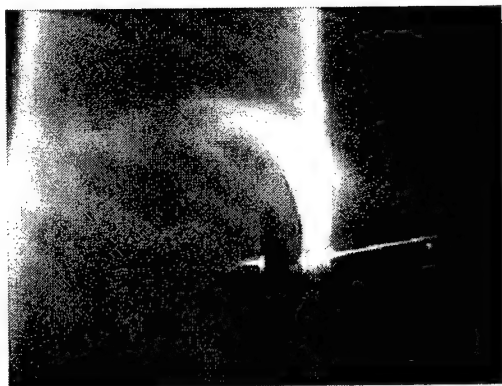
(a) V = 5 kts, n = 300 RPM, η = -0.571
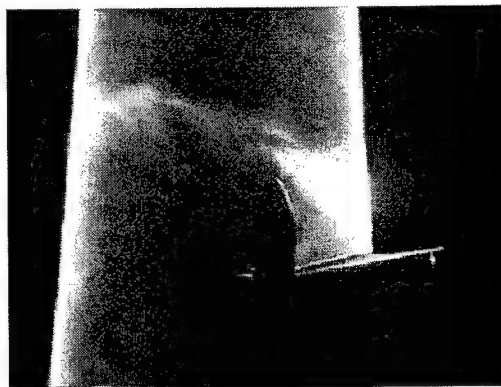
(b) V = 5 kts, n = 300 RPM, η = -0.571
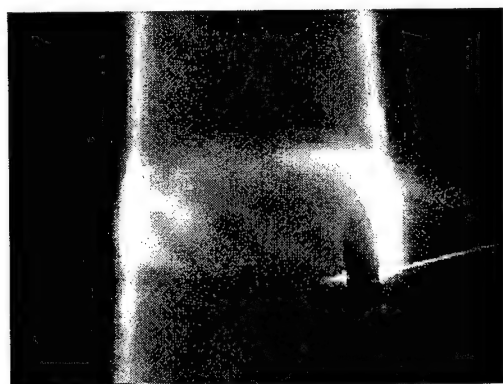
(c) V = 7.5 kts, n = 450 RPM, η = -0.580
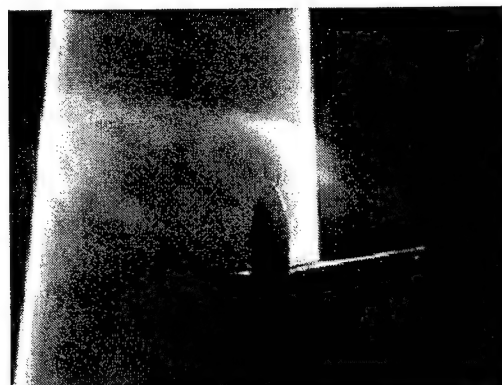
(d) V = 7.5 kts, n = 450 RPM, η = -0.580
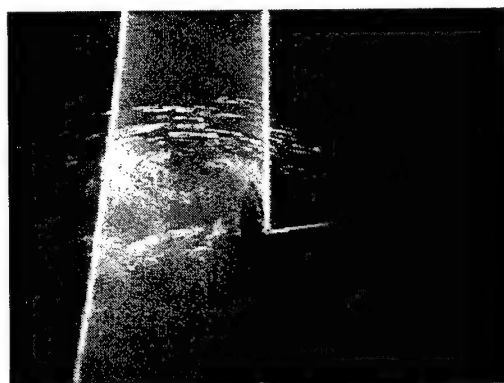
(e) V = 7.5 kts, n = 450 RPM, η = -0.580
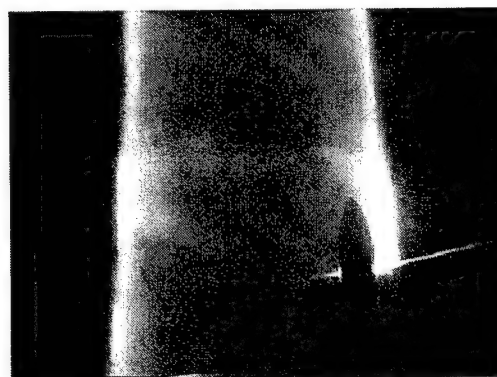
(f) V = 10 kts, n = 600 RPM, η = -0.585

Figure 4.38 Flow visualization results for $\eta \approx$ -0.6
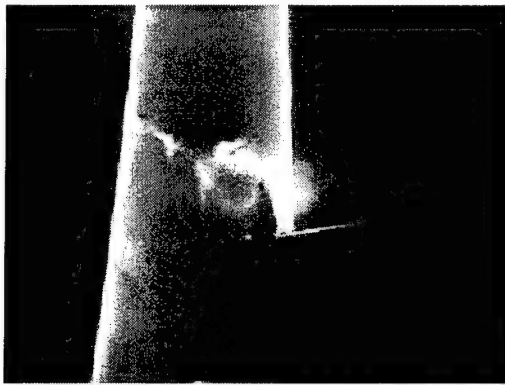
(a) V = 2.5 kts, n = 200 RPM, η = -0.725

(b) V = 5 kts, n = 375 RPM, η = -0.713
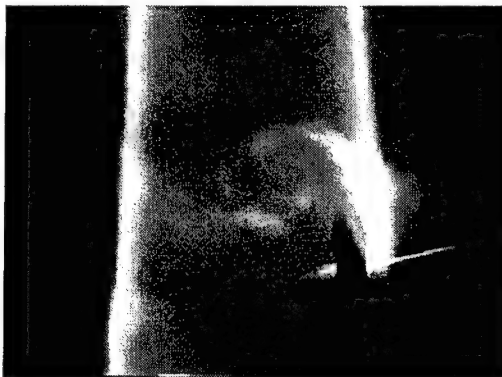
(c) V =2.5 kts, n = 200 RPM, η = -0.725
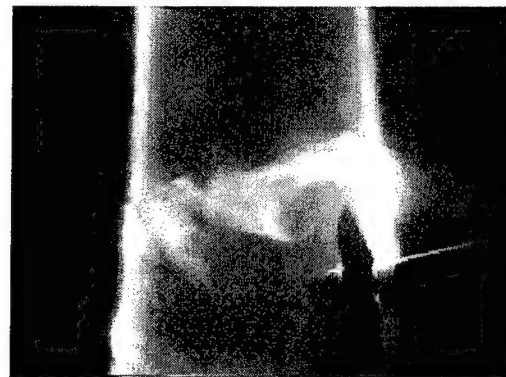
(d) V = 2.5 kts, n = 200 RPM, η = -0.725
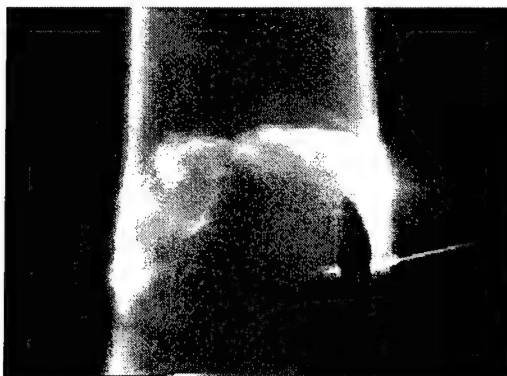
(e) V = 2.5 kts, n = 200 RPM, η = -0.725
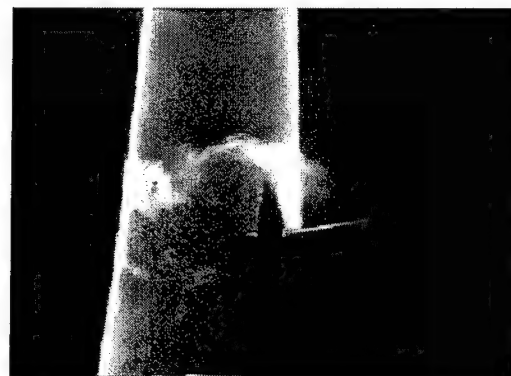
(f) V = 2.5 kts, n = 200 RPM, η = -0.725

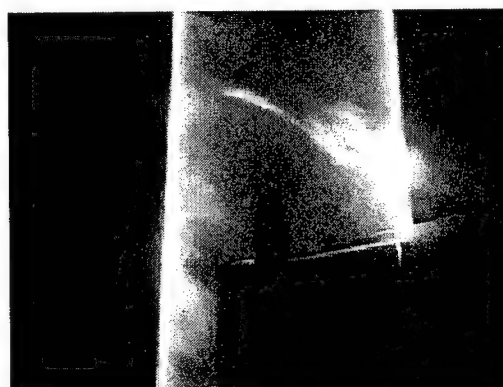**Figure 4.39** Flow visualization results for $\eta \approx$ -0.7

(g) V = 5 kts, n = 375 RPM, η = -0.713
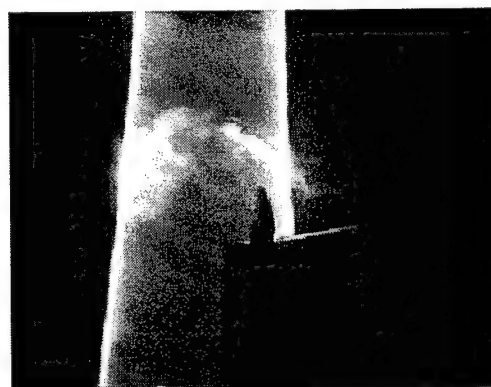
(h) V = 2.5 kts, n = 200 RPM, η = -0.725

Figure 4.39 Flow visualization results for $\eta \approx$ -0.7 (concluded)
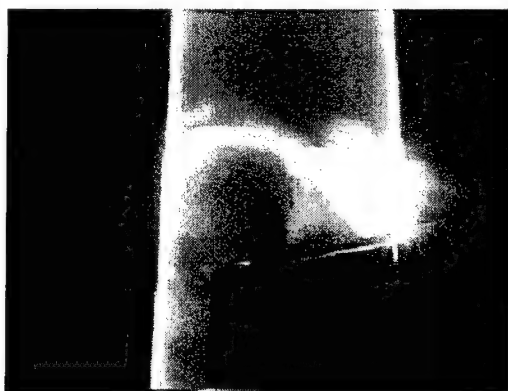
(a) $V = 5$ kts, $n = 425$ RPM, $\eta = -0.808$

(b) $V = 5$ kts, $n = 425$ RPM, $\eta = -0.808$

(c) $V = 5$ kts, $n = 425$ RPM, $\eta = -0.808$

(d) $V = 6.25$ kts, $n = 525$ RPM, $\eta = -0.807$

(e) $V = 7.5$ kts, $n = 640$ RPM, $\eta = -0.825$
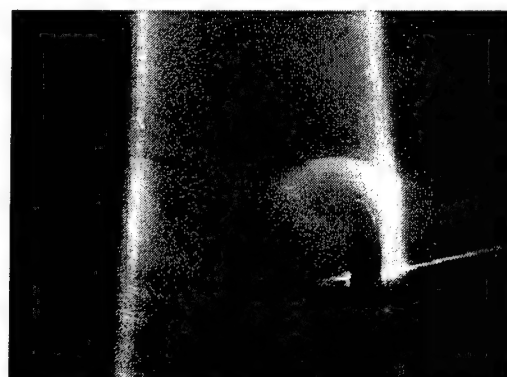
(f) $V = 7.5$ kts, $n = 640$ RPM, $\eta = -0.825$

Figure 4.40 Flow visualization results for $\eta \approx -0.8$
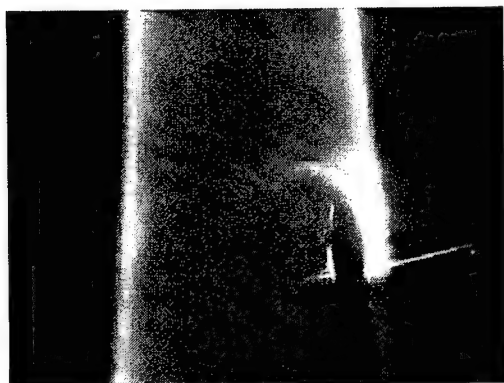
(g) $V = 10$ kts, $n = 800$ RPM, $\eta = -0.780$
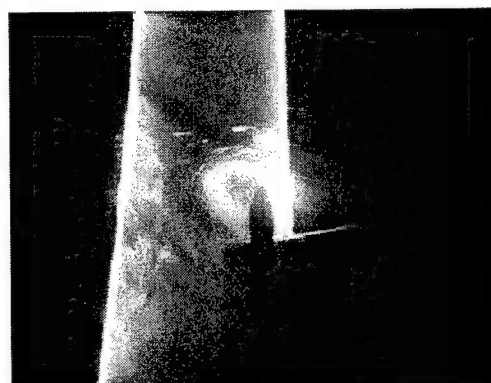
(h) $V = 7.5$ kts, $n = 640$ RPM, $\eta = -0.825$
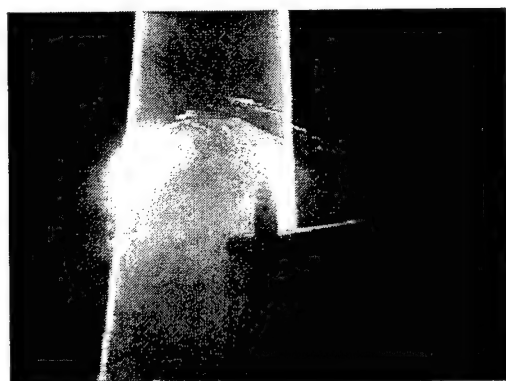
(i) $V = 7.5$ kts, $n = 800$ RPM, $\eta = -0.780$
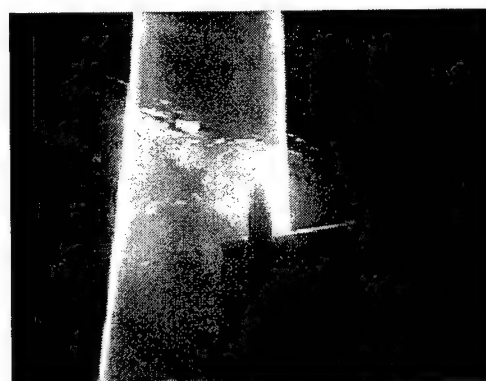
(j) $V = 7.5$ kts, $n = 800$ RPM, $\eta = -0.780$
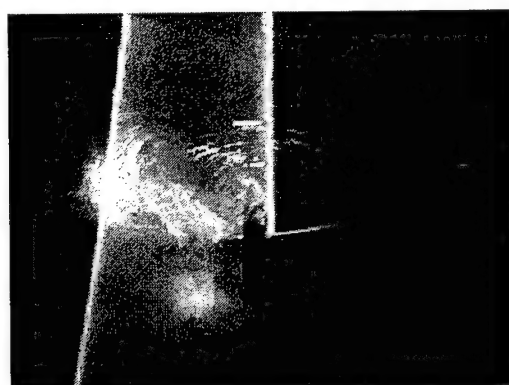
(k) $V = 7.5$ kts, $n = 800$ RPM, $\eta = -0.780$
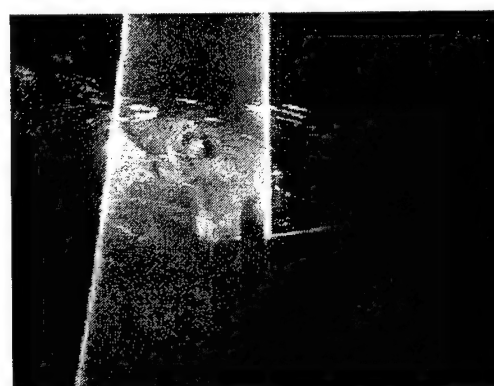
(l) $V = 7.5$ kts, $n = 800$ RPM, $\eta = -0.780$

Figure 4.40 Flow visualization results for $\eta \approx -0.8$ (concluded)
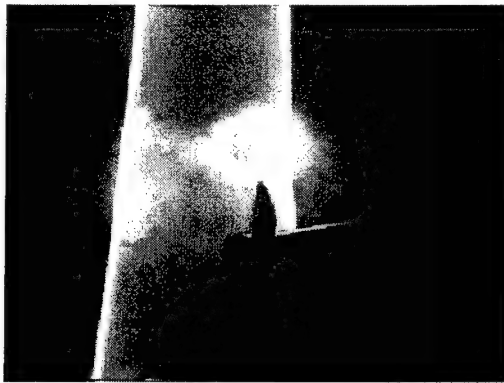
(a) V = 2.5 kts, n = 300 RPM, η = -1.087
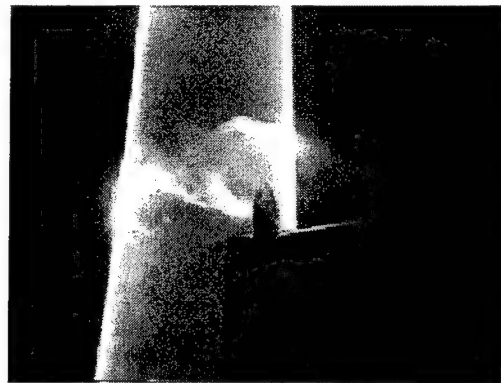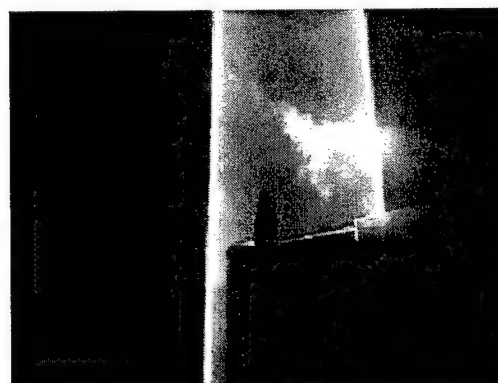

(b) V = 2.5 kts, n = 300 RPM, η = -1.087
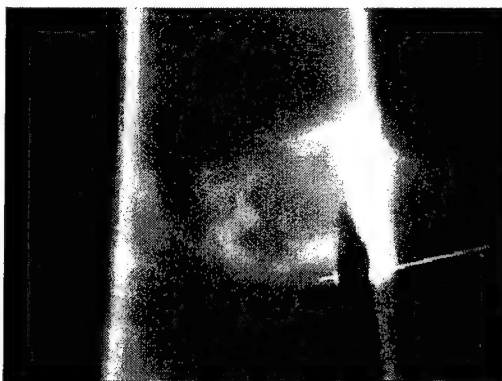
(c) V = 2.5 kts, n = 318 RPM, η = -1.152
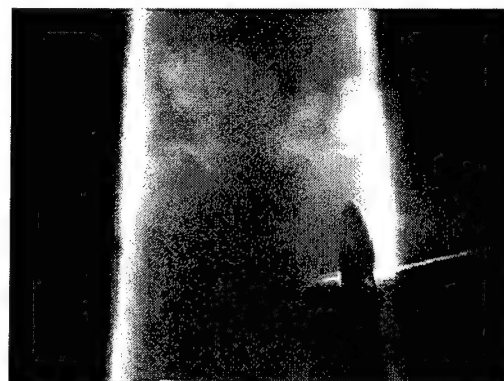
(d) V = 2.5 kts, n = 318 RPM, η = -1.152
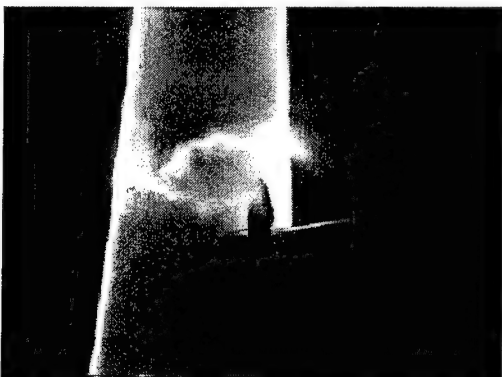
(e) V = 2.5 kts, n = 300 RPM, η = -1.087

(f) V = 5 kts, n = 600 RPM, η = -1.141

Figure 4.41 Flow visualization results for $\eta \approx$ -1.1
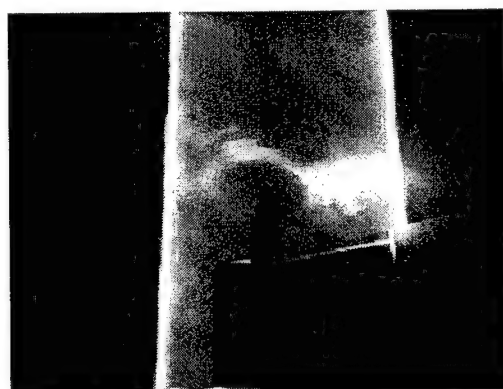
(g) V = 5 kts, n = 600 RPM, η = -1.141
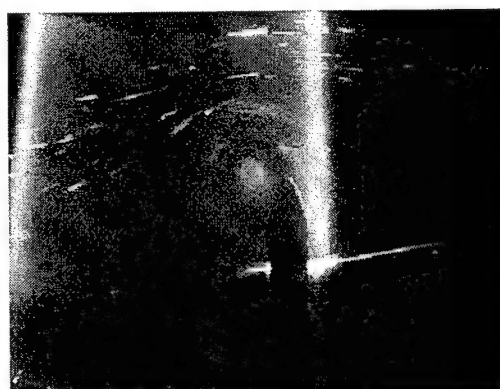
(h) V = 5 kts, n = 600 RPM, η = -1.141

(i) V = 5 kts, n = 600 RPM, η = -1.141

(j) V = 5 kts, n = 600 RPM, η = -1.141

(k) V = 5 kts, n = 600 RPM, η = 1.141
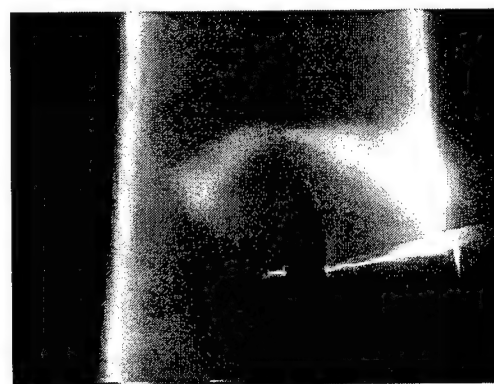
(l) V = 6.25 kts, n = 700 RPM, η = -1.076

Figure 4.41 Flow visualization results for $\eta \approx$ -1.1 (continued)
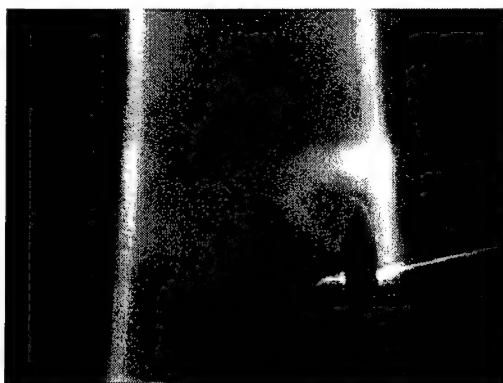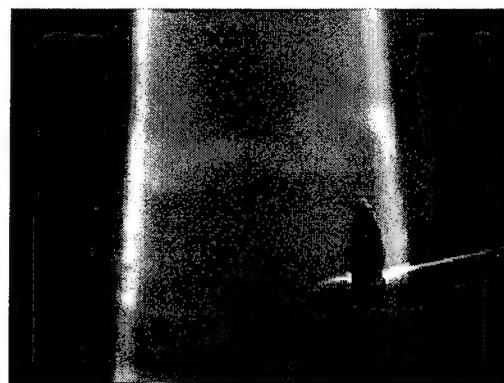
(m) V =7.5 kts, n = 900 RPM, η = -1.16   (n) V = 7.5 kts, n = 900 RPM, η = -1.16

Figure 4.41   Flow visualization results for $\eta \approx$ -1.1 (concluded)

(a) V = 2.5 kts, n = 420 RPM, η = -1.522

(b) V = 2.5 kts, n = 420 RPM, η = -1.522

(c) V = 2.5 kts, n = 420 RPM, η = -1.522

(d) V = 2.5 kts, n = 420 RPM, η = -1.522
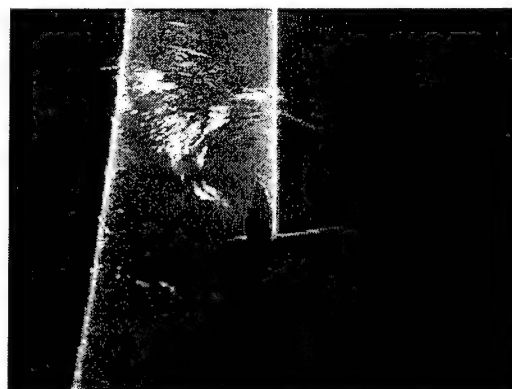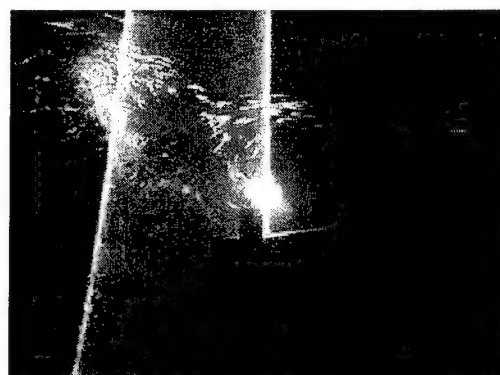
(e) V = 2.5 kts, n = 420 RPM, η = -1.522

(f) V = 2.5 kts, n = 420 RPM, η = -1.522

Figure 4.42 Flow visualization results for $\eta \approx$ -1.5
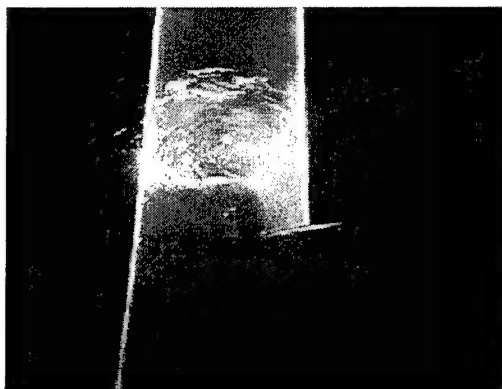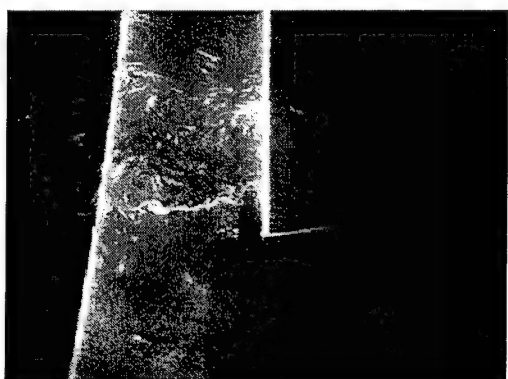
(g) V = 5 kts, n = 800 RPM, η = -1.521

(h) V = 5 kts, n = 800 RPM, η = -1.521
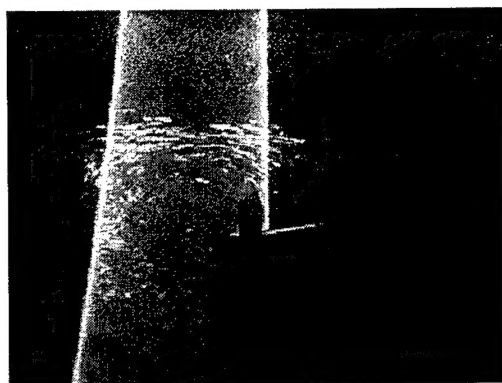

(i) V = 5 kts, n = 800 RPM, η = -1.521
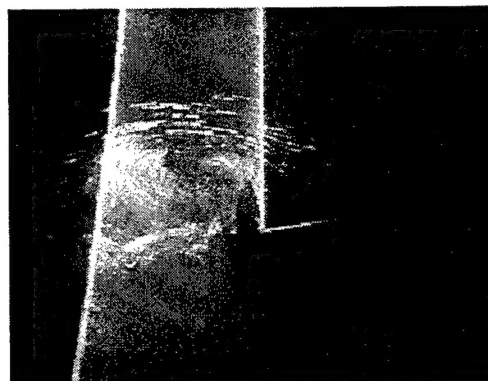

(j) V = 5 kts, n = 800 RPM, η = -1.521
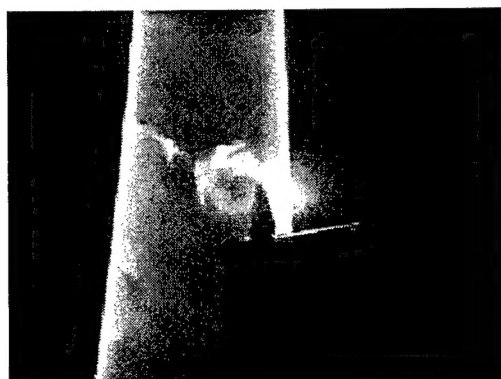

(k) V = 5 kts, n = 800 RPM , η = 1.521

Figure 4.42 Flow visualization results for η ≈-1.5 (concluded)
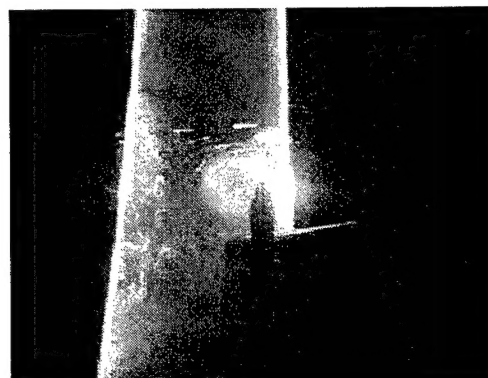
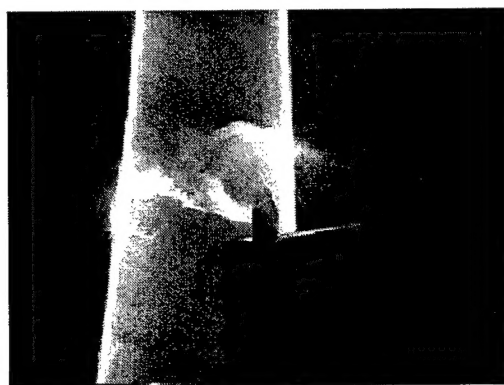(a) V = 7.5 kts, n = 300 RPM, η = -0.387

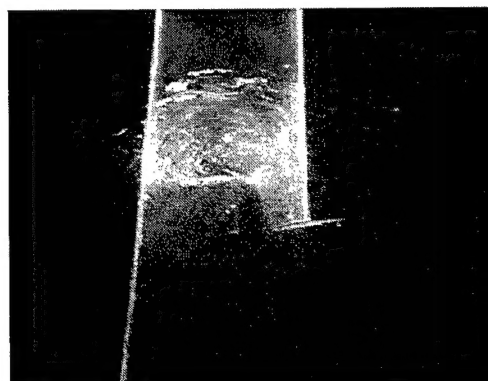(b) V = 7.5 kts, n = 450 RPM, η = -0.580

(c) V = 2.5 kts, n = 200 RPM, η = -0.725

(d) V = 7.5 kts, n = 640 RPM, η = -0.825

(e) V = 2.5 kts, n = 300 RPM, η = -1.087

(f) V = 5 kts, n = 800 RPM, η = -1.521

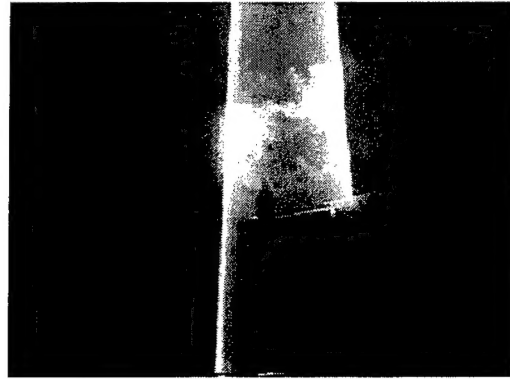**Figure 4.43** Comparison of "formed vortex" positions at different values of η
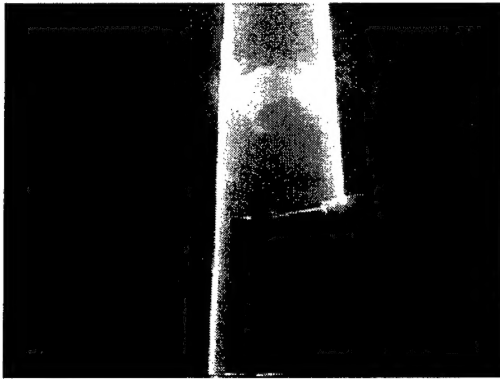
Figure 4.44 Flow visualization images at V = 2.5 kts, n = 600 RPM, η = -2.17
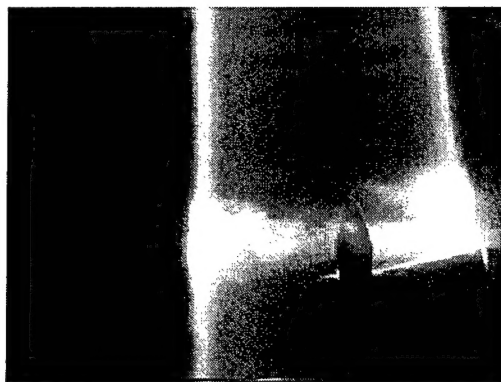

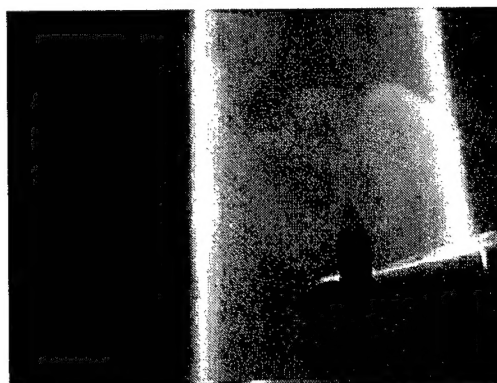**Figure 4.45** Example of flow for forward propeller rotation: V = 7.5 kts, n = 330 RPM (forward)

1

2

3

4

5

6

Figure 4.46 Example of flow visualization results for ramped propeller and tunnel speeds: $+330$ RPM $> n > -500$ RPM, 7.5 kts $> V > 0$ kts

REPORT DOCUMENTATION PAGE

Form Approved
OMB No. 0704-0188

The public reporting burden for this collection of information is estimated to average 1 hour per response, including the time for reviewing instructions, searching existing data sources, gathering and maintaining the data needed, and completing and reviewing the collection of information. Send comments regarding this burden estimate or any other aspect of this collection of information, including suggestions for reducing the burden, to Department of Defense, Washington Headquarters Services, Directorate for Information Operations and Reports (0704-0188), 1215 Jefferson Davis Highway, Suite 1204, Arlington, VA 22202-4302. Respondents should be aware that notwithstanding any other provision of law, no person shall be subject to any penalty for failing to comply with a collection of information if it does not display a currently valid OMB control number.
PLEASE DO NOT RETURN YOUR FORM TO THE ABOVE ADDRESS.

1. REPORT DATE *(DD-MM-YYYY)*	2. REPORT TYPE	3. DATES COVERED *(From - To)*
01-08-2004	Final	14-11-1997 -- 15-05-2001

4. TITLE AND SUBTITLE	5a. CONTRACT NUMBER
A Detailed Study of the Flowfield of a Submarine Propeller During a Crashback Maneuver	
	5b. GRANT NUMBER
	N00014-97-1-1069
	5c. PROGRAM ELEMENT NUMBER

6. AUTHOR(S)	5d. PROJECT NUMBER
Bridges, David H.	
	5e. TASK NUMBER
	5f. WORK UNIT NUMBER

7. PERFORMING ORGANIZATION NAME(S) AND ADDRESS(ES)	8. PERFORMING ORGANIZATION REPORT NUMBER
Department of Aerospace Engineering, Mississippi State University P.O. Drawer A Mississippi State, MS 39762	MSSU-ASE-04-01

9. SPONSORING/MONITORING AGENCY NAME(S) AND ADDRESS(ES)	10. SPONSOR/MONITOR'S ACRONYM(S)
Office of Naval Research ONR 333 -- Dr. L. Patrick Purtell 800 North Quincy Street Arlington, VA 22217-5660	ONR
	11. SPONSOR/MONITOR'S REPORT NUMBER(S)

12. DISTRIBUTION/AVAILABILITY STATEMENT

APPROVED FOR PUBLIC RELEASE

13. SUPPLEMENTARY NOTES

14. ABSTRACT

Tests were conducted in the Large Cavitation Channel of the submarine "crashback" maneuver using an existing submarine model and propeller to investigate the effects of the ring vortex that forms around the propeller during the maneuver. A range of steady crashback conditions with fixed tunnel and propeller speeds were investigated. Off-axis forces and moments were measured. The dimensionless force and moment data were found to collapse well when plotted against the ratio of the actual propeller speed to the propeller speed required for self-propulsion in forward motion. The force and moment coefficients were found to have a local maximum when this ratio was around -0.8 . Unsteady crashback maneuvers were also investigated with two different types of simulations, in which the propeller and tunnel speeds were allowed to vary. In some cases, the peak off-axis force and moment coefficient magnitudes exceeded those observed during the steady crashback measurements. The LDV studies showed that the ring vortex structure appeared to migrate upstream and outward as the reverse propeller speed increased in magnitude.

15. SUBJECT TERMS

submarine, crashback, maneuver, propeller, vortex, ring vortex

16. SECURITY CLASSIFICATION OF:			17. LIMITATION OF ABSTRACT	18. NUMBER OF PAGES	19a. NAME OF RESPONSIBLE PERSON
a. REPORT	b. ABSTRACT	c. THIS PAGE			David H. Bridges
U	U	U	UU	189	19b. TELEPHONE NUMBER *(Include area code)* 662-325-8298

Standard Form 298 (Rev. 8/98)
Prescribed by ANSI Std. Z39.18